Polarization and Two-Photon Spectroscopy of Xenon for Optical Magnetometry

by

Eric Robert Miller

B. Science, University of Northern British Columbia, 2011

A THESIS SUBMITTED IN PARTIAL FULFILLMENT
OF THE REQUIREMENTS FOR THE DEGREE OF

Doctor of Philosophy

in

THE FACULTY OF GRADUATE AND POSTDOCTORAL STUDIES

(Chemistry)

The University Of British Columbia

(Vancouver)

October 2018

The following individuals certify that they have read, and recommend to the Faculty of Graduate and Postdoctoral Studies for acceptance, the dissertation entitled:

Polarization and Two-Photon Spectroscopy of Xenon for Optical Magnetometry

submitted by ___Eric Miller___ in partial fulfillment of the requirements for the degree of ___Doctor of Philosophy___ in ___Chemistry___

Examining Committee:

Takamasa Momose, Chemistry
Supervisor

Ed Grant, Chemistry
Supervisory Committee Member

Andrew MacFarlane, Chemistry
University Examiner

Fei Zhou, Physics
University Examiner

Additional Supervisory Committee Members:

Akira Konaka, Chemistry
Supervisory Committee Member

Alex Wang, Chemistry
Supervisory Committee Member

Abstract

This dissertation presents work in the hyperpolarization of ^{129}Xe and in precision Xe spectroscopy using two-photon absorption. Both projects contribute to the development of optical magnetometry using ^{129}Xe. Motivating this work is the proposal for a new ^{129}Xe-based comagnetometer at TRIUMF for experiments searching for a permanent electric dipole moment of the neutron. In these proposed experiments ^{129}Xe will occupy the same experimental volume as ultracold neutrons and be used to measure drifts in an applied magnetic field. A scheme is described for optical magnetometry which involves the production of polarized ^{129}Xe followed by measurements using two-photon laser induced fluorescence as a probe.

Spin exchange optical pumping is used to produce polarized ^{129}Xe, which is a necessary precursor for optical magnetometry. The first part of this dissertation presents the implementation and operation of a polarizer using a diode laser and a Xe-Rb-N$_2$-He mixture. We have achieved hyperpolarization of ^{129}Xe up to $P_{Xe} \approx 5\%$, which is many times greater than the thermal equilibrium polarization. We measure the nuclear magnetic resonance signal from polarized ^{129}Xe using a low-field detection apparatus, and compare the signal with predictions based on a rate equation model. Efforts to optimize the degree of polarization in the present apparatus are described, as well as purification of Xe gas through freezeout.

The second part of this dissertation presents precision spectroscopy on natural abundance Xe using a narrow linewidth laser. The two-photon transition studied here ($5p^5 (^2P_{3/2}) 6p\ ^2[3/2]_2 \leftarrow 5p^6\ (^1S_0)$) is suitable to probe the ground state ^{129}Xe polarization for optical magnetometry. We present the implementation of a CW laser source with narrow linewidth followed by the excitation of Xe two-photon absorption in a resonant cavity. We measure and report hyperfine constants and isotope shifts from the observed laser induced fluorescence spectra. From the observed signal to noise ratio we estimate a magnetometric sensitivity based on this detection scheme over a range of Xe pressures. Results from this two-photon absorption measurement are essential in the determination of parameters for final implementation in the nEDM experiment.

Lay Summary

The effects of magnetism can change the way in which certain atoms absorb light. Some of the most precise magnetic sensors, used in both medical sciences and fundamental physics inquiries, are based on measuring these effects. Typically the atoms need to be prepared by aligning each atom's internal magnetic field to point in the same direction, producing a polarized state, before the effects of an external magnetic field can be detected. Only a few elements are suitable for use in sensors.

This dissertation studies the methods of producing polarized states in xenon atoms. It also studies the interaction between xenon atoms and light through a sensitive process called two-photon absorption, which only occurs when using powerful ultraviolet lasers. This work suggests a new technique for detecting the effects of magnetism on xenon atoms based on this process. The impact of this work is to enable the development of xenon-based precision magnetic sensors for specialty applications, such as measuring the magnetic field in a shared volume with ultracold neutrons, where sensors based on other atoms are not suitable.

Preface

This dissertation is based on the construction and operation of apparatus for the polarization and spectroscopy of ^{129}Xe, which was performed at UBC under the supervision of Dr. Takamasa Momose, with additional guidance from Dr. David Jones and Dr. Kirk Madison. The work performed was a joint effort in support of the international ultracold neutron collaboration at TRIUMF. Background information presented in Chapters 1 and 2 is the work of the collaboration ([1, 3, 126]), but none of the text of this dissertation is taken directly from previous work. The discussion of previous nEDM experiments at ILL and the ^{199}Hg comagnetometer are the work of the ILL collaboration, and figures are used with permission. The proposal to use two-photon excitation of ^{129}Xe comes from T. Chupp and A. Leanhardt [4]. The dual comagnetometer proposal and derivation of Section 2.1.4 are the unpublished work of Dr. C.A. Miller and Dr. Momose.

The ^{129}Xe polarizer presented in Chapter 3 was implemented by me with contributions and advice from Dr. Jeff Martin, Dr. Chris Bidinosti, and Mike Lang at U. Winnipeg and Dr. Jeff Sonier at Simon Fraser U. The Rb-filled glass cell used for spin exchange optical pumping (SEOP), and specifications for the gas mixture, were provided by Mike Lang. The NMR detector was provided by Dr. Sonier, and modified by me. Tomo Hayamizu did the COMSOL simulation which I used to calculate the field gradient induced relaxation. Dr. Jeff Martin provided the Python Bloch equations simulation used to optimize conditions for adiabatic fast passage (AFP). The results of the Bloch simulation and the rate equation model are my own work. Experimental work was mainly performed by myself with the help of two undergraduate students: Bill Wong and Aaron Ngai. Data collection and some of the data analysis on temperature dependence, batch mode polarization, and relaxation were performed by Aaron Ngai under my direction. Tomo Hayamizu installed SEOP cell heaters for optimizing heating conditions. The remaining experimental work and analysis was performed by me.

Chapter 4 presents two-photon spectroscopy with pulsed and continuous laser sources. The pulsed laser setup was implemented by Dr. Momose. I configured and installed the detection optics and implemented the data acquisition in LabView, and performed most of the data acquisition. Some of the data collection for polarization dependence was performed by Bill Wong under my direction. The analysis is my own work. The narrow-linewidth continuous laser was developed in Dr. Jones

lab by Emily Altiere and Joshua Wienands, who assembled the doubling stages and optimized mode matching and cavity locks. I helped locate and eliminate electronic noise sources to improve lock stability. Tomo Hayamizu offered suggestions based on parallel development of a laser for Hg spectroscopy. The doubling cavities and vacuum box were machined by Technical Services in the Physics and Chemistry Departments. I designed and assembled components for the vacuum box. The frequency comb used to obtain a beatnote reference was provided by Dr. Kirk Madison and Dr. Jones. Data collection for the high-resolution spectroscopy was performed by Emily Altiere and I. The LabView code used to frequency-sweep the laser and obtain the beatnote reference along with data acquisition is my work. The Matlab code used to stitch together frequency and signal measurements to calibrate the frequency axis was written by Emily Altiere and I. The multipeak implementation of the ODR fitting routine in Python and corresponding Lorentzian fit analysis was performed by me. The isotope shift analysis, Zeemax simulation of detector acceptance, and magnetometer sensitivity estimates are all my own work. The work in Chapter 4 has led to a publication "High-resolution two-photon spectroscopy of a $5p^56p \leftarrow 5p^6$ transition of xenon" in Physical Review A (2017) [8].

Table of Contents

List of Tables

List of Figures

Glossary

AFP   Adiabatic Fast Passage

BBO   Beta Barium Borate

CPT   Charge Parity Time reversal symmetry

DUV   Deep Ultraviolet

EMF   Electromotive Force

FID   Free Induction Decay

FSR   Free Spectral Range

LBO   Lithium Triborate

LIF   Laser Induced Fluorescence

NEDM   Neutron Electric Dipole Moment

NIR   Near Infrared

NMR   Nuclear Magnetic Resonance

OPSL   Optically Pumped Semiconductor Laser

PDH   Pound Drever Hall

PMT   Photomultiplier Tube

REMPI   Resonance-Enhanced Multiphoton Ionization

RF   Radiofrequency

RLC   Resistor-Inductor-Capacitor

SEOP   Spin Exchange Optical Pumping

SHG   Second Harmonic Generation

SQUID   Superconducting Quantum Interference Device

TALIF   Two Photon Absorption Laser Induced Fluorescence

TPA   Two Photon Absorption

TPE   Two Photon Emission

UCN   Ultracold Neutrons

Acknowledgments

Chapter 1

Introduction

Atomic magnetometry has found application in the investigation of fundamental symmetries in subatomic systems. In particular ^{199}Hg was used as a magnetometer to great success in the latest precision measurement looking for a non-zero permanent Neutron Electric Dipole Moment (NEDM) [15, 124]. Other diamagnetic atoms with nuclear spin have been proposed as superior candidates to ^{199}Hg ($I = 1/2$), subject to demonstration of suitable detection schemes. Among these is ^{129}Xe ($I = 1/2$).

The goal of this work is to perform precision spectroscopy on atomic Xe using two-photon transitions, and to develop techniques and apparatus for optical magnetometry using two-photon transitions. The longterm goal of the project is to build an atomic magnetometer based on the spin precession of ^{129}Xe, which will share a chamber with trapped Ultracold Neutrons in an experiment at TRIUMF measuring the neutron electric dipole moment. Such a magnetometer must detect magnetic fields in the experiment and be free of dielectric breakdown in the high voltage electric fields also being applied. The device is based on polarization of Xe via spin exchange optical pumping, and detection of the degree of polarization during spin precession using two photon absorption. Spin exchange optical pumping is a technique to polarize Xe through collisions with much more easily polarized alkali metal atoms. Two photon absorption is a technique using intense laser beams to cause atomic transitions into excited states through the simultaneous absorption of two photons of the requisite energy. The theory of these are covered in Chapter 2.

This introduction presents the motivation for development of a Xe-based comagnetometer. Section 1.1 describes the experimental goals of the neutron EDM measurement performed using ultracold neutrons, which tests time-reversal symmetry. Section 1.2 describes the need for magnetometry and some properties of ^{129}Xe that make it suitable as a comagnetometer. Section 1.3 summarizes the component techniques of polarization, precession, and two-photon detection necessary to utilize ^{129}Xe in a comagnetometer. Section 1.4 is the road map of the theory and research work for the rest of the thesis.

1.1 Ultracold Neutrons and the Neutron Electric Dipole Moment measurement

1.1.1 The search for Charge Parity (CP) violation

Table 1.1: Behaviour of measurables under the operators C,P,T.

		C	P	T
$\vec{s}$	Angular momentum	+	+	-
$\vec{\mu}$	Magnetic dipole moment	-	+	-
$\vec{d}$	Electric dipole moment	-	+	-
$\vec{E}$	Electric field	-	-	+
$\vec{B}$	Magnetic field	-	+	-

There are three transformations under which the laws of physics, in the past, were thought to be invariant[76]. These are charge-conjugation (C), referring to the replacement of every particle with its antiparticle; parity (P), referring to the coordinate transformation $(x, y, z) \rightarrow (-x, -y, -z)$; and time-reversal (T), referring to running a process backwards in time. Table 1.1 shows how spin and fields transform under the application of these operators. To date no experimental evidence has been observed for breaking of the combined operations (product) of Charge Parity Time reversal symmetry (CPT); and therefore CPT conservation is assumed in the present work. Nonetheless, certain violations of these symmetries have been observed to occur in specific combinations in nature, as described below.

CP-violating processes are implicated as a reason why we observe predominantly matter and very little antimatter in the present universe. The observed universe contains, almost exclusively, "normal" matter, e.g., positively charged protons and negatively charged electrons. One way to quantify the prevalence of normal matter over antimatter is by calculating the "baryon asymmetry" of the universe, defined as $\eta = (n_B - n_{\bar{B}})/n_\gamma$, with n_B, $n_{\bar{B}}$, and n_γ the number densities of normal baryons, antibaryons, and cosmic background radiation photons, respectively. The present observed baryon asymmetry is $\eta = (6.21 \pm 0.16) \times 10^{-10}$ [54]. In the early universe there should have been equal amounts of matter and antimatter, and at some time an interaction arose which favoured production of matter. CP-violation is one of the three "Sakharov conditions" necessary for interactions that favour production of matter, along with ii) baryon number violation and iii) non-equilibrium thermal conditions[146].

Strong and electromagnetic interactions are observed to conserve C, P, and T symmetries, but the weak interaction maximally violates C and P. The first experimental proof of parity violation was observed by Wu [167], who showed that there was an asymmetry in the beta decay of polarized cobalt-60, with electrons emitted exclusively in the direction of the nuclear spin. CP violation was

observed soon after by Fitch and Cronin [46], who observed a long lived beam of neutral kaons to occasionally decay into two pions, when CP invariance required it decay exclusively into three pions. CP violation has more recently been observed in the decays of neutral B mesons[13]. The observed CP violation comes from the complex phase of the quark mixing (Cabbibo-Kobayashi-Maskawa) matrix [40, 97].

The predominance of normal matter over antimatter, as defined by the baryon asymmetry, implies that CP violation occured at higher rates than the Standard Model currently accounts for by the above processes. Therefore there must be other sources of CP violation that we are missing.

New experiments are looking for evidence of symmetry violation in atomic systems and in free neutrons. The existence of a permanent electric dipole moment in a subatomic particle violates time-reversal (T) symmetry; both the electric and magnetic dipole moment will be parallel to spin, i.e. $\vec{d}_n || \vec{\mu}$. Under time-reversal the magnetic dipole moment reverses orientation, but an EDM does not. Thus there is a contradiction: the two dipole moments will be parallel in the normal particle and antiparallel in the time-reversed particle. Under the assumption that CPT symmetry is conserved then a permanent EDM is also a source of CP-violation. Placing a limit on the value of the EDM helps to constrain theoretical models of CP violation. The most recent measurements looking for a permanent neutron EDM have been performed using Ultracold Neutrons.

1.1.2 Ultracold Neutrons

Measurements of the nEDM require confinement of free neutrons for a suitable measurement time on the order of hundreds of seconds. Previous experiments used neutron beams in vacuum; however, the modern implementation of nEDM experiments use confined ultracold neutrons.

Ultracold Neutrons (UCN) are free neutrons (quark composition udd, charge $= 0$, mass $= 1.67 \times 10^{-27}$ kg [113]) with kinetic energies lower than 10^{-7} eV [71]. This is orders of magnitude lower energy than typical for subatomic particles, and corresponds to a velocity around $7 \, \text{m s}^{-1}$. UCN are so slow-moving that they can be confined in closed bottles, without magnetic or electric trapping. This is because UCN have long de Broglie wavelengths and can interact repulsively with nuclei in the walls of the bottle via the strong nuclear force. The exact kinetic energy of the UCN correspond to their gravitational potential energy of $102 \, \text{neV m}^{-1}$. This can be used advantageously in experiments; for example, the velocity distribution may be modified by placing a neutron absorber at a specified height in a cell to absorb all neutrons reaching that height; similarly, it is possible to provide enough kinetic energy to transmit UCN through a potential barrier such as a metal foil, merely by dropping them from an altitude of several meters. UCN may be produced by cooling the neutrons produced by nuclear fission or by spallation of nuclei. As with all free neutrons, the lifetime of UCN via β-decay is $877.7(8) \, \text{s}$ [121].

TRIUMF has installed a UCN source which aims to produce world-record UCN densities for fundamental physics experiments. The source produces highly energetic MeV neutrons through

3
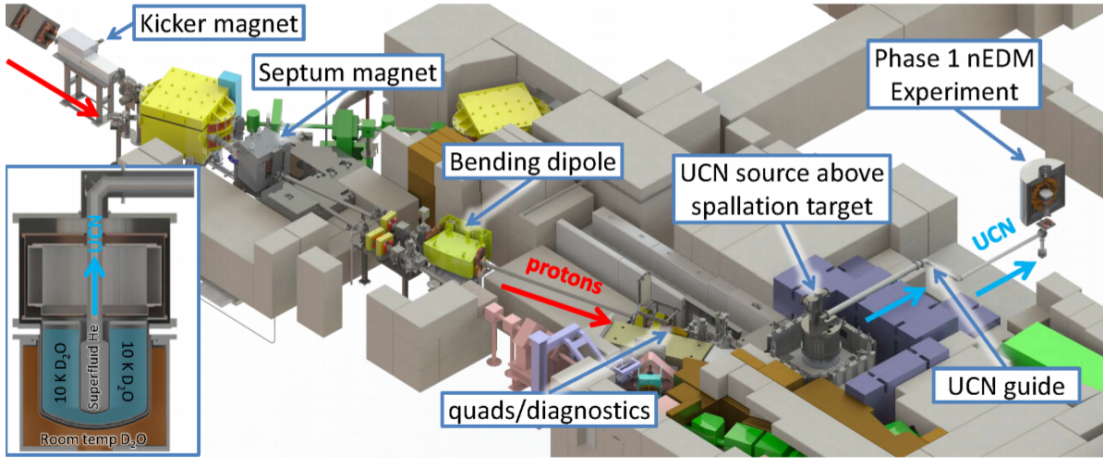
Figure 1.1: Beamline and superfluid He-II cryostat for producing UCN by spallation of a tungsten target. [126]

proton spallation on a tungsten target. A multi-layer cryostat cools these neutrons: first they are moderated in nested volumes of liquid and solid (cryogenic) D_2O to cold neutron energies; second, they downscatter in a superfluid $He-II$ filled volume to become UCN and are trapped by the strong interaction within the walls of the volume. From there UCN can be released through a valve and polarized via a strong magnetic field, and delivered to experiments. The flagship experiment for the new facility is the neutron electric dipole moment (EDM) measurement described below. The existing source was developed at the Research Center for Nuclear Physics (RCNP) in Osaka, Japan and produced a UCN density of $26\,UCN\,cm^{-3}$ [106] when irradiated with a 400 MeV, $1\,\mu A$ proton beam. The target density at TRIUMF is $7000\,UCN\,cm^{-3}$ in the source and $200\,UCN\,cm^{-3}$ in the EDM cell [3] This is attainable by irradiation with the higher intensity 500 MeV, $40\,\mu A$ proton beam available at TRIUMF.

1.1.3 Neutron Electric Dipole Moment measurement in UCN

Searching for the permanent electric dipole moment of a subatomic particle is a test of symmetry in the Standard Model. The existence of such a permanent charge separation in a nucleon or electron violates P and T; this can be derived from Table 1.1. The Hamiltonian of a fermion with magnetic dipole moment μ and electric dipole moment d_n in combined magnetic and electric fields is given by:

$$H = -\vec{\mu} \cdot \vec{B} - \vec{d_n} \cdot \vec{E} \tag{1.1}$$

The result of the parity operator acting on the Hamiltonian above is $P(H) = -\vec{\mu} \cdot \vec{B} - \vec{d_n} \cdot (-\vec{E}) \neq H$. Because the Hamiltonian is not invariant under the transformation, it violates parity. It is specifi-

4
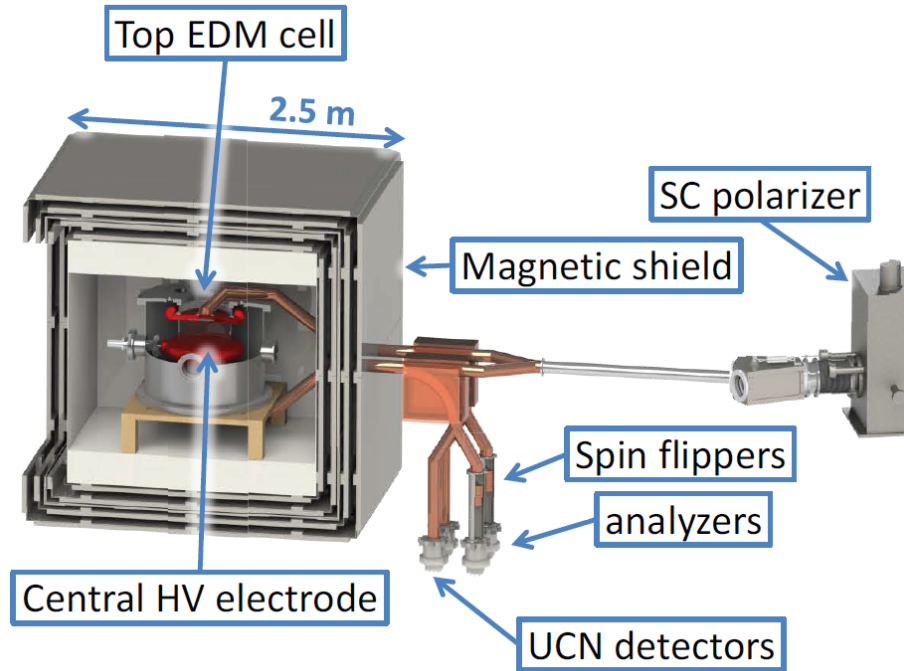
Figure 1.2: Proposed configuration for UCN guides and neutron EDM experimental cell. [126]

cally the term $\vec{d}_n \cdot \vec{E}$ which is the source of the parity violation; the magnetic dipole term is invariant. Likewise, under time reversal $T(H) = -(-\vec{\mu}) \cdot (-\vec{B}) - (-\vec{d}_n) \cdot \vec{E} \neq H$. As CPT is still assumed to be conserved, T-violation implies CP-violation also.

Electric Dipole Moment searches have been carried out on neutrons as well as in a number of atomic and molecular systems. The results of EDM experiments on some of these systems are presented in Table 1.2. The experimental EDM under study in each atom or molecule may arise from a combination of either an electron EDM d_e, a neutron EDM d_n, or certain electron-nucleon and pion-nucleon interactions, as described in Reference [47]; each system varies in its sensitivity to the above interactions, making the study of EDM in many systems a complementary effort. Many of the experiments listed in the table are ongoing; there are additional systems currently under study or proposed, including atomic Fr [88], and protons in a storage ring [9]. There has been no non-zero measurement of a permanent EDM to date; in the case of neutrons the EDM predicted by the Standard Model is $\approx 10^{-31}\,\mathrm{e}\cdot\mathrm{cm}$ [69]. For comparison, this is twenty-two orders of magnitude smaller than the dipole moment of a water molecule (1.85 debye $= 3.85 \times 10^{-9}\,\mathrm{e}\cdot\mathrm{cm}$). Extensions (Beyond Standard Model theory) predict larger values, thus nEDM measurements also serve as a test of Beyond Standard Model theories.

The typical procedure in an EDM measurement is the controlled application of parallel and

antiparallel electric and magnetic fields. Although the neutron is electrically neutral, it has a nuclear magnetic moment due to its spin $I = 1/2$ and will undergo precession at the Larmor frequency $\omega = \gamma B$. The interaction between electric dipole and electric field $\vec{d}_n \cdot \vec{E}$ imposes a slight frequency shift which can be detected as a difference $\delta\omega$ between runs with B and E either parallel or antiparallel.

Table 1.2: Experimental results of EDM searches in neutrons, and in atomic and molecular systems (adapted and updated from [47]). Each result is represented either as the total atomic or molecular EDM, or is interpreted as an EDM limit on the electron d_e. The neutron EDM is d_n.

System	Result (e.cm)	Year & Source
neutron	$d_n = -0.21(1.82) \times 10^{-26}\,\mathrm{e \cdot cm}$	2015 [124]
Cs	$d_{Cs} = -1.8(6.9) \times 10^{-24}\,\mathrm{e \cdot cm}$	1989 [115]
Tl	$d_{Tl} = -4.0(4.3) \times 10^{-25}\,\mathrm{e \cdot cm}$	2002 [139]
YbF	$d_e = -2.4(5.9) \times 10^{-28}\,\mathrm{e \cdot cm}$	2011 [84]
ThO	$d_e = -2.1(4.5) \times 10^{-29}\,\mathrm{e \cdot cm}$	2014 [17]
^{199}Hg	$d_{Hg} = -2.2(3.1) \times 10^{-30}\,\mathrm{e \cdot cm}$	2016 [74]
^{129}Xe	$d_{Xe} = 0.7(3.0) \times 10^{-27}\,\mathrm{e \cdot cm}$	2001 [142]
TlF	$d = -1.7(2.9) \times 10^{-23}\,\mathrm{e \cdot cm}$	1991 [45]
^{225}Ra	$d_{Ra} = 4(6) \times 10^{-24}\,\mathrm{e \cdot cm}$	2016 [23]

The first nEDM measurement was performed by Smith, Purcell, and Ramsey on a neutron beam in vacuum using separated oscillatory fields, a technique which has come to be known as Ramsey Resonance. This technique is described in detail in 2.1.1. This early measurement yielded the value $(-0.1 \pm 2.4) \times 10^{-20}\,\mathrm{e \cdot cm}$ [151]. Experiments since the 1980s used UCN confined in a bottle, starting with the research group at Leningrad Nuclear Physics Institute (LNPI) [6], to improve systematic uncertainties. This makes it possible to reduce the width of the magnetic resonance line for a fast-moving neutron beam. Additionally the long lifetime of UCN makes it possible to increase the interaction time with the applied fields. The best result to date [124] sets an upper limit of $3.0 \times 10^{-26}\,\mathrm{e \cdot cm}$ (90% C.L.). The TRIUMF experiment wants to lower the nEDM upper limit to $< 10^{-27}\,\mathrm{e \cdot cm}$ [3], representing an improvement over an order of magnitude. The target will be acheivable in large part due to an increase in neutron density attainable at TRIUMF. Fig. 1.2 shows the experimental configuration planned at TRIUMF for the neutron EDM measurement, which is described further in Reference [126]. UCN will be confined in a vacuum bottle (diameter $\approx 20 - 30\,\mathrm{cm}$) between high voltage electrodes separated by a cylindrical insulator ring. The experimental apparatus is decoupled from stray environmental magnetic fields by layers of mu-metal shielding and active field compensation; inside the shielding, additional field coils will produce a very uniform magnetic field ($|B_0| \approx 1\,\mu\mathrm{T}$). Precise magnetometry is required in the technique to reduce systematic uncertainties; this motivates development of the Xe comagnetometer described below.

1.2 Motivation for developing a Xe comagnetometer

The search for a neutron EDM is limited by many systematic effects. The experiment requires a very stable magnetic field, in order to track changes in the neutron precession frequency correlated only with a reversal in electric field. Drifts in magnetic field (on the order of a few tens of pT) due to changing ambient conditions can completely mask the true EDM signal and are a limiting factor to sensitivity. The most significant innovation of previous generation nEDM experiments reaching $10^{-26}\,\mathrm{e\cdot cm}$ was the installation of a cohabiting ^{199}Hg optically pumped atomic magnetometer to measure and account for magnetic field fluctuations [15, 75]. This "comagnetometer" shares the same experimental volume as UCN and samples the same time- and volume-averaged magnetic field with sub-pT accuracy. Optically pumped magnetometers themselves belong to a larger family of magnetic sensors technologies, including flux gates, Hall probes, proton-precession magnetometers, SQUID, nonlinear magneto-optical rotation magnetometers and magnetoresistive devices [104]. Each of these fulfill different requirements and have different limitations[77] [103]. A short description of some of the techniques is given in A.1. In the nEDM experiment, prior efforts to track the drifting magnetic field using external Rb vapour magnetometers mounted outside the experiment proved ineffective due to the separation distance between magnetometer and neutrons [75]. Only a comagnetometer occupying the same volume could suitably measure the field. Detailed description of the comagnetometer operation is given in Section 2.1.2.

1.2.1 Advantages of using ^{129}Xe

Optical magnetometry can in principle be performed using any atomic species possessing a non-zero total spin F in the ground state. This includes both paramagnetic (Rb, Cs) and diamagnetic atoms (^{3}He, ^{199}Hg, ^{129}Xe). ^{129}Xe possesses certain advantages particular to the nEDM experiment. One major advantage is that xenon has a cross section for neutron absorption which is two orders of magnitude smaller than that of mercury. The absorption cross sections for thermal neutrons are 2.1×10^1 barns (1 barn = $10^{-28}\,\mathrm{m}^2$) for ^{129}Xe and 2.15×10^3 barns for ^{199}Hg [99]. One of the original motivations for choosing ^{129}Xe at TRIUMF was the possibility to reduce the frequency shifts from the so-called geometric phase effect (described in Section 2.1.3) by increasing the atomic density enough to have a very short mean free path, although it remains to be determined if such high density is compatible with the high voltage ($15\,\mathrm{kV\,cm^{-1}}$) electrodes used in nEDM measurements. Additional advantages are that Xe is a noble gas, non toxic and inert in the nEDM cell, in constrast to alkali metal atoms. ^{129}Xe has the same $I = 1/2$ nuclear spin configuration as ^{199}Hg which results in a simple electronic and Zeeman level structure. Table 2.1 shows that the gyromagnetic ratio of ^{129}Xe is the same sign as that of the neutron and opposite to that of ^{199}Hg, which helps to identify effects of diurnal rotation in the (non-inertial) laboratory frame. ^{129}Xe can be easily polarized, as has been previously demonstrated by Spin Exchange Optical Pumping (SEOP) (see Section 2.2.2

7
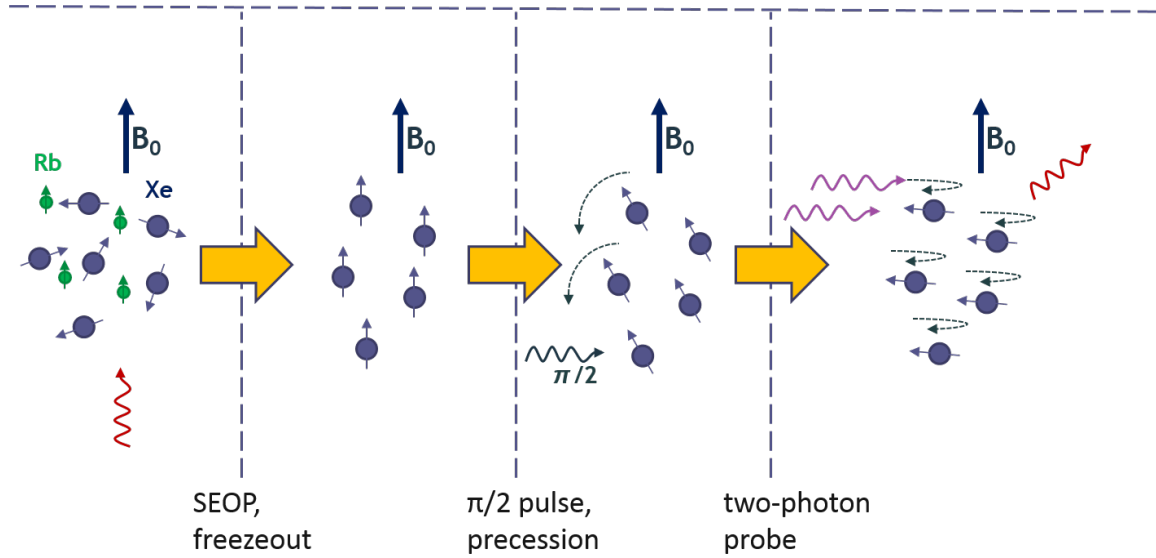
Figure 1.3: Scheme for ^{129}Xe-based comagnetometry: polarization of ^{129}Xe, (blue) via spin exchange optical pumping with polarized Rb (green), followed by freezeout, precession, and detection using a two-photon transition.

and Chapter 3); SEOP cross sections for Xe are the highest of the noble gases. [162]. Like ^{199}Hg, a suitable optical transition for ^{129}Xe has been identified; however, at convenient laser wavelengths, the excited electronic states of ^{129}Xe are accessible only by two photon transitions. Demonstrating optical detection of ^{129}Xe using two photon transitions is the focus of this current work. Finally, by providing a second nEDM-compatible comagnetometer species, we open the possiblity of measuring not only the magnetic field but also the vertical gradient dB_0/dz by simultaneous measurements on two comagnetometer species. This is discussed in Section 2.1.4.

1.3 Techniques planned for the Xe comagnetometer

The future xenon-based comagnetometer will make use of very similar techniques to that successfully used in previous nEDM measurements with mercury. The optical detection scheme proposed for ^{129}Xe is shown in Fig. 1.3. Samples of polarized ^{129}Xe will be prepared by spin exchange optical pumping, starting with (likely isopure) ^{129}Xe mixed with Rb vapour, He, and N_2. The polarization will be calibrated using Nuclear Magnetic Resonance (NMR) techniques. The polarized ^{129}Xe will be separated from Rb and purified via freezeout in a cryogenic trap under strong applied magnetic field, and the residual gas pumped away. Controlled heating of the trap will deliver a controlled vapour pressure of polarized ^{129}Xe to the experimental nEDM cell. The transport lines will be arranged to allow adiabatic transport into the cell without loss of polarization. Samples of polarized UCN, ^{129}Xe, and ^{199}Hg will be injected into the cell. Three separate Radiofrequency (RF)

pulses will initiate free spin precession of the three species. During the free spin precession time of ≈ 40s, each species undergoes hundreds of periods of precession; the UCN spin precession will be measured using Ramsey Resonance while spin precession of ^{129}Xe, and ^{199}Hg will be monitored optically. For ^{199}Hg, monitoring involves excitation with a weak 253.7 nm probe beam and detection of the transmitted light. For ^{129}Xe, monitoring involves two-photon excitation with 252.5 nm light and detection of the Laser Induced Fluorescence (LIF) at 823 nm. Both signals (^{129}Xe, and ^{199}Hg) will display modulation at their respective Larmor frequencies, and will take the form of a decaying sinusoid. For each species this signal will be digitized and fit to extract an average $\omega_{Xe(Hg)}$. The fitting routine will likely involve counting zero crossings of the several hundred detected spin precession periods to estimate the frequency and adding a small correction based on fitting to the initial and final phase.

The precession frequencies of ^{129}Xe and ^{199}Hg will be used to correct the neutron precession frequency for any time-dependant drift in the magnetic field. Additionally, the combined measurements of both precession frequencies can be used to correct for frequency shifts due to a vertical field gradient, as described in Section 2.1.4

1.4 Dissertation overview

This dissertation describes work developing a ^{129}Xe polarizer based on spin exchange optical pumping and a optical detection scheme based on two photon transitions. This introductory chapter described the motivation to develop a comagnetometer, namely, detection of magnetic field drifts to improve the sensitivity of neutron EDM experiments which search for new sources of CP violation.

The first section of Chapter 2 describes comagnetometry in greater detail, with an overview of experimental techniques used in the neutron EDM measurement. The remaining sections describe the theory behind two important techniques necessary for Xe comagnetometry: spin exchange optical pumping and two-photon absorption. The electronic structure of Xe is described along with the states accessible by two-photon absorption. Chapter 3 describes the implementation of a SEOP-based Xe polarizer and its operation. A modest polarization is generated as proof of polarization and detected by performing Adibatic Fast Passage, and compared with predictions based on a rate equation model. SEOP has been well studied and even commercialized elsewhere; the value of the work done in this lab lies in developing the ability to provide polarized Xe for testing of two-photon comagnetometer signals. Chapter 4 demonstrates a breakthrough in excitation of the two-photon transition with narrow linewidth light suitable to selectively probe the appropriate hyperfine levels in the scheme described above. The chapter describes initial experiments in excitation of the relevant two-photon transitions with a pulsed laser, followed by high-resolution spectroscopy enabled by development of a narrow linewidth CW laser. From this spectroscopic work we extract improved measurement of the hyperfine constants and isotope shifts. Measurements of pressure broadening and signal intensity are performed, motivated by the need to determine parameters for implemen-

tation in the nEDM experiment. Specifically, we consider the signal amplitude and corresponding estimates of magnetometric sensitivity at low Xe partial pressures (approaching 1 mTorr). Such low pressures may be required when Xe is introduced into the high-voltage nEDM cell, in order to avoid any electrical breakdown. The concluding chapter describes ongoing and future work focused on establishing the suitability of ^{129}Xe as a comagnetometer species.

Chapter 2

Literature and Theory

2.1 Comagnetometry and the Neutron Electric Dipole Moment experiment

Comagnetometers are optical magnetometers which rely on the detection of spin precession. The term comagnetometer refers to a separate spin-polarized gas that shares the same volume as the species under study in an EDM measurement, and provides a time- and volume- averaged measurement of the magnetic field. Comagnetometry was discussed by Lamoreaux [102], who proposed ^{199}Hg as a volume comagnetometer for the ILL nEDM experiment. Description of the techniques used for previous experiments utilizing ^{199}Hg are given in this section.

Other uses of comagnetometry

Comagnetometry was also used in a ^{129}Xe EDM measurement [142], with ^{3}He as the comagnetometer. The EDM of ^{3}He was assumed to be smaller than that of ^{129}Xe because the effects of CP-violation in the atom scale as Z^2 or more with atomic number, making ^{3}He a suitable comagnetometer. The ^{3}He resonance was detected using coils rather than optically. A new search for the ^{129}Xe EDM uses a ^{3}He comagnetometer with resonance detected via a Superconducting Quantum Interference Device (SQUID) magnetometer [101]. These applications will be discussed in Section 5.2.4.

2.1.1 Ramsey Resonance technique for nEDM measurements

It is necessary to describe the experimental technique used to measure the precession frequency of the neutrons, as the comagnetometer is subjected to the same fields, and in fact the techniques share many similarities. The TRIUMF nEDM experiment utilizes a technique known as Ramsey resonance, first described by Ramsey in 1950 [136]. The key to this technique is the use of separated oscillating fields to make a precise measurement of the precession frequency based on comparison
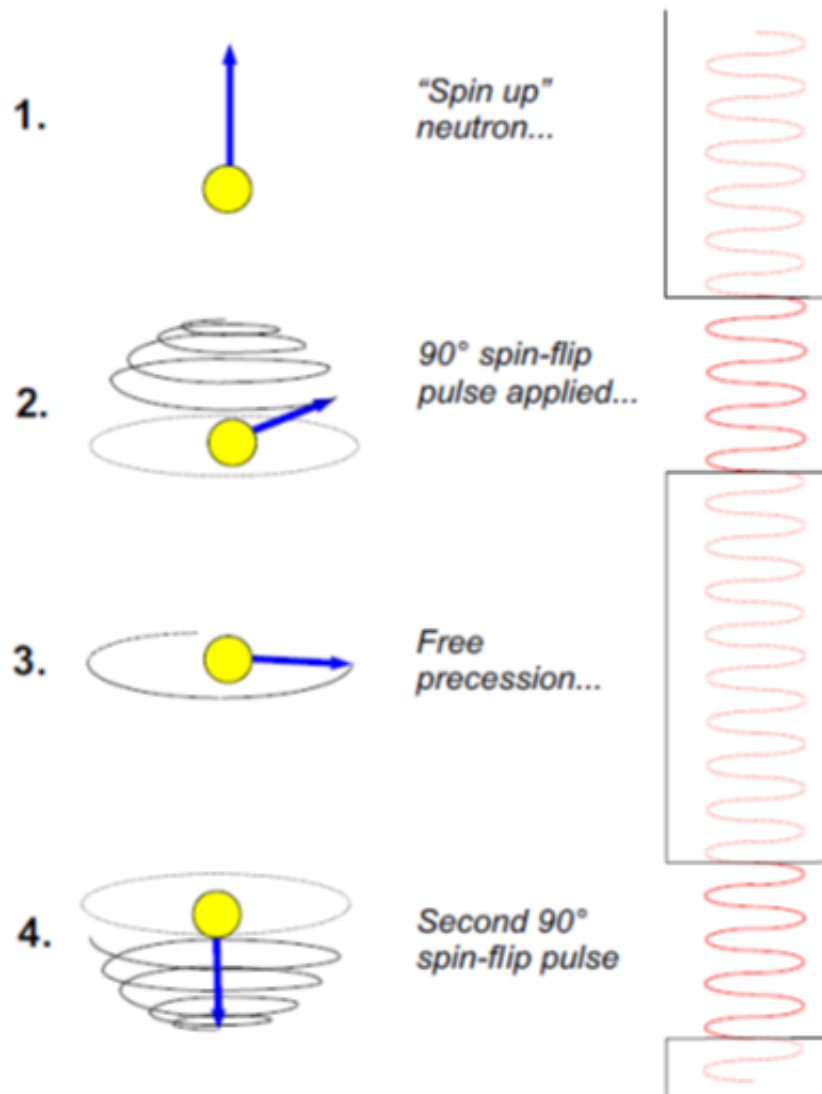
Figure 2.1: The Ramsey Resonance technique used for high precision measurements of neutron precession frequency. See text for description. $\vec{B}_0$ is vertical in the figure while $\vec{B}_1$ is horizontal. During the free precession time, neutrons complete hundreds of precession periods and may acquire a phase shift from the (gated off) stable oscillator ω_1 (red). (Reprinted from [16]pg.187 with permission from Elsevier)

of the phase difference with a stable oscillator. In initial neutron beam experiments the oscillating fields were separated in distance; in today's experiments with UCN the fields are separated in time. The technique proceeds as follows (see Fig. 2.1):

1. neutrons are prepared in a "spin up" $M_I = 1/2$ state in the presence of an applied homogeneous magnetic field $\vec{B}_0$ on the order of μT.

2. A rotating magnetic field B_1 perpendicular to $\vec{B}_0$ at frequency $\omega_1 \approx \gamma B_0$ is applied to rotate the spins away from $\vec{B}_0$. The magnitude and duration of $\vec{B}_1$ are controlled to ensure a spin flip of exactly 90 degrees $(\pi/2)$ and then gated off.

3. The spins are subjected to free spin precession about $\vec{B}_0$ for hundreds of precession cycles during time t. During this time which they acquire a phase $((\omega_1 - \gamma B_0)t)$.

4. A second $\pi/2$ pulse is applied to the spins. This rotates the spins either up or down depending on the accumulated phase, compared against the stable oscillator at ω_1. If the phase is an integer multiple of 180 degrees, the spins rotate back parallel to $\vec{B}_0$. If the phase is zero or an integer multiple of 360 degrees, the spins rotate downwards and become antiparallel to $\vec{B}_0$.

The population of one or both spin states is measured following the cycle and plotted against frequency ω_1. This is shown in Fig. 2.2 for the spin up population. Fringes appear for every accumulated phase shift of π between ω_1 and γB_0. The resonant Larmor frequency is determined by the value of ω_1 at the central fringe. As plotting the entire curve would require hundreds of data-taking cycles, a precise measurement of the resonant frequency is typically determined by taking data at four points, two on either side of the resonance, for which the change in counts is steepest. A fit to these points determines the resonant frequency. This technique is often used in EDM experiments to allow a long interaction time with an applied electric field $\vec{E} \parallel \vec{B}_0$. The phase shift acquired in step 3) can come from either term of the Hamiltonian in Eq. 1.1, which means that interaction of an EDM with $\vec{E}$ shifts the resonant frequency. Comagnetometry is used during step 3) to monitor $\vec{B}_0$ for drifts.

2.1.2 Need for comagnetometry and principle of operation

Comagnetometry is necessary to make a precise measurement of the EDM in the presence of field drifts and other systematic effects. It is readily apparent that some form of magnetometry is needed, because the effect of $\vec{B}_0$ is so much larger than the effect of $\vec{E}$. For example, taking $\vec{B}_0 = 1\,\mu\text{T}$ and $\vec{E} = 15\,\text{kV}\,\text{cm}^{-1}$ as typical parameters for an EDM search, the ratio between the effect of $\vec{B}_0$ and that of $\vec{E}$ for an EDM at the current $10^{-26}\,\text{e cm}$ level of sensitivity is $\frac{\mu B}{d_n E} \approx 10^9$. This means that ppb drifts in the magnetic field, left uncorrected, will completely mask the presence of an EDM. Drifts from external environmental sources, such as that of moving an overhead crane, have been identified and corrected for in past experiments using atomic magnetometers mounted outside the nEDM cell. However, certain local magnetic field changes affect the EDM cell in a way that such external magnetometers cannot readily detect. One of these effects is the local magnetic field generated by leakage currents flowing between HV electrodes through the EDM cell wall, which doubles as the electrode spacer [152]. Another possibility is the residual magnetization of an internal component. A comagnetometer occupies the same volume as the EDM species, and is precisely sensitive to the effects of leakage currents and other localized magnetic fields.
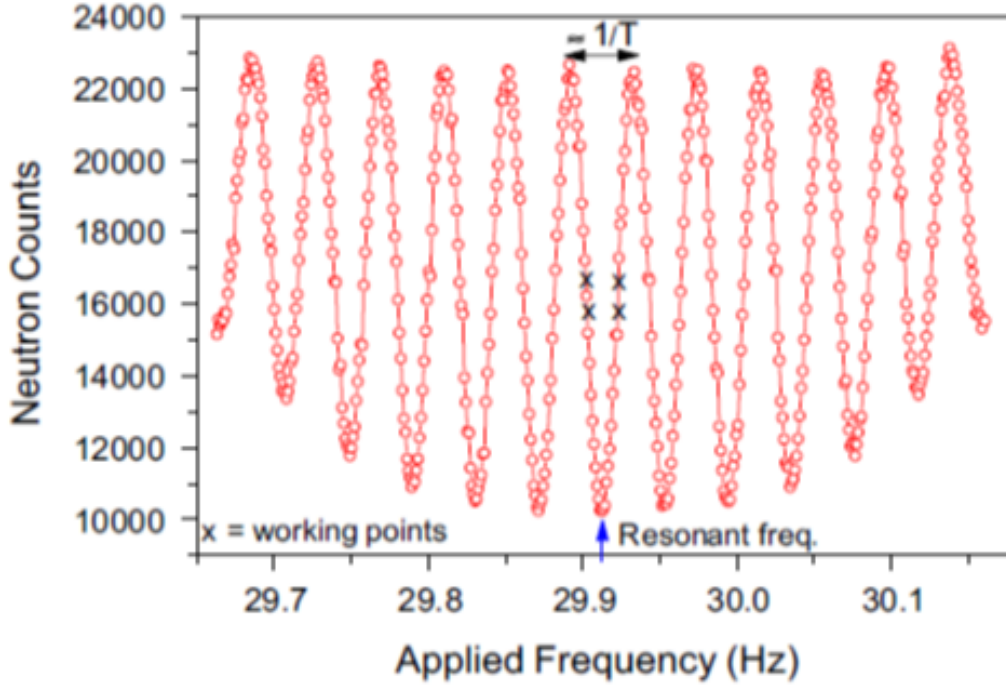
Figure 2.2: Ramsey Resonance fringes used to precisely measure the precession frequency. (Reprinted from [16]pg.187 with permission from Elsevier)

Principle of operation

As a type of optical magnetometer, the comagnetometer uses techniques of magnetic resonance and spin precession similar to the EDM species. This section describes the operation following the ^{199}Hg comagnetometer successfully operated in the nEDM measurement at ILL [16, 75]. The requirements on the species used as comagnetometer are: it must not itself have an EDM, at least not one large enough to introduce uncertainty in the interpretation of any measured frequency shift; it must occupy the same volume, and must be compatible with the requirements of the host experiment. ^{199}Hg satisfies these requirements. The intrinsic EDM of ^{199}Hg was measured to be smaller than $|d_{Hg}| < 7.4 \times 10^{-30}$e·cm [74], in an optical experiment conducted on a stack of four cells filled with ^{199}Hg exposed to $\vec{B}_0$ and $\vec{E}$ fields and externally shielded. The cells are optically pumped transverse to $\vec{B}_0$ by synchronous optical pumping.

The operation of the mercury comagnetometer essentially follows steps 1-3) of Fig. 2.1. First, ^{199}Hg atoms in an external cell are polarized parallel to $\vec{B}_0$ using optical pumping (see Section 2.2) of the transition $6s6p(^3P_1) \leftarrow 6s^2(^1S_0)$ with circular polarized light at 253.7 nm. Atoms are optically pumped for a period of approximately four minutes and injected into the nEDM cell at the start of an experimental cycle. The cell is filled with ^{199}Hg and UCN, and two $\pi/2$ pulses are applied at
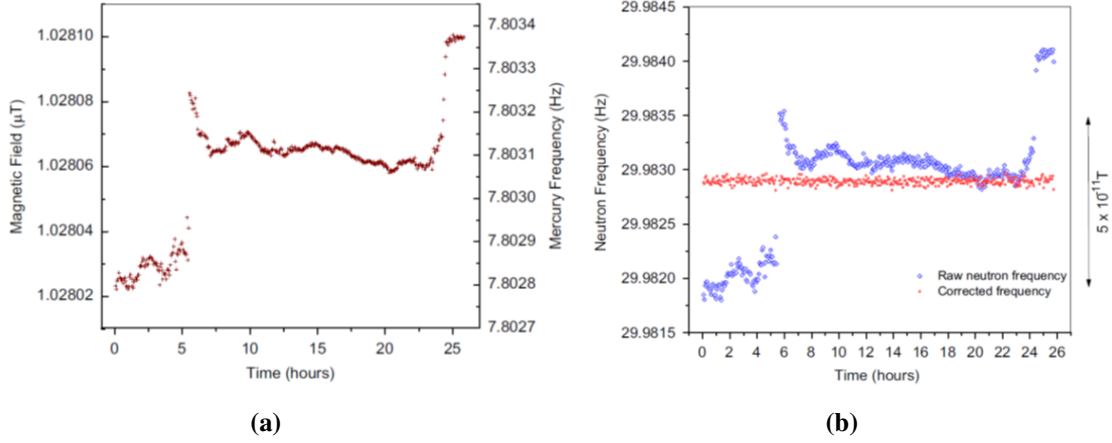
Figure 2.3: Comagnetometer performance in the ILL experiment. Magnetic field drifts (a) on the order of 70 ppm cause a corresponding shift in neutron precession frequency (b), which is corrected for by simultaneous monitoring of the precession frequency of ^{199}Hg. (Reprinted from [16]pg.193 with permission from Elsevier)

the respective Larmor frequencies for ^{199}Hg and UCN. Both species exhibit free spin precession about $\vec{B}_0$ in step 3) until the end of the cycle. During this free spin precession, the light absorption of ^{199}Hg is probed with circular polarized light propagating through the cell transverse to $\vec{B}_0$. The absorption of this light varies sinusoidally at the Larmor frequency ω_{Hg}. The transmitted light is detected and converted to a voltage signal with the shape of a sinusoidal decay curve. The time-averaged resonance frequency ω_{Hg} is determined by counting zero crossings and fitting waveforms to the first and last few seconds of data. A precise measurement of $\vec{B}_0$ was effectively determined from the Larmor frequency $\omega_{Hg}(=2\pi v_{Hg})=\gamma B_0$; typically, however, ω_{Hg} is used directly in a frequency ratio (with $\left|\gamma_n/\gamma_{Hg}\right| \approx 3.77$) to calculate the nEDM:

$$\frac{v_n}{v_{Hg}} = \left|\frac{\gamma_n}{\gamma_{Hg}}\right| + \frac{d_n + |\gamma_n/\gamma_{Hg}|d_{Hg}}{v_{Hg}}E \tag{2.1}$$

The performance of the comagnetometer in the presence of external magnetic field drifts is shown in Fig. 2.3. Over the course of a 25 hour run, a cycle-by-cycle field shift induced changes on the order of 70 ppm to the resonant frequency for both ^{199}Hg and UCN. That the change occurred in both channels indicates that it is due to magnetic field drift and not to an EDM. The resonant frequency can be corrected appropriately as shown in Fig. 2.3b; the ratio in Equation 2.1 is insensitive to such drifts.

2.1.3 Limitations of present comagnetometry and residual effects

The comagnetometry techniques described above can correct for magnetic field drifts smaller than ppm, but still suffer from systematic effects. One of these is the so-called light shift. This is a shift in the mercury precession frequency caused by a component of the probe light which is parallel to $\vec{B}_0$ and shifts the ground and excited energy levels. This depends on the intensity of the probe light, and can mimic an EDM if there happens to be any correlation between $|\vec{E}|$ and light intensity. Another systematic effect is that the UCN are slow enough that their center of mass is below the center of the EDM cell, so they sample a slightly different field than the thermal comagnetometer atoms. Finally, the geometric phase effect described below causes a frequency shift that can mimic an EDM in the presence of magnetic field gradients.

Geometric Phase Effect

The EDM experiment measures a shift in the neutron frequency, associated with a reversal in applied electric field $\vec{E}$. The underlying assumption is that the neutron magnetic moment is unaffected by such reversals. However, there is an effect which can shift the neutron frequency in the same way and can therefore be mistaken for an EDM[123]. This effect is caused by the motional magnetic field experienced by a particle moving through an electric field (Equations 2.2 through 2.9 are taken from [123]):

$$B_v = \frac{E \times v}{c^2},$$

(2.2)

combined with the horizontal component of a slightly inhomogenous magnetic field, which results from Maxwell's equations $\nabla \cdot \vec{B} = 0$:

$$B_{0xy} = -\frac{dB_{0z}}{dz}\frac{r}{2}$$

(2.3)

Both of these fields are small compared to $\vec{B}_0$, and orthogonal to $\vec{B}_0$. Unfortunately, for particles in certain orbits, the effects of these fields don't average out with particle motion in the trap but instead impart a measurable frequency shift. The shift is known as a geometric phase effect, since the particle's wavefunction obtains a so-called geometric phase[1] resulting from transport through a closed loop in its parameter space. For particles whose orbits have a distinct rotation in the xy plane, these horizontal fields induce a Ramsey-Bloch-Siegert shift in the precession frequency:

$$\Delta\omega = \frac{\omega_{xy}^2}{2(\omega_0 - \omega_r)}$$

(2.4)

---

[1] For slow moving transport that can be considered adiabatic, this geometric phase is directly related to the quantum mechanical Berry's phase[123].

where ω_0 is the natural Larmor precession, ω_r is the rotational frequency of the particle's trajectory, and where

$$\omega_{xy}^2 = \gamma^2 B_{xy}^2 = \gamma^2 \left(B_v + B_{0xy}\right)^2 = \gamma^2 \left(\left(\frac{dB_{0z}}{dz}\frac{r}{2}\right)^2 + \left(\frac{E \times v}{c^2}\right)^2 + 2\left(\frac{dB_{0z}}{dz}\frac{r}{2}\right)\left(\frac{E \times v}{c^2}\right)\right) \quad (2.5)$$

All three terms shift the precession frequency of the particle; however, only the latter term which is linear in E changes sign with electric field reversal. Since the neutron EDM experiment measures the difference in precession frequency under opposite direction electric fields, the last term has the potential to be interpreted falsely as an EDM. The shift has the potential to affect both EDM species and comagnetometer species alike, although the form is different for fast- and slow-moving particles. Slow moving particles such as UCN experience a shift which generates a false EDM given by:

$$d_{af} = \frac{J\hbar}{2}\left(\frac{dB_{0z}/dz}{B_{0z}^2}\right)\frac{v_{xy}^2}{c^2}\left[1 - \frac{\omega_r^2}{\omega_0^2}\right]^{-1} \quad (2.6)$$

Faster moving particles such as the comagnetometer atoms will experience a shift which generates a false atomic EDM d_{af} given by:

$$d_{af} = \frac{J\hbar}{2}\left(dB_{0z}/dz\right)\frac{\gamma^2 R^2}{c^2}\left[1 - \frac{\omega_o^2}{\omega_r^2}\right]^{-1} \quad (2.7)$$

The false atomic EDM will also be interpreted as a false neutron EDM given by:

$$d_{afn} = \frac{|\gamma_n|}{|\gamma_a|}d_{af}, \quad (2.8)$$

and may be larger in magnitude. In previous generation experiments at ILL[123], the intrinsic false EDM of the neutron was calculated to be $-1.1 \times 10^{-27}\,\mathrm{e \cdot cm}$, while the false EDM stemming from the false atomic EDM was a much larger $5.0 \times 10^{-26}\,\mathrm{e \cdot cm}$. One solution to reduce the geometric phase effect is to decrease the mean free path λ of comagnetometer atoms in the trap by increasing their partial pressure. This has the effect of introducing a suppression factor into the measured false EDM:

$$d_{af\lambda} = \left[\frac{\pi v_{xy}\lambda}{2R^2\omega_0}\right]^2 d_{af}, \quad (2.9)$$

where $R \approx 0.25\,\mathrm{m}$ is the cell dimension. Such an approach has been suggested for ^{129}Xe comagnetometry; however, it is still unknown whether the partial pressure of ^{129}Xe can be increased sufficiently while avoiding high voltage discharge.

2.1.4 Proposal to implement a dual magnetometer

The geometric phase effect described above generates a false EDM proportional to the magnetic field gradient, which is difficult to measure experimentally. However, it can potentially be solved for, to first order, by a technique involving two comagnetometer species. This has been proposed for the nEDM experiment at TRIUMF [111]. Essentially two polarized spin-1/2 species, ^{199}Hg and ^{129}Xe, would fill the EDM cell and be subjected to free spin precession. The sinusoidal decay of each would be fit independently to extract the precession frequency, given for mercury and xenon, respectively, by:

$$\omega_{Hg\uparrow\uparrow} = -\gamma_{Hg}B_{0z} - \frac{\gamma_{Hg}^2 R^2}{2c^2}\frac{\partial B_{0z}}{\partial z}E + \frac{\gamma_{Hg}^3 R^2}{2c^4}B_{0z}E^2 + \frac{3\gamma_{Hg}^3 R^4}{16\langle v_{Hg}^2\rangle}B_{0z}\left(\frac{\partial B_{0z}}{\partial z}\right)^2 \tag{2.10}$$

$$\omega_{Xe\uparrow\uparrow} = -\gamma_{Xe}B_{0z} - \frac{\gamma_{Xe}^2 R^2}{2c^2}\frac{\partial B_{0z}}{\partial z}E + \frac{\gamma_{Xe}^3 R^2}{2c^4}B_{0z}E^2 + \frac{3\gamma_{Xe}^3 R^4}{16\langle v_{Xe}^2\rangle}B_{0z}\left(\frac{\partial B_{0z}}{\partial z}\right)^2 \tag{2.11}$$

This results in a system of two equations and two unknowns, B_{0z} and $\frac{\partial B_{0z}}{\partial z}$. The second term is the cross term between electric field E and magnetic field gradient $\frac{\partial B_{0z}}{\partial z}$, and is linear in both. This term is the source of the false EDM. The last term is quadratic in $\frac{\partial B_{0z}}{\partial z}$, and is therefore small enough to be neglected. Then we can solve for B_{0z} and $\frac{\partial B_{0z}}{\partial z}$ according to:

$$B_{0z} = \frac{\gamma_{Xe}^2 \omega_{Hg} - \gamma_{Hg}^2 \omega_{Xe}}{\gamma_{Xe}\gamma_{Hg}\left(\gamma_{Xe} - \gamma_{Hg}\right)\left(\frac{1}{2c^4}\gamma_{Xe}\gamma_{Hg}R^2 E^2 + 1\right)} \tag{2.12}$$

$$\frac{\partial B_{0z}}{\partial z} = \frac{2c^2\left[\gamma_{Xe}\left(\gamma_{Xe}^2 R^2 E^2 - 2c^4\right)\omega_{Hg} - \gamma_{Hg}\left(\gamma_{Hg}^2 R^2 E^2 - 2c^4\right)\omega_{Xe}\right]}{\gamma_{Xe}\gamma_{Hg}R^2\left[\gamma_{Xe}\left(\gamma_{Hg}^2 R^2 E^2 - 2c^4\right) - \gamma_{Hg}\left(\gamma_{Xe}^2 R^2 E^2 - 2c^4\right)\right]} \tag{2.13}$$

Such knowledge of the magnetic field gradient can be used in the analysis of the neutron precession frequency to calculate a result free, to first order, of geometric phase effects. This motivates the development of optical magnetometry using polarized ^{129}Xe.

2.2 Optical Pumping and SEOP

In this section we describe the theory of optical pumping, and spin exchange optical pumping in particular. Optical pumping is a necessary step for magnetometer development because it provides the atoms with an alignment that makes them sensitive to magnetic fields. Spin exchange optical pumping (Section 2.2.2) is the specific technique by which polarized ^{129}Xe is produced.

2.2.1 Optical Pumping Theory

Optical pumping refers to the use of light to drive atoms into specific quantum states, or change the population distribution between states. In particular we study Zeeman optical pumping in the ground state of our atoms.

Zeeman splitting

Optical pumping relies on the energy difference between populated states. In particular, a quantum state with angular momentum number J has $2J+1$ degenerate sublevels, with projection values $M_J = J, J-1... -J$. Applying a weak magnetic field $\vec{B}$ breaks the degeneracy of the sublevels by causing a Zeeman shift governed by the Hamiltonian [166]

$$H = -\vec{\mu} \cdot \vec{B} = \frac{\left\langle \vec{\mu} \cdot \vec{J} \right\rangle}{J(J+1)} \vec{J} \cdot \vec{B},$$ (2.14)

where $\vec{\mu}$ is the magnetic dipole moment of the atom, given by $\vec{\mu} = -\mu_B \vec{L} - g_S \mu_B \vec{S} = -g_J \mu_B \vec{J}$. The energy shift of each Zeeman sublevel M_J is $\Delta E = g_J \mu_B B M_J$. g_J is the Lande g-factor, and under LS coupling conditions g_J is given by:

$$g_J = g_L \frac{J(J+1) + L(L+1) - S(S+1)}{2J(J+1)} + g_S \frac{J(J+1) - S(S+1) + L(L+1)}{2J(J+1)}$$ (2.15)

The sign conventions above are given such that g_J is a positive number. The value of g_J is different for each state J and indicates the strength of the magnetic dipole for that state. Experimental values of g_J have been tabulated for many atomic states; for examples in Xe see Ref. [147]. The jl coupling scheme described in Section 2.4.1 is a more accurate model for Xe. The g-factor for the jl coupling scheme is calculated by the equation:

$$g_J = \frac{2J+1}{2K+1} + 2\frac{K(K+1) + j(j+1) - l(l+1)}{(2K+1)(2J+1)}(g_{J_c} - 1),$$ (2.16)

where $J, K, j,, l$, and g_{J_c} follow the definitions in Section 2.4.1. In particular, g_{J_c} is the g-factor of the parent core with angular momentum J_c as described in that section and can be calculated from Equation 2.15.

For atoms posessing nuclear spin I, the magnetic dipole is modified by an additional term corresponding to the nuclear dipole $\vec{\mu}_I = g_I \mu_N \vec{I}$ [166]. The sign convention for $\vec{\mu}_I$ is opposite to $\vec{\mu}_J$; the g-factor g_I is often given in nuclear magnetons μ_N, and the sign of g_I may be positive or negative depending on the nucleus in question. The magnetic dipole including nuclear spin is given by:

$$\vec{\mu} = -g_J \mu_B \vec{J} + g_I \mu_N \vec{I} = -g_F \mu_B \vec{F}$$ (2.17)

and has corresponding Zeeman shifts:

$$\Delta E = g_F \mu_B B M_F \tag{2.18}$$

where F is the total angular momentum having projection M_F, with g-factor g_F given by:

$$g_F = \frac{F(F+1) + J(J+1) - I(I+1)}{2F(F+1)} g_J - \frac{F(F+1) - J(J+1) + I(I+1)}{2F(F+1)} \frac{\mu_N}{\mu_B} g_I \tag{2.19}$$

The second term, relating to the nuclear magnetic moment, is roughly three orders of magnitude smaller ($\frac{\mu_N}{\mu_B} \approx \frac{1}{1836}$) than the first term and is often neglected in calculations for paramagnetic atoms. In that case, the main effect of the nuclear spin is its contribution to the total angular momentum F, leading to an increase in splitting into $2F + 1$ sublevels. In ^{129}Xe and other diamagnetic atoms, the ground state has $J = 0$ and the ground state Zeeman splitting is due solely to the second term (nuclear magnetic moment). The nuclear magnetic moments for relevant paramagnetic and diamagnetic atoms are given in Table 2.1. The g-factor g_I and gyromagnetic ratio $\gamma = \frac{\mu}{I} = g_I \frac{\mu_N}{\hbar}$ there are both calculated based on data from [155]. The values in the table are those of the bare nuclei, and differ from reported NMR values in atoms (e.g. $\gamma/2\pi$ = 11.77 MHz in [125]) due to diamagnetic shielding of the magnetic dipole moment. The Zeeman splitting of the ^{129}Xe $^1S_0$ ground state and ^{129}Xe $6p[3/2]_2$ excited state are shown in Fig. 2.4 and Fig. 2.5. A state with a negative-slope Zeeman shift is called high-field seeking, and that with a positive Zeeman shift is called low-field seeking. In a $1\,\mu$T field, the ground state Zeeman splitting of ^{129}Xe is 11.86 Hz. The excited state splitting is larger due to the electron spin but still below MHz. The form of the Hamiltonian changes when the atom is subjected to strong fields where the interaction is greater than the hyperfine coupling $A\vec{I} \cdot \vec{J}$. The strong field case is not calculated here, because such strong fields are not necessary for optical pumping. The role of Zeeman splitting in optical pumping is to break the degeneracy between magnetic sublevels and keep them sufficiently well-separated in energy to prevent rapid relaxation between levels; practically, this is satisfied for room temperature atoms by a $1\,\mu$T field in EDM experiments. We take advantage of optical pumping to populate and depopulate particular sublevels.

Optical Pumping and Polarization

Optical pumping was first proposed and demonstrated by A. Kastler in the 1950s. A description of the method is given in [49]. Atoms possessing nuclear spin or electronic spin have degenerate ground state sublevels which experience Zeeman splitting in a weak magnetic field. Optical pumping is a method to change the population distribution between these sublevels using (typically circular) polarized light. An example for a spin-1/2 system is shown in Fig. 2.6. Absorption of circular-polarized light imparts angular momentum to the atom causing a change in the total angu-
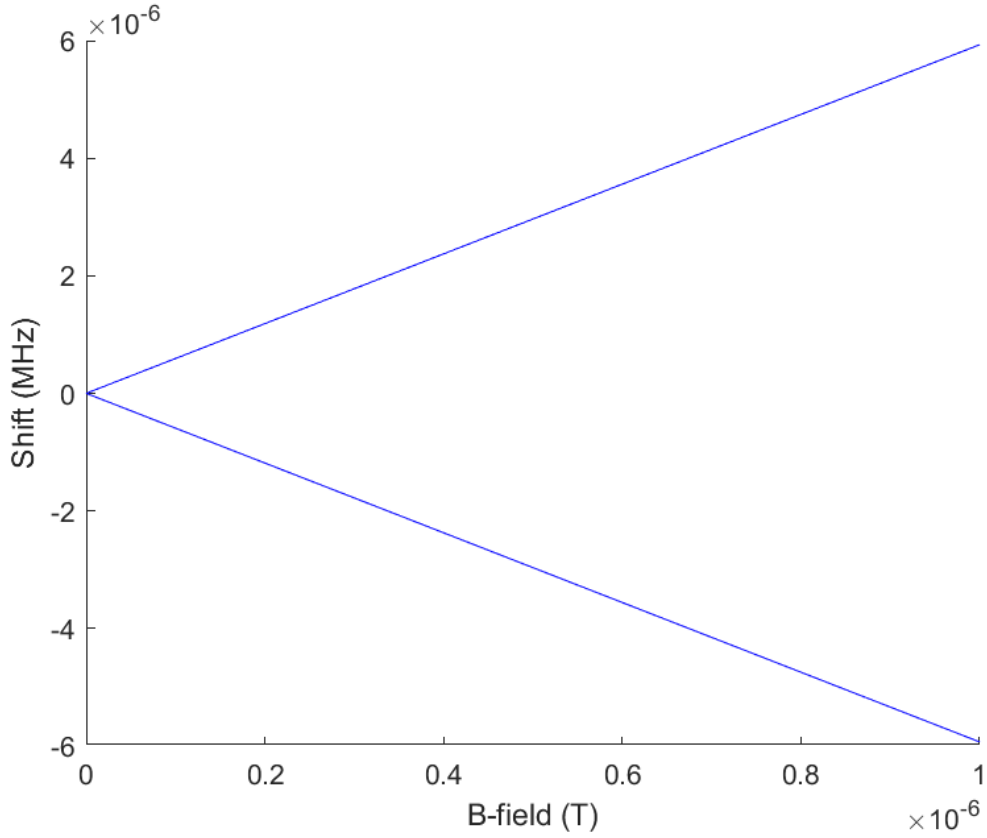
Figure 2.4: Zeeman splitting of the ^{129}Xe ground state due to nuclear spin.

Table 2.1: Nuclear magnetic moment, g-factor, and gyromagnetic ratios of relevant isotopes. Magnetic moments reported are from [155]

Nuclei	Spin	magnetic moment		g_I	$\gamma/2\pi$
		$[\mu_N]$	[J/T]		[MHz/T]
^{1}n	1/2	-1.91304(5)	-9.7×10^{-27}	-3.82609	-29.1647
^{1}H	1/2	2.792847(3)	1.41×10^{-26}	5.585695	42.57748
^{3}He	1/2	-2.1275(3)	-1.1×10^{-26}	-4.255	-32.4341
^{85}Rb	5/2	1.35298(10)	6.83×10^{-27}	0.541192	4.125286
^{87}Rb	3/2	2.75131(12)	1.39×10^{-26}	1.834207	13.98141
^{129}Xe	1/2	-0.777976(8)	-3.9×10^{-27}	-1.55595	-11.8604
^{131}Xe	3/2	0.6915(2)	3.49×10^{-27}	0.461	3.514015
^{199}Hg	1/2	0.505886(9)	2.56×10^{-27}	1.011771	7.712319
^{201}Hg	3/2	-0.5602257(14)	-2.8×10^{-27}	-0.37348	-2.84692
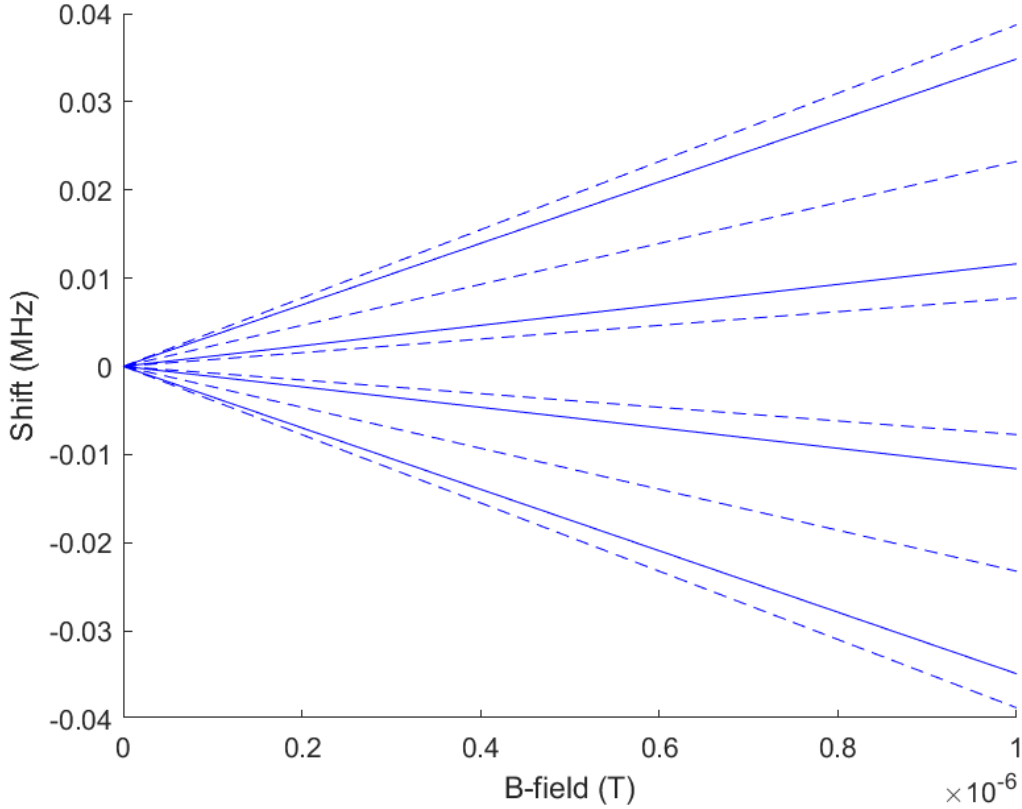
Figure 2.5: Zeeman splitting of the ^{129}Xe $6p[3/2]_2$ hyperfine components $F = 3/2$ (solid) and $F = 5/2$ (dotted), respective to their line zero-field energies. The hyperfine splitting (not pictured) between $F = 3/2$ and $F = 5/2$ is 2 GHz, with $F = 3/2$ having higher energy

lar momentum projection. In the case of one-photon transitions, the selection rule $\Delta M = +1$ applies for excitation with σ^+ light, and $\Delta M = -1$ for σ^- light. In the example shown, only the $M = -1/2$ state will absorb σ^+ light due to the selection rule; the nonabsorbing state is called a "dark state". Relaxation occurs from the excited state back to both sublevels, with the ratio determined by the Clebsch-Gordan coefficients. The result is that after many cycles of absorption and emission, the $M = -1/2$ state population will be depleted while the $M = +1/2$ state population will be increased.

The degree of polarization of the ground state for such a spin-1/2 system is defined by the relative population of the Zeeman sublevels as [107]:

$$P = \frac{N_+ - N_-}{N_+ + N_-} \tag{2.20}$$

where N_+ and N_- are the respective populations in the $M = 1/2$ and $M = -1/2$ states. In systems with more than two levels, polarization is defined by comparing the total magnetization per unit vol-
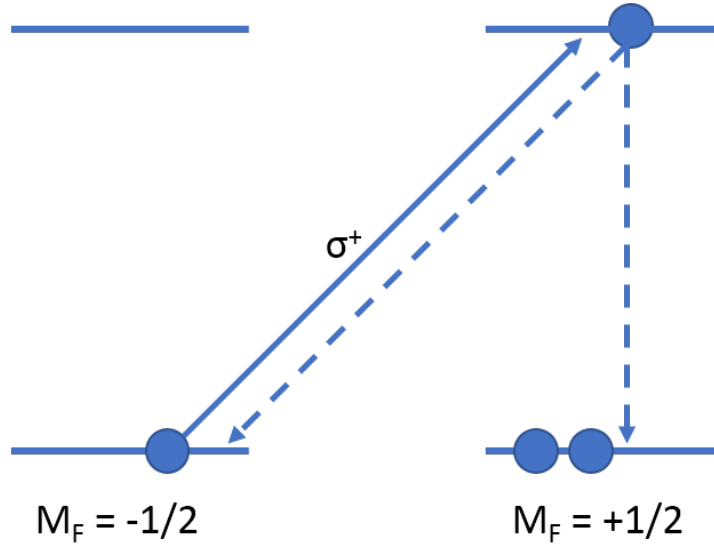
Figure 2.6: Optical pumping in a spin-1/2 system.

ume M_z to the theoretical maximum magnetization at absolute zero temperature, i.e. $P = \frac{M_z(T)}{M_z(T=0K)}$.
Under a weak magnetic field, the Zeeman splitting is sufficiently small that all ground state Zeeman sublevels are nearly equally populated at ambient temperatures (those satisfying the condition $kT \gg \hbar\omega_0$) according to a Boltzmann distribution. At absolute zero, only the lowest energy Zeeman sublevel is populated. At finite temperature $kT \gg \hbar\omega_0$, the thermal equilibrium polarization in a magnetic field B_0 is given approximately by [107]:

$$P_0 = \frac{|\gamma|\hbar B_0}{3k_B T}(I+1) \tag{2.21}$$

where γ is the gyromagnetic ratio, I the nuclear spin, and k_B is Boltzmann's constant. In optical pumping, the term hyperpolarized describes a species with polarization larger than the thermal equilibrium polarization. Optical pumping can produce polarization which is orders of magnitude larger than the thermal polarization. For example, the thermal polarization for ^{129}Xe in a 1 mT field is $P = 9 \times 10^{-10}$, compared to hyperpolarized ^{129}Xe which can have a polarization reaching several tens of percent.

Optical pumping is used as a precursor to spin exchange optical pumping, which is described below. Near-total polarization of rubidium and potassium is acheivable by diode lasers. In some optical magnetometers, precession is detected by monitoring the transmission of circular-polarized light through the ensemble of precessing atoms, making use of the same selection rules which give rise to optical pumping.

2.2.2 Spin Exchange Optical Pumping

Spin exchange optical pumping (SEOP) refers to the polarization of noble gas atoms through collisions with optically pumped alkali metal atoms that result in spin exchange. These collisions can be simple binary collisions, or can be three-body collisions leading to the formation of short lived alkali-metal-noble-gas molecules bound by van der Waals forces. Spin exchange is the transfer of angular momentum from one atom to the other, accompanied by a transition between Zeeman sublevels. During the interaction, spin exchange as well as relaxation can occur through the interactions between polarized spins and the magnetic field generated by moving electric charges. The Hamiltonian for spin exchange is [43, 162]

$$H = A\vec{I}_{AM} \cdot \vec{S} + \alpha \vec{I}_{NG} \cdot \vec{S} + \gamma_a \vec{N} \cdot \vec{S} + g_s \mu_B \vec{B} \cdot \vec{S} \tag{2.22}$$

where I_{AM} is the alkali metal nuclear spin, I_{NG} is the noble gas nuclear spin, $\vec{S}$ is the alkali metal electron spin, $\vec{N}$ is the molecular rotational angular momentum, and A, α, γ_a are respectively the coupling constants for the alkali metal hyperfine interaction, the isotropic hyperfine interaction between noble gas nuclei and alkali metal electron spin, and spin-rotation interaction. In particular the hyperfine interaction $\alpha \vec{I}_{NG} \cdot \vec{S}$ is responsible for spin exchange. The strength, α, of the interaction depends on the overlap of the electron wavefunction of the spin-polarized electron with the nucleus of the noble gas atom; the wavefunction is perturbed by the presence of the noble gas atom resulting in an enhancement in the overlap and in spin exchange for atomic separations on the order of an angstrom (Å)[162]. The spin-rotation interaction $\vec{N} \cdot \vec{S}$ between the alkali metal electron spin and molecular rotational angular momentum $\vec{N}$ causes spin relaxation.

2.2.3 SEOP Literature Review

A thorough review of spin exchange optical pumping was presented by Walker and Happer [162], and builds on the earlier theory published by Happer [82]. It presents the basic experimental technique, and theory of the dominant spin interactions of the Hamiltonian which govern polarization and relaxation via spin exchange. Rb is often used as the alkali metal of choice for spin exchange due to its easily-driven optical resonance at the D1 line (795 nm), for which high-power diode lasers are readily available. Typical SEOP starts with optical pumping of a small amount of Rb vapour in a heated reservoir, followed by addition of a gas mixture containing the noble gas atoms. N_2 and He are often present in the gas mixture; N_2 helps to quench the Rb excited state by collisional de-excitation and thereby prevent reabsorption of unpolarized Rb emission (radiation trapping), while He is a buffer gas which pressure broadens the absorption lineshape, in order to better take advantage of the typical pump laser power spectrum. These gases also participate in van der Waals molecule-forming collisions.

Bouchiat et al [31] first observed spin exchange optical pumping in ^{3}He used as a buffer gas

in Rb optical pumping cells. It was stated that the technique should be applicable to any noble gas having a nuclear moment. Indeed, SEOP has been demonstrated in He, Ar, Ne, Kr and Xe; Calaprice et at [41] demonstrated SEOP on metastable nuclei and radioactive [133]Xe [41]. SEOP on [129]Xe was first observed by Kanegsberg and later published by Grover [78]. Bouchiat [30] identified the role of "sticking collisions" between Rb and noble gas atoms due to van der Waals forces as a factor in the relaxation of optically pumped Rb.

Much of the work on SEOP has been to identify the relative contributions to the relaxation of either the alkali metal or noble gas polarization. Nelson et al [116] found that under high-pressure conditions with He buffer gas, Rb relaxation rates are dominated by Rb-Xe binary collisions, for which the rate is linearly proportional to the gas densities. Meanwhile, relaxation by formation of van der Waals molecules was responsible for less than 25% of the Rb relaxation (as the molecular lifetime becomes short at high pressure), followed by contributions from binary collisions of Rb or formation of Rb_2 dimers, and diffusion to cell walls. Similar results were found by Jau et al [93] for SEOP cells with higher Xe density. Cates et al [43] found that the spin exchange rates for Xe and Rb depend on the Xe pressure. At low Xe pressure, van der Waals molecules are the dominant source of spin exchange, while at high Xe pressure binary collisions dominate. Simulations carried out by Fink et al [63] studied the dependence of Xe polarization on temperature and partial pressure of each gas component, finding good agreement with experiment. Anger et al [11] studied spin-relaxation mechanisms of [129]Xe in the gas phase, confirming intrinsic spin relaxation at low field due to spin rotation interactions between [129]Xe nuclei. They found the dominant contribution was due to the formation of Xe_2 dimers bound by van der Waals forces. They also found significant extrinsic relaxation from collisons with cell walls.

Inexpensive diode lasers have increased SEOP rates. Wagshul and Chupp [161] demonstrated up to 70% polarization for [3]He pumped with a GaAlAs laser. Driehuys et al [59] used He to pressure broaden the Rb transition and better match the spectral profile of a 140 W diode laser. They demonstrated 5% polarization and predicted up to 60% was attainable for volumes up to one liter by choosing suitable flow rates. Double-digit polarizations have been acheived by many groups, including those from Princeton[42], New Hampshire [144], Harvard[119], Vanderbilt[118], Berlin[100], and Illinois[163]. A collaboration based at Vanderbilt demonstrated polarization up to 90.9% using a homebuilt open-source polarizer with a 200 W frequency-narrowed laser [117].

Spin-polarized noble gases have been used for studies of surface interactions [134], magnetic resonance imaging of the lungs [117], neutron polarizers [51], and fundamental symmetry tests of the Xe EDM [142].

2.2.4 Spin relaxation mechanisms for polarized Xe

The hyperpolarization of Xe is temporary; there are many processes by which the atoms can relax to their naturally unpolarized state. Relaxation is measured by the T_1 lifetime which describes the loss

of longitudinal polarization by various processes in gas, liquid, or solid phase. The most common process is the nuclear spin coupling to the angular momentum of a nearby particle [145]. In the case of gas-phase Xe, relaxation is dominated by "self-relaxation" caused by collisions with other nearby Xe atoms through the spin-rotation Hamiltonian $\vec{N} \cdot \vec{I}$ identified by Carr et al. [86]. The colliding Xe atoms form either a transient (in the case of binary collisions) or persistent dimer. Here $\vec{N}$ is the orbital angular momentum of the dimer and $\vec{I}$ is the spin of the polarized Xe atom. The resulting lifetime for binary collisions is inversely proportional to pressure, but is measured to be tens of hours at atmospheric pressure. Faster relaxations from persistent dimers can be reduced by introducing a buffer gas to breakup molecules. Another relaxation mechanism is through wall collisions. The atomic spin can couple with dipoles on the wall. It has been found that applying silane-based coatings to the walls of the gas cell help reduce the effect of wall collisions and can extend Xe T_1 lifetimes to 20-40 min [34], still limited by coupling to protons in the coating itself. Others choose to use specially selected glass with high purity (e.g GE180), and produce some cells with lifetimes of hours even without coatings. Field gradients in the cell contribute also to relaxation. Rapidly moving atoms can violate the adiabatic spin condition and rapidly flip when transiting small field gradients. This sort of gradient relaxation gives lifetimes on the order of minutes in inhomogeneous (eg. 10%) regions. Finally, any oxygen impurities in the gas will cause relaxation from coupling of ^{129}Xe to oxygen's large molecular magnetic dipole moment.

Lifetimes in the solid state can be up to hundreds of hours. Higher field strength and lower temperatures contribute to long lifetimes. Since Xe freezes at 161.4 K, a typical continuous flow SEOP polarizer uses a LN$_2$ cold trap at 77K to separate polarized Xe from the He/N$_2$ mixture. The same spin rotation interaction occurs, except in the solid phase it is lattice vibrations and phonon scattering that briefly couple the spins. At lower fields there is also a (weak) nuclear dipole-dipole interaction, and the potential of cross-polarization between ^{131}Xe and ^{129}Xe. A strong dependence on temperature makes it important to freezeout all Xe at as low temperature as possible. Previous designs [144] made efforts to maximize the cold trap surface area, because Xe atoms that stick directly to the wall are likely colder than Xe that stick atop an already-frozen layer. Sublimation of the frozen Xe helps to avoid the rapid relaxation which occurs in the liquid phase.

2.2.5   NMR techniques used to measure optical pumping

NMR techniques are used on the polarized nuclei to quantify the polarization as a percentage. The techniques of most practical use are Adiabatic Fast Passage (AFP) and Free Induction Decay (FID), which are described below. AFP is the simplest technique for measuring the polarization between species. FID serves as a testbed for applying $\pi/2$-pulses and testing the effects of transverse relaxation.

Adiabatic Fast Passage

AFP is an NMR technique used to assess the degree of polarization of a species by measuring the magnetic induction from a precessing sample during a pulse sequence that exactly inverts the nuclear spin. It is adiabatic in the sense that the magnetic moment maintains the same magnetic quantum number with respect to the field in a specially-defined rotating reference frame. The technique was proposed by Bloch [24] in 1946 while formulating the well-known Bloch equations, and was demonstrated the same year [25] in samples of water and paraffin.

The technique is illustrated in Fig. 2.7. In the technique, polarized atoms are subjected to two fields: first, a strong field $B_0\hat{k}$ which defines a Larmor frequency for the nuclei

$$\omega_L = \gamma B_0; \tag{2.23}$$

second, a weaker oscillating RF field $2 \times B_1\cos(\omega t)\hat{i}$ applied transverse to B_0 with nearly-resonant $\omega_{RF} \approx \omega_L$. The polarization, which may be the result of thermal Boltzmann polarization or optical pumping, results in a net magnetization $\vec{M}$ in the direction of B_0. The magnetization follows the Bloch equations and has components (M_x, M_y, M_z). In the presence of relaxation the components have the following time dependence [24]:

$$\frac{dM_x}{dt} = \gamma\left(\vec{M} \times \vec{B}\right)_x - \frac{M_x}{T_2} \tag{2.24}$$

$$\frac{dM_y}{dt} = \gamma\left(\vec{M} \times \vec{B}\right)_y - \frac{M_y}{T_2} \tag{2.25}$$

$$\frac{dM_z}{dt} = \gamma\left(\vec{M} \times \vec{B}\right)_z - \frac{M_z - M_0}{T_1} \tag{2.26}$$

The relaxation times T_1 and T_2 refer to longitudinal and transverse relaxation, respectively; M_0 is the (thermal) equilibrium magnetization under B_0.

Ramping B_0 field strength changes the Larmor frequency, bringing the atoms into and out of resonance with the fixed B_1 frequency. Under suitable ramp conditions (described below), the atoms adiabatically follow the effective field caused by the combination of B_0 and B_1. This effective field is most easily calculated in a rotating reference frame rotating at $\omega = \omega_{RF}$. The linear B_1 can be decomposed into a sum of two fields rotating in different directions, $(B_1)\left(\cos(\omega t)\hat{i} \pm \sin(\omega t)\hat{j}\right)$, one of which appears stationary in the rotating frame, the other of which is rapidly counter-rotating and can be neglected (more precisely, it contributes a small Ramsey-Bloch-Siegert shift). The effective field in the rotating frame is given by vector addition of B_0 and B_1 [132]:

$$\vec{B_{eff}} = \left(B_0 - \frac{\omega}{\gamma}\right)\hat{k} + B_1\hat{i} \tag{2.27}$$
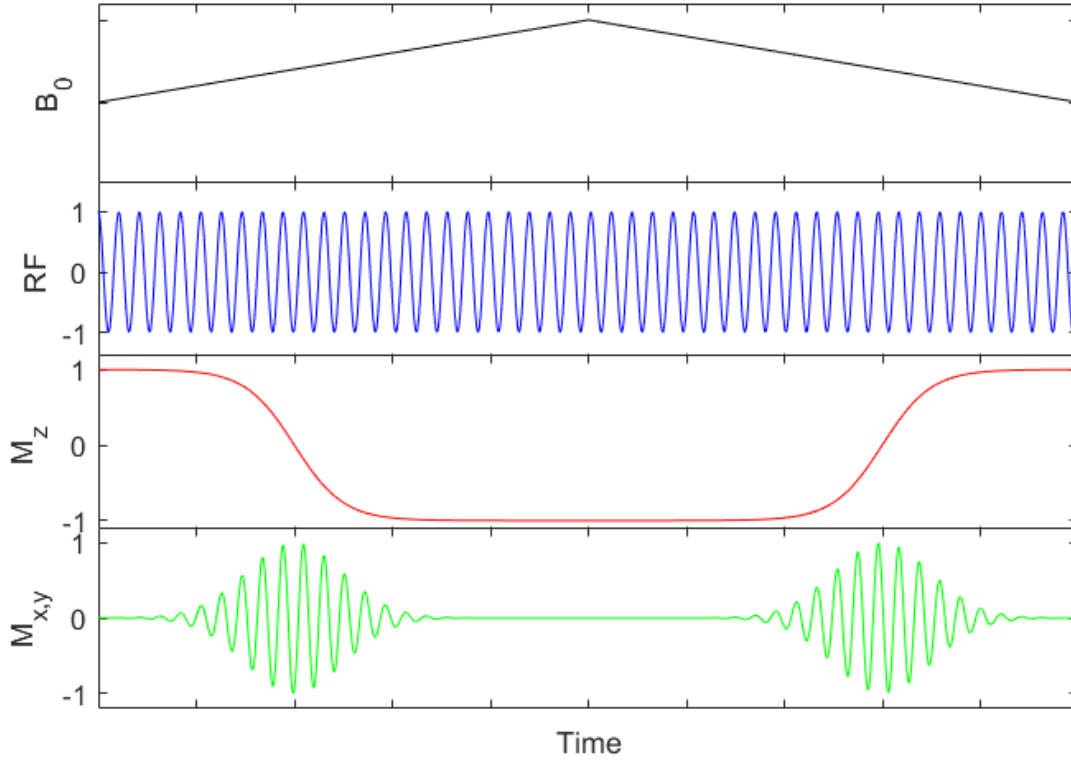
Figure 2.7: Applied field and magnetization response during the AFP technique, in the simplified case with no relaxation.

The additional term $\frac{\omega}{\gamma}$ is a result of the coordinate transformation. As B_0 is ramped from $B_0 > \frac{\omega}{\gamma}$ to $B_0 < \frac{\omega}{\gamma}$, the direction of $\vec{B}_{eff}$ changes from $\hat{k}$ to $-\hat{k}$. Under adiabatic conditions $\vec{M}$ follows $\vec{B}_{eff}$ and completely inverts. The adiabatic conditions are [24]:

$$\frac{B_1}{T_1}, \frac{B_1}{T_2} \ll \frac{dB_0}{dt} \ll \gamma B_1^2 \tag{2.28}$$

The left hand side indicates that the magnetization must pass through resonance before significant relaxation occurs; the right hand side indicates that precession around $|\vec{B}_{eff}|$ (having a minimum value B_1) must be sufficiently fast for the magnetization to remain "locked" to $\vec{B}_{eff}$. The detected signal is the Faraday induction produced by the precessing $\vec{M}$ in a pickup coil mounted along the y-axis. After a spin flip, the magnetization slowly relaxes to equilibrium value $\vec{M}_0$ with decay time T_1.
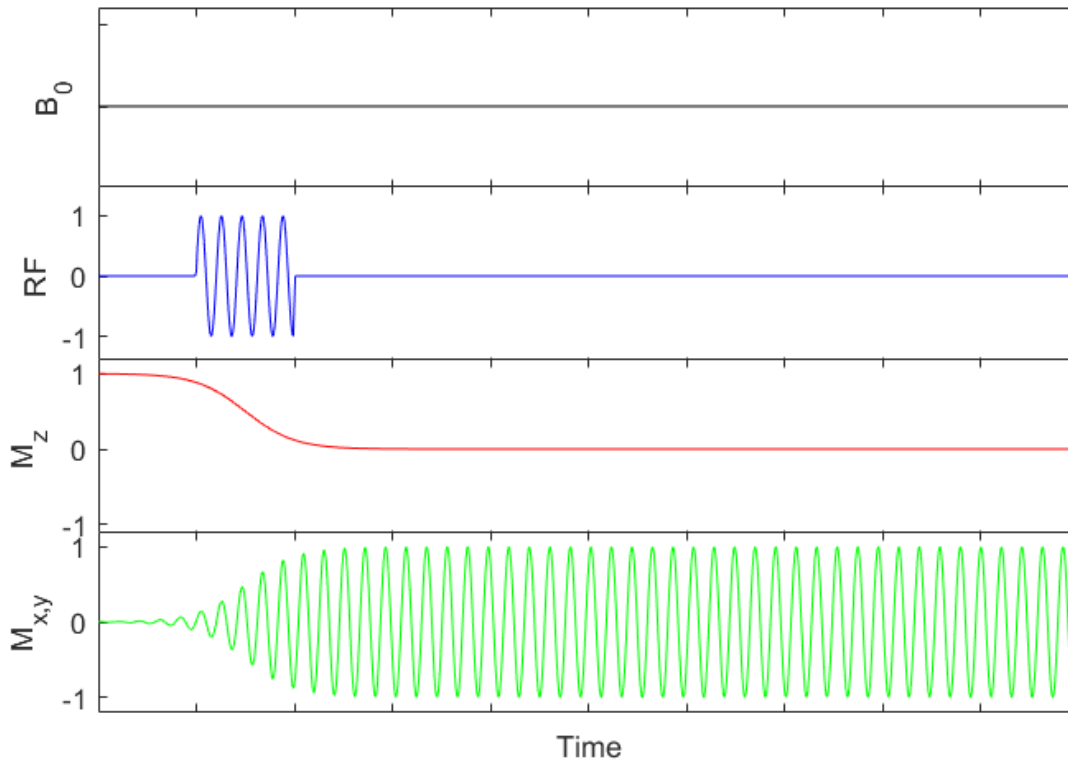
Figure 2.8: Applied field and magnetization response during the FID technique, in the simplified case with no relaxation.

Free Induction Decay

FID is another useful technique, which can measure the transverse lifetime T_2 of the spins. An illustration of the technique is shown in Fig. 2.8. The applied B_0 field is fixed and highly uniform. Polarized species are subjected to a gated oscillating RF field with rotating components $(B_1)\left(\cos(\omega t)\hat{i} \pm \sin(\omega t)\hat{j}\right)$. The gate time and amplitude of this RF field are carefully chosen to initiate a rotation of the magnetization vector through an angle $\pi/2$ into the xy-plane. After this the RF field is gated off and the spins undergo free spin precession about B_0 according to the Bloch equations. The magnetization dephases in the xy-plane with relaxation time T_2 and undergoes longitudinal relaxation with time T_1. Typically transverse relaxation dominates, a result of spin-spin relaxation and inhomogeneities in B_0. The detected signal again comes from Faraday induction produced by $\vec{M}$ precessing in the xy-plane. An identical pulse sequence is used in free spin precession magnetometers, but detection for magnetometry is performed using optical methods or sensitive SQUIDs.

2.3 Two Photon Transitions and Spectroscopy

Two photon transitions are those involving either the simultaneous absorption or simultaneous emission of two photons with total energy equal to the difference in initial and final states of the atom or molecule. The two photons can be of the same or different wavelength so long as the combined energy of the two satisfies conservation of energy. An example is shown in Fig. 2.9. The transition is often said to occur through a virtual intermediate state, which is in fact a sum over all off-resonant dipole-allowed states. Since there is no actual resonant intermediate state, two photon transitions differ from stepwise excitation obtained by two sequential electric dipole $E1$ transitions. Nor are they higher-order multipole (e.g., electric quadrupole $E2$) transitions. The transition probability comes from second-order perturbation theory following the dipole approximation. The selection rules for two photon transitions are different than those for one photon transitions; in particular, two photon transitions occur between states of the same parity.

Two Photon Absorption (TPA) is a process where two photons are absorbed "simultaneously" (meaning within the lifetime of the virtual state). The atom can reside in the virtual intermediate state only for a short time limited by the uncertainty principle. TPA requires absorption of the second photon within the virtual state lifetime; therefore high intensity excitation light must be used to excite TPA at detectable rates. The transition rate (see below) is proportional to the squared intensity of the incoming radiation. There is a corresponding emission process called Two Photon Emission (TPE), which can occur out of excited states. There is a finite, nonzero probability for two photon emission over a continuous spectrum of wavelengths. Two photon emission transitions can, however, be most readily observed in metastable states with long lifetimes, as single photon emission from such levels is dipole-forbidden.

A typical scheme involves excitation to a dipole-forbidden state by two-photon absorption, followed by stepwise relaxation by two dipole-allowed transitions. The observed fluorescence is termed Two Photon Absorption Laser Induced Fluorescence (TALIF). These transitions are particularly useful, as the dipole allowed LIF transitions typically occur at wavelengths far from that of the excitation light, and so are easy to resolve. A common use of two-photon absorption [66] is the use of a single high-power laser to investigate transitions between states of same parity, in particular those transitions that would otherwise require VUV radiation. Another is the ability to excite Doppler-free transitions (see section below).

2.3.1 Derivation of two photon transition probability

The theory of two photon transitions was first developed in 1931 by Maria Goeppert Mayer [72], who showed the possibility of two photon absorption and emission, as well as Raman transitions, by performing second order perturbation theory in the second quantization (where both the energy levels and the number of photons are quantized).
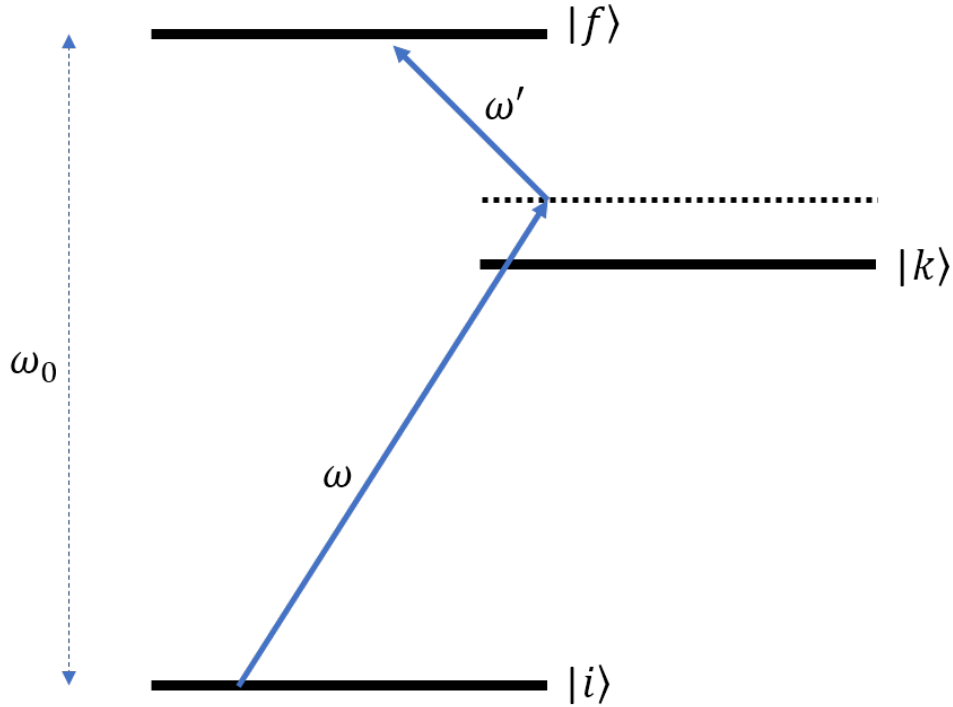
Figure 2.9: General representation of a two-photon transition (in this case, absorption) between two states $|i\rangle$ and $|f\rangle$. Excitation is by two photons ω and ω', which satisfy the conservation of energy $\hbar(\omega + \omega') = \hbar\omega_0$. The transition occurs through a virtual state (dotted line), given by a sum over off-resonant intermediate states $|k\rangle$ which are dipole-allowed.

We derive here the transition probability for two photon absorption based on the above work. We consider a stationary atom with initial state $|i\rangle$, intermediate state $|k\rangle$, and final state $|f\rangle$, excited by two laser beams of electric field strength E_1, E_2 (intensity I_1, I_2) and of the same polarization, with respective frequencies ω_1, ω_2. The intermediate state is not resonant with either of ω_1, ω_2. Under the dipole approximation, the perturbing Hamiltonian between photon and atom is:

$$H = \sum_r E_1 e\vec{r}\cos(\omega_1 t) + E_2 e\vec{r}\cos(\omega_2 t) \tag{2.29}$$

where $e\vec{r}$ is the usual electric dipole operator. Expressed in terms of matrix elements $H_{ki,n} = E_n\langle k|\sum_r e\vec{r}|i\rangle$, where $n = 1, 2$ refers to the two beams, the perturbation is (neglecting counter-

rotating terms):

$$H_{ki} = \frac{H_{ki1}}{2} e^{-i\omega_1 t} + \frac{H_{ki2}}{2} e^{-i\omega_2 t} \tag{2.30}$$

First order perturbation theory describes transitions between the initial and intermediate state, with probability amplitude $a_k^{(1)}$:

$$a_k^{(1)} = \frac{1}{2\hbar} \left[\frac{H_{ki1} \left(e^{i(\omega_{ki} - \omega_1)t} - 1 \right)}{\omega_{ki} - \omega_1} + \frac{H_{ki2} \left(e^{i(\omega_{ki} - \omega_2)t} - 1 \right)}{\omega_{ki} - \omega_2} \right] \tag{2.31}$$

Evaluating the perturbation to second order with perturbing Hamiltonian H_{fk} describes transitions to the final state. This yields four terms of the following form (each with different $H_{fk1}H_{ki2}$):

$$\frac{H_{fk1}H_{ki1}}{4\hbar(\omega_{ki} - \omega_1)} \left[\frac{e^{i(\omega_0 - 2\omega_1)t} - 1}{\hbar(\omega_0 - 2\omega_1)} - \frac{e^{i(\omega_{kf} - \omega_1)t} - 1}{\hbar(\omega_{fk} - \omega_1)} \right] \tag{2.32}$$

where $\omega_0 = \omega_{fk} + \omega_{ki}$. The second term in the expression can be neglected [72], as it is an artifact of turning on the perturbation abruptly at $t = 0$. The resulting probability amplitude $a_f^{(2)}$ summed over all intermediate states $|k\rangle$ is therefore:

$$a_f^{(2)} = \frac{1}{4\hbar^2} \sum_k \left(\frac{H_{fk1}H_{ki1}}{(\omega_{ki} - \omega_1)} \frac{e^{i(\omega_0 - 2\omega_1)t} - 1}{(\omega_0 - 2\omega_1)} + \frac{H_{fk2}H_{ki2}}{(\omega_{ki} - \omega_2)} \frac{e^{i(\omega_0 - 2\omega_2)t} - 1}{(\omega_0 - 2\omega_2)} \right.$$
$$\left. + \frac{H_{fk2}H_{ki1}}{(\omega_{ki} - \omega_1)} \frac{e^{i(\omega_0 - \omega_1 - \omega_2)t} - 1}{(\omega_0 - \omega_1 - \omega_2)} + \frac{H_{fk1}H_{ki2}}{(\omega_{ki} - \omega_2)} \frac{e^{i(\omega_0 - \omega_1 - \omega_2)t} - 1}{(\omega_0 - \omega_1 - \omega_2)} \right) \tag{2.33}$$

The transition probability is proportional to $|a_f^{(2)}|^2$. The first denominator of each term describes the off resonant interaction of photon $\omega_{1,2}$ with the intermediate state $|k\rangle$, which has energy defect $\hbar(\omega_{ki} - \omega_{1,2})$. The second denominator is the energy conservation term which yields the absorption lineshape described in the following section. The sum over all (off-resonant) one-photon allowed intermediate states $|k\rangle$ is often described as a transition to a short lived "virtual" state. Since the transition dipole for each intermediate state is weighted by its respective energy defect, only the states with energy levels close to the energy of the incident photon contribute significantly.

Selection rules for two photon transitions

The levels accessible by two photon transition are the same as those accessible by two sequential electric dipole transitions [66]. A consequence of this is that two photon transitions only occur between states of the same parity. The selection rules for two photon absorption are given in [28], and come from angular momentum conservation. The rules can be determined by evaluating the Clebsch-Gordan coefficients. The general rule is $\Delta F \leq 2$ for an atom with total angular momentum

F and projection M_F. The values of allowed ΔF and ΔM_F depend upon the orientation and polarization of the incident light. For two photons from a single beam with linear polarization parallel to the quantization axis (sometimes denoted π) we have $\Delta F = 0, \pm 2$ and $\Delta M_F = 0$. For two photons from a single beam with circular polarization σ^+, we have $\Delta F = 0, \pm 2$ and $\Delta M_F = +2$. A result of the selection rules is that one can selectively probe certain levels, e.g.) circular polarized light can be used in the detection of polarized Xe to selectively probe the ground state $M_F = -1/2$ population as described in Section 2.4.3.

2.3.2 Doppler-Free Two Photon Spectroscopy

In Section 2.3.1, we considered only a stationary atom. If we expand the treatment to include an atom moving with velocity $\vec{v}$ and consider two laser beams with wave vectors $\vec{k_1}, \vec{k_2}$, Equation 2.33 becomes:

$$
\begin{aligned}
a_f^{(2)} = \frac{1}{4\hbar^2} \sum_k \Bigg(& \frac{H_{fk1}H_{ki1}}{(\omega_{ki} - \omega_1 - \vec{v}\cdot\vec{k_1})} \frac{e^{i(\omega_0 - 2\omega_1 - 2\vec{v}\cdot\vec{k_1})t} - 1}{(\omega_0 - 2\omega_1 - 2\vec{v}\cdot\vec{k_1})} \\
& + \frac{H_{fk2}H_{ki2}}{(\omega_{ki} - \omega_2 - \vec{v}\cdot\vec{k_2})} \frac{e^{i(\omega_0 - 2\omega_2 - 2\vec{v}\cdot\vec{k_2})t} - 1}{(\omega_0 - 2\omega_2 - 2\vec{v}\cdot\vec{k_2})} \\
& + \frac{H_{fk2}H_{ki1}}{(\omega_{ki} - \omega_1 - \vec{v}\cdot\vec{k_1})} \frac{e^{i(\omega_0 - \omega_1 - \omega_2 - \vec{v}\cdot(\vec{k_1}+\vec{k_2}))t} - 1}{(\omega_0 - \omega_1 - \omega_2 - \vec{v}\cdot(\vec{k_1}+\vec{k_2}))} \\
& + \frac{H_{fk1}H_{ki2}}{(\omega_{ki} - \omega_2 - \vec{v}\cdot\vec{k_2})} \frac{e^{i(\omega_0 - \omega_1 - \omega_2 - \vec{v}\cdot(\vec{k_1}+\vec{k_2}))t} - 1}{(\omega_0 - \omega_1 - \omega_2 - \vec{v}\cdot(\vec{k_1}+\vec{k_2}))} \Bigg) \quad (2.34)
\end{aligned}
$$

As a result of the interaction between $\vec{v}$ and $\vec{k}$, lineshapes of atomic transitions at room temperature are typically Doppler-broadened on the order of GHz, requiring techniques such as saturated absorption spectroscopy to achieve better resolution. Each photon's frequency in the atom's rest frame is Doppler-shifted by $\vec{v}\cdot\vec{k}$. Typically, only one velocity class of atoms can absorb light from ω_1 or ω_2 for a given detuning, equal to its Doppler shift. With two-photon absorption it is possible to choose $\vec{k_1}$ and $\vec{k_2}$ such that the sum of the respective Doppler shifts is zero. This can be achieved by using counterpropagating $\vec{k_1}$ and $\vec{k_2}$, either by splitting or retroreflecting a single laser source, or by using counterpropagating light from two laser sources. If the Doppler shifts sum to zero, then atoms of all velocity classes can participate simultaneously in the on-resonance absorption by absorbing one photon from each beam. The result is a large Doppler-free absorption signal on-resonance with a narrow Lorentzian lineshape, superimposed on a much broader Doppler-broadened Gaussian peak. The amplitude of the on-resonance signal is inversely proportional to the linewidth via the lineshape function $g(\omega)$.

Vasilenko was the first to calculate the Doppler-free lineshape for two counterpropagating beams [159]. For the case of equal intensities $I_1 = I_2 = I$ and equal frequencies $\omega_1 = \omega_2 = \omega$, Grynberg

et. al [79] showed that the area of the Doppler-free Lorentzian curve for counterpropagating beams is two times the area of the Doppler-broadened Gaussian curve. To demonstrate this the terms of Equation 2.34 must be considered independently. The Gaussian curve comes from the sum of the two independant transition probabilities for the first two terms, integrated over the velocity distribution; the area is two times larger than the area for a single travelling wave. The Lorentzian curve comes from the transition probability of the indistinguishable third and fourth terms, for which the amplitudes must be squared; the corresponding area is four times larger than the area for a single travelling wave. The sum of the Lorentzian and Gaussian curves therefore has a total area six times larger than the single travelling wave case. The two-photon absorption transition probability is given by [57, 159]:

$$W = |a_f^{(2)}|^2 = \sum_k \frac{|H_{fk}|^2 |H_{ki}|^2}{16\hbar^4(\omega_{ki} - \omega)^2} \left\{ \frac{1}{(\Omega - 2k\upsilon)^2 + \gamma^2} + \frac{1}{(\Omega + 2k\upsilon)^2 + \gamma^2} + \frac{4}{(\Omega)^2 + \gamma^2} \right\} \quad (2.35)$$

where $\Omega = \omega_0 - \omega_1 - \omega_2 = \omega_0 - 2\omega$ is the detuning and γ is the homogeneous linewidth. After averaging over the velocity distribution this yields the transition probability W:

$$W = \frac{|H_{fk}|^2 |H_{ki}|^2}{16\hbar^4(\omega_{ki} - \omega)^2} 6g(\omega) \quad (2.36)$$

with lineshape $g(\omega)$:

$$g(\omega) = \frac{1}{6} \left(2 \times \frac{2}{2\sqrt{\pi}k\upsilon} e^{-\Omega^2/(2k\upsilon)^2} + 4 \times \frac{2}{\pi} \frac{\Gamma_L/2}{\Omega^2 + (\Gamma_L/2)^2} \right). \quad (2.37)$$

The Doppler-broadened Gaussian FWHM is $\Gamma_G = 4\sqrt{\ln(2)}k\upsilon$,while Γ_L is the homogeneous (e.g., pressure-broadened) Lorentzian FWHM of the Doppler-free peak. The lineshape is normalized by the factor $\frac{1}{6}$ such that $\int g(\omega)d\omega = 1$. The combined lineshape profile is shown in Fig. 2.10. On exact resonance ($\Omega = 0$), we have:

$$g(0) = \frac{1}{6} \left(\frac{2}{\sqrt{\pi}k\upsilon} + \frac{16}{\pi\Gamma_L} \right). \quad (2.38)$$

The Gaussian FWHM is typically orders of magnitude larger than Γ_L under room temperature and at pressures of a few Torr. Therefore the first term of Equation 2.38 is typically less than 1% and can be neglected.

High-resolution spectroscopy is made possible by Doppler-free two photon excitation. The first experimental Doppler-free two photon absorption spectrum was obtained by Biraben et. al. [22] for the sodium $3s - 5s$ transition, with a signal roughly an order of magnitude larger than the Doppler-broadened background. They also showed complete elimination of the Doppler background by

circular polarizing the light in such a way that the selection rules for the particular transition forbid absorption of two co-propagating photons. Simultaneous observations were made by [105, 130]. Next, Hansch et al [80] measured the Doppler free spectrum in hydrogen of the metastable $1s - 2s$ transition, and measured the Lamb shift very precisely. In xenon, Raymond et al [138] measured the two photon absorption coefficients of three dipole-allowed $6p \leftarrow 5p$ Xe transitions using a pulsed laser and high Xe pressures to measure collisional excitation between excited states for pressures 100 Torr or greater. Later, Plimmer et al [128] used a CW dye laser to perform high-resolution Doppler-free two-photon spectroscopy on the 249 nm transition in Xe, which showed no hyperfine structure as the ground and excited states are both $J = 0$. This made for ease of identifying isotope shifts, on the order of 130 MHz between neighbouring even isotopes as well as between ^{129}Xe and ^{131}Xe. The measurement was enabled in part by the use of an optical cavity enclosed in a cell, which enhanced the intensity of excitation light by an order of magnitude, and enabled two-photon absorption measurements at Xe pressures as low as 100 mTorr. At higher pressures they measured a Lorentzian line shape and pressure broadening of FWHM of 28.8 MHz/Torr, and a shift of 9.5 MHz/Torr towards lower frequency. Seiler et al [150] perform high-resolution Doppler-free two photon spectroscopy on the 249 nm transition of xenon in a gas jet, and use subsequent ionization by a third photon for detection. They were able to obtain isotope shifts with resolution limited to 10 MHz by their pulsed laser linewidth.

Cross section and transition rate

A review article by Rumi and Perry defines the two-photon cross section δ (with units of GM $= 10^{-50}$cm^4 s after Maria Goeppert-Mayer) analogous to the single-photon cross section σ in terms of the change in photon flux $\phi = I/\hbar\omega$ per path length z, for excitation with a single beam [143, 156]:

$$\frac{d\phi}{dz} = -\sigma n\phi - \delta n\phi^2, \tag{2.39}$$

where n is the number density of atoms, and goes on to show the two-photon excitation rate (number of atoms per unit time and volume) is:

$$\frac{dn}{dt} = \frac{1}{2}\delta n\phi^2, \tag{2.40}$$

More common in the literature is the definition $\sigma^{(2)} = \frac{1}{2}\delta$ such that

$$\frac{dn}{dt} = \sigma^{(2)}n\phi^2, \tag{2.41}$$

Literature often reports the transition rate $W = \frac{1}{n}\frac{dn}{dt}$ per atom:

$$W = \sigma^{(2)}(I/\hbar\omega)^2, \tag{2.42}$$
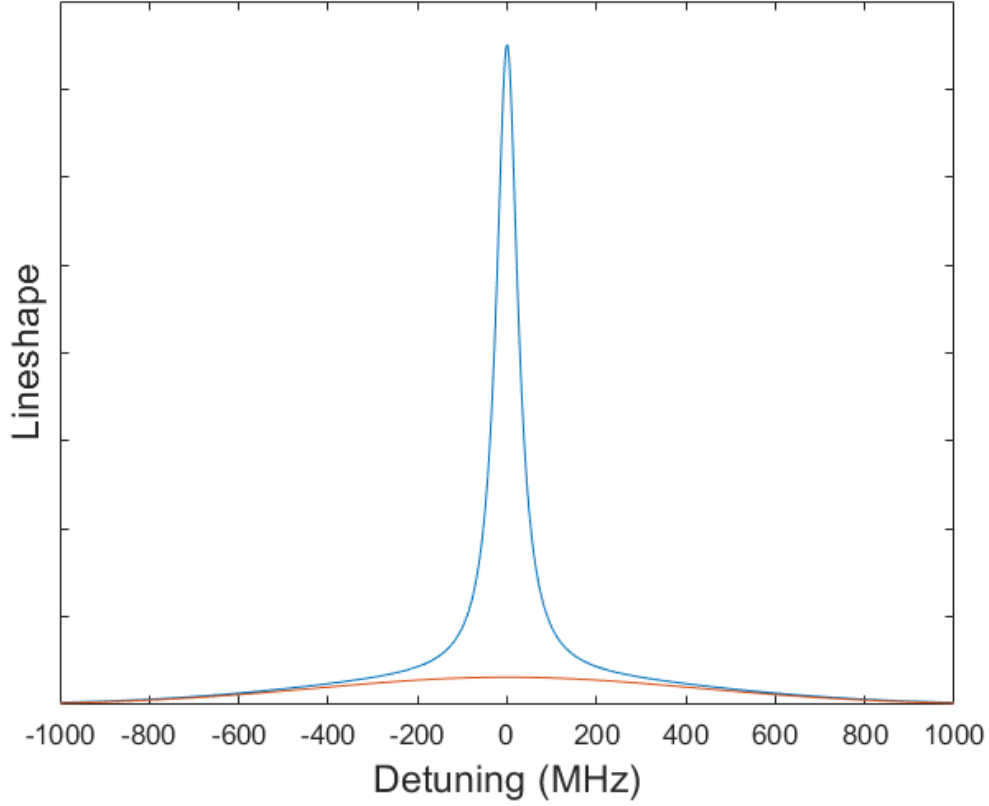
Figure 2.10: Example plot of the combined lineshape for Doppler-free excitation (blue) com-
pared with the Doppler-free background (red) as a function of detuning. The on-
resonant lineshape value can be many times larger than the Doppler broadened value
for a sufficiently small homogeneous linewidth. The Doppler-broadened width is typ-
ically wider than shown, but is exaggerated here to make the amplitude visible. The
area of the Lorenztian Doppler-free profile is twice that of the retroreflected Doppler-
broadened profile, and four times that of a Doppler-broadened profile for absorption of
a travelling wave.

It must be noted that the cross section $\sigma^{(2)}$ is dependant on lineshape $g(\omega)$ and frequency ω. One
can alternately define [148] a lineshape-independant cross section $\sigma_0^{(2)}$ with units of cm^4:

$$\sigma^{(2)} = \sigma_0^{(2)} G^{(2)} g(\omega). \tag{2.43}$$

where $G^{(2)}$ is a dimensionless photon statistical factor that accounts for photon coherence in ex-
citation with multimode pulsed lasers, and $g(\omega)$ is the absorption lineshape function. In our CW
measurements we assume $G^{(2)} = 1$. The lineshape function $g(\omega)$ used depends on the experimental
conditions, such as the beam configuration, laser linewidth, and atomic linewidth due to homo-

geneous (lifetime, pressure) and inhomogeneous (Doppler) broadening. In general it should be normalized such that $\int g(\omega)d\omega = 1$. The cross section $\sigma_0^{(2)}$ is then directly related to the quantum state by Equation 2.35:

$$\sigma_0^{(2)} \propto \sum_k \frac{|H_{fk}|^2 |H_{ki}|^2}{16\hbar^4(\omega_{ki} - \omega)^2} \left(\frac{\hbar\omega}{I}\right)^2 \tag{2.44}$$

Often experimental reports in the literature define a two-photon coefficient α in $\mathrm{cm}^4\,\mathrm{J}^{-2}$ which is also lineshape-independant. For excitation with a single laser of intensity I, the two photon excitation rate W may be written as [127, 138]:

$$W = \alpha I^2 g(\omega) \tag{2.45}$$

where the lineshape $g(\omega)$ is typically Doppler-broadened and resembles only the first term of Equation 2.37. The total number of atoms excited per second is given by:

$$\frac{dN}{dt} = WnV = \alpha I^2 g(\omega)nV \tag{2.46}$$

where $N = nV$ is the number of Xe atoms in excitation volume V. By comparison of Eqns. 2.42 and 2.45, one can infer the relation:

$$\alpha = \frac{\sigma_0^{(2)}}{(\hbar\omega)^2} \tag{2.47}$$

(One can never have too many conventions. There is yet another definition $\alpha^* = \sigma^{(2)}/\hbar\omega$, which is still lineshape dependent and has units of $\mathrm{cm}^4\,\mathrm{W}^{-1}$. Table 2.2 lists the various expressions.)

Table 2.2: Common notations for two photon cross section in the literature.

Symbol	Formula	Units
δ	-	$\mathrm{cm}^4\,\mathrm{s}$
$\sigma^{(2)}$	$\delta/2$	$\mathrm{cm}^4\,\mathrm{s}$
$\sigma_0^{(2)}$	$\sigma^{(2)}/(g(\omega)G^{(2)})$	cm^4
α	$\sigma_0^{(2)}/(\hbar\omega)^2$	$\mathrm{cm}^4\,\mathrm{J}^{-2}$
α^*	$\sigma^{(2)}/\hbar\omega$	$\mathrm{cm}^4\,\mathrm{W}^{-1}$

Earlier in this section we discussed the enhancement in transition rate when performing Doppler-free two photon absorption. We make this enhancement explicit by multiplying Equation 2.45 by a factor of six following Raymond [138]:

$$W = 6\alpha I^2 g(\omega) \tag{2.48}$$

with the lineshape $g(\omega)$ normalized to unity by Equation 2.37. This accounts for the combined

Doppler-broadened and Doppler-free profiles, and ensures that the value of α is consistent with that observed from Doppler-broadened excitation. This allows us to compare our results with those in the literature from previous experiments, the majority of which are Doppler-broadened.

2.3.3   Superradiance

In 1954 Dicke predicted spontaneous coherent emission coming from excited atoms [58], which has since been observed. In his highly mathematical paper, Dicke modeled a system of two-level atoms with a state that had a positional part and an internal energy part. While in general the emission intensity of spectroscopy experiments is proportional to the number of emitters N, in superradiance it is the electric field emission which is proportional to N, making the emission intensity proportional to N^2. The lifetime of an excited state under superradiance decreases (according to N). The lifetime of a superradiant state also decreases with higher excitation laser power. An effect which displays some of the properties of superradiance has been observed in Xe [137] under two photon excitation. Section 4.1.2 presents our experimental observation of this effect using a pulsed laser. If an enhancement in LIF emission intensity can be observed under the excitation conditions in the planned Xe comagnetometer, it means lower Xe pressures can be used in the experimental cell.

2.4   Xenon

Xenon was discovered in 1898 by Ramsay and Travers [135] through fractional distillation of air. It found early use in flashlamps [60] and as an anesthetic [52]. Neil Bartlett discovered the first noble gas compound at UBC in 1962; xenon formed an ionic compound with the strongly-oxidizing platinum hexafluoride PtF_6, due to similarity of xenon's ionization energy (12.13 eV) and that of dioxygen (12.2 eV) which had been previously shown to undergo oxidation [18]. This discovery sparked the renaming of the inert gases as noble gases.

Xenon is a noble gas with atomic number 54. Natural abundance xenon consists of eight stable isotopes between masses 124-134 and one slightly radioactive isotope 136 (half-life$\approx 10^{21}$ yr), listed in Table 2.3. The two stable odd isotopes possess non-zero nuclear spin. Xenon has a ground state electron configuration of [147]

$$1s^2 2s^2 2p^6 3s^2 3p^6 4s^2 3d^{10} 4p^6 5s^2 4d^{10} 5p^6 \tag{2.49}$$

and corresponding angular momentum term symbol $^1S_0$, and is therefore diamagnetic. The lowest-lying electronic states of Xe are shown in Fig. 2.11. As a noble gas, xenon has a closed valence shell meaning electrons are tightly bound. Xe has a first ionization energy of 97833.79 cm^{-1} or 12.1 eV [147]. Excitation to the first excited electronic states $6s$ or $6s'$ requires either discharge or VUV photon. The next excited state $6p$, however, (around 78000 cm^{-1}) is accessible by two-photon transitions at Deep Ultraviolet (DUV) wavelengths and is the focus of this work.
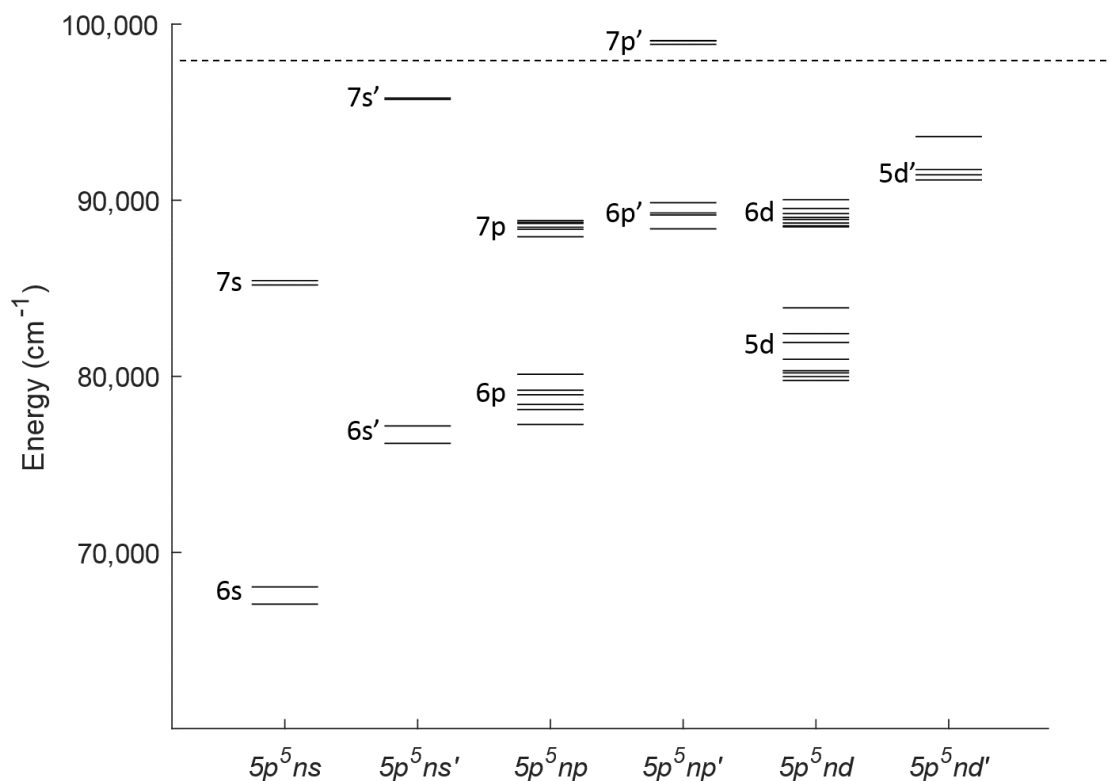
Figure 2.11: Excited state energy levels of Xe I relative to the ground state energy, shown with their respective electron configurations. Here a prime on the configuration indicates the state with a core term symbol $^2P_{1/2}$, and the unprimed state indicates the $^2P_{3/2}$ core. Spin-orbit coupling is determined by the jl or Racah coupling scheme. The dotted line indicates the ionization threshold for the $^2P_{3/2}$ core. Created using the values for energy levels cited in [147]

There are two-photon allowed transitions to $6p$ states (see Fig. 2.12) at 249.6, 252.5 and 255.9nm, labelled in Racah's notation (see Section 2.4.1) as $^2[1/2]_0$, $^2[3/2]_2$, and $^2[5/2]_2$, respectively. Additionally, based on the ionization energy it is possible for a (2+1) Resonance-Enhanced Multiphoton Ionization (REMPI) process to ionize Xe following TPA upon absorption of a third UV photon. This is not studied in the present work. The TPA excited $6p$ levels above can spontaneously decay to $6s$ levels $^2[3/2]_1$ and $^2[3/2]_2$ by emitting a Near Infrared (NIR) photon, and subsequently decay to the ground state by emitting 147.0 nm light [147]. One $6s$ state in particular ($^2[3/2]_2$) is metastable. Spectroscopic study of the above $6p$ states by two-photon absorption is covered in Chapter 4.
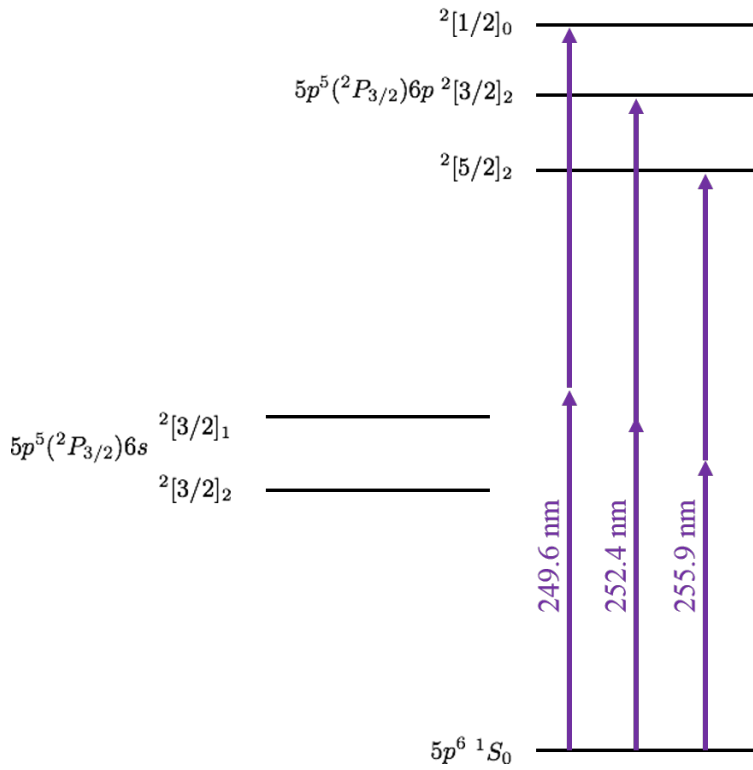
Figure 2.12: Allowed two-photon transitions to the Xe 6p states $^2[1/2]_0$, $^2[3/2]_2$, and $^2[5/2]_2$. The transitions occur between states of the same parity (here both ground and excited state are even parity).

Table 2.3: Natural abundances and nuclear spin I of the stable xenon isotopes.

Isotope	Natural Abundance	I
^{124}Xe	0.095%	0
^{126}Xe	0.089%	0
^{128}Xe	1.91%	0
^{129}Xe	26.40%	1/2
^{130}Xe	4.10%	0
^{131}Xe	21.20%	3/2
^{132}Xe	26.90%	0
^{134}Xe	10.40%	0
^{136}Xe	8.90%	0

2.4.1 Angular momentum coupling schemes in Xe

LS **coupling**

The splitting of energy levels within each electron configuration is determined by electrostatic interactions and spin-orbit interactions. The most commonly encountered scheme is called *LS* (or Russell-Saunders) coupling [153], and is used when the electrostatic interactions dominate. The total orbital angular momentum L and total electron spin S are individually determined and sum to $J = L + S$. The opposite extreme where spin-orbit interactions dominate is called jj coupling. In that case $j_i = l_i + s_i$ is determined for each electron i before summing to a total $J = \sum_i j_i$.

These schemes hold approximately for light and heavy atoms, respectively. Various intermediate coupling schemes exist including the jl coupling observed in xenon and described below. In singly-excited xenon, *LS* coupling is used to describe the Xe $(^2P_{1/2}$ or $^2P_{3/2})$ core.

jl **coupling and Racah notation**

For xenon and other noble gases, the filled outermost $p-$ shell is tightly bound. Any excited electron has much lower binding energy than the tightly bound core. For these atoms the suitable coupling scheme is the jl coupling described by Racah [133], which describes coupling between a parent core with total angular momentum J_c (described well by *LS* coupling) and a valence electron with orbital angular momentum l. The two momenta add to form an intermediate angular momentum, $K = J_c + l$ which then couples with the spin s of the excited electron to form a total angular momentum $J = K + s$. The commonly-used notation (found in tables published by Moore [114] and Saloman [147]) is that suggested by Racah (where $n_c l_c$ is the electron core configuration):

$$n_c l_c (^{2S+1}L_{J_c}) nl \, ^{(2s+1)}[K]_J \qquad (2.50)$$

The result of the spin-orbit coupling to the single valence electron means every term is a doublet with two values, $J = K \pm 1/2$. Thus, the term $^2[1/2]_0$ describes a doublet with intermediate angular momentum $K = 1/2$ and total angular momentum $J = 0$.

Some authors (see, e.g. [168]) label the excited states of xenon using Paschen notation, in which $1s_1, 1s_2, ...$ are labels for singly excited states with the lowest electron configuration $(5p^5 6s)$, followed by $2p_1, 2p_2, ...$ for states of configuration $(5p^5 6p)$. The subscripts indicate terms of successively lower energies. For xenon, the $5p^5(^2P_{3/2})6s^2[3/2]_2$ state is labelled $1s_5$ in Paschen notation.

2.4.2 History of Xenon Spectroscopy

The first systematic spectra were obtained in discharge cells by Meggers [108] and Humphreys [109], motivated by a search for new wavelength standards. By analysis of the complicated discharge spectra, Jones [95] was able to confirm the nuclear spin $I = 1/2$ for ^{129}Xe and recommend

$I = 3/2$ for ^{131}Xe. This was followed by many studies of hyperfine structure and isotope shifts. In particular, Jackson et al. [50, 89–92] undertook a systematic study of the hyperfine structure and isotope shifts of emission spectra. In time more detailed observations were made possible by Doppler free methods of saturated absorption [21] and two photon absorption [128]. Measurements were made also of excited level natural lifetimes and collisional deexcitation rates [35, 61].

Optical pumping was demonstrated in Xe as early as 1969 in metastable Xe [149]. Later efforts showed the ground state could be polarized through spin exchange with Rb [78]. The theory of spin exchange was presented in detail by Happer [81, 82]. There are recent efforts producing large volumes of hyperpolarized Xe with polarization approaching 100% [117, 144]. These find application in clinical studies, in particular lung imaging.

Starting in the 1980s two photon excitation and REMPI were studied with an aim of single atom detection using powerful new pulsed lasers [44, 73]. Plimmer [128] demonstrated high precision Doppler-free spectroscopy using retroreflected narrow-linewidth CW light. As resolution improved efforts were made to determine absolute transition frequencies [33, 122, 150]. Goehlich et al [70] use two-photon absorption in xenon as a calibration to determine the number density of atomic oxygen via laser-induced fluorescence at similar wavelengths.

2.4.3   Detection scheme for polarized ^{129}Xe

Two photon excitation enables a scheme for detection of the Xe ground state spin polarization which is analogous to that of one-photon optical pumping in alkali atoms. The scheme is depicted in Fig. 2.13. Using circular polarized light at 252.5 nm, one can selectively excite transitions with $\Delta M = +2$. The ground state of ^{129}Xe is twofold degenerate with total angular momentum $F = 1/2$; therefore only the $M_F = -1/2$ sublevel can be excited following the $\Delta M = +2$ rule. The other sublevel $M_F = 1/2$ becomes a dark state. We target the level $^2[3/2]_2(F = 3/2)$; an equivalent scheme is also possible for $^2[5/2]_2(F = 3/2)$. The rate of two-photon transitions in a coherent ensemble of Xe atoms precessing in the plane of $\vec{k}$ will therefore oscillate at the Larmor frequency, which will in turn generate an oscillating rate of laser induced fluorescence. We detect emission of NIR light at 895.5 nm and 823.4 nm from the $6p - 6s$ transition, although it is in principle possible to also detect VUV emission from $6s \rightarrow 5p$.

$^2[1/2]_0$

$5p^5(^2P_{3/2})6p\ ^2[3/2]_2$

$^2[5/2]_2$

$5p^5(^2P_{3/2})6s$ $^2[3/2]_1$ $F = \dfrac{3}{2}, \dfrac{1}{2}$

$^2[3/2]_2$ $F = \dfrac{5}{2}, \dfrac{3}{2}$

$5p^6\ ^1S_0$

$F = 1/2$

-1/2 1/2

-3/2 -1/2 1/2 3/2

-5/2 -3/2 -1/2 1/2 3/2 5/2

$F = 3/2$
$F = 5/2$

-3/2 -1/2 1/2 3/2

-5/2 -3/2 -1/2 1/2 3/2 5/2

$F = 3/2$
$F = 5/2$

895.5 nm

823.4 nm

252.4 nm

-1/2 1/2 M$_F$

$F = 1/2$
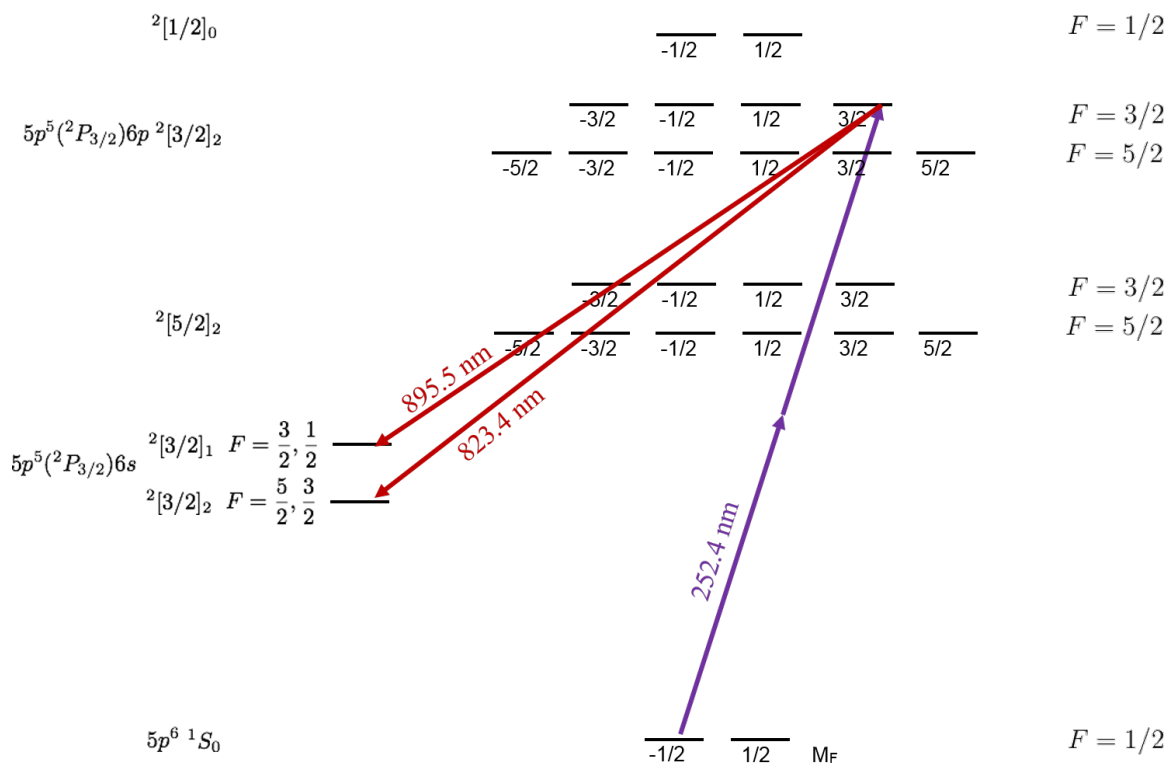
Figure 2.13: Detection scheme for polarized ^{129}Xe using two photon transitions.

Chapter 3

Production of polarized ^{129}Xe by Spin Exchange Optical Pumping

Before Xe can be used in an optical magnetometer it must be polarized. The purpose of this chapter is to describe the methods used to produce polarized ^{129}Xe, namely spin exchange optical pumping (SEOP) with Rb vapor. We describe the apparatus used for SEOP and for NMR detection; a rate equation model used to estimate polarization and relaxation rates for comparison with experimental results; and measurement of some of the factors affecting the polarization.

3.1   Experimental Apparatus and Technique

We constructed a SEOP polarizer and low-field NMR spectrometer for the Xe polarization process, with components contributed by J. Martin (U. Winnipeg) and J. Sonier (SFU). These are both described under their own headings below:

3.1.1   Spin Exchange Optical Pumping Apparatus

Spin exchange optical pumping in our apparatus occurs in a mixture of Xe, Rb, N_2, and He in a pressurized Pyrex cell irradiated with polarized NIR 795nm photons. The N_2 facilitates the spin-exchange process and provides the collisional de-excitation of the Rb vapour commonly known as "quenching" to prevent radiation trapping. Helium is used as a buffer gas to pressure broaden the D1 transition and maximize laser absorption. This section describes the SEOP cell, optical and gas-handling setups. A schematic of our polarizer is shown in Fig. 3.1.

The polarizer cell provided by our collaborators is designed by the Steacie Institute for Molecular Sciences (National Research Council, Ottawa), [34] and manufactured by U. Winnipeg glass-blowing. It is a Pyrex-constructed flow through cell consisting of i) a 2.54 cm diam. reservoir volume filled with 1 gram Rb metal connected by a 1 cm diam. stem to ii) a 2.54 cm diam. cylindri-
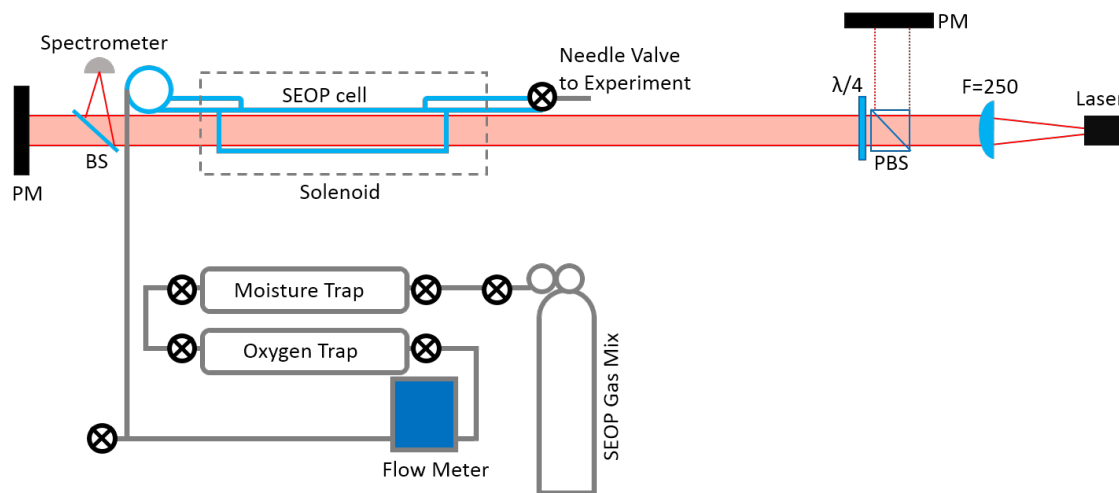
Figure 3.1: Gas flow and optics of the SEOP polarizer. BS: beam splitter, PBS: polarizing beam splitter, PM: power meter, $\lambda/4$: quarter wave plate.
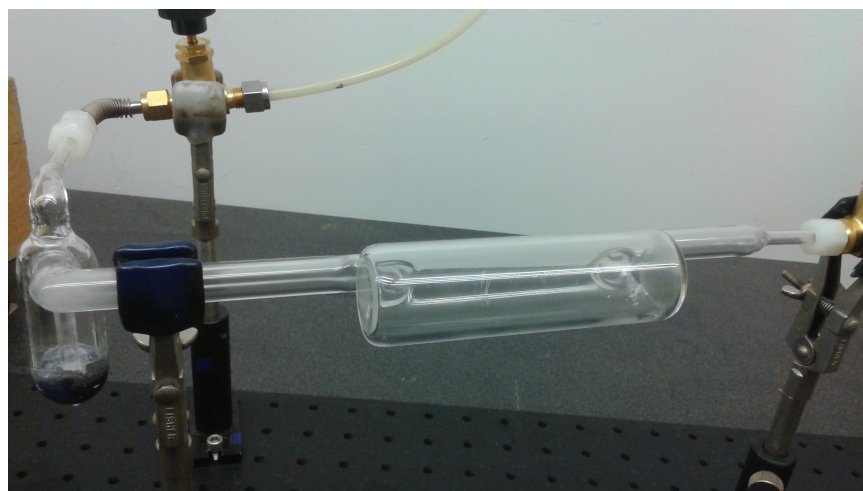
Figure 3.2: SEOP cell with heater tape and solenoid removed, showing the Rb reservoir (left) and optical pumping volume (center).

cal volume, 10 cm in length, with IR-transparent optical flats at both ends for Rb optical pumping. The pumping volume is coated with Surfasil to reduce depolarization on the cell walls. Fig. 3.2 shows a picture of the cell.

Typical SEOP parameters are listed in Table 3.1. We use a gas sample of of 1% natural abundance Xe, 3% N_2, and 96% He (Praxair, premixed), at total pressure 60 psi(g) controlled by a pressure regulator. The premixed gas passes through two gas chromatography filters via stainless steel 1/4-inch lines: a Model 1000 oxygen purifier (Chromatography Research Supplies) and a combined oxygen/moisture trap (Agilent, OT3-4-SS). A purge valve before each trap helps remove impurities

Table 3.1: Typical SEOP parameters

Parameter	Value
Typical Rb reservoir temp	200-300 C
Typical SEOP temp	80-100 C
SEOP solenoid field	10 mT
Density of gases at 50 PSIg:	
He	8×10^{19}cm^{-3}
N$_2$	2.4×10^{18}cm^{-3}
Xe	8×10^{17}cm^{-3}
Rb (at 400K)	6×10^{12}cm^{-3}
Rb (at 500K)	4×10^{15}cm^{-3}
Resonant laser flux of 1.2 W	5×10^{18}photon s^{-1}

and extend the trap lifetime. The purified gas passes through a mass flow meter (Kofloc 8100) to the Rb reservoir, mixes with Rb vapour ($n_{\text{Rb}} \approx 10^{12} - 10^{15}$ cm^{-3}), and enters the pumping volume where spin exchange occurs. The SEOP cell is centered in a 6.5" long solenoid (750 turns of 20-AWG magnet wire, magnet constant 5 mT/A), which produces a 10 mT magnetic field for Zeeman splitting, aligned antiparallel to the direction of gas flow. The cell and reservoir are both individually wrapped with heater tape controlled by separate Variac transformers. Three K-type thermocouples are fixed to the cell body, near the center and at each window, to aid in uniform heating. Downstream of the cell, a small piece of glass wool condenses out the remaining Rb vapour. A needle valve with a custom brass needle (Swagelok B-4MG, modified by UBC Chemistry Mechanical Engineering) controls the flow rate of the polarized gas. The mixture is pushed along by the pressure difference (slightly greater than 1 atm), through 1/4-inch tubing to the NMR apparatus.

The pumping laser is a Coherent fiber array packaged diode laser producing up to 30 W of 795nm (Rb D1) light with a 2nm linewidth. The unpolarized multimode output is circularly polarized by using a polarizing beam splitter (Casix, BPS0402) and quarter wave plate (Casix, WPZ1425-800). An additional lens mounted before the beamsplitter helps collimate the multimode light exiting the laser head to achieve a roughly 2cm beam diameter. We later installed beam recombination optics (Fig. 3.3) to "recycle" the s-polarized light which is otherwise wasted. An additional quarter wave plate converts the secondary beam to the same circular polarization as the primary beam, and then it is injected into the cell at a slight beam path angle to the primary beam.

The polarizer is shown operating in Fig. 3.4. Due to the multimode nature of the pump laser, the output cannot be well collimated. This is apparent by the significant divergence and scatter of the light as it appears on the downstream power meter. Detection of the transmitted power through the SEOP cell is by a fiber-coupled optical spectrum analyzer (HP 86142A) with 0.1 nm resolution bandwidth and a sweep rate ≈ 1 Hz. A spectrum of the optically pumped Rb transmission is shown in Fig. 3.5. The evidence for optical pumping is the increased transmission of resonant light that

46
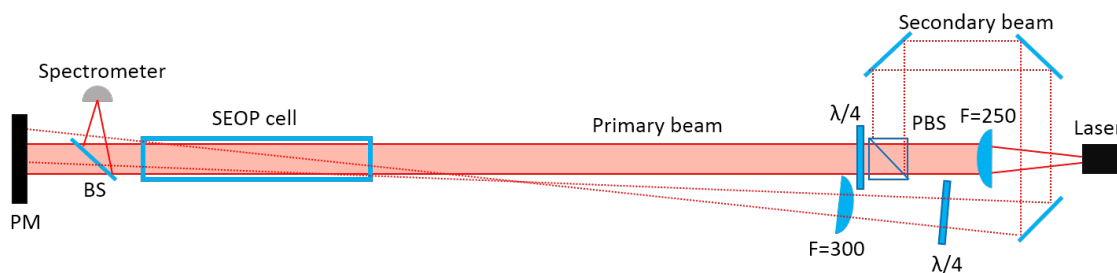
Figure 3.3: Beam recombination optics "upgrade" used to circular polarize and overlap both linear polarized outputs (the primary p-pol and secondary s-pol) from the PBS. BS: beam splitter, PBS: polarizing beam splitter, PM: power meter, $\lambda/4$: quarter wave plate.
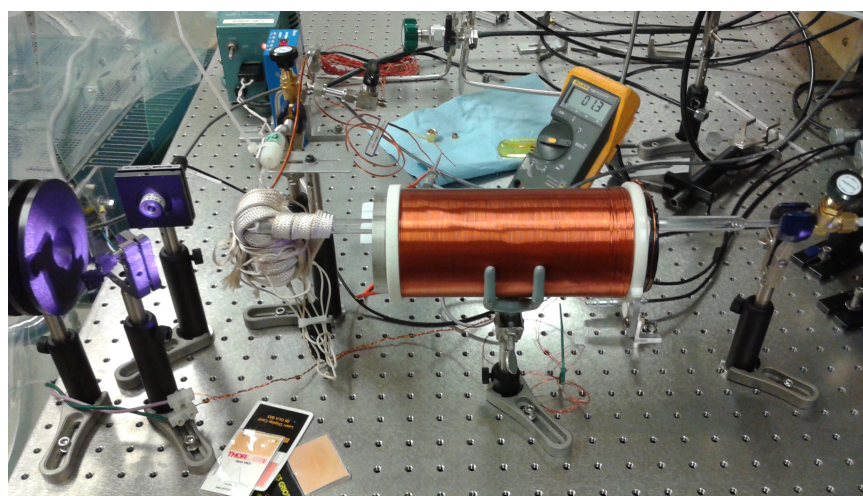
Figure 3.4: SEOP cell during operation. Scattered D1 pumping light appears in false-color as purple on the camera's sensor.

occurs rapidly (within 1s) when the SEOP solenoid magnetic field is switched on. There is a dramatic difference in light transmission between field ON/OFF conditions, such that the cell becomes almost completely transparent to the pumping light. Light in the spectral wings is not absorbed because our laser linewidth is significantly broader than the pressure-broadened atomic linewidth. The "useful" power of our beam therefore depends on the pressure broadening determined in Section 3.3.3. Based on integration of the spectral power density in Fig. 3.5, we estimate that less than 12 % of photons in the laser beam are resonant with the optical pumping transition.

3.1.2 NMR Apparatus

Detection of polarized Xe is by the NMR technique of Adiabatic Fast Passage (AFP) described in Sec. 2.2.5. The NMR detector used was modified from an existing system constructed in the Sonier Lab at SFU, itself modeled on the polarizer design by Ruset [144]. It was previously conceived as
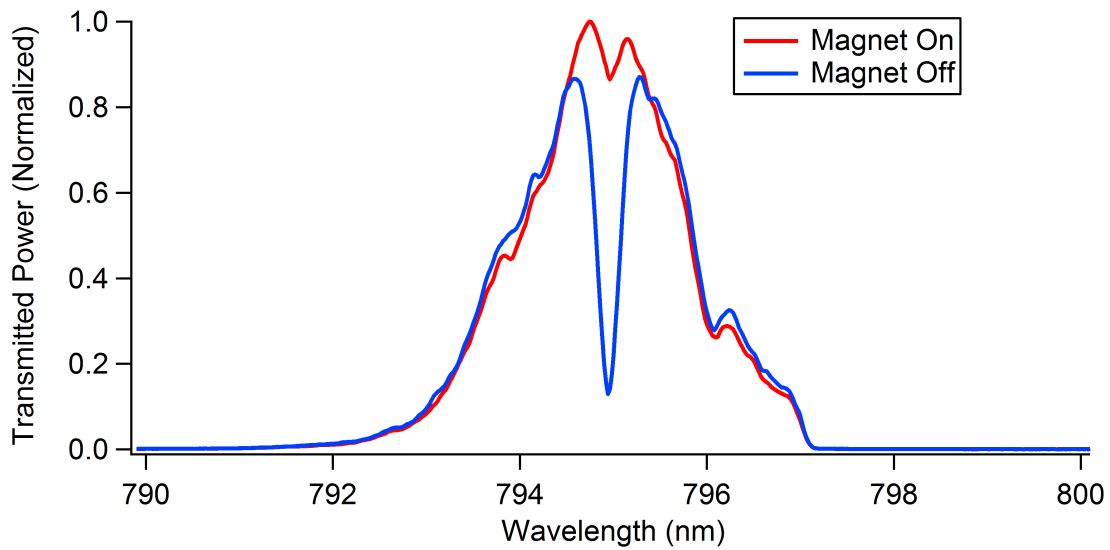
Figure 3.5: Optical pumping of Rb is observed when an applied B field breaks the degeneracy of Zeeman levels. The level probed by circular polarized light only absorbs with the field OFF; with the field ON, atoms are rapidly pumped into the dark state.
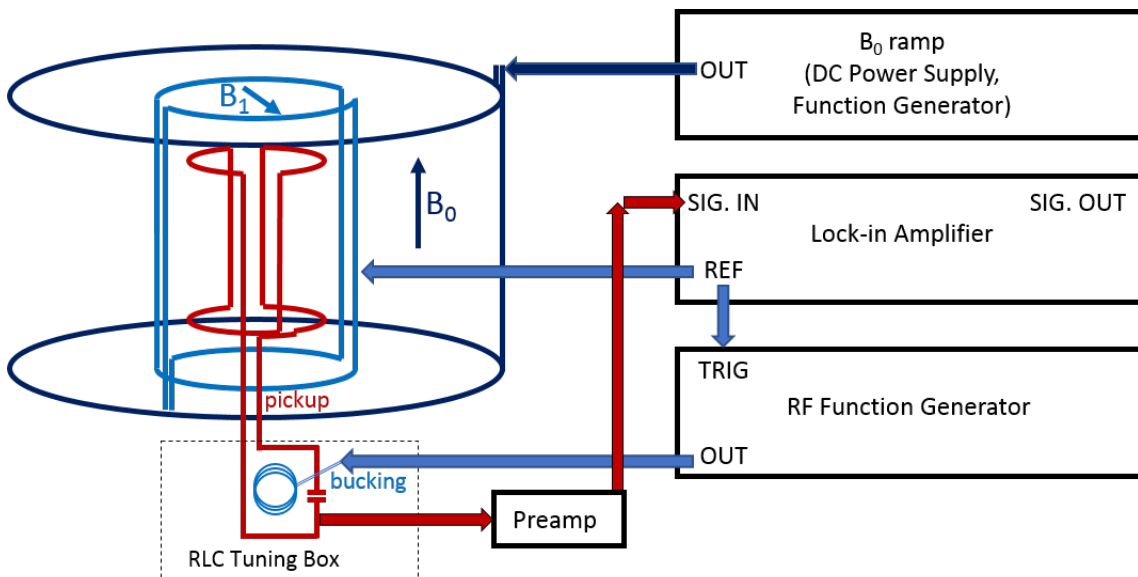
Figure 3.6: Coils and detection electronics for the free-standing NMR spectrometer .

a stacked spin-exchange polarizer and NMR detector, with the NMR coils mounted atop a vertical oven and polarizer cell. We decommissioned the polarizer portion and reconfigured this detector for high field uniformity in the NMR region. A separate design, with even higher field uniformity suitable for Free Induction Decay, is described in Ref. [165] and will be used in future work.

The free-standing spectrometer consists of three orthogonal pairs of coils (B_0, B_1, pickup) shown schematically in Fig. 3.6. The B_0 coil is a Helmholtz pair (96 turns/coil), with 55 cm diameter. The coils are driven by a DC power supply (KEPCO BOP-50-8D) which can be ramped by means of a control voltage input from a function generator. The B_0 field inhomogeneity from calculation is less than 0.02% change over the 10 cm sample region for the Helmholtz configuration. The B_1 coil is a 5-turn saddle pair orthogonal to B_0, driven by RF radiation (usually provided by the lock-in amplifier described below). B_1 is typically driven at fixed amplitude for AFP experiments, with frequency corresponding to the Larmor frequency imposed by B_0. It can also be pulsed in the case of FID. The pickup coil is another saddle pair concentric with B_1 and oriented orthogonal to it. A 3D printed worm gear (shown in Fig. 3.7) permits fine tuning of the angle between the B_1 and pickup coil axes to minimize cross-talk, described below. The pickup coil is sensitive to precession of the net magnetization through Faraday induction, which converts it to an Electromotive Force (EMF). The pickup is wired to a capacitor in a small tuning box outside the coil system; this forms a tuned Resistor-Inductor-Capacitor (RLC) resonance circuit which increases the signal strength at the desired resonance frequency by the quality factor Q (see Appendix A.2). The voltage across this capacitor is amplified by a preamp (Stanford SRS552) and measured by a lock-in amplifier (Stanford SRS830) locked to the B_1 frequency.

Coil constants are listed in Table 3.2. Typically we obtain an AFP signal by ramping the B_0 field slowly through resonance and recording the lock-in output. Table 3.3 lists typical parameters used during a scan.

Table 3.2: Coil Parameters for NMR.

	B_0	B_1	pickup	SEOP
Radius (m)	0.28	0.05	0.025	0.038
Length (m)	-	0.2	0.1	0.165
Turns	96	5	100	750
Resistance (Ω)		1.4	9.85	6
Inductance (mH)	4.6	.034	4.7	19
Magnet constant (mT/A)	0.30729	0.05426	2.2848	5.0908
Voltage, typ. (V)	36	1	-	20
Current, typ. (A)	4	0.714286	-	2
Field, typ. (mT)	1.22916	0.038757	-	10.1816
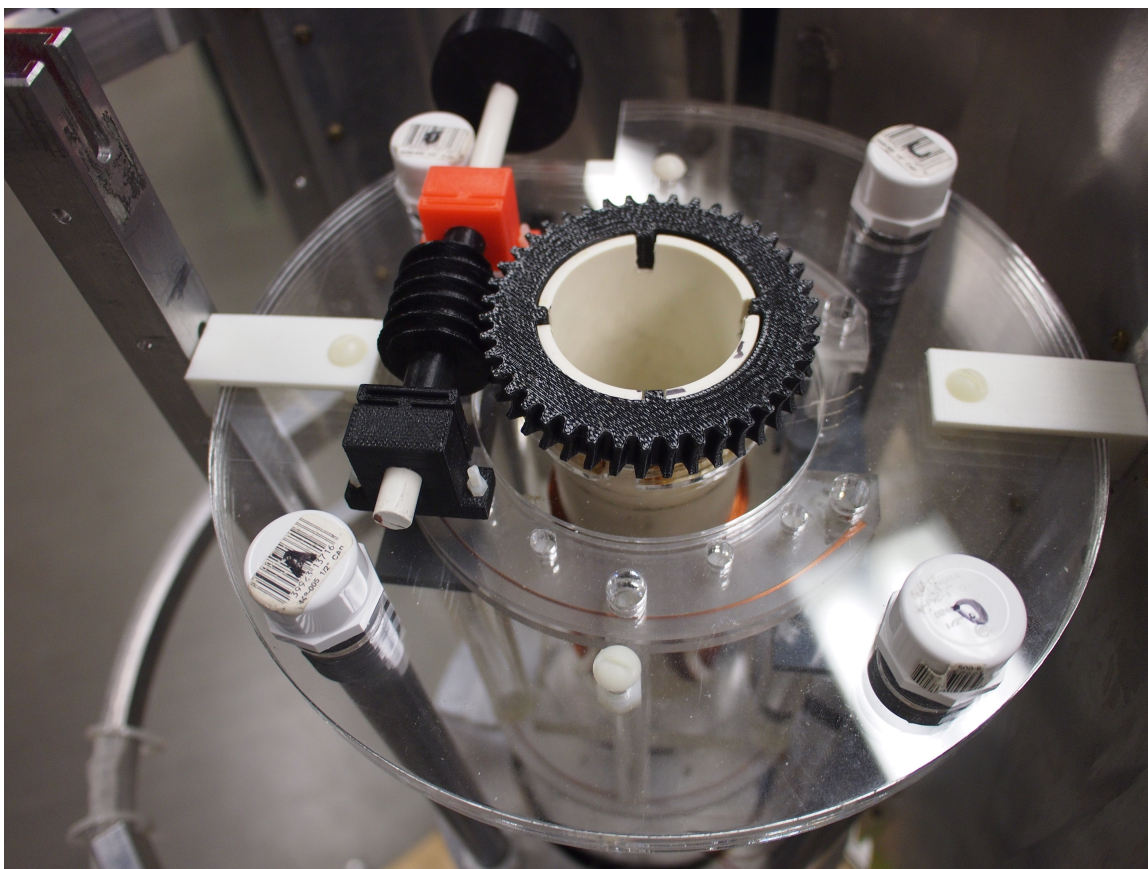
Figure 3.7: Worm gear used for coarse adjustment to minimize cross-talk between NMR coils.

Adiabatic Fast Passage Technique

The theory of AFP is presented in Section 2.2.5. Here we present the technical details of our implementation of AFP. We apply a B_1 field using the lock-in reference output, at the nominal Larmor frequency ω_1 of either water or Xe. After thermal stabilization, we align the B_1 and pickup coils orthogonal by rotating the worm gear to minimize the background signal. We call this background cross-talk; it results from mutual induction (or possibly capacitive coupling) between B_1 and the pickup owing to imperfect alignment. Any residual cross-talk is eliminated by a different method: A small bucking coil, pictured in Fig. 3.8, is mounted in the tuning box overlapping the area of the tuned RLC circuit and driven also at ω_1 by a function generator (with a suitable phase shift from the lock-in amplifier output). The amplitude of the bucking coil is chosen to match the experimentally measured cross-talk, and then phase shifted 180 degrees to completely cancel it. Noise from external RF sources is cancelled using a 2m long cylindrical aluminum shield. This cancellation yields signal sensitivity better than 1 mV.

The sample volume is a 147 mL Nalgene bottle. We measure AFP signals from both H_2O and
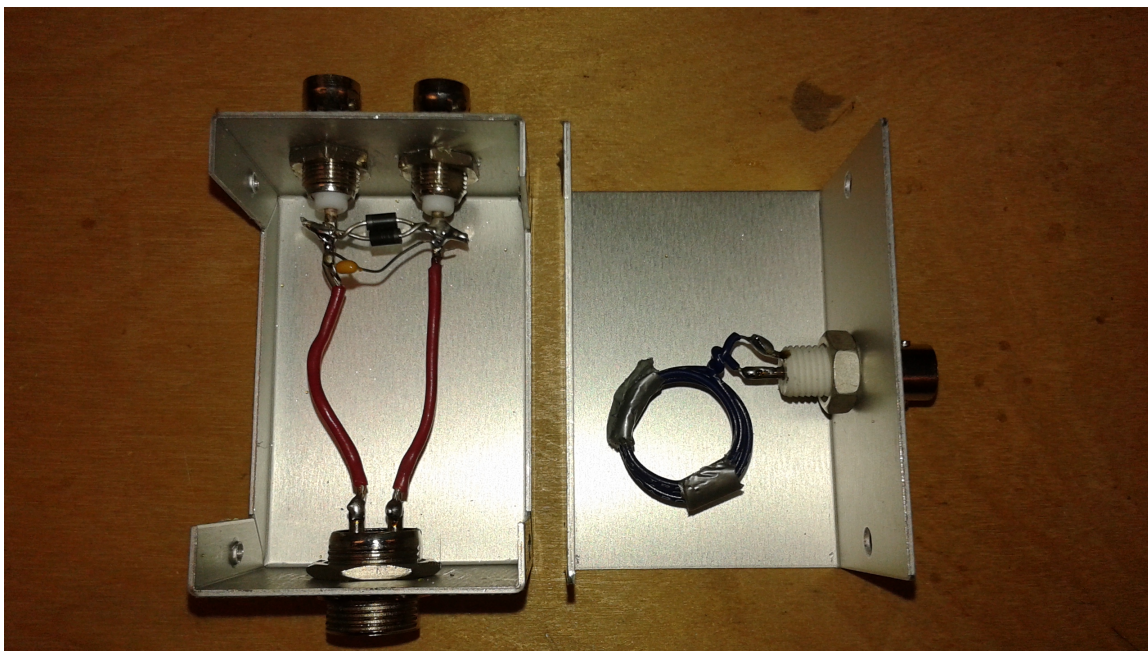
Figure 3.8: Bucking coil (right) used to eliminate residual cross talk in the RLC circuit tuning box.

Xe samples at two nominal Larmor frequencies (58.82 kHz and 15.555 kHz, respectively). Many of the H_2O samples are doped with $CuSO_4$. The $CuSO_4$ is known to shorten the T_1 lifetime , e.g. to 0.116 s at 16 mM concentration[131, 158] so we can rapidly acquire scans. The H_2O was thermally polarized in a field nominally set at 1.4 mT and a ramp applied through resonance. Ramp rates and lock-in time constants were chosen to minimize noise while preserving the fast rise times of AFP signals. The on-resonance precession signal is demodulated by the lock-in amplifier and recorded using an oscilloscope or computer data acquisition (DAQ).

Xe AFP signal is obtained in a similar fashion. An empty 147 mL Nalgene bottle is connected by tubing to the SEOP system. The mixture of Xe, N_2 and He, containing hyperpolarized Xe, flows into the measurement region. Care is taken to avoid any rapid field changes or zero-field regions along the tubing path, to prevent loss of polarization. B_1 is driven at a lower RF frequency ($\approx$15 kHz) for the same nominal B_0 field, as determined by the smaller Xe gyromagnetic ratio.

3.2 Rate equation model for SEOP

We present here a simple rate-equation model of the processes happening during spin exchange optical pumping, in order to identify their relative contributions and look for ways to increase the polarization. The phenomena are grouped as follows: polarization of Rb by optical pumping, loss of Rb polarization by collisions and radiation trapping, polarization of ^{129}Xe through spin exchange,

Table 3.3: Typical NMR parameters

Parameter	Value
B_0 current	3.95-4.25 A
B_0 voltage	36 V
B_0 nominal field	1.4 mT
B_0 ramp frequency	200 mHz (5s period)
B_0 ramp amplitude	100mV
B_1 voltage from lock-in	1.00 V
B_1 field strength (rotating, 1.0V driving)	0.628 μT
B_1 frequency	15.555 kHz (H_2O)
	58.82 kHz (H_2O)
lock-in sensitivity	1mV
preamp setting	100x
on screen signal amplitude	1 V
signal amplitude	10 uV
noise amplitude	5 uV

and subsequent depolarization of Xe. The rate equation model is based primarily on a description summarized by Brunner [36], and uses our experimental values given in Table 3.1. Estimates of the pumping and spin exchange rates are given in Table 3.4.

Briefly, resonant 795 nm light drives the optical pumping of Rb. Collisions of the polarized Rb with other species lead in general to a loss of Rb polarization (non-spin-conserving collisions), while a fraction of the Rb-Xe collisions lead to the spin-exchange reactions which transfer polarization from the Rb electron spin to the Xe nuclear spin. Polarized Xe, likewise, undergoes polarization-destroying collisions with other Xe, other species and with the cell walls. The equilibrium polarization of Xe in the cell comes from a balance of these rates.

Rb optical pumping

Circular-polarized radiation is used to selectively pump on the $M_J = -1/2$ sublevel (the "bright state") and deplete its population. Atoms relax either by emission to the ground state sublevels with rates determined by the corresponding dipole matrix elements, or by collisional deexcitation by a buffer gas used to prevent radiation trapping (see below). Collisional mixing of the excited state sublevels is assumed. The Rb polarization builds up in the $M_J = +1/2$ sublevel. The optical pumping rate, meaning the absorption rate per Rb atom, is given by

$$\rho_{opt} = \int \Phi_{opt}(\lambda)\sigma_{opt}(\lambda)d\lambda \tag{3.1}$$

Table 3.4: Estimate of optical pumping and relaxation rates inside the SEOP cell. Rate constants k_i come from Reference [63]. ρ_i represents the (per-atom) rate of spin polarization production or loss for the relevant species. d[X]/dt represents the same overall rate including number density, i.e. [X] = [Rb] or [Xe]. Each rate's contribution to the overall spin polarization production or loss is evaluated as a percent in the final column. The rates in each section sum to 100%.

		k_i $(\mathrm{m^3 s^{-1}})$	rate ρ_i $(\mathrm{s^{-1}})$	d[X]/dt $(\mathrm{m^{-3} s^{-1}})$	(Percentage)
Rb spin production rate					
Optical pumping:			1.16E+03	1.2E+23	
Rb spin polarization loss rate					
Binary collisions:					
Rb-Rb	k_{Rb}	4.00E-20	4.14E+00	4.29E+20	0.01%
Rb-Xe	k_{Xe}	6.48E-20	5.82E+04	6.02E+24	92.86%
Rb-N$_2$	$k_{\mathrm{N_2}}$	9.00E-24	2.42E+01	2.51E+21	0.04%
Rb-He	k_{He}	2.00E-24	1.72E+02	1.78E+22	0.28%
Radiation Trapping			957.7476	9.92E+22	1.53%
Spin Exchange collisions					
Binary spin exchange collisions	$k_{se,binary}$	3.00E-22	2.69E+02	2.79E+22	0.43%
He-mediated spin exchange collisions	$k_{se,\mathrm{He}}$	1.70E+04	1.77E+02	1.83E+22	0.28%
Xe-mediated spin exchange collisions	$k_{se,\mathrm{Xe}}$	5.23E+03	2.87E+03	2.97E+23	4.58%
Xe spin polarization production rate					
Binary collisions	$k_{se,binary}$	3.00E-22	3.11E-02	2.79E+22	8.13%
He-mediated collisions	$k_{se,\mathrm{He}}\,(\mathrm{s^{-1}})$	1.70E+04	2.04E-02	1.83E+22	5.35%
Xe-mediated collisions	$k_{se,\mathrm{Xe}}\,(\mathrm{s^{-1}})$	5.23E+03	3.31E-01	2.97E+23	86.52%
Xe spin polarization loss rate					
Self-relaxation/ "transient dimers"	$k_{\mathrm{Xe-Xe}}$	1.86E-31	1.67E-07	1.50E+17	0.02%
Persistent dimers/vanderWaals			5.86E-06	5.26E+18	0.60%
Wall relaxation			0.000417	3.74E+20	42.59%
Gradient relaxation			0.000556	4.99E+20	56.79%
Rb equilibrium polarization	P_{Rb}				1.82%
Xe equilbrium polarization	P_{Xe}				1.82%

where $\Phi_{opt}(\lambda)$ and $\sigma_{opt}(\lambda)$ are the photon flux and the absorption cross section of Rb at wavelength λ, respectively. Based on the roughly 12% absorption shown in Fig. 3.5, we calculate the total absorbed photon flux to be $5 \times 10^{18}\,\mathrm{photons\,s^{-1}}$. The per-atom rate ρ_{opt} is difficult to estimate as the cell is optically thick; the optical pumping rate is nonuniform throughout the cell and is likely highest near the entrance window. As a rough estimate we assume uniform absorption over the full 10 cm cell length and calculate $\rho_{opt} \approx 10^3\,\mathrm{s^{-1}}$.

Rb spin losses

Rubidium spin relaxation occurs through binary collisions with other species, through radiation trapping, and through successful spin-exchange reactions during the lifetime of short-lived van der Waals molecules. Quoted here are per-alkali atom loss rates, as opposed to integrated rates d[Rb]/dt.

The net polarization of Rb is determined by a balance of optical pumping ρ_{opt} and spin-destruction ρ_{sd} rates:

$$P_{Rb} = \left(\frac{\rho_{opt}}{\rho_{opt} + \rho_{sd}} \right) \times 100\% \tag{3.2}$$

where the spin destruction is given by:

$$\rho_{sd} = \sum_X \rho_X + \rho_{trap} + \sum \rho_{SE}. \tag{3.3}$$

The rates for each relaxation mechanism are listed in Table 3.4. Binary collisions are of the form $Rb_{pol} + X \longrightarrow Rb_{unpol} + X$. The relaxation rate for binary collisions with each species X is given by :

$$\frac{d[Rb]}{dt} = \rho_X [Rb] = k_X [X][Rb] \tag{3.4}$$

For [Xe] mixing ratios of a few percent, Rb-Xe binary collisions are a dominant source of loss, accounting for over 92% of Rb relaxation in the current model as shown in Table 3.4.

Radiation trapping describes the reabsorption by one Rb atom of previously emitted Rb fluorescence from a nearby atom. Due to collisional mixing of the upper state, the emission is assumed to have a random direction and orientation, and thereby depolarizes any atom that reabsorbs it. Therefore a buffer gas such as N_2 is usually added to collisionally de-excite atoms and prevent fluorescence. The rate of loss due to radiation trapping in the presence of a buffer gas is given by [36, 63]:

$$\rho_{trap} = \frac{3A}{3 + 7.5 P_{N_2}} \tag{3.5}$$

where $A = 40000 \, \text{s}^{-1}$ from literature [63] and P_{N_2} is the N_2 partial pressure given in kPa. As a result of including 3% N_2 in our gas mixture, relaxation due to radiation trapping is predicted to be small in comparison with other loss mechanisms.

Even successful spin-exchange naturally results in a loss of Rb spin polarization. In our current model this represents about 5% of all Rb loss, and is covered in the section below.

Xe spin polarization production

Xe spin exchange occurs via the Hamiltonian $\vec{I}_{Xe} \cdot \vec{S}$ both through binary collisions and through polarization transfer during the formation and breakup of short-lived van der Waals molecules. The cross section for spin exchange in spin-conserving binary collisions leads to a per-atom rate for

xenon polarization given by [59]:

$$\rho_{SE,binary} = k_{se,binary}[Rb] \tag{3.6}$$

The probability of a successful spin-exchange collision in a van der Waals molecule depends on the lifetime of the molecule. Collisions with a third body facilitate the formation and breakup of the vdW molecule and control the lifetime. Increasing the background pressure increases the rate of these collisions. The spin-exchange rate via vdW molecules is given by [63]:

$$\rho_{SE,Xe,He} = [Rb] \left(\frac{k_{se,He}}{[He]} + \frac{k_{se,Xe}}{[Xe]+0.275[N2]} \right) \tag{3.7}$$

It is apparent from the formula that molecule-mediated spin exchange plays an important role at lower SEOP pressures. In our current setup, the model indicates that spin-exchange in van der Waals molecules where Xe is the third body account for more than 80% of the total rate of spin-exchange.

Xe spin relaxation

Polarized Xe and polarized Rb in the same cell will eventually reach an equilibrium, with spin exchange reactions happening in both directions. The Rb number density is orders of magnitude smaller that the Xe number density, so loss of Xe polarization due to reverse spin exchange with Rb is negligible. Another loss of Xe polarization occurs through the formation of Xe-Xe dimers. These can be either "transient", equivalent to a binary collision, or "persistent," corresponding to the formation of a Xe_2 van der Waals molecule. Two other mechanisms for relaxation are wall collisions and depolarization near a magnetic gradient. The glass cells used can contain paramagnetic impurities near the surface which can depolarize the Xe. A common solution is to coat the walls with a wax or sillicon coating to increase the separation between impurities and polarized Xe; in our model we use the relaxation rate of our wall coating Surfasil for which the relaxation lifetime is $1/\rho_{wall} = 40\,\text{min}$ as reported by [145]. The lifetime is still limited by collisions with protons in the coating, which are still capable to a lesser extent of depolarizing the Xe. Finally, large magnetic gradients can depolarize Xe if the atoms have a large enough velocity. We calculated the magnetic field gradients using a model of the SEOP solenoid in COMSOL, shown in Fig. 3.9. From the model we estimated the depolarization rate ρ_{grad} based on the formula[145]:

$$\rho_{grad} = D \frac{|\nabla B_x|^2 + |\nabla B_y|^2}{B_0^2}, \tag{3.8}$$

where D is the diffusion coefficient in $\text{cm}^2\,\text{s}^{-1}$. Wall collisions and gradient relaxation yield comparable loss rates in the model, both approximately $5 \times 10^{-1}\,\text{s}^{-1}$.
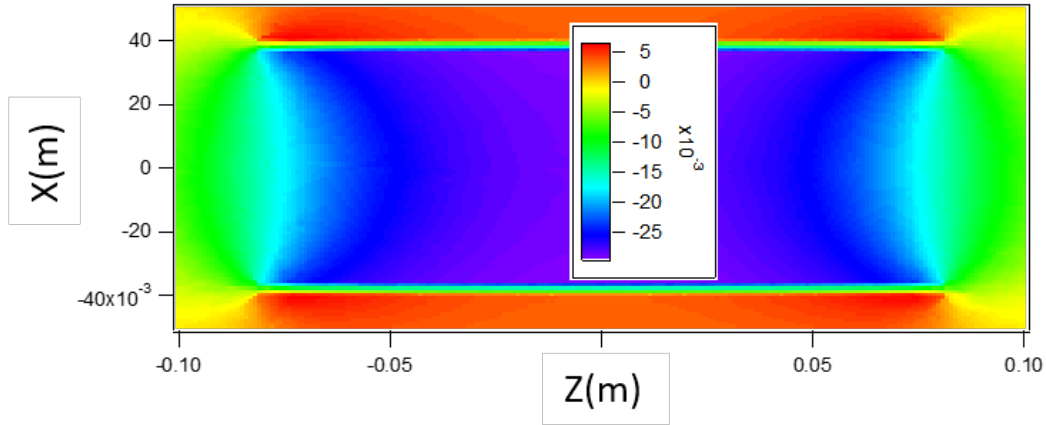
(a) Longitudinal magnetic field B_z.
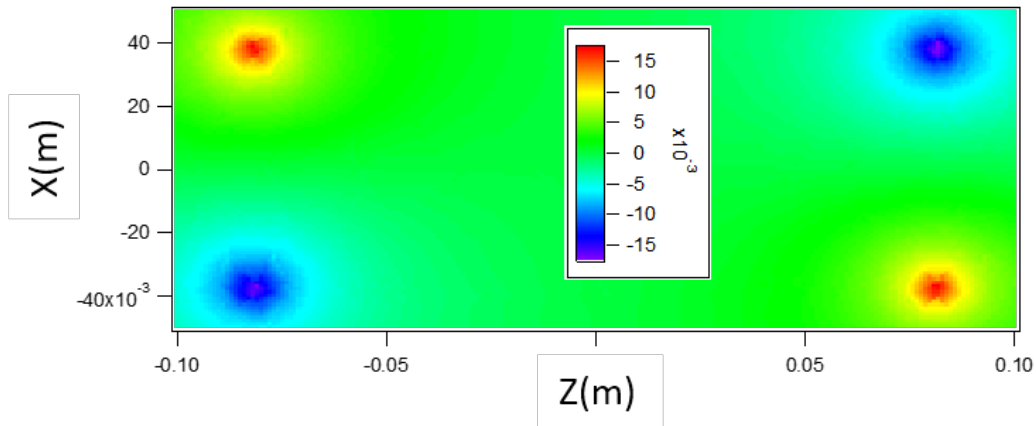
(b) Transverse magnetic field B_x.

Figure 3.9: Longitudinal (a) and transverse (b) field components of the SEOP solenoid magnetic field (in units of 10^{-3} T), modelled in COMSOL for the calculation of gradient relaxation ρ_{grad}.

Results of rate equation model

The steady-state Xe polarization P_{Xe} for which spin exchange rates ρ_{SE} and loss rates ρ_{loss} are equal is given by:

$$P_{Xe} = P_{Rb} \left(\frac{\rho_{SE}}{\rho_{SE} + \rho_{loss}} \right). \tag{3.9}$$

The model predicts $P_{Xe} = 1.8\%$ based on a Rb number density corresponding to a reservoir temperature of 423 K (150 C). We suspect the polarization is correct within an order of magnitude. The largest uncertainty in the prediction comes from the estimates of the Rb number density and the corresponding optical pumping rate, which as we previously indicated is not uniform through the SEOP cell. Fig. 3.10 shows the polarization dependence on Rb number density from the model.
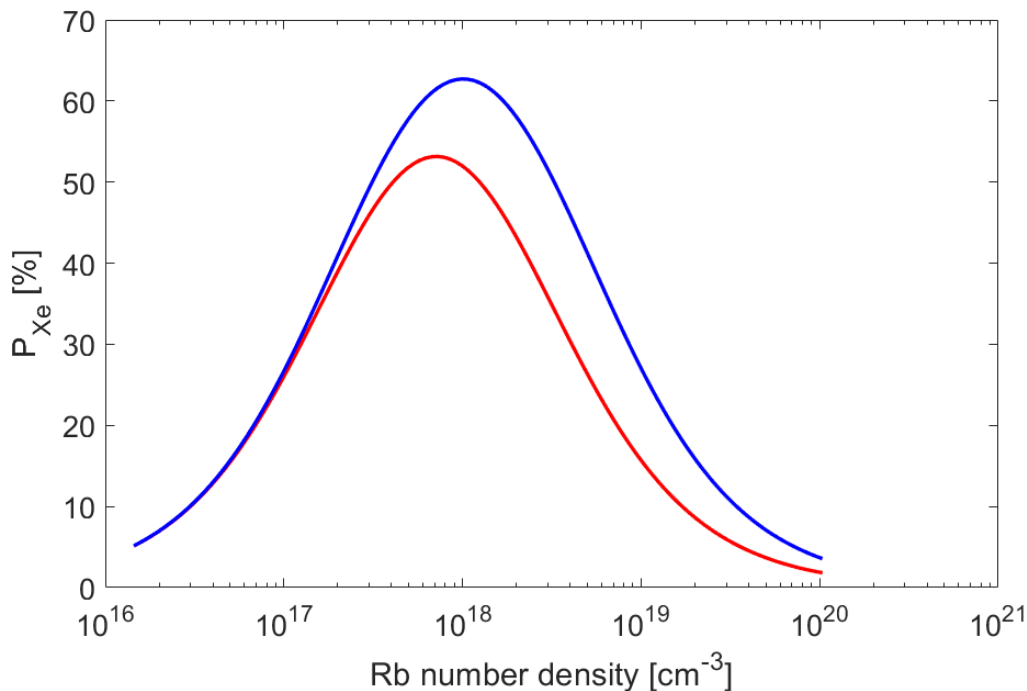
Figure 3.10: Simulation results for dependence of xenon polarization on Rb number density, using a resonant laser power of 1.2 W (red) and 2.4 W (blue). The range of number densities shown corresponds to Rb saturation vapour pressure for the temperature range 300-423 K.

One observes the predicted polarization to peak and then fall; this is due to an increase in SEOP efficiency at low Rb number density, and decrease in P_{Xe} related to the overall decrease in P_{Rb} at higher number density. Section 3.3.4 compares this rate equation model result with experimental observations from heating the SEOP cell.

3.3 Experimental Results

In this section we present results from both the SEOP polarizer and NMR detection. Many of the experiments studied the relationship between SEOP parameters (changing temperature, pressure, etc) and Xe polarization using AFP, and are presented here qualitatively, due to day-to-day variation in operational parameters. A quantitative estimate of the Xe polarization based on calibration of our Xe AFP signals against water AFP is also presented. Finally, first efforts are shown to purify polarized ^{129}Xe in a freezeout cell.

A typical H_2O AFP signal is shown in Fig. 3.11. Signals from H_2O display successive up and down peaks which indicate precession in phase and out of phase, respectively, with the lock-in reference signal. This is a result of near-complete longitudinal relaxation between scans, since
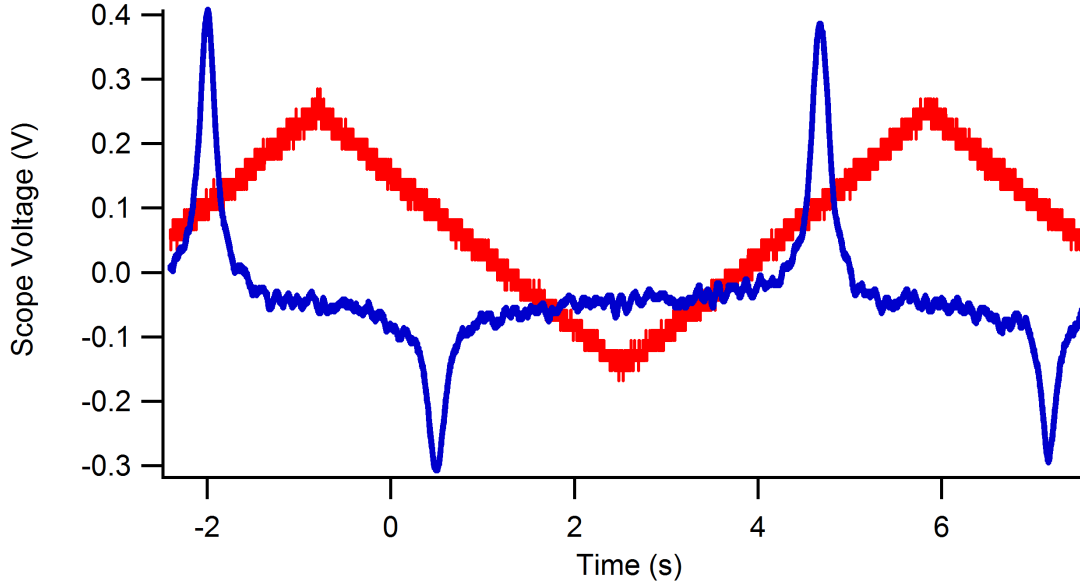
Figure 3.11: A typical water AFP signal during continuous ramping. The change in peak direction is due to rapid relaxation between ramps, which creates a signal out of phase with the Lock-in reference. (Conditions: B_0 coil current $= 4.63$ A, ramp $= 400$ mV, 200 mHz.)

the time between ramps is longer than the T_1 lifetime of a few hundred milliseconds; however, the asymmetry in amplitudes for up and down peaks may indicate that equilibrium has not been reached. An AFP signal for Xe is shown in Fig. 3.12. Xe has a gas phase T_1 lifetime on the order of minutes or even hours; therefore successive peaks may be seen in the same direction, depending on the ramp rate and flow rate. If the Xe peak changes sign between ramps under continuous flow conditions, it indicates that the sample volume is being replenished with fresh polarized Xe from the SEOP polarizer at a rate faster than the rate of spin flips.

3.3.1 Determining and Optimizing Adiabatic limits

Adiabatic Fast Passage requires a ramp rate well within the limits established by Formula 2.28. Approaching too close to either the upper or lower limit causes a decrease in signal due to either loss of adiabaticity or relaxation. Optimization of the adiabatic conditions is possible by changing either B_1 or dB_0/dt. Xe and H_2O possess different T_1 lifetimes and different gyromagnetic ratios, which means that the adiabatic limits will be different for both species. Most of the AFP signals were obtained by driving the B_1 coil at $1.0\,\mathrm{V_{RMS}}$, which yields $B_1 = 0.628\,\mu\mathrm{T}$. From Equation 2.28 we find for Xe (taking $T_1 = 878$ s as measured in Section 3.3.6):

$$0.00072\,\frac{\mu\mathrm{T}}{\mathrm{s}} \ll \left(\frac{dB_0}{dt}\right)_{\mathrm{Xe}} \ll 29.2\,\frac{\mu\mathrm{T}}{\mathrm{s}} \tag{3.10}$$
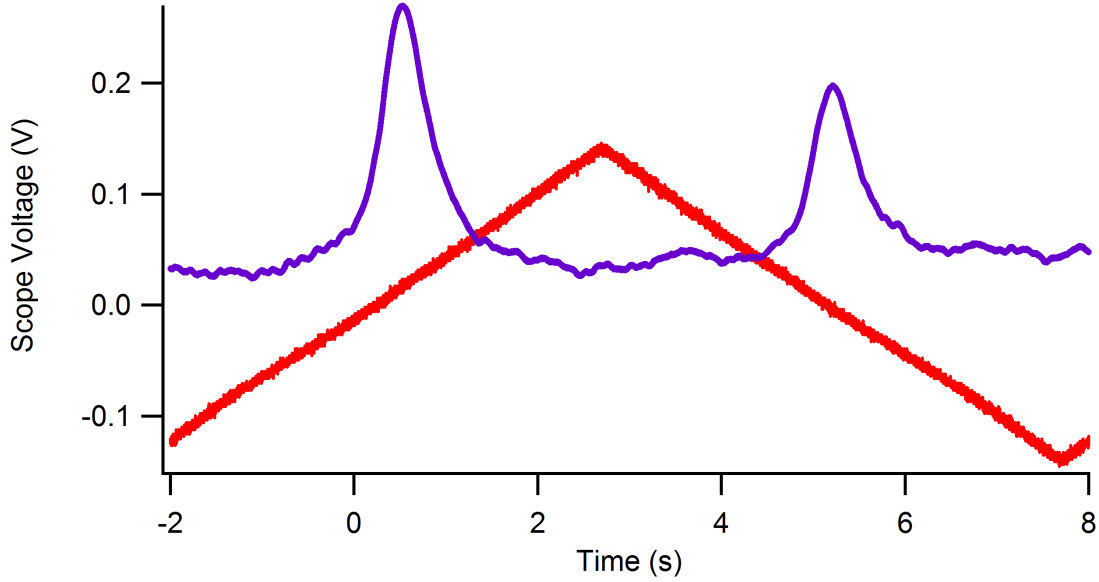
Figure 3.12: A typical xenon AFP signal during continuous ramping. (Conditions: B_0 coil current = 4.43 A, ramp = 250 mV, 100 mHz.)

For water with 2mM $CuSO_4$, the longitudinal relaxation lifetime is $T_1 = 0.274$s and we have:

$$2.3\,\frac{\mu\mathrm{T}}{\mathrm{s}} \ll \left(\frac{dB_0}{dt}\right)_{\mathrm{p}} \ll 105.5\,\frac{\mu\mathrm{T}}{\mathrm{s}} \tag{3.11}$$

In the experiments with $B_1 = 0.628\,\mu\mathrm{T}$, the optimal H_2O signal was found for a ramp rate approximately $dB_0/dt = 3\,\frac{\mu\mathrm{T}}{\mathrm{s}}$. However, it is clear from inspection of Equation 2.28 that increasing B_1 strength also increases the range between upper and lower limits. The upper limit is proportional to B_1^2 and grows faster than the lower limit which is proportional only to B_1. Increasing the range between limits could result in signal increase if we can ramp B_0 at a rate which better satisfies the adiabatic conditions.

We simulated evolution of the Bloch equations to test the AFP limits, using an ordinary differential equation (ODE) solver written in Python by Jeff Martin at U. Winnipeg. The code models the net magnetization M under the effects of parameters B_0, B_1, T_1 and T_2. We modified the script to accept arbitrary functions for the B_0 field as input. The new B_0 function ramps once through resonance, holds B_0 constant for time $T \gg T_1$ to allow time for relaxation, then ramps through resonance a second time. We vary dB_0/dt and B_1 using this code to determine conditions for AFP that yield the highest signal.

The simulation shows that at higher B_1, increasing the ramp rate yields a larger AFP signal. An example of this is given in Fig. 3.13, for water AFP at 56 kHz resonance driven by either low or high B_1 fields. (It should be noted that higher B_1 also slightly increases the off-resonant horizontal
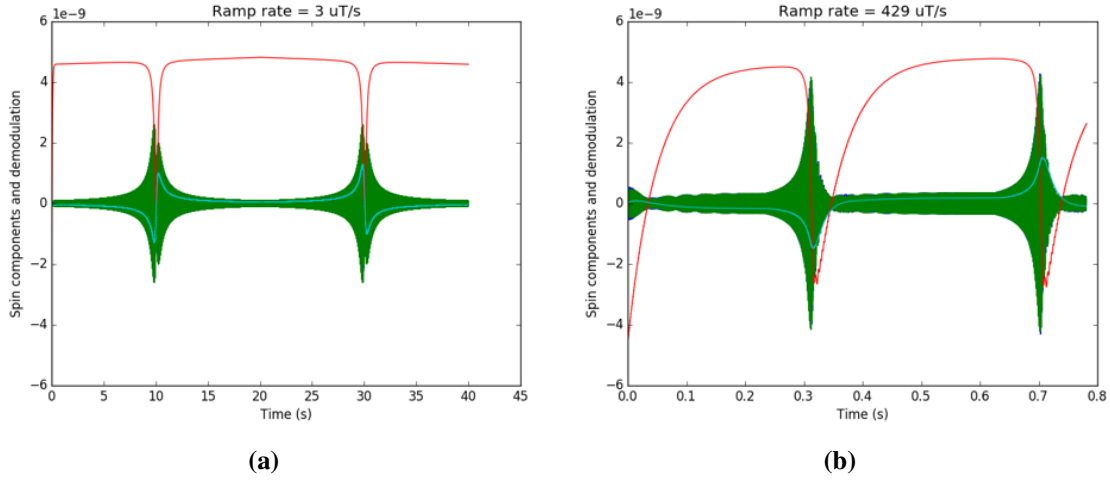
Figure 3.13: Bloch equation simulation shows H_2O AFP signal increase for simultaneous increase of B_1 and $\frac{dB_0}{dt}$. (a) low field conditions with $B_1 = 0.628\,\mu T$ and $\frac{dB_0}{dt} = 3\,\frac{\mu T}{s}$. (b) high field conditions with $B_1 = 2.52\,\mu T$ and $\frac{dB_0}{dt} = 429\,\frac{\mu T}{s}$. Red: longitudinal magnetization M_z. Green: transverse magnetization M_x.

components.) The simulation indicates that increasing B_1 to $2.52\mu T$ and ramp rate to $429\mu T/s$ would increase the AFP signal by approximately 2x.

We found experimentally that we could increase B_1 up to $3.14\,\mu T$, corresponding to the maximum $5.0\,V_{RMS}$ output of the lock-in amplifier reference, and still adequately cancel cross-talk. This made it possible to increase the ramp rate dB_0/dt while still satisfying the adiabatic limits. At high field ($B_1 = 3.14\,\mu T$), the adiabatic limits for Xe are given by:

$$0.0036\,\frac{\mu T}{s} \ll \frac{dB_0}{dt} \ll 729\,\frac{\mu T}{s} \tag{3.12}$$

and the corresponding limits for H_2O are:

$$11.5\,\frac{\mu T}{s} \ll \frac{dB_0}{dt} \ll 419\,\frac{\mu T}{s}. \tag{3.13}$$

We found a 2x increase in water AFP signal at high B_1 field by increasing the ramp rate from $3\mu T/s$ to $40\mu T/s$, and a corresponding 3x increase in ^{129}Xe signal obtained under continuous Xe flow conditions. Inspection of Equations 3.12 and 3.13 suggest that we are well within the adiabatic limits; however, it may still be possible to increase B_1 and optimize the AFP signals further. Non-adiabatic conditions for either Xe or H_2O cause a decrease in the AFP signal (from the theoretical maximum) that can result in either an underestimation or overestimation, respectively, of the ^{129}Xe polarization.

60

3.3.2 Estimation of the degree of ^{129}Xe polarization

There are two techniques to measure polarization, which we label relative and absolute. An absolute measurement determines the polarization of one species directly from the NMR signal it produces. Absolute measurements require calibration of the gain parameters in the electronics. Relative measurements determine the polarization from a ratio of signal strengths for different species. We use water NMR to make relative measurements because its thermal Boltzmann polarization is known. Results for calculating xenon polarization by relative and absolute methods are given in Table 3.5 and described below.

Absolute Polarization Measurements

We can estimate the expected NMR signal directly by considering the Faraday induction caused by a precessing magnetization in the pickup coil. An order-of-magnitude estimate for the induced EMF is

$$\varepsilon = -\frac{d\Phi}{dt} = N_c A \omega \mu_0 M = N_c A \omega \mu_0 \frac{N}{V} \mu_i P_i \tag{3.14}$$

where N_c and A are the number of turns and area of the pickup coil, ω is the angular precession frequency, μ_0 is the permeability of free space, and $M = \frac{N}{V}\mu_i P_i$ is the sample magnetization per unit volume. μ_i and P_i are the magnetic dipole moment and polarization, respectively, of the precessing nuclei i. We employ the resonant RLC circuit described in Section 3.1.2 to increase the detected signal by a factor $Q = \frac{\omega}{\Delta\omega}$, where ω and $\Delta\omega$ are the center frequency and full width at half power, respectively, of the RLC circuit transfer function. In Appendix A.2 we calculate the value $Q = 26.0$ for the 15.555 kHz circuit used for Xe. The resonance-enhanced signal is then further amplified by a preamp with gain $G_{preamp} = 100$ before detection at the lock-in amplifier. The signal expected at the lock-in amplifier input is therefore:

$$S_p = G_{preamp} Q \varepsilon \tag{3.15}$$

Applying the derivation to xenon and solving for P_{Xe}, we arrive at:

$$P_{Xe} = S_{Xe} \left[G_{preamp} Q_{Xe} N_c A \omega_{Xe} \mu_0 \frac{N_{Xe}}{V} \mu_{Xe} \right]^{-1} \tag{3.16}$$

The largest AFP signal measured to date is $S_{Xe} = 520\,\mu V$ for 15.555 kHz resonance when polarizing in batch mode (see Section 3.3.5). Based on this result and the parameters in Table 3.5, we estimate $P_{Xe} = 0.5\%$, which will be discussed further in the section below.

Relative Polarization Measurements

Our relative measurements compare the ^{129}Xe signal strength to that of thermally polarized protons in a H_2O sample. The protons occupy both spin states almost equally at room temperature, with exact populations determined by a Boltzmann distribution. The thermal polarization P_p of protons in the B_0 field is given by Equation 2.21. We calculate $P_p = 1.24 \times 10^{-9}$ at $\omega/2\pi =$15.555 kHz resonance and $P_p = 4.70 \times 10^{-9}$ at $\omega/2\pi =$58.82 kHz resonance.

Spin exchange creates hyperpolarized populations of Xe atoms, with polarization orders of magnitude larger than the thermal polarization. Hence Equation 2.21 applies in this case only to water. We measure the relative NMR signal strengths of the two species, taking into account different number densities and magnetic moments, and calculate the Xe polarization from the ratio $\frac{S_{Xe}}{S_p}$ using Equation 3.16 [55, 164]:

$$P_{Xe} = P_p \frac{S_{Xe}}{S_p} \left| \frac{\mu_p}{\mu_{Xe}} \right| \frac{N_p}{N_{Xe}} \frac{Q_p}{Q_{Xe}} \frac{\omega_p}{\omega_{Xe}} \tag{3.17}$$

Here S_{Xe} is the signal strength, μ_{Xe} the magnetic moment and N_{Xe} the number of precessing nuclei. A gain factor defined by $\frac{G_p}{G_{Xe}} = \frac{Q_p}{Q_{Xe}} \frac{\omega_p}{\omega_{Xe}}$ represents the potentially different experimental gain for the two samples. We can perform measurements at fixed frequency or fixed fields (different frequency). When comparing NMR signal obtained at different frequencies, we need to account for both (i) the gain due to the different Q factors of the resonant pickup RLC circuits, and (ii) the larger induced EMF at faster frequency ω_p due to the changing flux $\frac{d\phi}{dt}$. When comparing signals from Xe and H_2O at fixed frequency, we use the same RLC circuit for both samples and therefore the gain is by definition unity, i.e. $\frac{G_p}{G_{Xe}} = 1$. Under fixed frequency conditions at 15.555 kHz, the best values measured to date are $S_{Xe} = 520\mu$V and $S_p = 40\mu$V. The number of proton spins and ^{129}Xe spins are 9.81×10^{24} and 1.04×10^{19}, respectively. From these values we calculate $P_{Xe} = 5.4\%$. (It must be noted that a higher polarization was estimated under fixed field conditions at 58.82 kHz, but this is attributed to underestimation of S_p caused by an accidental detuning of the lock in amplifier away from the RLC resonance.)

Estimates of P_{Xe} by the absolute method are an order of magnitude lower than predictions from relative measurements. One source of discrepancy is overestimation of the coil flux and therefore the induced EMF, due to the angle between sample and pickup coil; another source is uncertainty in the measurement of the Q-factor. Both of these strongly affect the absolute measurement but not the relative measurements. Finally, it should be emphasized that our best measurement of $S_{Xe} = 520\mu$V was obtained under low B_1 field conditions, before the AFP optimization of Section 3.3.1, and was not repeated after optimization due to deterioration of the SEOP cell. We expect that estimates of P_{Xe} based on the unoptimized conditions therefore underestimate the true polarization by roughly a factor of three.

Table 3.5: Parameters used for the estimation of xenon polarization based on observed NMR signal. All ^{129}Xe signals were obtained at $\omega_{Xe}/2\pi = 15.555$ kHz resonance frequency. Relative measurements were made against H_2O signals obtained at either 15.555 kHz or 58.82 kHz, and denoted as "fixed frequency" or "fixed field", respectively.

		Fixed frequency	Fixed field
$\omega_P/2\pi$	(kHz)	15.555	58.82
$\omega_{Xe}/2\pi$	(kHz)	15.555	15.56
T	(K)	300	300
P_p	-	1.24×10^{-9}	4.70×10^{-9}
S_{Xe}	(μV)	520	520
S_p	(μV)	40	600
G_{preamp}	-	100	100
N_{coil}	-	200	200
A	(m^2)	5.80×10^{-3}	5.80×10^{-3}
$N_{^{129}Xe}$	-	1.05×10^{19}	1.05×10^{19}
N_p	-	9.81×10^{24}	9.81×10^{24}
Volume V	(cm^3)	147	147
μ_p	(J/T)	1.41×10^{-26}	1.41×10^{-26}
$\mu_{^{129}Xe}$	(J/T)	3.93×10^{-27}	3.93×10^{-27}
$\mu_p/\mu_{^{129}Xe}$	-	3.59	3.59
$Q_{^{129}Xe}$	-	26	26
Q_p	-	26	38.9
$G_p/G_{^{129}Xe}$	-	1	5.66
P_{Xe} (Relative)	(%)	5.4	7.8
P_{Xe} (Absolute)	(%)	0.5	0.5

3.3.3 Improvement of Rb absorption by pressure broadening

The NIR laser used for pumping is broadband, with a linewidth of roughly 2 nm. This is much wider than the Rb transition Doppler-broadened linewidth; therefore much of the light is nonresonant and does not contribute to optical pumping. Pressure broadening the resonance with He allows us to deliver more power to the Rb and increase the optical pumping rate ρ_{opt}. Our SEOP gas mixture contains 96% Helium by volume, the primary purpose of which is to pressure broaden the Rb D_1 absorption line. We measured pressure broadening by operating the SEOP cell at a range of pressures between 20 and 60 psi(g), controlled by a regulator on the gas cylinder. We recorded the transmission spectrum of circular polarized light through the Rb cell using the optical spectrum analyzer with the solenoid field switched "ON" and "OFF" and while flowing gas through the polarizer at flow rates 0.1 slm[1] and below, and measured the width of the absorption feature in the spectrum analyzer signal (see Fig. 3.5), calculated from a fit to the lineshape of the transmission ratio I/I_0. Fig. 3.14 shows the increase in absorption linewidth as we increase the pressure; the

---

[1]standard litre per minute
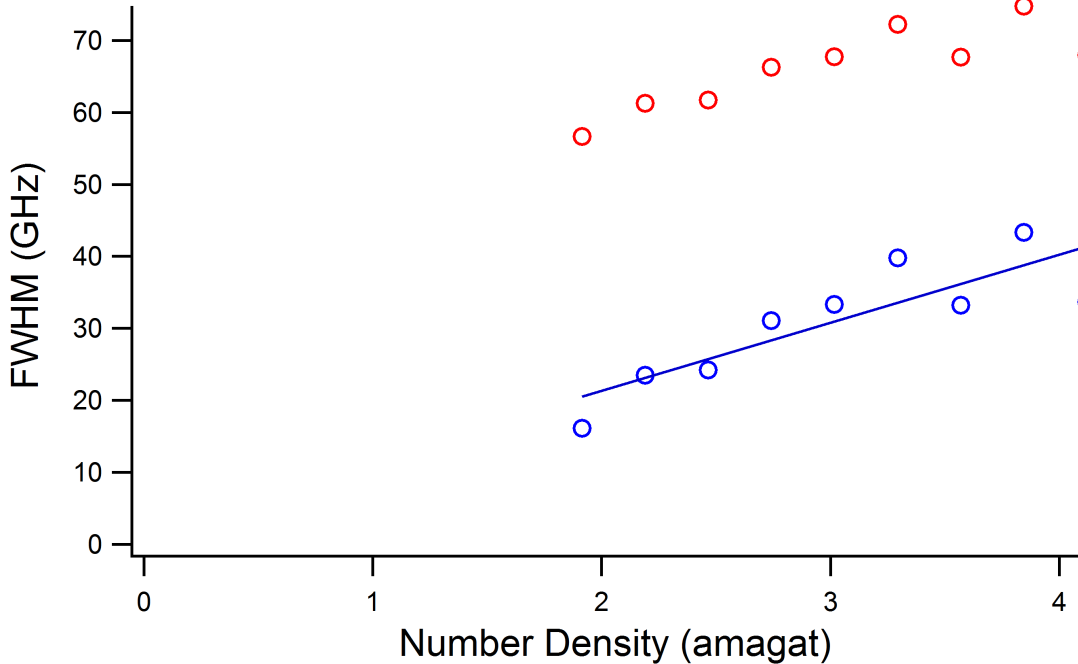
Figure 3.14: The absorption linewidth of Rb increases as the Rb vapour is pressure broadened by collisions with He gas. Red: measured signal linewidth (convolved with 0.1 nm resolution bandwidth of spectrum analyzer). Blue: linewidth after deconvolution.

expected qualitative behaviour (linear increase with pressure) is observed. However, the observed linewidth is dominated by the instrument resolution bandwidth of 0.1 nm (50 GHz). We approximate the observed linewidth (red) to be the Voigt profile convolution of the true pressure broadened Lorentzian (blue) with a Gaussian resolution bandwidth, and extract the Lorentzian linewidth via the approximation [120] $\Gamma_V \approx 0.5346\Gamma_L + \sqrt{0.2166\Gamma_L^2 + \Gamma_G^2}$. We find 9 ± 2 GHz amagat^{-1} from our data[2], which is not in agreement with the $\Delta \nu = 18.0 \pm 0.2$ GHz amagat^{-1} linewidth measured by Romalis [141]. Quantitative agreement requires analysis of the spectrum with higher resolution hardware.

3.3.4 SEOP cell temperature dependence

Rb melts at 312 K and boils at 961 K. Heating the body of the SEOP cell increases the Rb number density (and absorbance) as shown in Fig. 3.15 by causing Rb to desorb from the cell walls. It also therefore increases the rate of spin-exchange collisions with Xe. We measured the effect of temperature by heating the SEOP cell with heater tape wrapped at the entrance and exit windows while flowing gas at a fixed rate. We limited the heating range to below 150 °C to avoid damage to the SurfaSil coating. By careful adjustment we maintained a temperature uniformity of 2 K during

---

[2]1 amagat = 2.69×10^{25} m^{-3}
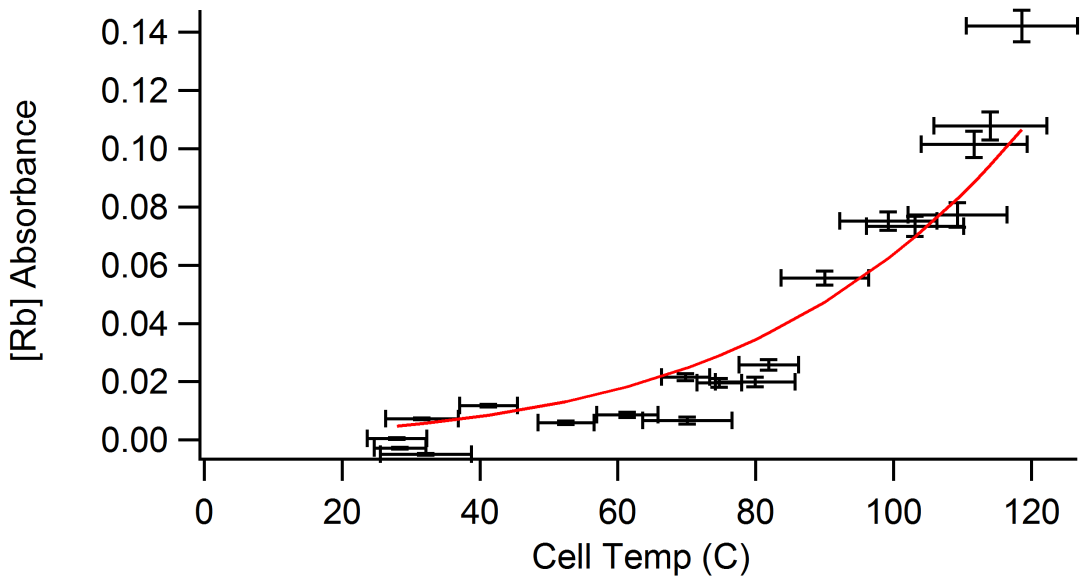
Figure 3.15: Rb absorbance as a function of cell temperature compared with theoretical number density temperature dependence based on vapor pressure.
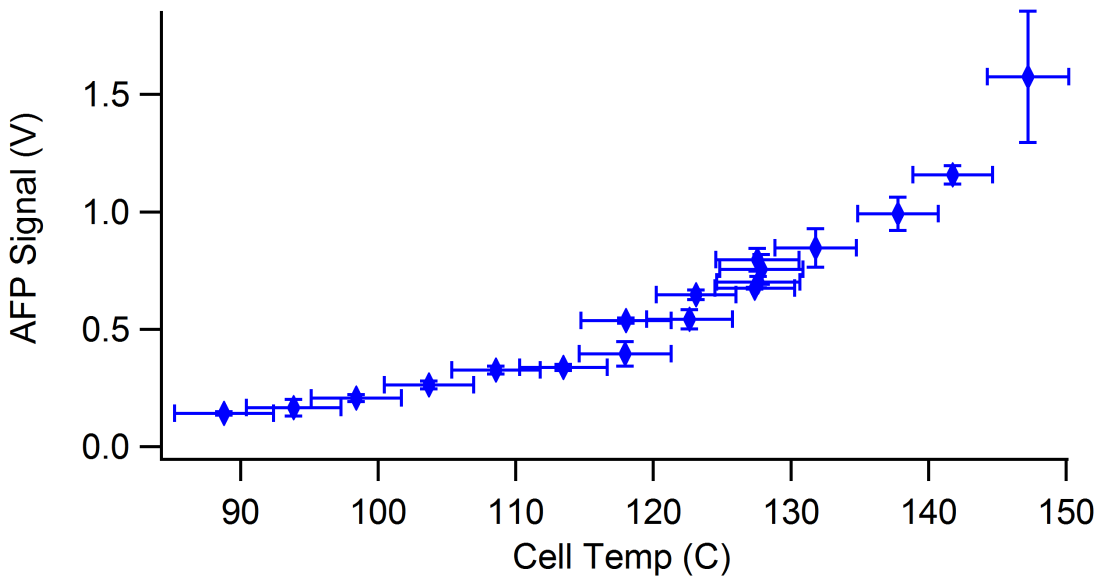
Figure 3.16: AFP signal dependence on SEOP cell average temperature during continuous flow at 0.3 slm.

continuous flow as measured by three K-type thermocouples mounted along the cell body. Fig. 3.16 shows the AFP signal plotted against average cell body temperature. The cell body temperature is, however, a poor proxy for the internal temperature; the temperature of the SEOP gas mixture could be even higher. Using the empirical formula for vapor pressure [36]

$$\log\left(\frac{p_{\mathrm{Rb}}}{\mathrm{Pa}}\right) = 9.550 - \frac{4132}{T/\mathrm{K}}, \tag{3.18}$$

predicts $[\mathrm{Rb}] = 4 \times 10^{18}\,\mathrm{m}^{-3}$ based on cell body temperature and $[\mathrm{Rb}] = 1 \times 10^{20}\,\mathrm{m}^{-3}$ based on reservoir temperature. However, from comparison with the model results in Fig. 3.10, we note that the experimentally observed increase in AFP signal with increasing cell temperature suggests lower than expected Rb number density. The first reason for this discrepancy is that the optical pumping rate is nonuniform across the pumping cell and becomes increasingly nonuniform as the Rb vapour becomes more optically thick with heating. This nonuniformity is not well accounted for in the model. One factor which supports lower than expected Rb number density is that during continuous flow the cell will not reach equilibrium with the Rb saturation vapour pressure; the number density could also be lower than expected due to reactions between Rb and contaminants on the cell walls, or due to Rb condensation on localized cold spots between the Rb reservoir and cell body.

3.3.5 Continuous vs. stopped flow effects on ^{129}Xe polarization

The polarizer can either be operated with a continuous stream of SEOP gas or with a stopped flow by adjusting the downstream needle valve. Both are described below:

Flow rate

Adjusting the flow rate has two effects. First, it directly controls the time Xe experience spin-exchange collisions with optically pumped Rb. Second, it controls the transport time between SEOP polarizer and NMR cell (which are nominally separated by 4 m of tubing), during which T_1 relaxation can occur. One expects an optimized flow rate that gives Xe a long interaction time followed by quick delivery to the NMR. We adjust the needle valve downstream of the SEOP cell, and measure the flow rate upstream in the pressurized gas line before the polarizer (the flowmeter is located upstream to prevent it from depolarizing the Xe), keeping cell temperatures constant. Flow rates in the low pressure downstream lines were confirmed with an additional flow meter prior to starting the experiment. Results are shown in Fig. 3.17 with flow rate measured in standard litres per minute (slm). The best continuous-flow signal is observed at 0.1 slm flow rate. This corresponds to a Xe interaction time $t \approx 30\,\mathrm{s}$ in the SEOP cell.
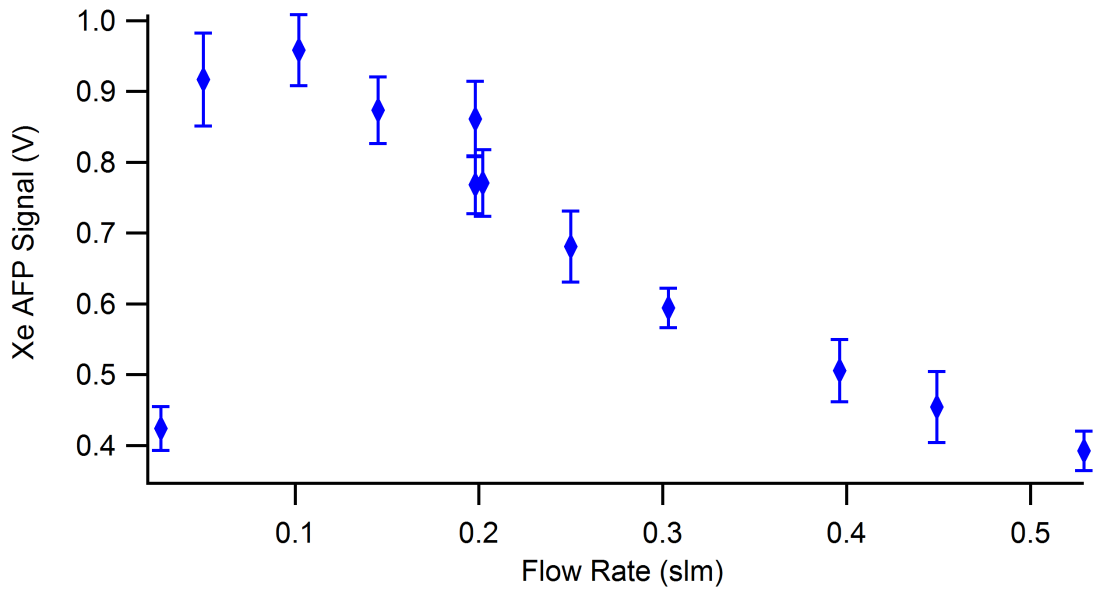
Figure 3.17: AFP signal dependence on flow rate under continuous flow-conditions.
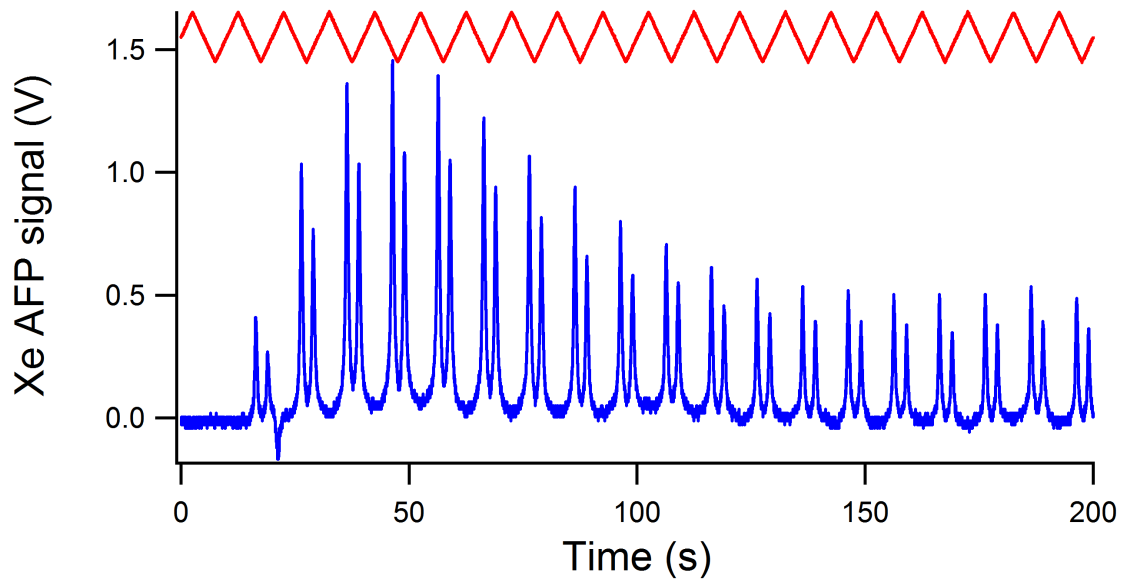
Figure 3.18: Blue: AFP signal from batch mode operation with 8 min. buildup time, followed by transfer to NMR at 0.200 slm. The peak at $t = 50\,\text{s}$ represents the batch polarization, while signal at $t > 150\,\text{s}$ is the continuous-flow (steady-state) polarization at 0.200 slm. Red: AFP ramp dB_0/dt.
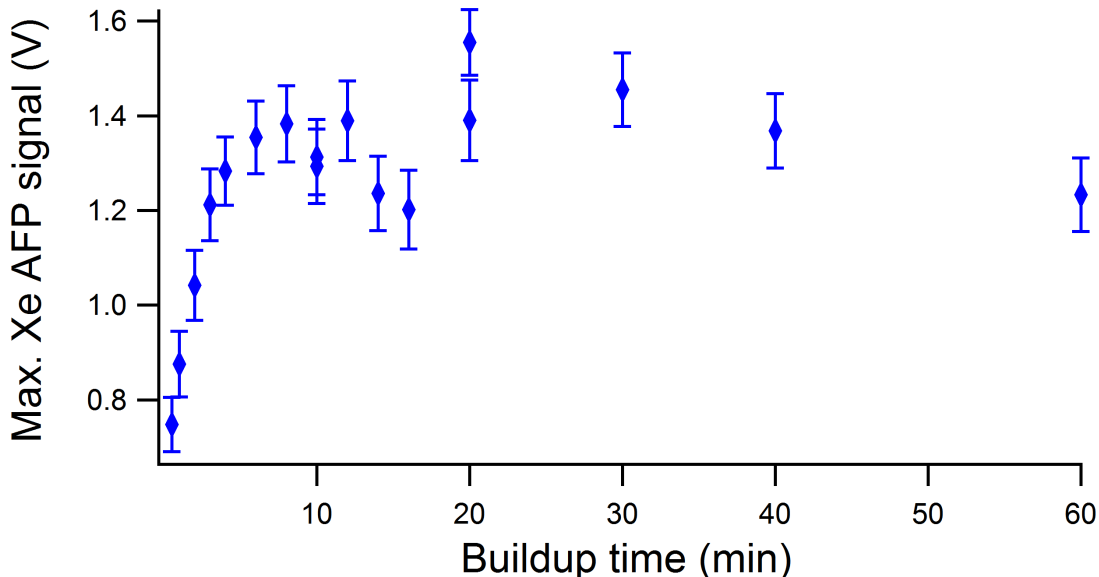
Figure 3.19: Batch mode conditions for buildup times up to 60 min, followed by transfer to NMR at 0.200 slm.

Stopped-flow "batch" mode

Under continuous flow conditions often the Rb polarization does not reach equilibrium along the entire length of the cell. Fig. 3.19 shows the AFP signal amplitude from operation under stopped-flow "batch-mode" conditions. The needle valve is closed for a buildup time up to 60 min to allow the polarization to reach an equilibrium value, after which the valve is opened and the sample is transferred through tubing to the NMR region. Equilibrium polarization is observed after 8-10 min in the SEOP cell. The stopped-flow polarization can be much larger than that under continuous flow conditions. This can be seen from Fig. 3.18, where the maximum signal from stopped-flow polarization at $t = 50\,\mathrm{s}$ is nearly three times larger than the continuous-flow signal observed for $t > 150\,\mathrm{s}$. Stopped-flow polarization has an added technical advantage: after polarization is complete, the polarized samples can be rapidly transferred to the NMR cell at arbitrarily fast flow rates. This will help minimize relaxation during transfer; in contrast to continuous flow conditions in which the flow rate through the SEOP cell also determines the flow rate to the NMR experiment.

The largest Xe AFP signal measured to date was obtained by stopped-flow polarization, with a signal magnitude $S_{\mathrm{Xe}} = 520\mu\mathrm{V}$ at the lock-in amplifier input. This signal however represents an underestimate of the true Xe polarization for two reasons. First, the signal was obtained before the optimization of AFP abiabatic conditions discussed in Section 3.3.1. Second, the B_0 ramp was on during the transfer of polarized Xe into the NMR cell, which causes some mixing of gas in opposite spin states. (We were able to minimize the mixing by adjusting B_0 such that resonance occurs near the bottom of the ramp, and thereby minimize the time Xe spends in the spin down
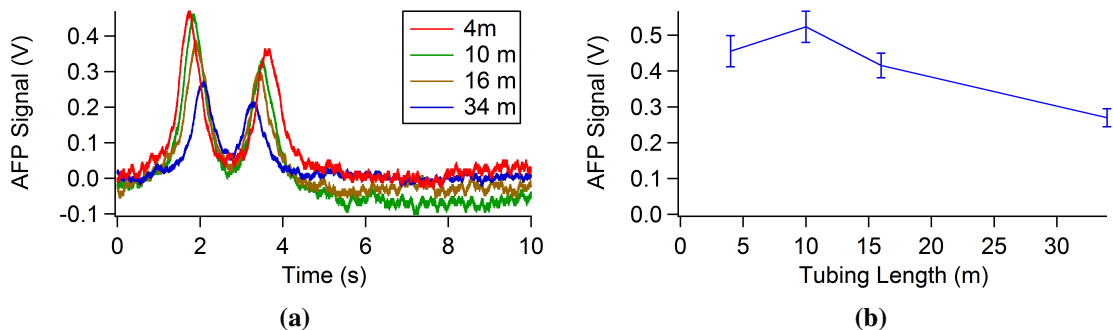
Figure 3.20: The Xe AFP signal decreases as polarized Xe travels through longer lengths of tubing. Signal peaks from consecutive runs in (a) appear closer together due to a slow B_0 drift. Error bars in (b) are from detection noise only and do not account for the slowly-changing experimental conditions.

state). Larger Xe AFP signals are expected following optimization of the adiabatic conditions and following improvements to the polarization transfer method (i.e., without any B_0 ramp).

Tubing Length Dependence

Ideally we should locate the SEOP polarizer as close as possible to the detection chamber; however, to meet the requirements of nEDM measurements at TRIUMF it may be necessary to locate the polarizer several metres from the EDM cell. We measured AFP signals while changing the path length from SEOP cell to NMR bottle, in order to observe how quickly the Xe becomes depolarized. This was achieved by flowing at 0.200 slm through lengths of nylon tubing (between 4 m and 34 m) coiled up between the SEOP polarizer and NMR. The coiled tubing was supported at least 10 cm above the optics table to prevent relaxation, because we previously observed complete loss of polarization when the tubing was allowed to contact the magnetized table. Fig. 3.20 shows the signal dependence on path length. The extra path length increases the transit time (up to 115 s), allowing more T_1 relaxation and wall collisions. Therefore the decrease in AFP signal with path length is expected. An exponential fit of signal against transit time yields a rough estimate of $\tau = 190 \pm 40\,\mathrm{s}$ for decay time during transport.

3.3.6 Measurements of polarization relaxation time

Hyperpolarized Xe has a surprisingly long relaxation lifetime in the gas phase. Efforts to measure this relaxation are described below.
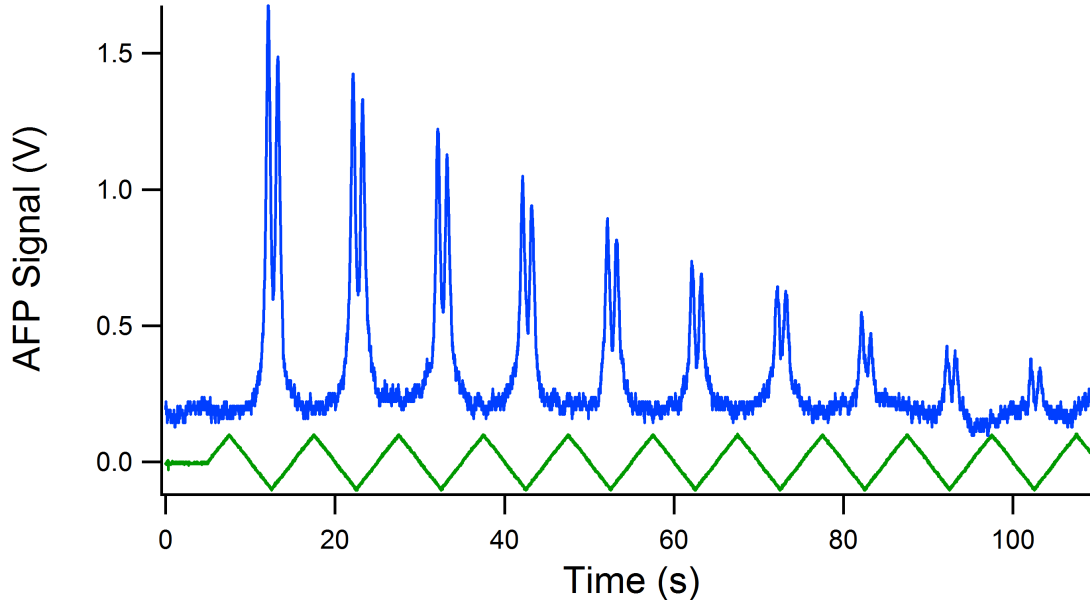
Figure 3.21: Xe relaxation under repeated AFP. The decay of signal here is dominated by T_2 effects and the incomplete inversion that occurs near the bottom of the B_0 ramp.

Relaxation during repeated AFP

The first measurements of Xe spin relaxation in the lab come from a Xe sample subjected to the continuous AFP ramping sequence shown in Fig. 3.21. The cell is first filled with polarized Xe under a fixed B_0 field, flowing gas at a fixed flow rate for long enough ($> 30\,$s) to completely replenish the NMR sample volume. The sample volume was sealed off immediately prior to turning on the B_0 ramp. The observed signal rapidly decays while repeatedly undergoing AFP. We expect that under repeated AFP ramping, both T_1 and T_2 decay contribute to the observed relaxation. Additionally, Fig. 3.21 reveals that there is incomplete polarization inversion from the negative-going ramp before the positive-going ramp begins, such that two overlapping peaks occur near the bottom of each B_0 ramp. We observe rapid signal relaxation between the overlapping peaks, for which the decay time constant (averaged over the first five pairs) is $\tau = 12(3)\,$s. The relaxation is slower from one pair of overlapping peaks to the next, and we determine $\tau = 67(4)\,$s, based on fitting only the first peak of each overlapping pair. This lifetime is short compared to that obtained by more direct measurements of T_1 (presented in the following section), which indicates that T_2 relaxation and incomplete polarization inversion dominate under the continuous AFP ramping conditions presented here.
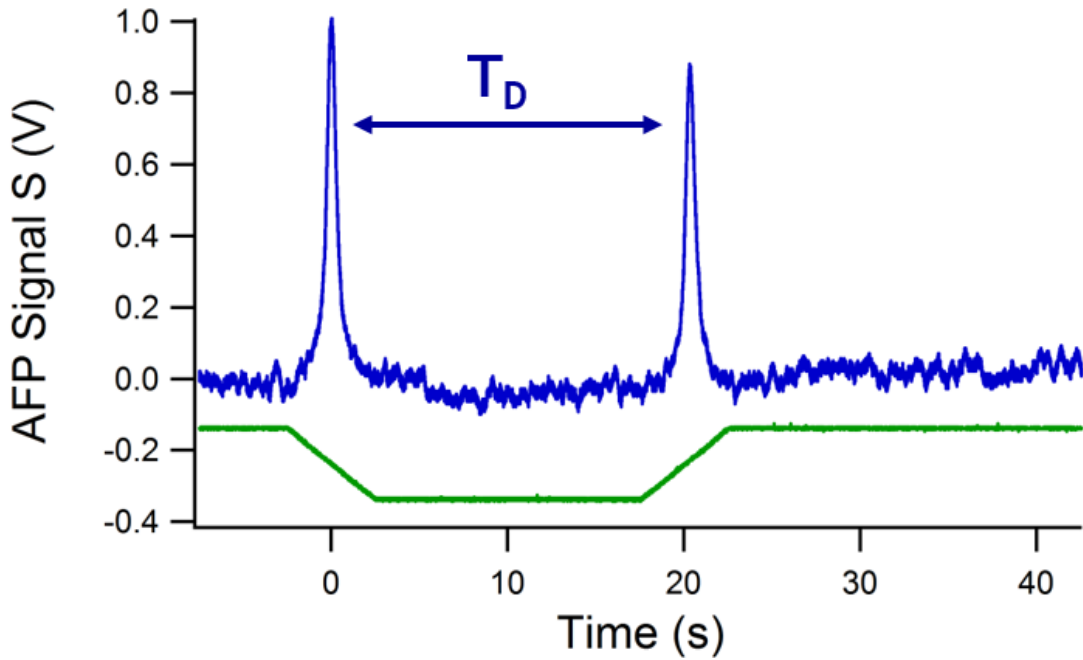
Figure 3.22: The ramp technique for a T_1 measurement. We implement a variable time delay T_D between successive up/down ramps and measure the decrease in AFP signal due to T_1 relaxation.
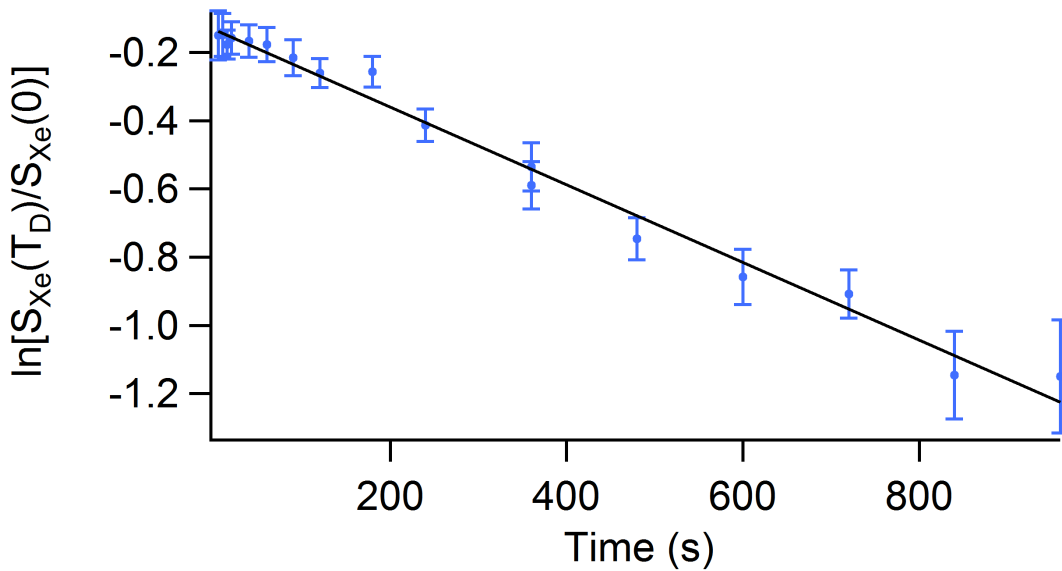
Figure 3.23: Exponential decay of AFP signal using the ramp technique above. The T_1 lifetime is inferred from the empirical fit $\tau = 878 \pm 26$ s.
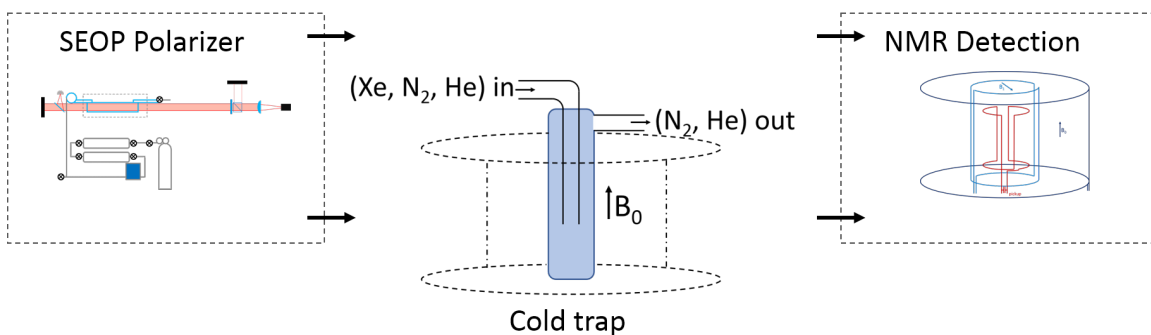
Figure 3.24: Schematic of Xe cold trap located between polarizer and NMR detector, with $B_0 = 8\,\text{mT}$ provided by a solenoid.

T_1 Lifetime Measurement

T_1 is longitudinal relaxation towards the thermal equilibrium polarization given by the Boltzmann distribution, and occurs even when there is no transverse polarization component. We measure T_1 by inducing two consecutive AFP ramps separated by a time delay T_D, as shown in Fig. 3.22. The cell is first filled with polarized Xe under a fixed B_0 field, flowing gas at a fixed flow rate for long enough (> 30s) to completely replenish the NMR sample volume. After shutting off flow, the B_0 ramp sequence shown in green is applied. The sample polarization decays through wall collisions, gradient-induced relaxation, and dipole-induced relaxations, resulting in the smaller signal which appears after delay time T_D. We plot the logarithmic ratio of the peak height $\ln(S_{\text{Xe}}(T_D)/S_{\text{Xe}}(0))$ while varying delay time T_D to measure the decay rate. We measured for up to 1000s, shown in Fig. 3.23, and found $\tau = 878 \pm 26$ s from the fit. Because additional (e.g. T_2) relaxation can occur during the resonance part of the AFP ramp, this measurement τ represents only a lower bound for T_1.

3.3.7 Xe purification by freezeout and initial attempt at polarization recovery

To perform high-resolution spectroscopy free of Doppler broadening, and ultimately to use Xe as a comagnetometer, the Xe must be separated out from the Rb, He, and N_2. Separation of Rb occurs naturally through condensation of Rb on the walls downstream of the SEOP cell. We separate Xe from the N_2 and He by using a cold trap immersed in liquid N_2. Xenon possesses a higher freezing point (161.4 K) than either N_2 or He, so can be effectively purified using a standard freeze/pump/thaw technique.

Apparatus for proof-of-principle tests of freezeout are shown in Fig. 3.24. We flow mixed gas through a 1-inch diameter cold trap while pumping on the trap and gas line with a scroll pump, and monitor the pressure with a Baratron gauge. The trap and gas lines have a combined volume of 104 mL. After 45s of flow at 0.14 slm flow rate, the total volume of gas through the trap equals 105
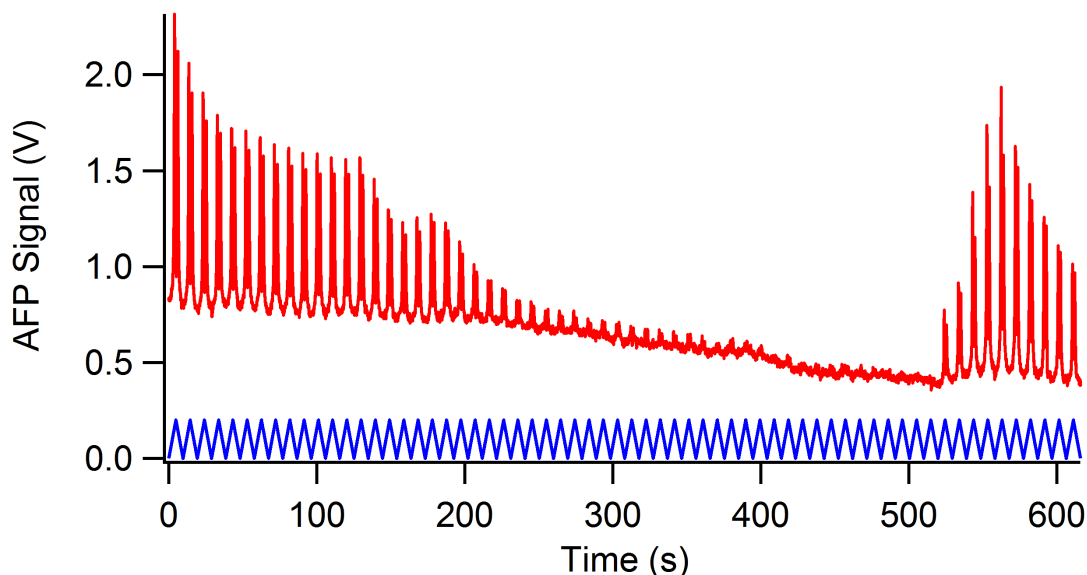
Figure 3.25: The downstream AFP signal disappears while performing freezeout during $t = 200 - 500$ s, with all the Xe condensing in the cold trap; signal recovery occurs post-thaw at $t = 500$ s, but without the anticipated signal increase (see text).

mL, of which 1% by volume is Xe. The flow of gas is stopped and the trap is isolated by shutoff valve. The trap contains visible solid Xe which forms a frost on the walls. Thawing the trap yields a pressure increase of 6.7 torr, which indicates that 87% of the Xe was captured by the freezeout.

It has been shown [42, 64, 68] that the Xe polarization can be preserved in the solid state under a strong magnetic field, with a T_1 lifetime of many hours. Fig. 3.25 shows an attempt to purify polarized Xe in a cold trap. The trap is cooled with LN_2 while flowing polarized Xe from the SEOP polarizer in continuous flow mode. Another solenoid applies an 8 mT field surrounding the trap, which corresponds to a relaxation rate $1/T_1 = 10^{-2} \sim 10^{-3}$ s^{-1} in solid state Xe at 77 K according to Ref. [64]. The loss of AFP signal between $t = 200 - 500$ s, while maintaining a continuous flow of polarized Xe throughout, again indicates successful, near-complete freezout of Xe in the trap. We estimate the collection of pure Xe to be 7 mL at STP. At $t = 500$ s we thaw the cold trap while maintaining gas flow. A continuous flow of (freshly-polarized) mixed gas from the SEOP polarizer pushes the thawed gas sample into the NMR cell for detection. Technical constraints prevented operation of the NMR cell under vacuum, which would allow the free expansion of Xe into the cell post-thaw; a new rigid cell is under construction. The sample which gives rise to the signal appearing after $t = 500$ s is likely a mix of thawed purified Xe and freshly polarized mixed gas; the signal amplitude shows no increase over pre-freezeout conditions, and likely indicates loss of polarization in the purified Xe sample. We anticipate that the post-freezeout signal for a pure Xe gas sample with polarization maintained will be larger than the continuous flow signal by at least an

order of magnitude, due to the increase in Xe number density.

3.4 Discussion

In this section we have described the design and operation of a flow-through polarizer. We have demonstrated polarization of ^{129}Xe using spin exchange optical pumping with polarizations of a few percent. The rate equation model used to estimate the polarization indicates that the Rb polarization is limited by binary collisions with Xe (the dominant source of Rb polarization loss). Measurements of the pressure broadening up to 60 psi indicates resonant absorption of at most 12% of the optical pumping light. An increase in polarization of Rb, and therefore of ^{129}Xe, could be acheived either by increased broadening in a high-pressure cell, or by increasing the power spectral density with a narrowed pump laser. We find the best polarizations are acheived in batch-mode operation for at least 10 minutes buildup time. The long T_1 lifetimes observed are sufficiently longer than the neutron EDM experimental cycle; even longer T_1 is expected in an experimental cell with improved uniformity. The freezeout and purification of ^{129}Xe is necessary for future integration with the neutron EDM cell and for experiments probing the polarization by two photon transitions. Experiments at TRIUMF including the Xe comagnetometer are planned to begin in late 2020. Development of freezeout apparatus will continue at UBC and U. Winnipeg.

Chapter 4

Spectroscopy

As discussed in Section 2.4.3, optical magnetometry of ^{129}Xe requires a suitable electronic transition and optical probe. This chapter covers spectroscopic results from two photon absorption in Xe $6p \leftarrow 5p$ transitions[1]. Section 4.1 presents early experiments with a pulsed laser: we observed LIF from all two-photon allowed $6p$ levels, tested the light polarization dependence of the 249 nm transition rate, and observed an on-axis LIF enhancement due to coherent emission. Section 4.2 describes the experimental setup and results of high-resolution spectroscopy with a CW laser on the $5p^5(^2P_{3/2})6p\,^2[3/2]_2 \leftarrow 5p^6\,(^1S_0)$ transition. Hyperfine constants and isotope shifts for the transition were determined with high accuracy and compared with literature, as well as the two-photon transition probability. The results of this section, including hyperfine constants and isotope shifts, have been published in Physical Review A [8]. Section 4.3 calculates the theoretical comagnetometer sensitivity based on the observed SNR for two-photon detection at the Xe pressures studied, and extrapolates to predict the sensitivity down to 1 mTorr pressure.

4.1 Two-Photon Spectroscopy of Xe with Pulsed UV laser

The first experiments in our lab were done using a pulsed laser to a) find the peaks, b) test the polarization dependence of the selection rules and c) investigate previously-reported bidirectional emission.

4.1.1 Experimental Setup

The schematic of the pulsed setup is shown in Fig. 4.1. We generated the UV light for these pulsed experiments using a grating-tunable dye laser (LambdaPhysik Scanmate) with Coumarin 307/MeOH dye. The gain medium was pumped by 355 nm third harmonic light from a Q-switched Nd:YAG laser (Coherent Surelight, 10Hz, 650mJ/pulse) (This particular dye efficiently absorbs UV

---

[1]We use the spectroscopic convention where a left arrow indicates absorption and a right arrow indicates emission.

pump light in the 360-420 nm range, and fluoresces around 485-546 nm with a peak at 508 nm and 15% efficiency[32]). The dye laser grating was tuned to 499.2 nm. We used a non linear (phase-matched) BBO crystal to produce the UV 249.6 nm light using Second Harmonic Generation (SHG). Phase matching was obtained by manually rotating the BBO crystal. After separating the fundamental and harmonic using a Pellin-Broca prism, the doubled radiation was loosely focused (f=+500 mm) into a 20 cm long vacuum cell constructed from a KF40 tee with 25 mm diameter MgF windows (Fig. 4.1). The cell was evacuated and backfilled with a partial pressure of research-grace natural abundance xenon (Praxair) between 12 mTorr and 1 Torr. Using computer control we stepped the dye laser output frequency through the two photon resonance. The gas absorbed at three wavelengths corresponding to $5p \leftarrow 6p$ ($J = 0, 2$) transitions and emitted fluorescence light in the NIR corresponding to $6p \rightarrow 6s$ transitions. We measure fluorescence both orthogonal and parallel to the excitation light. Off axis, emission was filtered by a monochromator (SPEX 1680) and recorded by a Photomultiplier Tube (PMT) (Hamamatsu R943-02) with a quantum efficiency of approximately 10% at the fluorescence wavelengths and operated with an approximate gain of 10^6. The monochromator was operated with a wide 3.6 nm bandpass to obtain maximum light collection, by setting the entrance and exit slits to 2.0 mm (the dispersion of the gratings is 1.9 nm/mm), as it was only necessary to separate spectral lines more than 60 nm apart. Smaller spectral features were on the order of 2 GHz and not resolvable by the monochromator. We used a gated integrator and boxcar averager (Stanford SR250) set to integrate signals over the 5 ns pulse duration of the detected emission. The averaged DC signal was recorded using an oscilloscope or DAQ system.

4.1.2 Observation of Laser-Induced Fluorescence

To first identify the lines we set the monochromator to detect 823 nm emission and scanned the dye laser grating across the 252.5 nm two-photon resonance in 0.0001 nm wavelength increments until we observed fluorescence. Figure 4.2 shows the observed TALIF signal, with a FWHM of 0.002 nm corresponding to a laser bandwidth of approximately 30 GHz. With such a broadband laser we are unable to resolve the hyperfine levels of the transition ($F = 3/2$ and $F = 5/2$), which are separated by only 2 GHz, or isotope shifts. Similar spectra are obtained at 249.6 nm and 255.9 nm.

Once the excitation wavelengths were determined we fixed the dye laser frequency at the center of a resonance and stepped the monochromator by 0.1 nm increments to resolve the emission spectra as in Figure 4.3. The resolution of the monochromator is sufficient to resolve the fine splitting of spin-orbit coupled levels but not that of hyperfine levels. The results are summarized in Table 4.1.

Bidirectional Emission

A paper by Rankin[137] on two-photon excitation of xenon reported detection of an enhanced on-axis 828 nm LIF signal following excitation at 249 nm with a pulsed UV laser beam. This enhancement was labelled bidirectional emission as it was observed in both the forward and backwards
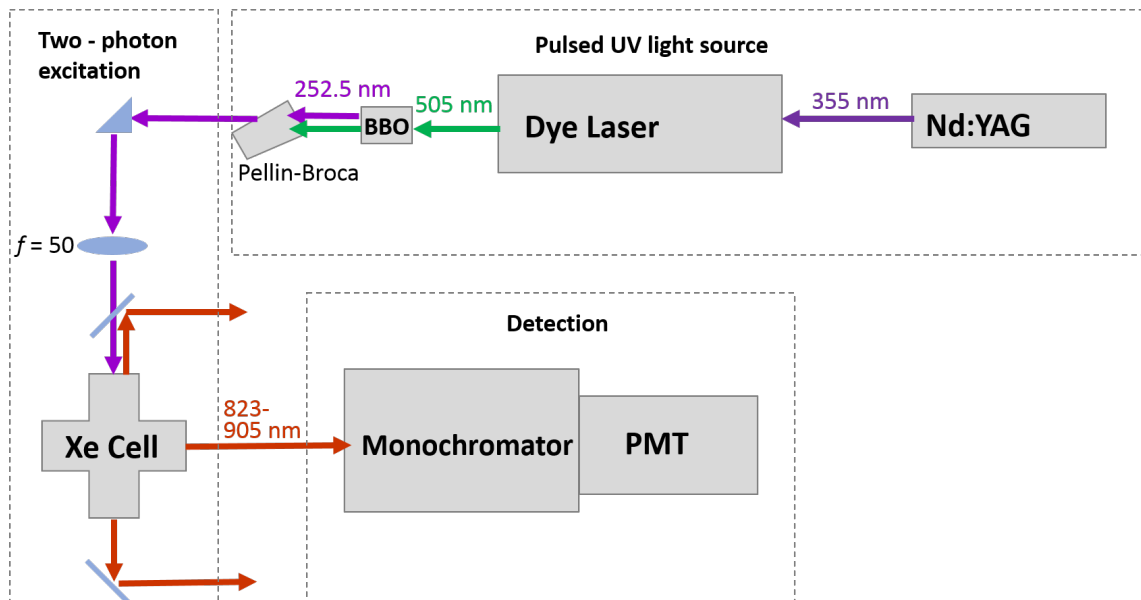
Figure 4.1: Schematic of the setup used for pulsed laser spectroscopy. Two-photon absorption in the Xe cell creates laser-induced fluorescence, which may be detected parallel or transverse to the pump beam.
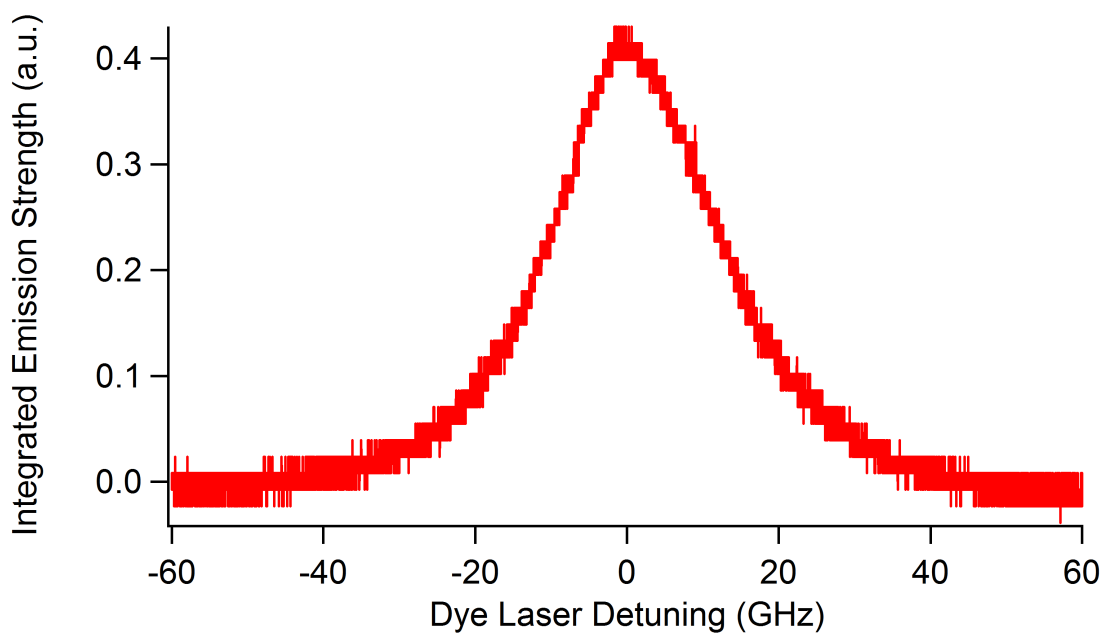
Figure 4.2: Laser-induced fluorescence from 252.5 nm two-photon excitation of Xe.
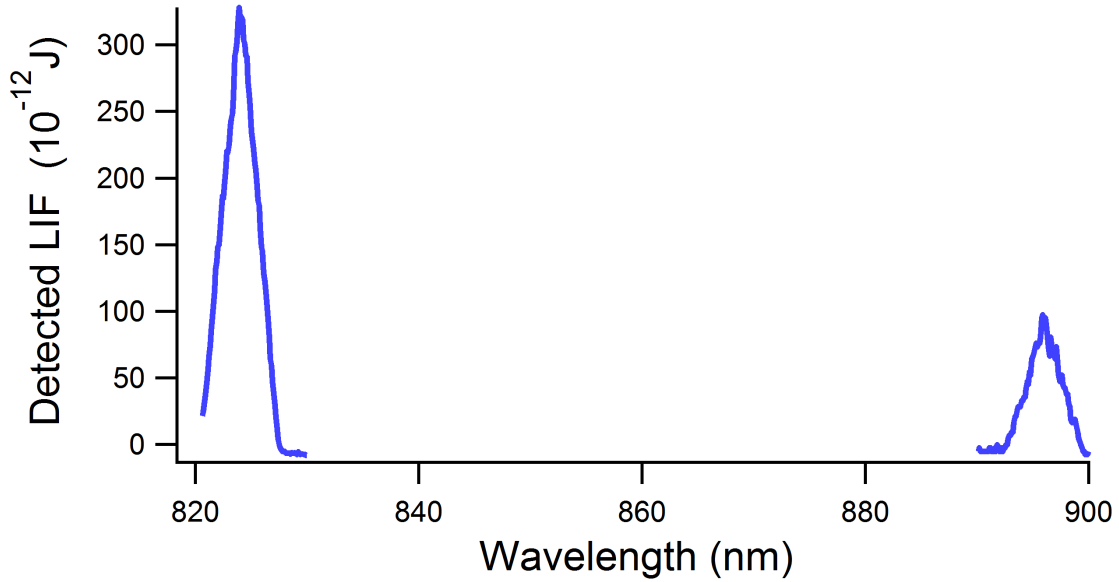
Figure 4.3: Frequency scan of the fluorescence following 252.5 nm two-photon excitation. The LIF signal has been corrected for PMT sensitivity and monochromator efficiency at the LIF wavelengths 823 nm and 895 nm.

Table 4.1: Pulsed laser excitation results. The initial laser used had a laser bandwidth over 30 GHz.

TPA Transition	$5p^5(^2P_{3/2})6p\,^2[1/2]_0$ $\leftarrow 5p^6\,(^1S_0)$		$5p^5(^2P_{3/2})6p\,^2[3/2]_2$ $\leftarrow 5p^6\,(^1S_0)$		$5p^5(^2P_{3/2})6p\,^2[5/2]_2$ $\leftarrow 5p^6\,(^1S_0)$	
λ_{TPA} (nm)	249.6		252.5		256.0	
FWHM (nm)	0.0125		0.0127		0.0157	
LIF Transition	$\rightarrow\,^2[3/2]_1$		$\rightarrow\,^2[3/2]_2$	$\rightarrow\,^2[3/2]_1$	$\rightarrow\,^2[3/2]_2$	$\rightarrow\,^2[3/2]_1$
λ_{LIF} (nm)	828.0		823.2	895.2	904.5	992.3
FWHM (nm)	2.28		2.36	2.26	2.19	-

direction collinear with the axis of the excitation light. This phenomenon has been investigated in subsequent papers and is now thought to result from a mixture of amplified spontaneous emission (ASE), occurring exactly at the two-photon resonance, and nonlinear parametric emission processes such as four-wave mixing or stimulated electronic Raman scattering, which can occur even for near-resonant light [5]. To test for bidirectional emission we set up photomultiplier tubes on-axis and off-axis of the excitation beam to compare the bidirectional and spontaneous fluorescence signals. The forward LIF signal was separated from the intense UV laser light using a UV-reflective mirror as a low pass filter. The backwards-emitted LIF signal was observed by using a beamsplitter and repositioning the spectrometer and photomultiplier tube. The optics collected light from a solid angle of approximately 0.01 steradian for the on-axis backwards emission. We varied the excitation light
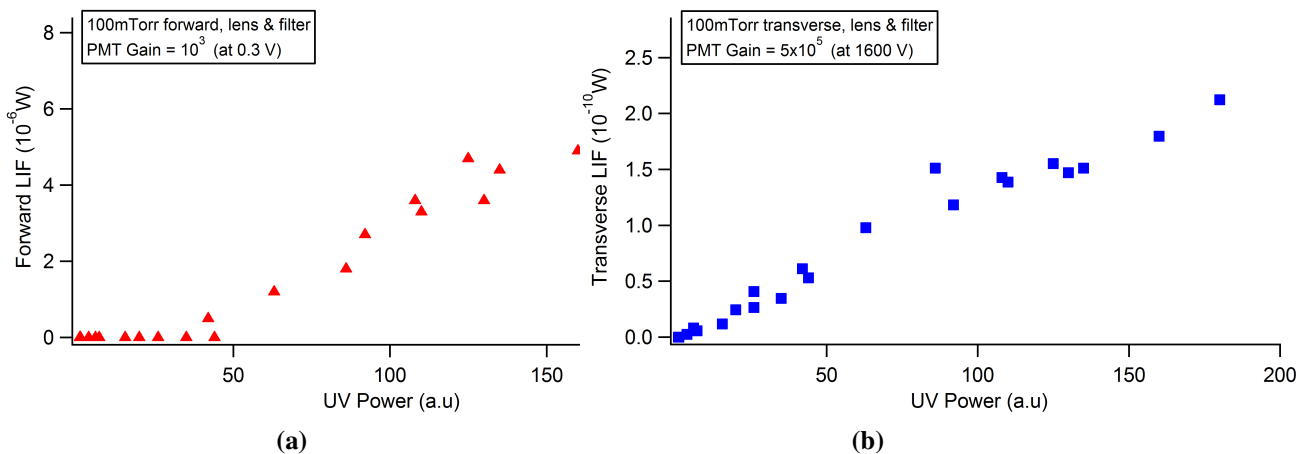
Figure 4.4: (a) Forward and (b) transverse LIF at 828nm vs UV pulsed laser intensity at 249 nm. (a) demonstrates the threshold at 50 a.u. for the onset of bidirectional emission.
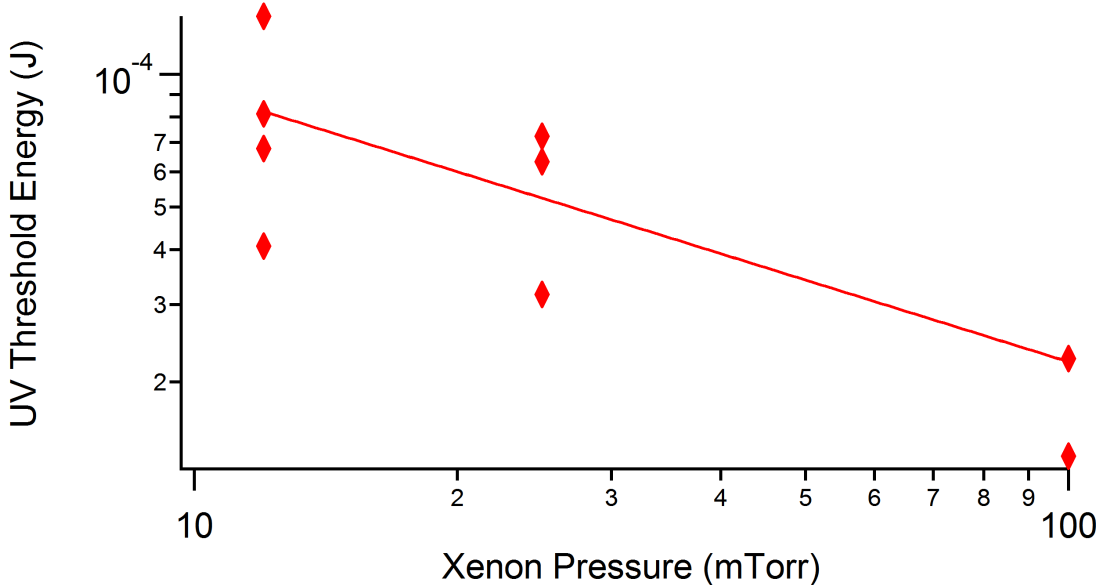
Figure 4.5: Pressure dependence of threshold energy (and power density) for observation of strong bidirectional emission at 828 nm.

intensity with a neutral-density filter and recorded LIF intensity. A clear threshold was observed for the onset of bidirectional emission as can be seen in Fig. 4.4, which agrees qualitatively with the literature observations. We observed bidirectional emission following both 249 nm and 252.5 nm excitation. The detected power in the forward signal is several orders of magnitude higher than for transverse, without any correction for solid angle collection or monochromator efficiency. The threshold power density for this enhanced emission depends upon pressure as shown in Fig. 4.5. Calibrating the absolute threshold power density for a given Xe pressure requires better knowledge of the focusing parameters of the UV excitation beam. Assuming a Gaussian beam profile, we yield a beam waist $w_0 = 20\,\mu$m and a power density threshold of roughly 10^9 W/cm^2 at 10 mTorr. This is three orders of magnitude higher than previously reported [137]. The disagreement indicates that the Gaussian beam model is likely not accurate for our laser. We find the threshold power dependence for 828nm LIF to be $I_0 \propto p^{(-0.6\pm0.3)}$ which agrees with the dependence $I_0 \propto p^{-0.65}$ observed by Rankin [137]. The extrapolated threshold at 5 mTorr Xe from previously reported values is approximately 10^8 W/cm^2. This indicates tight focusing is required if we want to utilize this effect to see enhancement of LIF at low Xe pressures.

Polarization Dependence

Different excited levels are accessible by different polarizations of UV light. For example, referring to Fig. 2.13 for ^{129}Xe, the 249 nm transition $5p^5(^2P_{3/2})6p\,^2[1/2]_0 \leftarrow 5p^6\,(^1S_0)$ is an $F = 1/2 \leftarrow F = 1/2$ transition for which the change in angular momentum can only be $\Delta M = 0,1$. Two equal-frequency photons with linear polarization parallel to the quantization axis (and wavevector $\vec{k} \perp \vec{B}_0$) can only impart an angular momentum change of $\Delta M = 0$. Two circular polarized photons with $\vec{k} \parallel \vec{B}_0$ change the angular momentum by $\Delta M = \pm 2$. Therefore only linear polarized light (or a combination of both circular polarizations) can excite the 249 nm transition. To test this we probed the Xe cell with 249 nm light and monitored the absorption via 828 nm fluorescence as we changed the UV light polarization. The linearly polarized dye laser pulses generate a UV second harmonic in the BBO crystal, orthogonal to the incident light. We pass this UV light through a polarizing beam splitter, followed by a quarter wave plate, with the QWP slow axis and beam splitter axis initially parallel. We then rotate the QWP fast axis in 5-degree increments while recording fluorescence signals at 828 nm. An alignment of 0 degrees or 90 degrees corresponds to linear polarized light, while a 45 degree alignment produces σ^+ circular polarized light; in between these orientations the polarization is elliptical. As observed in Fig. 4.6, emission reached a maximum for the 0 degree and 90 degree linear polarizations, while no signal was observed from circular polarized light at 45 degrees. No excitation can occur due to the selection rules; thus both sublevels of the ^{129}Xe ground state form a dark state with respect to circular polarized 249 nm radiation.

The same selection rules which prevent σ^+ excitation at 249nm also make optical pumping at 252.5 nm possible. Specifically, the transition $5p^5(^2P_{3/2})6p\,^2[3/2]_2(F = 3/2) \leftarrow 5p^6\,(^1S_0)$ to the
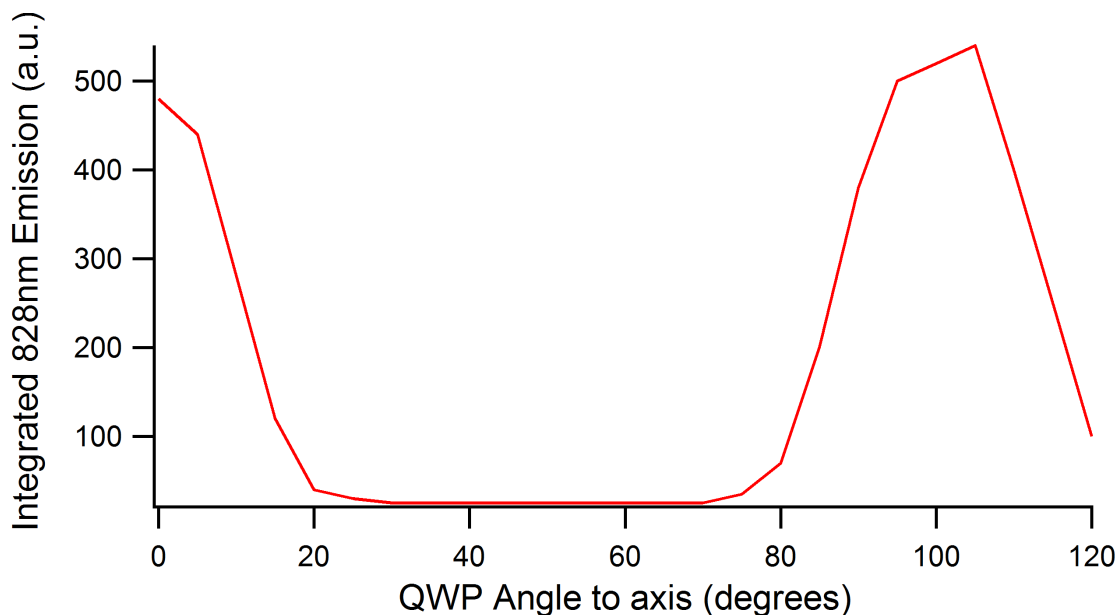
Figure 4.6: Observed LIF dependence on QWP rotation angle for the 249 nm transition. For this transition only $\Delta M = 0$ is allowed. This simple demonstration of the selection rules for unpolarized Xe vapour in the J=0 state is indicative of the expected behavior for polarized Xe vapour in the J=2 states.

excited state F=3/2 hyperfine level has magnetic sublevels M=$\pm$3/2, $\pm$1/2; when we pump with σ^+ light the ground state M=-1/2 sublevel is absorbing while the M=+1/2 sublevel is dark. Continuous pumping will populate the dark state; however with the broadband pulsed laser we used to make these measurements we cannot resolve the excited state F=3/2 from the F=5/2 hyperfine level, for which both ground state sublevels are absorbing. A narrower-linewidth laser is necessary for optical pumping.

4.1.3 Efforts to reduce bandwidth

With a broadband pulsed laser, it is not possible to resolve the hyperfine transitions in any of our two-photon processes. The hyperfine levels of $6p\,^2[3/2]_2$ for example, are separated by 2 GHz [53]. We attempted to narrow the pulsed laser linewidth using a single plate etalon, and also an etalon formed by a pair of high-reflectivity mirrors. Neither was successful; even with an etalon installed, our pulsed laser linewidth is greater than 8 GHz. The linewidth of the pulsed laser was a limiting factor that motivated excitation with the narrow linewidth laser described in the following section.
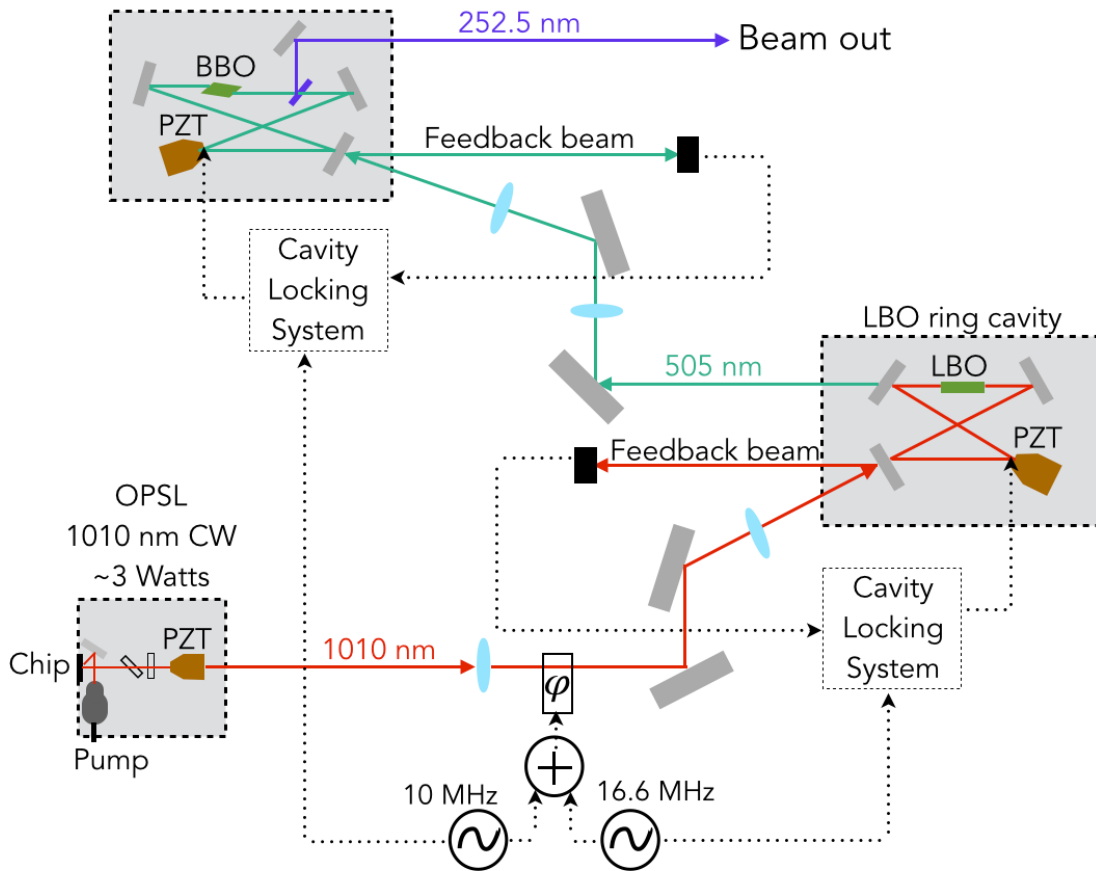
Figure 4.7: Layout of the CW laser system. Schematic made by E.Altiere [7]

4.2 Two-Photon Spectroscopy with Narrow Linewidth CW Laser

We developed a tunable, narrow (sub-MHz) linewidth CW laser at 252.5 nm in collaboration with David Jones lab. The design follows that of ([7]) for Lyman-alpha generation and is based on harmonic generation from a 1010 nm Optically Pumped Semiconductor Laser (OPSL) in two successive cavities. The design was for 200 mW of CW UV output at 252.5 nm.

4.2.1 CW Narrow Laser Development

A tunable UV CW laser using an OPSL and doubling crystals was recently developed at UBC to generate narrow linewidth DUV light at 243 nm, and presented in the Master's thesis of E. Altiere [7]. The design of the present system shown in Fig. 4.7 is a replica of the system in that work, using a new custom OPSL chip. For full details we refer the reader to the description in her thesis. This laser is used to excite two photon Xe transitions. The laser uses an 808nm diode laser (pump power approximately 20 W) to pump a custom-made semiconductor stack which emits multimode around

1010 nm. A birefringent filter mounted at Brewster's angle and etalon mounted internally to the OPSL cavity force single mode operation (see section below). The fundamental light is doubled to 505 nm and quadrupled to 252.5 nm by nonlinear Lithium Triborate (LBO) and Beta Barium Borate (BBO) crystals, respectively. The doubling crystals are each placed in a resonant cavity to increase the intensity of SHG generated. Each doubling cavity has an input coupler with a reflectivity specially chosen to satisfy impedance matching conditions for maximum intensity buildup. Doubling cavities are made resonant by changing the length of the cavity using a piezoelectric transducer, and are locked to resonance using a Pound Drever Hall (PDH) scheme. A ring cavity was chosen so that light only travels one direction in the cavity; there are no standing waves and this results in one SHG beam instead of two. Optics were used to match the near-Gaussian beam profile to match the TEM_{00} mode accepted by the cavity. The previously demonstrated coupling in the first cavity was 74%, and 83.6% in the second cavity. The buildup in the cavity is approximately $85\times$ for the LBO and $55\times$ for the BBO cavity. The typical conversion efficiency from IR to UV is 11%.

The similar laser developed by our collaborator in [7] was shown in that work to have a 87 kHz linewidth in the fundamental OPSL frequency when locked. The linewidth increases by a factor of $\sqrt{2}$ in each second harmonic conversion stage; hence we expect a 174 kHz linewidth for the frequency-quadrupled UV light. Without frequency stabilization of the OPSL, the free-running laser drifts slowly by up to 200 MHz on a timescale of 25 minutes. The OPSL is tunable over a range of roughly 1-2 GHz before a mode hop occurs (see section below); this corresponds to a UV tuning range of up to 8 GHz, which covers 16 GHz in the (two-photon) Xe spectrum.

Single-mode operation of the OPSL

The gain bandwidth of the OPSL chip is large, so this design uses an intracavity birefringent filter and etalon to force single-mode operation. The OPSL cavity itself is 60 mm long with a Free Spectral Range (FSR) of roughly 2.5 GHz, and sets the narrow linewidth described above. The cavity is tunable by means of a piezoelectric mounted to the output coupler. Mounted intracavity is an etalon 0.8 mm thick made of fused silica (with a FSR of 129 GHz) which serves to modify the transmittance of the various modes as in Fig. 4.8a. The birefringent filter has a similar effect; by rotating the polarization of light it introduces a frequency-dependent loss to the various modes depicted in Fig. 4.8b. Figs. 4.8c and 4.8d show the combined effect of the two intracavity elements: the cavity acquires a frequency-dependent transmission function which prefers one single frequency mode over all others. Changing the cavity length by PZT fine-tunes the exact frequency over a range up to the cavity FSR; any further tuning causes a mode-hop, where a neighbouring mode becomes more favoured.

(a) Etalon

(b) Birefringent filter

(c) Supported mode structure

(d) Magnified view of (c) to show individual modes.
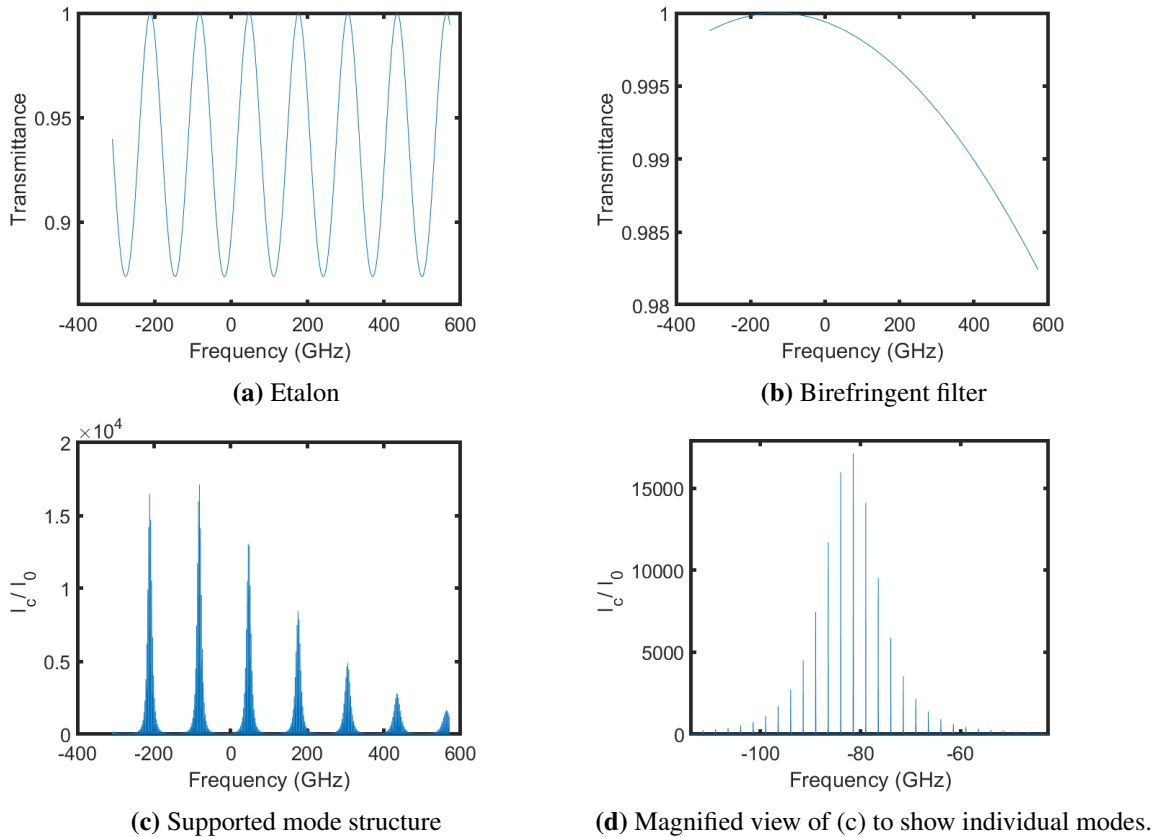
Figure 4.8: MATLAB simulation of frequency modes supported by the OPSL cavity, showing the effect of intracavity elements to force single mode lasing. The x-axis shows the OPSL frequency, offset by 296841 GHz. (a) Free spectral range of the intracavity etalon. (b) Transmittance function of intracavity birefringent filter mounted near the Brewster's angle. (c) Cavity mode structure modified by the intracavity elements. (d) Magnified view of (c) showing preferential gain for one frequency mode.

Pound-Drever Hall scheme for locking doubling cavities

Light generated at 1010 nm for the Xe laser is frequency quadrupled using two SHG doubling cavities. A crystal of LBO or BBO provided the phase matching conditions to generate SHG. The process of conversion is nonlinear: the efficiency is greater for higher intensity radiation. Thus, to maximize generation of SHG we used a buildup cavity to enhance the fundamental. The buildup used a bowtie configuration and was locked using a piezo-controlled mirror in a Pound-Drever-Hall scheme.

This scheme adds frequency sidebands to the light and uses them to generate a signal proportional to the deviation from resonance. In this scheme, the incoming fundamental light is phase-modulated at about 11 MHz by an EOM (see Fig. 4.7). This generates two sidebands on the 1010 nm light, each 11 MHz away from the fundamental. The two sidebands are out of phase,
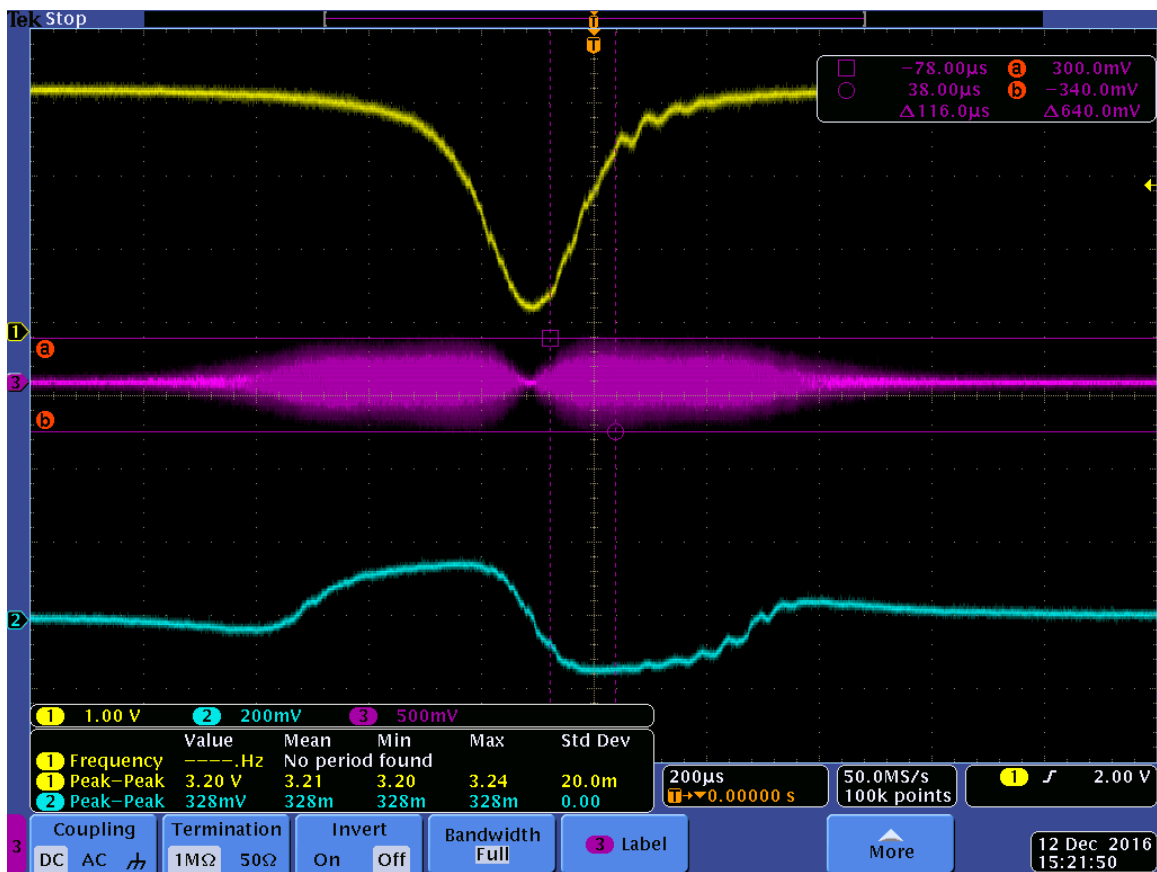
Figure 4.9: Trace of signals used for PDH lock on the LBO cavity, obtained by applying a monotonic voltage ramp to the cavity PZT. The signals shown are the photodiode DC signal (yellow), photodiode AC signal (pink), and error signal (blue) derived from the phase of the AC signal. The slope of the error signal determines which direction to drive the cavity. The oscillation that appears on the right-hand side of the photodiode DC and error signals may result from mechanical vibrations.

and as such the total intensity of the beam is constant. This light is coupled into the buildup cavity, which has a narrow linewidth (4 MHz) and a large FSR (1.29 GHz). We use a photodiode to record the feedback beam, which is the superposition of (i) the initial reflected intensity with (ii) a component of the enhanced circulating intensity in the cavity, transmitted through the input coupler. On resonance, the feedback signal is close to zero. The fundamental reflection and its transmitted component destructively interfere, and so do the two out-of phase sidebands. Slightly above resonance, the positive (high-frequency) sideband is more strongly enhanced than the fundamental. The built-up sideband reacts with the reflected (and incompletely cancelled) fundamental to create an 11 MHz beat frequency on the PD. Slightly below resonance, the same is true for the negative (low-frequency) sideband, with a beat frequency of opposite phase. The signal from the PD is then mixed with the original 11 MHz oscillator and a low-pass filter: the result is a DC-signal called the

85

error signal, which is proportional to the phase - negative for one sideband and positive for the other. The phase dependence is vital, because it generates the slope of the error signal which determines which direction to drive the cavity. The error signal is used in a feedback loop to adjust the position of the piezo and lock to the fundamental frequency. The cavity lock follows the fundamental frequency, and remains locked during ramping of the fundamental frequency. An oscilloscope trace of the signals from the feedback beam PD while ramping the cavity PZT is shown in Fig. 4.9. As described above, the feedback signal DC component (yellow) decreases almost to zero, while an 11 MHz AC component (pink) can be observed on either side of resonance. Noise on these signals is an important factor limiting the stability of the cavity locks.

4.2.2   Vacuum chamber for two photon excitation

We coupled the UV light from the laser described above into a linear Fabry-Perot enhancement cavity enclosed in a vacuum chamber. A schematic of the cavity inside the vacuum chamber is shown in Fig. 4.10 and a photo in Fig. 4.11. The reasons for an additional cavity are twofold: first, since the probability of two-photon absorption depends quadratically on light power, we want to maximize the UV power available. Second, the cavity provides the retroreflection of the UV beam which is necessary to perform Doppler-free two-photon spectroscopy with counterpropagating photons. The cavity was designed with a length of 260 mm, intended to simulate the dimensions of the $d \approx 200$ mm UCN test cell used at RCNP for neutron EDM tests, as reported in Ref. [1]. Two mirrors with radius of curvature = 150 mm were used, an input coupler and high reflector. The reflectivities of the two mirrors chosen were based on the initial plan to install an intracavity spectroscopy cell with AR-coated UV windows (ATFilms). The high reflector mirror was chosen for the highest available reflectivity, while the input coupler reflectivity was chosen to impedance match with the losses from the cell windows. In practice, however, we found that even the best available AR-coated UV windows with reflectivities up to 98.2% were still too lossy; they reduced the cavity finesse to unacceptable levels such that the circulating UV power was less than the input power. Therefore we constructed the vacuum chamber to enclose the cavity, as an alternative which does not require intracavity windows. For future integration with the nEDM experiment, it is necessary to source suitable AR-coated UV windows with higher transmission.

We enclosed our Fabry-Perot cavity in vacuum and backfilled the entire volume with a partial pressure of Xe. The entire volume is pumped with a dry scroll pump (Agilent SH-110). The base pressure achieved with this pump is 0.1 Torr, and the leak rate with the chamber sealed is 0.01 Torr/min. The cavity was stabilized by a dither lock, monitored by a photodiode on the cavity reflection which dips at resonance. Turning mirrors inside the vacuum were mounted with picomotor steppers to accurately couple the UV light to the cavity. At the time of data collection, the UV laser output was 40 mW; buildup in the Fabry-Perot cavity increased the power by five times, yielding a circulating power of 200mW. We filled the box with a partial pressure of 0.8 - 10 Torr xenon.
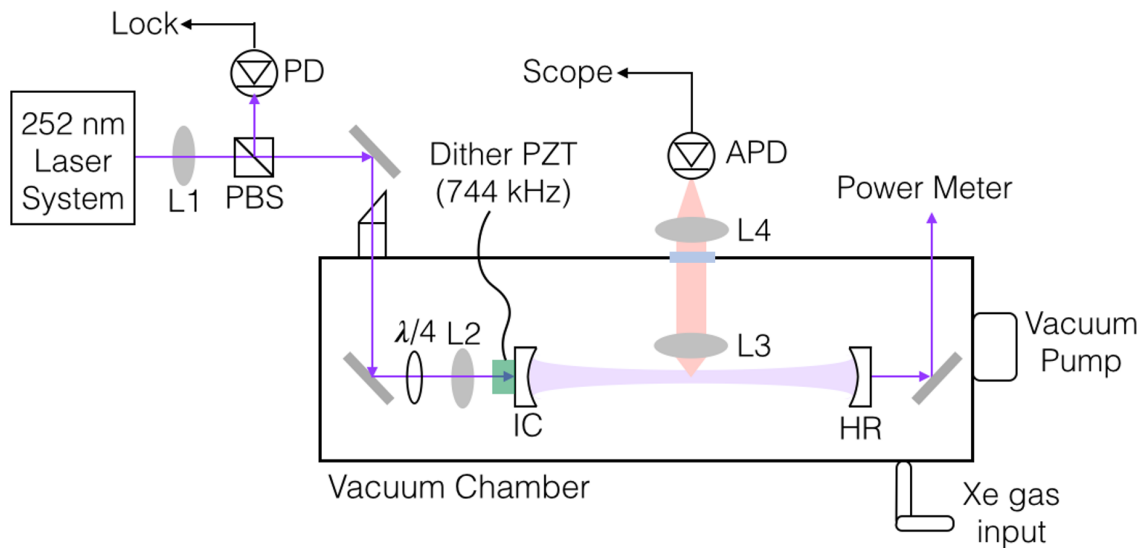
Figure 4.10: Schematic of the vacuum chamber and detection optics used for two-photon LIF spectroscopy. L1, L2: modematching lenses. L3: $f = 19\,\text{mm}$ collection lens. L4: $f = 50\,\text{mm}$ collection lens. PBS: polarizing beam splitter. PZT: piezoelectric transducer. $\lambda/4$: quarter wave plate. IC: input coupler. HR: high reflectivity mirror. APD: avalanche photodiode.

Figure 4.11: Photo inside the vacuum box, showing turning mirror from brewster window UV input; holder for QWP and lens; input coupler and PZT mounted to hollow copper block; LIF collection lens; HR mirror; turning mirror to UV cavity monitor.

It was found that in a pure Xe environment at such low pressures, the cavity finesse deteriorated in less than a minute. A small partial pressure of oxygen (around 1 Torr) prevented this loss of cavity finesse. We suspect that the oxygen undergoes UV photolysis and generates O_3 which helps remove deposits of hydrocarbon or other residual gases from the dielectric mirrors.

4.2.3 Experimental Setup for two-photon detection

A schematic of the detection optics in the vacuum box is shown in Fig. 4.10. We couple UV light in to the cavity to excite two photon transitions at the beam waist. An avalanche photodiode (APD, Hammamatsu C5460-01 with onboard preamplifier) is set up outside vacuum, orthogonal to the beam axis and centered on the beam waist to detect LIF at 823 nm and 895 nm. Collection optics L3 and L4 collimate the LIF to pass through an AR-coated window in the vacuum box, and focus on the APD. For the sake of maximum LIF collection, we make no attempt to separate the emission wavelengths; instead we calibrate our LIF signal using the previously observed branching ratios of 823 nm and 895 nm LIF multiplied by the different APD sensitivities.

The OPSL is tunable across a maximum 1 GHz range, with the locked doubling stages and Fabry-Perot cavity automatically adjusting to track any wavelength change. The OPSL laser wavelength is sampled by a Bristol wavemeter which determines absolute frequency up to a 30 MHz calibration uncertainty. A more accurate measure of relative frequency change is obtained by beating the OPSL light against a fiber-based self-referenced frequency comb available in our lab and recording the beat spectrum. The comb frequency is locked around 125 MHz; knowledge of the comb frequency and offset allows for absolute frequency determination. The wavemeter allowed determination of the frequency up to the nearest comb tooth, and the addition of the beatnote frequency potentially allows determination of the absolute frequency. Details of the comb are presented in Section A.3.

4.2.4 Results: Detection, Hyperfine splitting, and Isotope shifts

We observed LIF from two-photon excitation of the transition $5p^5(^2P_{3/2})6p\ ^2[3/2]_2 \leftarrow 5p^6\ (^1S_0)$ using 0.8-10 Torr of natural abundance Xe mixed with a small partial pressure of oxygen. The data is shown in Fig. 4.12. We scanned the OPSL over a 300 MHz IR range, which corresponds to 2.5 GHz in the Xe energy spectrum, as follows from two successive SHG stages and a two-photon transition. LIF peaks were observed from all stable isotopes with mass 129-136. The natural abundance of ^{124}Xe, ^{126}Xe, and ^{128}Xe were too small to observe peaks from these isotopes. At 1.5 Torr and below, the absorption linewidth was sufficiently narrow to resolve each of the observed peaks. We fit these peaks to a Lorentzian lineshape; as the Doppler-free nature negated the need for a Voigt profile, as described below. In the low-pressure data, all fit parameters were left free to vary. In 5 and 10 Torr data, it became necessary to lock the amplitude ratios to reasonably fit the profile of the unresolved peaks. From the difference in peak positions we are able to extract hyperfine constants
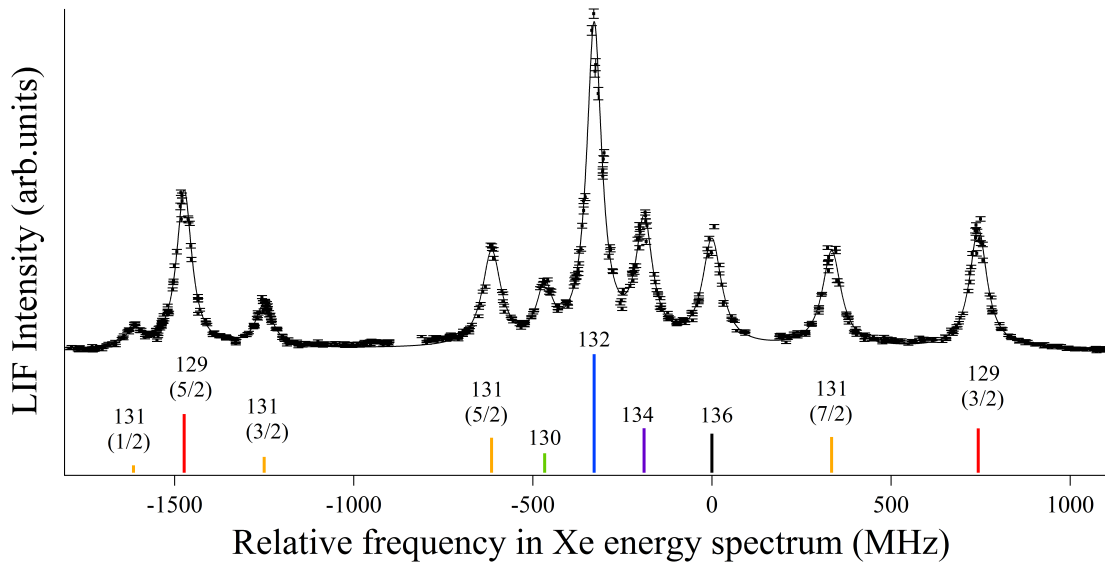
Figure 4.12: Excitation spectrum $5p^5(^2P_{3/2})6p\,^2[3/2]_2 \leftarrow 5p^6\,(^1S_0)$ transition in natural abundance Xe. The total pressure was 1.6 Torr, with a 50-50 ratio of Xe and O_2. The x-axis corresponds to the Xe transition frequency, eight times larger than the OPSL frequency. The y-axis is the observed LIF intensity of the combined 895 nm and 823 nm emission. The peaks are shown with the fitted Lorentzian lineshape as described in the text. Each peak is labeled with its mass number; additionally, odd isotopes are labeled with their excited state hyperfine level F in parentheses. The stick diagram shows the calculated peak positions and intensities obtained from the Lorentzian fit.

A and *B* as well as isotope shifts.

Fitting of Doppler-free lineshape

We expect from Section 2.3.2 that the Doppler-free spectra should be well described by a Lorentzian profile. To confirm this, we test fit a data sample using the built-in Gaussian, Lorentzian, and Voigt profiles of the IGOR software multipeak fit package. Using the Voigt fit function returns estimates of the FWHM for the convoluted Gaussian and Lorentzian components of each peak. We compared these to the FWHM given by a Lorentzian function alone. Table 4.2 lists the Lorentzian and Voigt fits. With the exception of two peaks, the analysis using a Voigt profile supports a completely Lorentzian lineshape. The difference in peak center between the two fits is also less than 0.5 MHz. We use only Lorentzian fits in the remaining data analysis. The residual contribution of the Gaussian to the on-resonance signal less than 1%, and is accounted for in the fit by the same constant that accounts for the APD stray light background.

To determine the exact resonance frequencies of the Xe spectral lines, we fit Lorentizan lineshapes to a plot of LIF signal vs. laser frequency. The OPSL frequency measurement was made by

a spectrum analyzer (Advantest) with a resolution bandwidth of RBW = 125 kHz. This means upon conversion to Xe energy, our resolution is 1 MHz. Therefore 1 MHz is is the uncertainty in the frequency axis. Since Ordinary Least Squares fitting routines assume no error in the independant axis, we had to resort to more sophisticated fitting techniques. In particular, we used Orthogonal Distance Regression [27], so named because it measures the orthogonal distance between each sample point and the estimated fit function. There is a readily available public domain software package called ODRPACK, now implemented with a Python interface, which we used for our fitting. We created a user-defined multipeak fit function comprised of a superposition (sum) of independant Lorentzian peaks each with a free position and amplitude parameter. A single FWHM parameter described all peaks in the dataset. In the case of the odd isotopes, each peak position was fit according to the formula for hyperfine splitting described in Section 4.2.6 below.

Table 4.2: Comparison of absorption lineshape fitting using either a Voigt profile or a Lorentzian profile. Peak widths are in MHz. Also shown is the difference in center frequency fitting parameter between the two profiles in MHz.

Peak	Voigt fit				Lorentzian fit		Difference
	Gaussian		Lorentzian				
	FWHM	σ	FWHM	σ	FWHM	σ	$v_{0,Voigt} - v_{0,Lor}$
1	52.7	4.3	2.7	6.4	42.4	1.6	-0.3
2	0.0	0.0	51.1	0.5	50.3	0.4	-0.3
3	0.0	0.0	57.1	0.5	57.9	0.8	0.1
4	0.0	0.0	62.7	0.4	61.3	0.6	-0.4
5	0.0	0.0	54.8	1.2	54.5	1.1	0.3
6	8.7	2.7	51.4	0.7	52.4	0.4	0.0
7	0.0	0.0	56.8	0.4	57.4	0.6	0.0
8	0.0	0.0	63.0	0.7	63.3	0.7	0.0
9	0.0	0.0	60.6	0.8	63.2	0.6	-0.2
10	0.0	0.0	57.4	0.5	57.8	0.5	0.0

4.2.5 Pressure broadening

We obtained data for a 50-50 mix of Xe and O_2 at pressures ranging 1-10 Torr. The results are shown in Fig. 4.13. The slope has a value of 31.3(0.3)MHz/Torr, which is comparable to Plimmer's value of 28.8(2.6) MHz/Torr for the 249 nm line [128].

We also measured the pressure broadening over the same range of total pressure, with a fixed 1 Torr partial pressure of O_2, as shown in Fig. 4.14. For this data we measure 32.6(0.3) MHz/Torr.
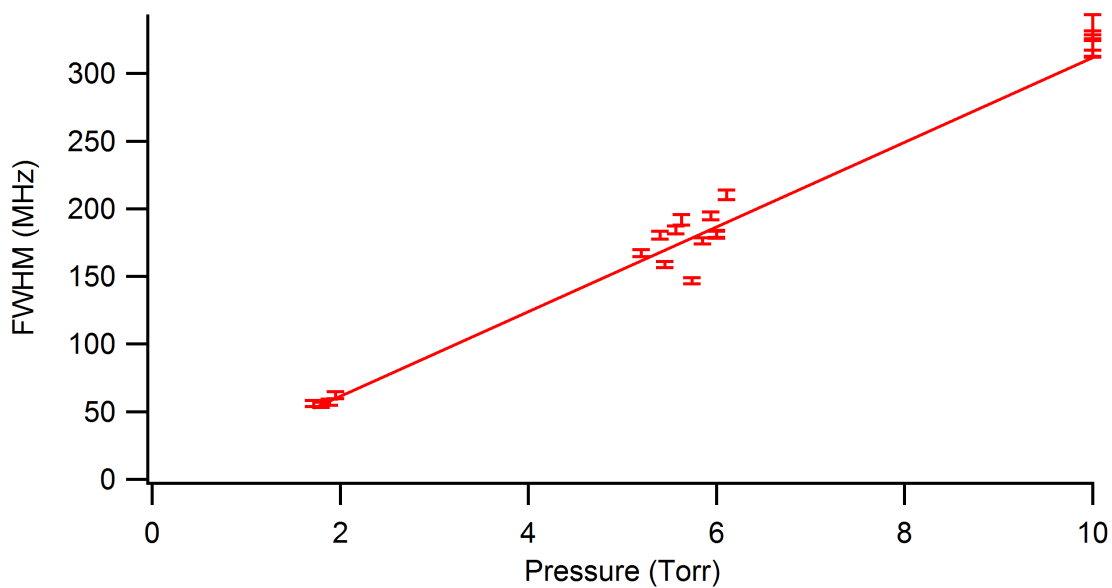
Figure 4.13: Pressure broadening for a 50-50 mix of Xe and O_2. The x-axis reports total pressure.
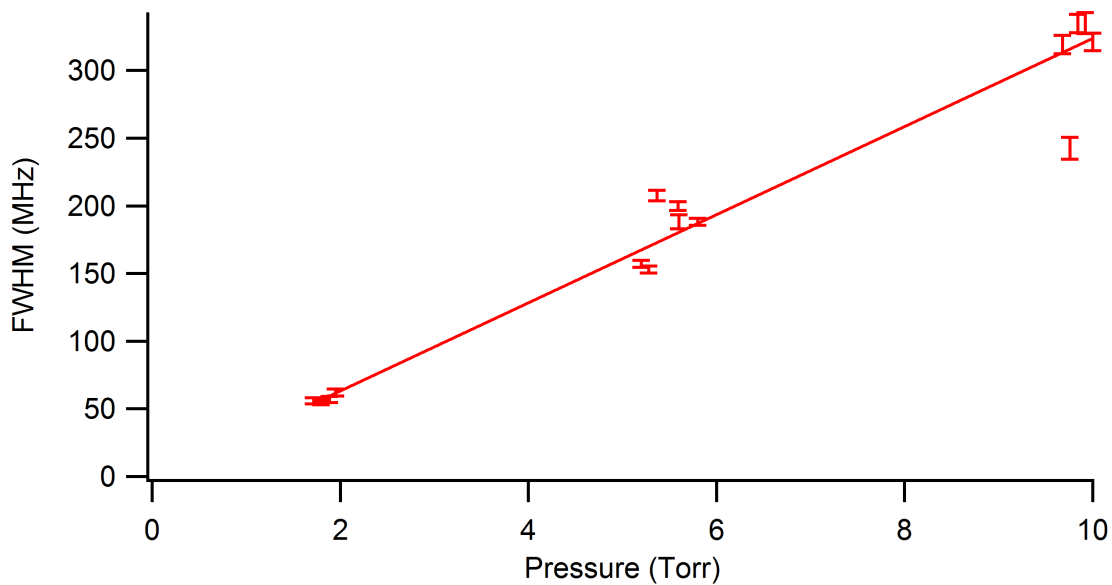
Figure 4.14: Pressure broadening for Xe with 1 Torr of O_2. The x-axis reports total pressure.

Table 4.3: Hyperfine splitting constants (in MHz) for the $5p^5(^2P_{3/2})6p\,^2[3/2]_2$ excited state of ^{129}Xe and ^{131}Xe. Values obtained by previous works are listed in the last column for comparison. Values in parentheses are the 1σ standard deviation of the last digit.

Hyperfine Splitting Constant	This Work	Previous Works
A_{129}	$-886.3(2)$	$-886.1(8)$[29], $-889.6(4)$[53], $-886.2(28)$[157]
A_{131}	$262.6(10)$	$263.1(6)$[29], $262.7(4)$[53], $263.2(13)$[157]
B_{131}	$34.8(5)$	$29(2)$[29], $21.3(6)$[53], $26.8(60)$[157]

4.2.6 Hyperfine constants

Odd isotopes exhibit hyperfine splitting due to the interaction of their nuclear spin I with electron angular momentum J. A common model used to derive the Hamiltonian is the potential of a magnetic dipole in the field caused by the orbiting electrons. The vector sum of these angular momenta leads to the total angular momentum $F = J + I$. The hyperfine splitting is well approximated (to second order) by magnetic-dipole and electric-quadrupole interactions. The ground state of Xe is $^1S_0$ with $J = 0$ so it has no hyperfine splitting; only the excited state exhibits splitting. The transition frequency of the peak $\nu_i(I,J,F)$ corresponding to hyperfine level F is shifted away from its center of gravity $\nu_{0,i}$ by an amount: [154]

$$\nu_i(I,J,F) = \nu_{0,i} + A_i\frac{K}{2} + B_i\frac{\frac{3}{2}K(K+1) - 2I(I+1)J(J+1)}{4I(2I-1)J(2J-1)}, \tag{4.1}$$

where

$$K = F(F+1) - I(I+1) - J(J+1), \tag{4.2}$$

$\nu_{0,i}$ is the center of gravity frequency for isotope i (i = 129 or 131), and A_i and B_i are the magnetic-dipole and electric-quadrupole hyperfine constants, respectively. The next order term is magnetic-octopole and is typically of order kHz. This formula was used in the multipeak Python fit by specifying I, J and F, with $\nu_{0,i}$, A_i and B_i left as free parameters for their respective peaks. In ^{129}Xe the quadrupole term vanishes because $I = 1/2$.

We report values for hyperfine constants A_i and B_i of the $5p^5(^2P_{3/2})6p\,^2[3/2]_2$ state in Table 4.3, alongside previously reported results. The magnetic dipole constants A_i agree well with the previously reported values for both ^{129}Xe and ^{131}Xe shown in Table 4.3. On the other hand, the electric-quadrupole term B_{131} is 20 % - 40 % larger than previous measured values. Our determined B_{131} value is expected to be more accurate than the previous values since, unlike previous measurements, it was determined by a transition directly from the ground state which is free of hyperfine
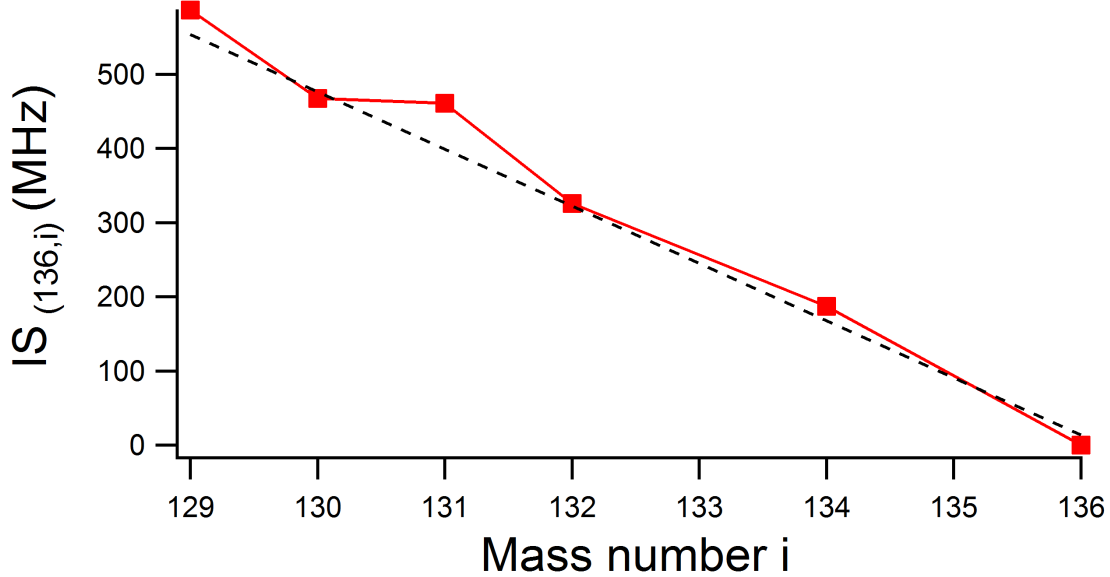
Figure 4.15: Isotope shift relative to mass 136. A line of best fit for the even isotopes shows the odd-even staggering observed by King. Error bars are smaller than the data points.

splitting. Previous measurements for the splitting of the $5p^56p$ state are based on transtions to the $6s(J=2)$ state, which has its own hyperfine splitting and respective uncertainty.

Since A_i is proportional to the nuclear g-factor $g_I = \mu_I/(\mu_N I)$ [154], we can compare directly with values determined via nuclear magnetic resonance. We calculate the ratio $A_{129}/A_{131} = -3.38(1)$, which agrees with the value $g_{129}/g_{131} = -3.375(1)$ calculated from the magnetic moments and spins given in reference [155].

4.2.7 Isotope shifts

Table 4.4: Isotope shifts $\delta v_{i,136} = v_{136} - v_i$ of the transition $5p^5(^2P_{3/2})6p\,^2[3/2]_2 \leftarrow 5p^6\,(^1S_0)$. We follow the sign convention for isotope shift outlined in [14]. Shifts for the odd isotopes were determined using the center of gravity from the hyperfine splitting.

i	Isotope Shift (MHz)
129	586.8(4)
130	467.7(5)
131	461.2(4)
132	326.0(3)
134	187.0(4)

The addition or removal of neutrons from an atom's nucleus will slightly shift the electronic

energy levels, causing each isotope to have a slightly different transition frequency. This effect is known as isotope shift. Both the ground and excited state energy levels of a transition may be shifted for each isotope, with a net result of a shift of the transition frequency between those levels. There are two contributions to the isotope shift:

- A mass shift, where the extra nuclei shift the reduced mass of the atom, and

- A field (or volume) shift, where the extra nuclei change the nuclear charge distribution and resulting electric field.

The isotope shift $\delta v_{i,i'}$ is conventionally defined as the difference in transition frequency between a heavy and light isotope (with corresponding energy gap $h\delta v_{i,i'}$) [96]:

$$IS = \delta v_{i,i'} = (v_{i'} - v_i) = \Delta v_{mass} + \Delta v_{field} \tag{4.3}$$

where $v_{i'}$ and v_i are the transition frequencies of the heavy and light isotope, respectively. A positive shift indicates the heavy isotope has the larger energy difference. Typically a single isotope (in our case, ^{136}Xe) is chosen as a point of reference for all other isotope shifts in an element.

The observed isotope shifts are tabulated in Table 4.4 and plotted against atomic mass in Fig. 4.15. To first order the isotope shifts are roughly linear in atomic mass. Odd isotopes display a staggering effect, where the odd isotope lies closer in frequency to the lighter even isotope; King explained this as due to a smaller change in mean square radius of the nuclear charge distribution when adding a neutron to an even-N isotope than for an odd-N isotope [96]. Similar staggering was found in Xe for transitions to $8d$ and $7s$ by [33].

Mass shift

One can calculate the mass and field shift to varying levels of detail. The mass shift is commonly split into "normal" and "specific" mass terms. Normal mass shift is the mass shift that would be observed for a single-electron atom, and has the form [66, 96]:

$$\delta v_{i,i'}^{NMS} = v_0 \left(\frac{m_e}{u} \right) \left(\frac{i' - i}{ii'} \right) \tag{4.4}$$

where v_0 is the nominal transition frequency, m_e is the electron mass, and u is the unified atomic mass unit. The formula predicts that heavier isotopes i' have the higher wavenumber (more energetic transition).

In multielectron atoms, the mass shift is a sum of normal and specific mass shifts; this sum is often expressed by a dimensionless parameter K.

$$\Delta v_{mass} = \delta v_{i,i'}^{NMS} + \delta v_{i,i'}^{SMS} = K \delta v_{i,i'}^{NMS} \tag{4.5}$$

Often the specific mass shifts (of terms) are of opposite sign to the normal mass shift, such that $K < 1$. This is a result of electron momenta.

Field shift

The field shift measures the interaction of electrons with the nucleus. It affects most strongly those electrons which have a probability density function that overlaps the nuclear charge radius, i.e. *s*-orbital electrons. Electrons in higher orbitals can have a small but finite charge density at the nucleus; additionally, non-*s* electrons can screen *s*-electrons, which changes the charge density of the *s* orbital.

In particular, the shift for an *s*-orbital is: [96]

$$\delta E = h\Delta v_{field} = \pi|\psi(0)|^2 \frac{a_0^3}{Z} f(Z)\delta\langle r^2\rangle_{i,i'} \tag{4.6}$$

where $|\psi(0)|^2$ is the electron probability density at the nucleus, a_0 is the Bohr radius, and Z is the atomic number. $f(Z)$ is a function of Z which accounts for distortion of the electronic wavefunction by the nucleus. $\delta\langle r^2\rangle_{i,i'}$ is the change in the mean square radius of the nuclear charge distribution between isotopes. For an $s - p$ transition: the energy level of the *s* level is raised for the heavier isotope (i.e. the term value is smaller); while the effect on the *p* orbital is smaller. Thus for the heavier isotope there is a smaller transition energy and an overall negative field shift as observed in [157]. In contrast, we find for a $p - p$ transition, that the heavier isotope has a larger transition energy. This is consistent with observations by Plimmer for the 249 nm transition [128]. The terms in Equation 4.6 which don't vary between isotopes can be collected together as a field shift constant F, such that $\Delta v_{field} = F\delta\langle r^2\rangle_{i,i'}$. The resulting expression for isotope shift is:

$$\delta v_{i,i'} = K\delta v_{i,i'}^{NMS} + F\delta\langle r^2\rangle_{i,i'}. \tag{4.7}$$

King Plot

Since the isotope shift differs for every electronic transition, it has become standard to plot the (modified) isotope shifts of one transition at v_A against those of another transition at v_B in a way that sheds light on their respective mass shift and field shift components. This is done by solving both isotope shift equations for their shared value $\delta\langle r^2\rangle$,

$$\delta\langle r^2\rangle_{i,i'} = \frac{\delta v_{i,i'} - K\delta v_{i,i'}^{NMS}}{F}, \tag{4.8}$$

95

substituting together against a data point from the other set:

$$\frac{\delta v_{i,i'}^A - K^A \delta v_{i,i'}^{A,NMS}}{F^A} = \frac{\delta v_{i,i'}^B - K^B \delta v_{i,i'}^{B,NMS}}{F^B}, \tag{4.9}$$

(where subscripts A and B indicate the isotopes shifts of the two respective transitions), multiplying each pair by a factor $\left(\frac{ii'}{i'-i}\right)$ that accounts for the different masses, and finally rearranging to solve for one of the modified shifts in terms of the other:

$$\delta v_{i,i'}^A \left(\frac{ii'}{i'-i}\right) = \frac{F^A}{F^B} \delta v_{i,i'}^B \left(\frac{ii'}{i'-i}\right) + \left(K^A \delta v_{i,i'}^{A,NMS}\left(\frac{ii'}{i'-i}\right) - \frac{F^A}{F^B} K^B \delta v_{i,i'}^{B,NMS}\left(\frac{ii'}{i'-i}\right)\right). \tag{4.10}$$

The advantage of such a method is that it produces a linear plot; by plotting $\delta v_{i,i'}^A \left(\frac{ii'}{i'-i}\right)$ against $\delta v_{i,i'}^B \left(\frac{ii'}{i'-i}\right)$, the slope and intercept are both independant of the particular choice of isotopes pairs (i, i'). One can use pairs of neighbouring isotopes or pairs of widely different masses. The resulting plot is known as a King plot. The slope yields the ratio of field shifts $\frac{F^A}{F^B}$ for the two levels. The intecept yields a relation between the mass shifts. The limitation of this method is that it does not yield absolute values for either K or F.

A slight variation is to define the modified mass shift M^A relative to a standard pair of isotopes, in this case ^{136}Xe and ^{134}Xe, by dividing by the mass shift by the factor $g(i,i') = \left(\frac{i'-i}{ii'}\right)\left(\frac{136 \times 134}{136 - 134}\right)$ such that:

$$M^A = \frac{K^A \delta v_{i,i'}^{A,NMS}}{g(i,i')} = K^A v_0 \left(\frac{m_e}{u}\right)\left(\frac{136 - 134}{136 \times 134}\right). \tag{4.11}$$

as defined by King [96]. The advantage is that the modified shifts are of similar size to the measured shifts and have dimensions of frequency. The resulting fit line simplifies to:

$$\delta v_{i,i'}^{*A} = \frac{F^A}{F^B} \delta v_{i,i'}^{*B} + \left(M^A - \frac{F^A}{F^B} M^B\right). \tag{4.12}$$

where $\delta v_{i,i'}^* = \frac{\delta v_{i,i'}}{g(i,i')}$ is the modified isotope shift.

An example of a King plot for our data is shown in Fig. 4.16. We plot our modified isotope shifts (using the second definition) against those of the two photon transition to the $2p^5$ state, measured at 249 nm by Plimmer et. al [128]. The two levels in the comparison differ only in their angular momentum J, due to different orbital angular momentum terms. Plimmer's data is from the $6p(J = 0)$ state. The slope of the resulting King plot yields $\frac{F^{249}}{F^{252}} = 1.00(.01)$, and the intercept yields $M^{249} - \frac{F^{249}}{F^{252}} M^{252} = -0.8(1.8)\,\text{MHz}$. The respective mass shifts and field shifts are equal within error. This shows to first order, both mass shift and field shift depend on quantum number n but are independant of J. Further analysis of the isotope shifts are presented below. While the fit is very good, one observed that the data point at upper right is more than 1σ off the fit line. In fact King
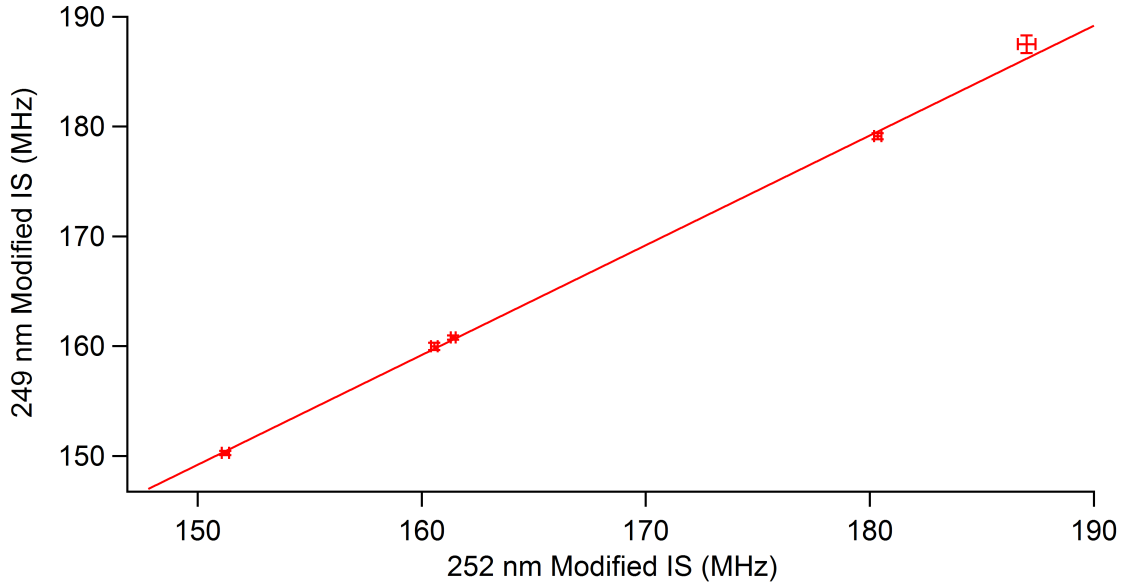
Figure 4.16: King Plot of isotope shifts for two different two-photon transitions at 252.5 nm (present work) and 249 nm (as measured by Plimmer et al. [128])

plots are linear to first order only; there is a quadratic dependence on atomic number Z, and some nuclear polarizability dependence. Recent papers [20, 65, 110] have studied the next to leading order terms which cause the nonlinearity. After these corrections are accounted for, any remaining nonlinearity could indicate new physics such as an interaction between a new light boson and the nucleus. Transitions which do not involve s-orbital electrons are especially suitable to look for new physics as both the field shift and quadratic field shift nonlinearity are typically smaller than for transitions involving s-orbital electrons. The field shift is calculated in the following section; in our case the magnitude is similar to that of certain $s - p$ transitions [53], possibly due to the effects of p electrons in screening inner s electrons [128]. The nonlinearity observed in Fig. 4.16 is likely due to measurement error. The frequencies of some atomic clock transitions are known with sub-Hz accuracy. As the accuracy of isotope shift measurements improves, these measurements can be used to constrain the search for new physics interactions.

Determining charge radii based on isotope shifts

Eq. 4.7 above indicates that the field shift is dependent in part on the nuclear charge radii. To date these values have been measured by various techniques, including by x-ray, muonic atom, and optical spectroscopy. Values of $\delta \langle r^2 \rangle_{i,i'}$ from several measurement techniques are shown in Table 4.5. We can use these values to determine directly the mass shift and field shifts. Because our data is high resolution, we can use it to compare the different literature values. We used data from three sources for $\delta \langle r^2 \rangle$: Aufmuth [14] is a nuclear data table derived from optical spectroscopy

Table 4.5: Nuclear charge radii values $\delta\langle r^2\rangle_{i,136} = \langle r^2\rangle_{136} - \langle r^2\rangle_i$ relative to ^{136}Xe, used in the calculation of absolute K and F. Some of the data has been rearranged from ladder-type pairs which entails some propagation of error. In the actual fits, our data was rearranged to match the published format, to avoid propagation of error. Also shown are our calculations for K and F for our transition based on the respective source. [14],[29],[67]

		Aufmuth[14]	Borchers[67]	Fricke[29]
$\delta\langle r^2\rangle_{i,136}$	129	0.133(30)	0.152(40)	0.220
	130	0.097(24)	0.117(40)	0.153
	131	0.115(26)	0.124(30)	0.172
	132	0.075(18)	0.0844(200)	0.115
	134	0.046(9)	0.0518(120)	0.067
K		0.54(8)	0.36(2)	0.47(16)
F (MHz fm^{-2})		2391(292)	2640(80)	1631(384)
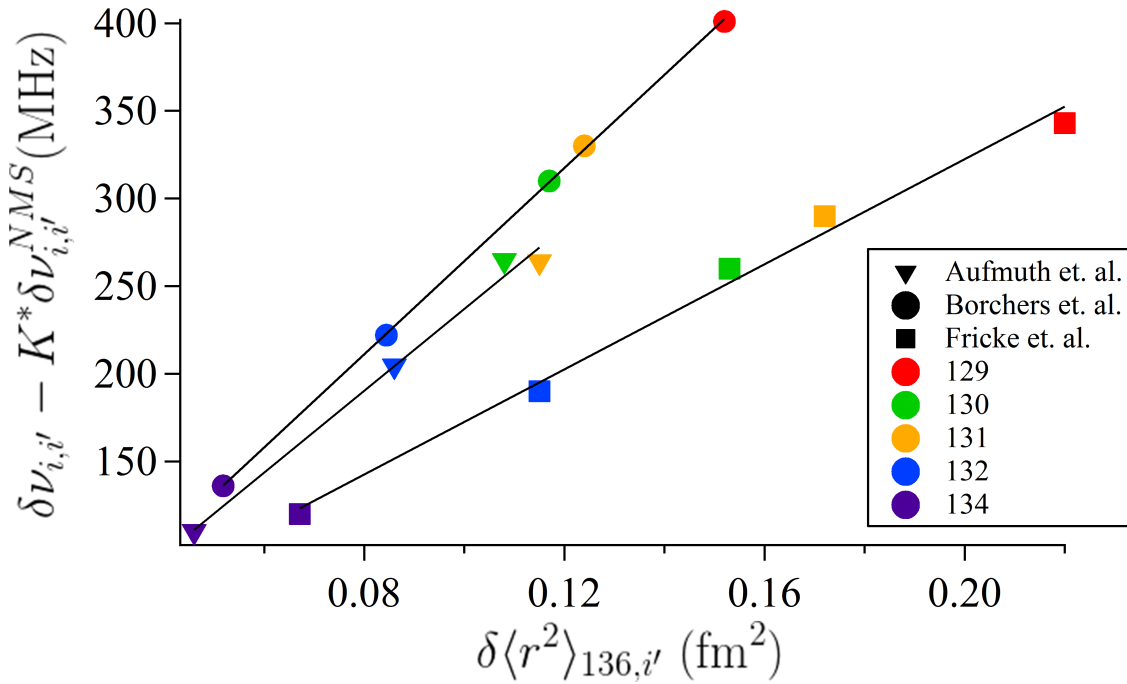
Figure 4.17: Linear fits to the calculated field shift vs. charge radii parameter $\delta\langle r^2\rangle$, plotted for each of the three data sets in Table 4.5. The field shift is determined using the respective values for mass shift parameter K to subtract off the mass shift from the total isotope shift.
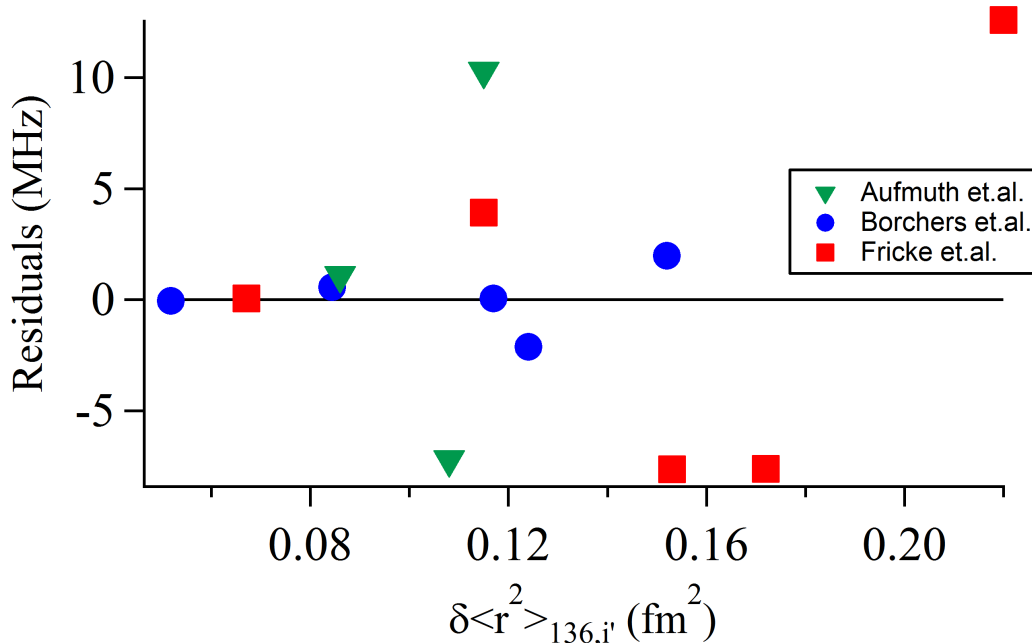
Figure 4.18: Residuals $(\Delta v_{field,calc} - \Delta v_{field,fit})$ of the fits plotted in Fig. 4.17 for field shift vs. charge radii parameter $\delta\langle r^2\rangle$. We calculate the mean squared error of these residuals to determine the goodness of fit.)

of many isotopes, with a stated uncertainty of 10%. The values for Xe come from observing the NIR discharge spectra from isotopically enriched samples. Fricke [67] publishes nuclei data for muonic atom transition energies, electron scattering, and x-ray isotope shifts. Muonic atoms have an electron replaced by a muon, yielding smaller Bohr orbits. The Xe values published here come from muonic atoms. In particular, muonic values should be viewed with some uncertainty due to the proton radius puzzle.[2] Borchers et. al. [29] published charge radii measurements in Xe based on optical detection of isotopes produced by the ISOLDE collaboration. In their analysis they make the assumption of specific mass shift equal to zero plus or minus the normal mass shift. (i.e., an uncancelled normal mass shift), allowing them to directly estimate $\delta\langle r^2\rangle$.

The charge radii results of all three sources are listed in Table 4.5, along with our calculated values for K and F resulting from a fit to the published $\delta\langle r^2\rangle_{i,i'}$. Charge radii data in the table are shown as differences relative to ^{136}Xe. Both Borchers and Fricke present data in that format. In the case of Aufmuth, data were tabulated as differences in charge radii for closest neighbouring isotopes with corresponding uncertainty. To avoid propagation of errors, our isotope shift data was rearranged to match that particular dataset, rather than rearrange the published data. Using the

---

[2]Measurements of the proton radius from laser spectroscopy on muonic hydrogen [129] yield a precise value for the proton radius that disagrees with the previous accepted value by almost five standard deviations.

data reported by Borchers et. al [29] yields the fit with the smallest uncertainties and the values $K = 0.36(2)$ and $F = 2640(80)\,\mathrm{MHz\,fm^{-2}}$.

A clearer comparison was facilitated by subtracting off the mass shift from the isotope shift, using the respective fit parameters for K. This leaves only the field shift term which is linear in $\delta\langle r^2 \rangle$. We performed a linear fit of field shift vs. $\delta\langle r^2 \rangle$ as shown in Fig. 4.17, and calculated the mean squared error (MSE) of the residuals shown in Fig. 4.18:

$$MSE = \frac{1}{n}\sum_i^n (\Delta\nu_{field,calc} - \Delta\nu_{field,fit})^2 \tag{4.13}$$

We calculate the MSE values $1.7\,\mathrm{MHz^2}$ for Borchers' data, and $38.8\,\mathrm{MHz^2}$ and $57.9\,\mathrm{MHz^2}$ for Aufmuths' and Fricke's data, respectively. The much smaller error on Borchers data indicates that our observed isotope shifts are consistent with Borchers' values of $\delta\langle r^2 \rangle$. We find similar agreement with Borchers' data for the isotope shifts measured by Plimmer et. al [128] for two-photon excitation to the nearby $5p^5(^2P_{3/2})6p\,^2[1/2]_0$ state. The most recent data tables [10] cite Borchers' data.

4.2.8   Comparison of signal amplitude and natural abundance

The peak height we observe in the LIF signal is proportional to the transition probability, which depends among other parameters on both the number density and transition dipole moment. For these experiments we used natural abundance Xe, so we expect the signal for each isotope to be proportional to its respective natural abundance. These are listed in Table 4.6, where the observed signals have been normalized to the largest peak ^{132}Xe. For the odd isotopes ^{129}Xe and ^{131}Xe, we sum the amplitude of the two or four hyperfine peaks, respectively. We find agreement between the peak heights and natural abundance to within 4%.

Table 4.6: Observed peak heights and natural abundance for each isotope relative to ^{132}Xe.

	Peak height (relative to 132)	Natural Abundance (relative to 132)
^{129}Xe (sum of 2 peaks)	0.94	0.98
^{130}Xe	0.16	0.15
^{131}Xe (sum of 4 peaks)	0.82	0.79
^{132}Xe	1	1
^{134}Xe	0.41	0.39
^{136}Xe	0.35	0.33
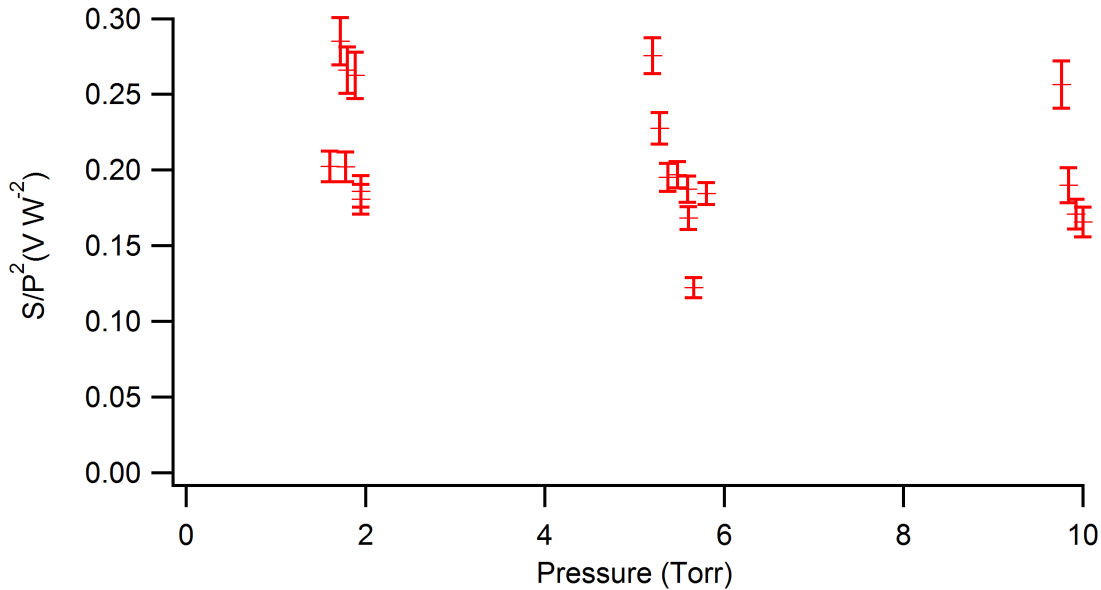
Figure 4.19: Signal S (at resonant frequency) normalized to power P squared for a mixture of natural abundance Xe and 1 Torr O_2, as a function of total pressure.

Signal amplitude pressure dependence

The number density of xenon in the cell n, under the ideal gas law, is proportional to the Xe partial pressure. The lineshape parameter $g(\omega)$ discussed in Section 2.3.2 is inversely proportional to the linewidth $\Delta\omega$. Under a certain range of pressures the lineshape will be dominated by collisional broadening (pressure broadening), for which the linewidth will be linearly proportional to the total pressure. Under those conditions, a sample of pure Xe would have a two-photon transition rate that is independent of pressure, emitting a constant LIF signal at any pressure. The same does not hold for a fixed partial pressure of Xe collisionally broadened by other gases, or for a linewidth determined by another broadening regime.

To demonstrate this pressure independence we collected data at 1, 5 and 10 Torr for Xe and O_2 mixtures, shown in Fig. 4.20 and Fig. 4.19. The fixed O_2 data shows that the signal is approximately constant. The data for the 50-50 mixture is less convincing, suggesting a calibration error; however, it is at least apparent that the signal does not decrease with pressure, as might be expected due to the decrease in n_{Xe}.

Horiguchi et al [83] reports a lifetime of 38 ± 2 ns for the $5p^5(^2P_{3/2})6p\,^2[3/2]_2$ level, which suggests a natural linewidth of 4 MHz . In that case we can reduce the pressure to about 130 mTorr and see the same signal; beyond this we expect the signal to decrease linearly with pressure.
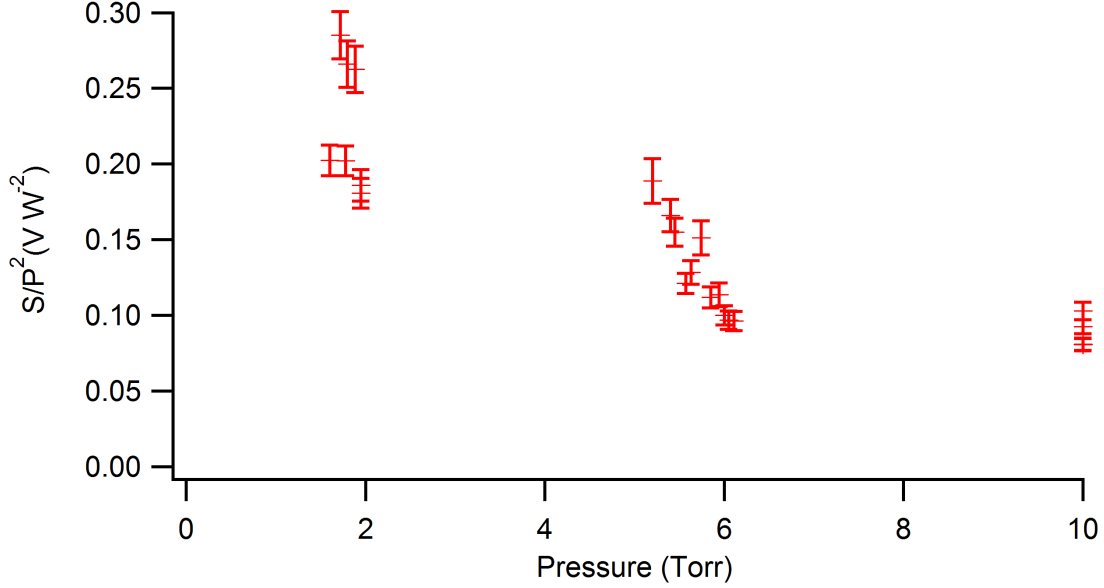
Figure 4.20: Signal S (at resonant frequency) normalized to power P squared for a 50-50 mixture of natural abundance Xe and O_2

4.2.9 Determination of two-photon transition probability from LIF signal

Based on the observed LIF signal intensity, we calculate the transition probability for two-photon absorption.

Derivation of transition rate

Excitation of two photon transitions occurs along the UV beam axis, with the largest transition rate at the beam waist. As a starting point, we approximate our excitation region as a long cylindrical volume V with beam waist w_o and Rayleigh range z_R. Taking into account the spatial variation of the UV beam profile, Equations 2.46 and 2.48 give the total number of excitations N per second in volume V for Doppler-free excitation as:

$$\left(\frac{dN}{dt}\right)_{tot} = 6\alpha g(\omega)n \int I(r,z)^2 dV \tag{4.14}$$

One should distinguish between the total transition rate, at the detected photon rate at the APD. Assuming isotropic emission of one NIR photon for every two-photon absorption, and neglecting nonradiative decay, the detected photon count rate is:

$$\left(\frac{dN}{dt}\right)_{det} = 6\alpha g(\omega)n \int I(r,z)^2 A_{det}(r,z)dV, \tag{4.15}$$
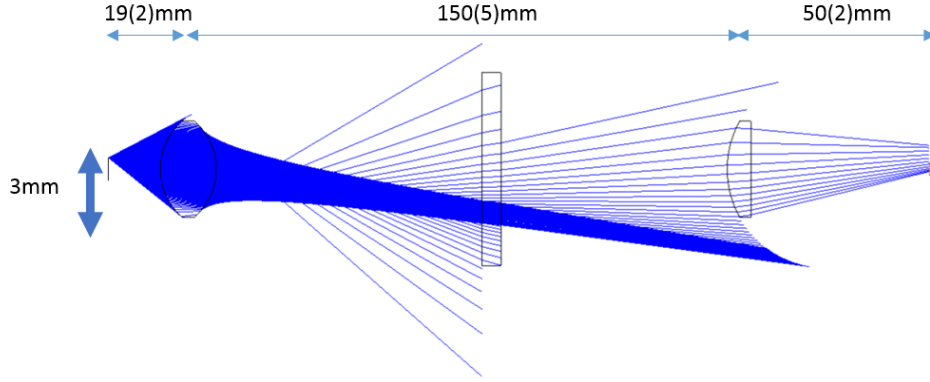
Figure 4.21: Zeemax simulation showing the path of rays from a point 3mm from the UV focus, to illustrate the vignetting. The detection configuration is strongly sensitive to emission less than 1 mm from the UV beam focus.

where A_{det} is the dimensionless acceptance fraction of the APD. This integral can be evaluated explicitly. Since the beam waist is over an order of magnitude smaller than the sensitive radius of the detector acceptance, we integrate over $r = (0, \infty)$ and approximate the acceptance to be constant over the beam radius such that $A_{det}(r, z) \approx A_{det}(z)$ is a function of z only. The integral becomes:

$$\int I^2(r,z) A_{det}(r,z) dV = \int I_0^2 (\frac{w_0}{w(z)})^4 (\frac{\pi w^2(z)}{4}) A(z) dz \tag{4.16}$$

Where I_0 is the (circulating) laser intensity at the beam waist. The beam radius $w(z)$ only increases by $\sqrt{2}$ along the Rayleigh range. For integration of length $l \ll z_R$ along the beam axis, we can approximate $w(z) \approx w_0$ to get:

$$\int I^2(r,z) A_{det}(r,z) dV = \frac{P_0^2}{\pi w_0^2} \int A_{det}(z) dz = \frac{P_0^2}{\pi w_0^2} A_{avg} l \tag{4.17}$$

where P_0 is the light power and A_{avg} is the acceptance fraction averaged over length l. Estimation of the acceptance fraction by a ray tracing simulation is shown in the following section.

Detector acceptance

Detection in these experiments was by an avalanche photodiode (APD) transverse to the UV beam axis as shown in Fig. 4.10 and described in Section 4.2.3. Two convex lenses were used to collect the light: one to collimate the (assumed) isotropic emission through the vacuum box exit window, and another to focus the now-collimated light onto the APD. Due to this configuration, it is clear that the APD is most sensitive to emission from the focal point. Therefore detection of LIF is limited
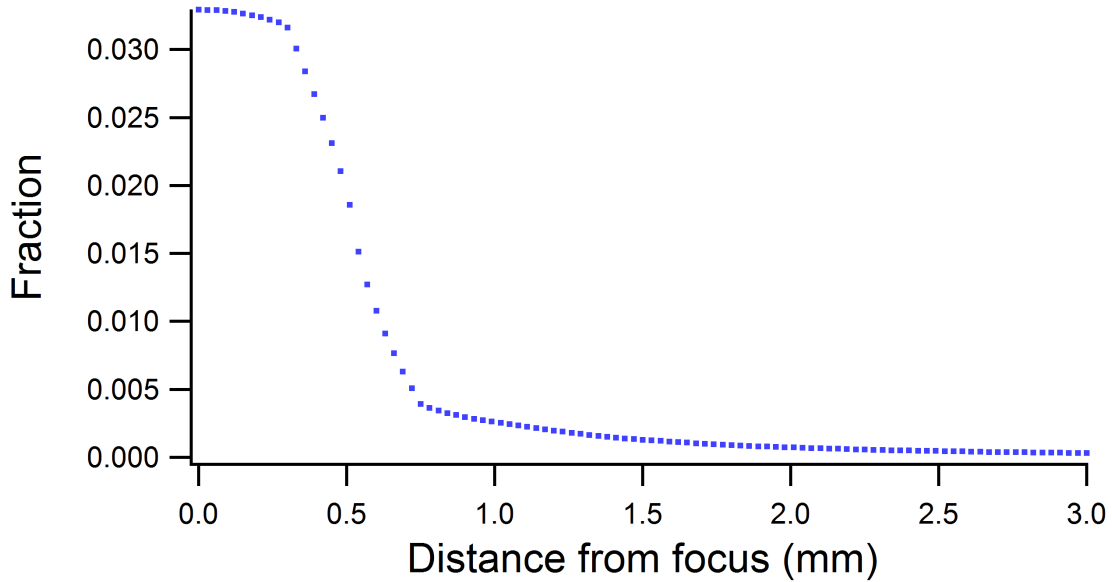
Figure 4.22: Vignetting fraction (over 4π) of rays emitted isotropically from a point on the beam axis. The detection configuration is most sensitive to fluorescence emitted within 1 mm from the UV beam focus.

to emission near the beam waist, and not along the whole Raleigh range as initially assumed. In addition, the lenses are sufficiently thick that the thin lens approximation does not hold.

We used ray tracing software Zeemax OpticStudio to simulate the propagation of light through the detection optics. The UV beam axis defines the object plane, and the APD detector defines the image plane. Rays of LIF emission produced within 3 mm of the UV focus are traced through lenses and windows, to the APD, as shown in Fig. 4.21. The simulation shows that the chromatic dispersion for 823 nm vs. 895 nm emission is negligible. The vignetting feature is used to measure the fraction of rays that reach the APD window in the image plane, assuming isotropic emission, in contrast to rays that are vignetted by the physical edges of the detection optics and the box. We find that 3.3% of the rays emitted from the focus into 4π reach the detector. The acceptance rapidly drops for points more than $z = 1$ mm from the focus as shown in Fig. 4.22. In contrast, the UV beam in these experiments had a waist $w_0 = .064$ mm and $z_R = 51$ mm. Thus the detected LIF is a small fraction of the total emission.

We averaged the simulation results for points on the UV beam axis up to ± 2 mm from the focus, finding an average collection fraction of $A_{avg} = 0.010(2)$.

Photon count rate and transition probability

In the section above we showed that detection of LIF is limited to emission which occurs within ± 2 mm of the UV beam waist. The excitation region used for the following calculations is a cylinder

104

Table 4.7: Experimental values used in the determination of two photon α for the isotope ^{132}Xe

Signal (V)	S	-0.0247(5)
FWHM (Hz)	$\Gamma_L/2\pi$	$55.8(6)\times10^6$
Lineshape (s)	$g(0)$	$2.42(2)\times10^{-9}$
Circulating Power (W)	P_0	0.228(11)
Beam Waist(m)	w_0	0.0000640(3)
Total pressure (Torr)	P_{tot}	1.61(4)
^{132}Xe Partial Pressure(Torr)	$P_{^{129}\text{Xe}}$	0.216(5)
^{132}Xe Number Density (m^{-3})	$n_{^{129}\text{Xe}}$	$6.97(16)\times10^{21}$
Branching Ratio	F_{823}	0.7
	F_{895}	0.3
Photon Energy (J)	E_{823}	2.41×10^{-19}
	E_{895}	2.22×10^{-19}
APD Sensitivity (V/W)	Q_{823}	-1.5×10^8
	Q_{895}	-1.2×10^8
Peak Detector Acceptance	$A(0)$	0.033
Volume-integrated Intensity (W^{2}m^{-1})	$\int I^2(r,z)A(r,z)dV$	164.09
Detector Acceptance, averaged over l = 4mm	A_{avg}	0.010(2)
Excitation length (m)	l	0.004
Two-photon coefficient (cm^4/J^2)	α	4.5(1.1)

with beam waist w_0 and length 4 mm, centered at the beam waist. Our detector is sensitive to $6p-6s$ fluorescence at both wavelengths 823 nm and 895 nm. The observed APD signal voltage S is:

$$S(V) = \left(\frac{dN}{dt}\right)_{det}(E_{823}Q_{823}F_{823} + E_{895}Q_{895}F_{895}) \tag{4.18}$$

where E_{895} is the photon energy in J, Q_{895} is the detector sensitivity in V/W, and F_{895} is the fluorescence branching fraction from the upper level. From [83] we find the branching fractions $F_{895} = 0.30$ and $F_{823} = 0.70$. Solving for excitation rate, we find:

$$\left(\frac{dN}{dt}\right)_{det} = \frac{S}{(E_{823}Q_{823}F_{823} + E_{895}Q_{895}F_{895})} \tag{4.19}$$

From Equation 4.19, our ^{132}Xe peak signal corresponds to a photon count rate 7.4×10^8 photons s^{-1} at the APD, and an estimated total emission of 10^{10} photons s^{-1} in the excitation region near the UV beam waist.

Comparing Equations 4.19 and 4.15, we can use the observed photon count rate to solve for α by the following substitution:

$$\alpha = \frac{1}{6G(\omega)n(E_{823}Q_{823}F_{823} + E_{895}Q_{895}F_{895})}\frac{S}{\int I^2(r,z)A_{det}(r,z)dV} \tag{4.20}$$

Table 4.7 lists the relevant parameters for the largest isotope LIF peak, that of ^{132}Xe. Based on these values we calculate $\alpha = 4.5(1.1)\,\text{cm}^4\text{J}^{-2}$. This finds agreement with the result $\alpha = 4.5(2)\,\text{cm}^4\text{J}^{-2}$ reported by Raymond et al [138].

4.3 Estimate of Magnetometer Sensitivity

4.3.1 Mercury Comagnetometer uncertainty

Comagnetometry performed in the ILL nEDM experiment determined the ^{199}Hg precession frequency by fitting to an exponentially decaying modulation of optical transmission. The accuracy of the magnetometer depends in part on the signal to noise ratio (SNR) achieved in the ^{199}Hg spectroscopy. The uncertainty in precession frequency is parametrized as follows [75]:

$$\sigma_f \approx \frac{1}{4T'} \frac{a_n}{a_s} \frac{1}{\sqrt{n}} (1 + e^{2T'/\tau})^{1/2} \tag{4.21}$$

Here a_n is the RMS noise in the ring-down signal (decaying sinusoid), a_s is the signal amplitude at the start of precession, n is the number of points fit, T' is the precession time and τ is the decay time. The fraction $\frac{a_s}{a_n}$ is the RMS signal to noise ratio. This frequency fitting uncertainty translates to a field uncertainty σ_B according to

$$2\pi\sigma_f = \gamma\sigma_B. \tag{4.22}$$

The typical performance of the magnetometer in the 1 μT field had an uncertainty of $\sigma_B \approx 50$ fT, or 50 ppb [75].

4.3.2 Sensitivity estimate based on Xe two photon SNR

Based on our current signal to noise ratio, we can extrapolate our current results to estimate an effective magnetometer sensitivity using Equation 4.21, with a_s/a_n determined from the (modulated) LIF signal following two photon excitation. We focus here on estimation of the signal size at low pressure, such as is required to avoid dielectric breakdown under the high voltage conditions of the nEDM experiment. We consider the following:

1. partial pressure of isopure vs. natural abundance Xe: other isotopes contribute to pressure broadening and a lineshape-related loss in signal.

2. partial pressure of O_2: it is expected that without a buildup cavity in vacuum, O_2 will not be necessary.

3. polarization of ^{129}Xe: 50% polarization has been demonstrated by commercial SEOP polarizers.

Table 4.8: Extrapolation of magnetometer uncertainty at low Xe pressure. Calculated using Equation 4.21 with $T' = 150$ s, $n = 1500$, $\tau = 160$ s. We consider the following cases: (i) Current experimental conditions, with 1.6 Torr of mixed 50-50 Xe (nat. abund.) and O_2, (ii) 1.6 Torr isopure ^{129}Xe. (iii-vi) 10 mTorr isopure Xe at current laser power (iii) and maximum achievable to date (iv), 1mTorr isopure Xe at current laser power (v) and maximum achievable to date(vi)

Case	Detector	P_{tot} (Torr)	P_{laser} (W)	a_s (V)	a_n (V)	SNR	σ_f (μHz)	σ_B (fT)
(i)	APD	1.6	0.228	0.00531	0.0021	2.5	46.7	3965
(ii)	APD	1.6	0.228	0.040846	0.0021	19.5	6.07	515
(iii)	PMT	0.01	0.228	4.54×10^{-6}	0.00000005	90.8	1.3	110
(iv)	PMT	0.01	0.4	1.4×10^{-5}	0.00000005	279	0.42	36
(v)	PMT	0.001	0.228	4.54×10^{-7}	0.00000005	9.1	13	1105
(vi)	PMT	0.001	0.4	1.4×10^{-6}	0.00000005	27.9	4.22	359

4. detector: detection of weak LIF signals requires a detector with high SNR.

TRIUMF has a stated goal in the 2015 CDR of 30fT uncertainty per cycle.[1]

We evaluate a few cases in Table 4.8. Based on our current LIF signals, we anticipate 6 μHz (500 fT) uncertainty for 1.6 Torr of isopure ^{129}Xe, assuming a polarization of 50%. Extrapolating to 1 mTorr, the signal decreases due to a change of broadening regime: the lineshape factor $g(\omega)$ reaches its maximum, while number density continues to decrease. It may be possible to mitigate the loss by increasing the laser intensity, and replacing the APD with a low-noise cooled PMT, which can have orders of magnitude better SNR when cooled, and a low noise current preamp. We estimate $\sigma_B = 36$ fT may be attainable at 10 mTorr pressure for a 400 mW laser power.

4.4 Discussion

In this section we described the observation of LIF signals from two-photon transitions in Xe using both a broadband pulsed laser and narrow linewidth CW laser. Using the pulsed laser, we investigated all two-photon allowed transitions to the $6p$ level, namely, to $^2[1/2]_0$, $^2[3/2]_2$, and $^2[5/2]_2$ states, and measured the LIF wavelengths. While the pulsed laser linewidth is too broad to perform optical pumping, we did demonstrate the selection rules which forbid excitation to $^2[1/2]_0$ by circular polarized light. We compared LIF emission on- and off-axis and measured the threshold for bidirectional emission.

We performed high-resolution spectroscopy with the CW laser and successfully measured hyperfine constants of the $5p^5(^2P_{3/2})6p\,^2[3/2]_2$ level and isotope shifts for the $5p^5(^2P_{3/2})6p\,^2[3/2]_2 \leftarrow 5p^6\,(^1S_0)$ transition at 252.5 nm. The uncertainties in the isotope shifts are small enough to assign mass shift and field shift parameters with uncertainty of only a few percent. We compare our isotope shifts to measured charge radii values reported in the literature and verify the values reported by Borchers

et al. We calculate the two-photon absorption coefficient (i.e. cross-section) for the 252.5 nm transition and find agreement with literature. We find some evidence that LIF signal is constant down to 1.6 Torr based on the pressure broadened absorption lineshape, and predict a continuation of this trend with decreasing pressure down to the natural linewidth at 130 mTorr. Pressure broadening measurements at lower Xe pressure are currently underway in this lab. Finally, we extrapolate the observed signal to low pressures to estimate the SNR of polarized ^{129}Xe for comagnetometry, and estimate the acheivable magnetic field measurement uncertainty. We predict detection with 36 fT sensitivity is possible using very low-noise PMTs.

Chapter 5

Conclusions

5.1 Conclusion

This chapter outlines work done to date and the current status of experiments working towards polarization of ^{129}Xe and high resolution spectroscopy at low pressures. This is an exploratory work investigating experimental parameters necessary for the implementation of ^{129}Xe as a comagnetometer in the neuton EDM experiment at TRIUMF's ultra cold neutron facility, which is the motivation described in Chapters 1 and 2. We outlined the nEDM measurement technique and the properties of ^{129}Xe which make it a suitable magnetometer candidate. Chapter 2 outlined a scheme comprising hyperpolarization of ^{129}Xe through spin exchange optical pumping, purification through freezeout, and detection of the polarization by two-photon transition using circular polarized light. Transitions to excited states $^2[3/2]_2(F = 3/2)$ and $^2[5/2]_2(F = 3/2)$ were identified as having suitable selection rules to facilitate polarization detection.

A review of spin exchange optical pumping literature shows that many of the factors governing the production and relaxation of hyperpolarized noble gases have been identified and suitably controlled. This has lead to near-unity polarizations and relaxation lifetimes of many hours, especially in the solid state. Chapter 3 covers the development of SEOP capabilities in our lab at UBC, motivated by the need to have a source of polarized ^{129}Xe to measure changes in the two-photon transition spectra. Using a broadband diode laser, we demonstrated SEOP by detecting Adiabatic Fast Passage NMR signals from polarized ^{129}Xe samples. We observed that high SEOP cell temperatures and pressures correspond with higher polarization. We compared batch mode operation with continuous flow operation, finding the highest polarization for 10 min batch mode preparation. We calibrated our ^{129}Xe AFP signals against those of a H_2O sample and find $P_{Xe} = 5.5\%$ based on the relative signals. In comparison with the literature, we find that higher polarization can be achieved using frequency-narrowed pump lasers.

Chapter 4 described measurements on the properties of two-photon transitions to $6p$ states

$^2[1/2]_0$, $^2[3/2]_2$ and $^2[5/2]_2$. We measured LIF signals with a pulsed laser and verified the two-photon selection rules prohibiting excitation to the $6p^2[1/2]_0$ state by circular polarized light. We also made qualitative measurements of the on-axis LIF enhancement by bidirectional emission. This was followed by high-resolution CW laser spectroscopy. We generated CW UV light at 252.5 nm, using an OPSL and nonlinear doubling, to excite Xe to the $6p^2[3/2]_2$ state inside a vacuum chamber at 1.6 Torr total pressure. The hyperfine constants and isotope shift we found improve the precision of these measurements over previous literature values. The high resolution permits selective excitation of the transition to the $^2[3/2]_2(F = 3/2)$ hyperfine level. Therefore this transition can be used as a probe of optical pumping with no background from excitation of even isotopes, or even of the $^2[3/2]_2(F = 5/2)$ state. We measured $\alpha = 4.5(1.1)\,\mathrm{cm}^4\mathrm{J}^{-2}$ for the two-photon coefficient, in good agreement with literature. Based on observed signals, we extrapolated to low pressures to predict $\sigma_B = 36\,\mathrm{fT}$ magnetometer uncertainty at 10 mTorr.

5.2 Future Work

5.2.1 Improvement of ^{129}Xe Polarization and Freezeout

The polarization of ^{129}Xe affects the visibility of the Larmor precession, and therefore directly affects the signal to noise ratio used to determine the magnetometer uncertainty. For this reason, the polarization should be made as high as possible. Values over $P_{\mathrm{Xe}} = 90\%$ have been reported in the literature using frequency narrowed lasers. There is a tradeoff between high-volume and high-polarization production. For the purposes of nEDM measurements at TRIUMF, the ^{129}Xe consumption can be loosely estimated as:

$$(0.001\,\mathrm{Torr}) \left(\frac{2.59 \times 10^{19}\,\mathrm{atoms\,cm}^{-3}}{760\,\mathrm{Torr}} \right) \left(20 \times 10^3\,\mathrm{cm}^3\mathrm{cell}\right) \left(\frac{24\,\mathrm{hr/day}}{4\,\mathrm{min/cycle}} \right) \tag{5.1}$$

which yields 2×10^{20} atoms/day, or less than 10 mL at STP. The amount used by the experiment will be likely small compared to amounts lost through the filling and thawing process. These volume requirements are small enough to be satisfied by methods that favour high polarization production, typically in batch mode operation. The T_1 lifetimes for ^{129}Xe in the solid state are such that the SEOP polarizer should be operated several times per day. Per experimental cycle, a controlled pressure of the gas can be released by slightly warming solid Xe in a cold trap. Continued work on freezeout at UBC is necessary to perform two-photon spectroscopy on polarized ^{129}Xe free from the pressure broadening effects of the mixed He and N_2.

5.2.2 Towards optical polarization detection at low pressure

Optical polarization detection for comagnetometry requires polarized ^{129}Xe and low-pressure spectroscopy. In this thesis we performed high-resolution Xe spectroscopy at 1.6 Torr total pressure driving two-photon transitions with approximately 200 mW of UV light in an optical cavity. Experiments are currently underway to measure the pressure dependence of the two-photon absorption and LIF signal down to a few tens of mTorr. This will be accomplished by replacing the vacuum chamber and optical cavity with a short gas cell and retroreflection mirror. An increase in laser power and tighter UV focus can be used to compensate for the loss of the optical cavity. Removal of the cavity removes the need for a partial pressure of O_2, as transmission loss at the windows is not compounded by multiple reflections. Additionally, the gas cell and lines can be baked while pumping to reduce the offgassing rate which was previously 0.01 Torr/min. We will test the prediction from Section 4.2.8 that as the pressure-broadened linewidth is reduced, down to the limit established by the excited state lifetime, the excitation rate remains constant.

Freezeout of polarized ^{129}Xe is necessary to perform optical detection at low pressure with sufficient signal to noise ratio. The SEOP gas mixture is only 1% Xe by volume. As noted above, the buffer gas He and N_2 must be removed to prevent pressure broadening of the linewidth and a corresponding 100x reduction in LIF signal. It is necessary also to preserve the polarization during freezeout. The currently observed LIF signal corresponds to unpolarized ^{129}Xe with cross section given by the two photon coefficient α. For polarized ^{129}Xe, there is an effective increase $(1 + P_{Xe}) \alpha$ in the two photon absorption coefficient, which linearly affects the LIF signal. Detection of a change in the LIF signal upon polarization is a current priority. This requires performing spectroscopy on the atoms while under magnetic field, and in part motivates the replacement of the vacuum chamber, and its magnetic parts, with a glass vapour cell.

At pressures below 130 mTorr the LIF signal is expected to decrease linearly with pressure/number density. The enhancement of bidirectional emission observed in pulsed experiments could potentially compensate for this decrease in signal. This has been proposed as a way to achieve the maximum sensitivity to the two-photon transition rate. Ongoing experiments will compare the LIF emission detected on- and off-axis of the UV excitation, and determine if the same phenomena is observed for excitation with CW light. The estimated threshold at 5 mTorr, 10^8 W/cm^2, is several orders of magnitude larger than the CW intensity used in the current experiments. However, even if enhancement from bidirectional emission is not observed, on-axis detection is still anticipated to yield larger LIF signals, as an on-axis detector can collect emission from along the entire Rayleigh range and not only at the beam waist.

5.2.3 Determination of absolute two-photon transition frequencies

Experiments in Chapter 4 used a self-referenced frequency comb. The absolute frequency resolution attainable by the frequency comb could potentially allow us to set a new reference standard for the

absolute energies of excited Xe electronic states. The NIST reported value of the absolute transition frequency for $5p^5(^2P_{3/2})6p\,^2[3/2]_2 \leftarrow 5p^6\,(^1S_0)$ is 79 212.465 cm^{-1} or 2 374 729. 958 GHz, with an absolute uncertainty of 0.0035 cm^{-1} or 100 MHz[147]. The values cited were determined by taking values from [85] which measured excited state transitions in ^{136}Xe, and applying a shift of about 0.5 cm^{-1} to match the absolute frequencies found by [33] for certain VUV transitions to $5d$, $8d$, and $7s$. These absolute frequencies had been calibrated by scanning the excitation laser through nearby iodine resonance lines and counting the number of interferometric fringes produced by a reference etalon while scanning. Using our technique one could set a reference standard traceable to a GPS reference oscillator.

Using the frequency comb described in A.3, we measured the isotope weighted average for the absolute transition frequency to be 2374730. 490 GHz. This is 0.532 GHz higher than the NIST reported value. Factors affecting the uncertainty of this measurement are as follows: (i) frequent loss of connection with the 10 MHz GPS reference oscillator (which has since been resolved), and (ii) drift in the unlocked comb offset frequency due to technical limitations (namely, the lack of an additional branch to simultaneous lock the comb offset and obtain our beat note). If both these limitations are overcome, the frequency comb method can provide an accurate measure of the absolute transition frequency with sub-MHz precision. While this is of great theoretical interest, current measurements of the transition frequency are sufficient for neutron EDM experiments. In particular, it is the uncertainty in precession frequency which determines magnetometer accuracy, rather than the uncertainty in absolute transition frequency.

5.2.4   Measurement of Xenon Electric Dipole Moment

Xenon can only be used as a comagnetometer if its own permanent electric dipole moment is known to high accuracy, and is substantially smaller than that of the neutron. From equation 2.1 we observed that the uncertainty of the nEDM measurement d_n is limited by the uncertainty in the EDM of the comagnetometer species, e.g. d_{Xe}. Additionally, since the origin of an EDM in Xe has a different theoretical basis than that of the neutron (i.e, the Xe EDM may originate from the electron EDM, or also from T- and P-violating electron-nucleon or pion-nucleon interactions), the search for a Xe EDM is complementary to the nEDM experiments [47]. Development work on ^{129}Xe comagnetometry using two-photon transitions simultaneously offers new tools to be used in the search for the ^{129}Xe EDM.

Vold et al. [160] measured the ^{129}Xe EDM in a Rb-Xe mix, using SEOP on a stack of three cells under applied $\vec{B}$ and $\vec{E}$ fields. They optically pumped in an applied 10 mG field followed by free spin precession in a 0.1 mG transverse field. Pumping and detection were both performed using Rb D1 light at 795nm. While ^{129}Xe precesses, the Rb polarization maintains a large polarization component parallel to the pump light, due to the effect of optical pumping. This component is driven with a controlled oscillation, and becomes sensitive to the ^{129}Xe precession which is detected using

a lock-in amplifier. The measured EDM was $(-0.3 \pm 1.1) \times 10^{-26}\,\mathrm{e \cdot cm}$.

Rosenberry and Chupp [48, 142] measured the ^{129}Xe EDM with ^{3}He added as a comagnetometer. Their apparatus implemented a spin-maser configuration with separate pumping and maser cells. In the pumping cell, both noble gas species were spin polarized through collisions with Rb optically pumped at the D1 line. N_2 buffer gas was used to prevent radiation trapping. Polarized atoms diffuse down to the maser cell where precession is monitored by a separate pickup coil for each gas. The pickup coil forms part of a resonant tank circuit, which uses feedback on the spontaneous relaxation to drive Rabi oscillations. The ^{129}Xe signal in one coil is mixed down with a reference frequency standard using phase-sensitive detection and used to lock the ^{129}Xe precession frequency by active correction of the static B field. This also maps any $\vec{E}$-correlated frequency shifts onto the ^{3}He precession frequency where they can be detected. They report $(-0.7 \pm 3.3(\mathrm{stat}) \pm 0.1(\mathrm{syst}) \times 10^{-26}\,\mathrm{e \cdot cm}$ for the Xe EDM limit.

Other ^{129}Xe EDM experiments are underway. Asahi et al [12, 87, 169] optically probe the steady state precession of ^{129}Xe in a single maser cell containing Rb using D1 light, and generate a feedback magnetic field which locks the precession frequency. Kuchler et al [101] measure the simultaneous free spin precession of polarized ^{129}Xe and ^{3}He using SQUID detection to measure the magnetization of the precessing nuclei. In this experiment, ^{3}He is used as a comagnetometer to account for static field drifts. They measure precession for over 4000 s, with relaxation lifetimes in excess of 2500 s, and predict $10^{-28}\,\mathrm{e \cdot cm}$ sensitivity per cycle to the ^{129}Xe EDM.

Direct optical detection of the two-photon transition can be performed without disrupting the spin ensemble significantly. For example, the current two photon excitation rate in the cell is only $10^{10}\,\mathrm{s}^{-1}$. In contrast, using spin exchange with Rb for detection introduces additional relaxation which can shorten the free precession lifetime. The ability to record spin precession without introducing additional relaxation processes or the cryogenics and electronics requirements of SQUIDs make two-photon detection a potentially useful tool in ^{129}Xe EDM searches.

Bibliography

[1] T. Adachi et al. International UCN source and nEDM experiment at TRIUMF conceptual design report 2015. *Japan-Canada UCN Collaboration*, 2015. → pages v, 86, 107

[2] S. Afach, G. Ban, G. Bison, K. Bodek, Z. Chowdhuri, Z. Grujić, L. Hayen, V. Hélaine, M. Kasprzak, K. Kirch, et al. Highly stable atomic vector magnetometer based on free spin precession. *Optics Express*, 23(17):22108–22115, 2015. → pages 130

[3] S. Ahmed et al. Conceptual design report for the next generation UCN source at TRIUMF. *The TUCAN Collaboration*, 2018. → pages v, 4, 6

[4] E. A. Alden, S. M. Degenkolb, T. E. Chupp, and A. E. Leanhardt. Prospects for two-photon optical magnetometry. In *APS Division of Atomic, Molecular and Optical Physics Meeting Abstracts*, May 2011. → pages v

[5] V. Alekseev, P. Van der Burgt, and D. Setser. Stimulated directional emission induced by two-photon excitation of the xe 6 p and xe 7 p states. *The Journal of Chemical Physics*, 146 (9):094304, 2017. → pages 78

[6] I. Altarev, Y. V. Borisov, A. Brandin, A. Egorov, V. Ezhov, S. Ivanov, V. Lobashov, V. Nazarenko, G. Porsev, V. Ryabov, et al. A search for the electric dipole moment of the neutron using ultracold neutrons. *Nuclear Physics A*, 341(2):269–283, 1980. → pages 6

[7] E. Altiere. *The adventures of Nikita and Casper: high power ultraviolet lasers for precision spectroscopy*. PhD thesis, University of British Columbia, 2014. → pages xvi, 82, 83

[8] E. Altiere, E. R. Miller, T. Hayamizu, D. J. Jones, K. W. Madison, and T. Momose. High-resolution two-photon spectroscopy of a $5p^56p \leftarrow 5p^6$ transition of xenon. *Physical Review A*, 97(1):012507, 2018. → pages vi, 75

[9] V. Anastassopoulos, S. Andrianov, R. Baartman, S. Baessler, M. Bai, J. Benante, M. Berz, M. Blaskiewicz, T. Bowcock, K. Brown, et al. A storage ring experiment to detect a proton electric dipole moment. *Review of Scientific Instruments*, 87(11):115116, 2016. → pages 5

[10] I. Angeli and K. Marinova. Table of experimental nuclear ground state charge radii: An update. *Atomic Data and Nuclear Data Tables*, 99(1):69–95, 2013. → pages 100

[11] B. Anger, G. Schrank, A. Schoeck, K. Butler, M. Solum, R. Pugmire, and B. Saam. Gas-phase spin relaxation of Xe 129. *Physical Review A*, 78(4):043406, 2008. → pages 25

[12] K. Asahi, T. Furukawa, T. Inoue, A. Yoshimi, T. Nanao, M. Chikamori, K. Suzuki, M. Tsuchiya, H. Hayashi, M. Uchida, et al. Search for an electric dipole moment in ^{129}Xe atom with nuclear spin oscillator technique. In *Journal of Physics: Conference Series*, volume 302, page 012039. IOP Publishing, 2011. → pages 113

[13] B. Aubert, D. Boutigny, J.-M. Gaillard, A. Hicheur, Y. Karyotakis, J. Lees, P. Robbe, V. Tisserand, A. Palano, G. Chen, et al. Observation of CP violation in the B^0 meson system. *Physical Review Letters*, 87(9):091801, 2001. → pages 3

[14] P. Aufmuth, K. Heilig, and A. Steudel. Changes in mean-square nuclear charge radii from optical isotope shifts. *Atomic Data and Nuclear Data Tables*, 37(3):455–490, 1987. → pages xi, 93, 97, 98

[15] C. Baker, D. Doyle, P. Geltenbort, K. Green, M. Van der Grinten, P. Harris, P. Iaydjiev, S. Ivanov, D. May, J. Pendlebury, et al. Improved experimental limit on the electric dipole moment of the neutron. *Physical Review Letters*, 97(13):131801, 2006. → pages 1, 7

[16] C. Baker, Y. Chibane, M. Chouder, P. Geltenbort, K. Green, P. Harris, B. Heckel, P. Iaydjiev, S. Ivanov, I. Kilvington, et al. Apparatus for measurement of the electric dipole moment of the neutron using a cohabiting atomic-mercury magnetometer. *Nuclear Instruments and Methods in Physics Research Section A: Accelerators, Spectrometers, Detectors and Associated Equipment*, 736:184–203, 2014. → pages xii, 12, 14, 15, 130

[17] J. Baron, W. C. Campbell, D. DeMille, J. M. Doyle, G. Gabrielse, Y. V. Gurevich, P. W. Hess, N. R. Hutzler, E. Kirilov, I. Kozyryev, et al. Order of magnitude smaller limit on the electric dipole moment of the electron. *Science*, 343(6168):269–272, 2014. → pages 6

[18] N. Bartlett. Xenon hexafluoroplatinate (V) Xe+ [PtF6]-, 1962. → pages 38

[19] W. E. Bell and A. L. Bloom. Optically driven spin precession. *Physical Review Letters*, 6 (6):280, 1961. → pages 130

[20] J. C. Berengut, D. Budker, C. Delaunay, V. V. Flambaum, C. Frugiuele, E. Fuchs, C. Grojean, R. Harnik, R. Ozeri, G. Perez, et al. Probing new light force-mediators by isotope shift spectroscopy. *arXiv preprint arXiv:1704.05068*, 2017. → pages 97

[21] N. Beverini, G. Genovesi, and F. Strumia. Xenon saturation spectroscopy by diode laser. *Il Nuovo Cimento D*, 17(5):515–522, 1995. → pages 42

[22] F. Biraben, B. Cagnac, and G. Grynberg. Experimental evidence of two-photon transition without doppler broadening. *Physical Review Letters*, 32(12):643, 1974. → pages 34

[23] M. Bishof, R. H. Parker, K. G. Bailey, J. P. Greene, R. J. Holt, M. R. Kalita, W. Korsch, N. D. Lemke, Z.-T. Lu, P. Mueller, et al. Improved limit on the ra 225 electric dipole moment. *Physical Review C*, 94(2):025501, 2016. → pages 6

[24] F. Bloch. Nuclear Induction. *Physical Review*, 70(7-8):460–474, Oct. 1946. doi:10.1103/PhysRev.70.460. URL http://link.aps.org/doi/10.1103/PhysRev.70.460. → pages 27, 28

[25] F. Bloch, W. W. Hansen, and M. Packard. The Nuclear Induction Experiment. *Physical Review*, 70(7-8):474–485, Oct. 1946. doi:10.1103/PhysRev.70.474. URL http://link.aps.org/doi/10.1103/PhysRev.70.474. → pages 27

[26] A. L. Bloom. Principles of operation of the rubidium vapor magnetometer. *Applied Optics*, 1(1):61–68, 1962. → pages 129

[27] P. T. Boggs and J. E. Rogers. Orthogonal distance regression. *Contemporary Mathematics*, 112:183–194, 1990. → pages 90

[28] K. D. Bonin and T. J. McIlrath. Two-photon electric-dipole selection rules. *JOSA B*, 1(1): 52–55, 1984. → pages 32

[29] W. Borchers, E. Arnold, W. Neu, R. Neugart, K. Wendt, G. Ulm, I. Collaboration, et al. Xenon isotopes far from stability studied by collisional ionization laser spectroscopy. *Physics Letters B*, 216(1-2):7–10, 1989. → pages xi, 92, 98, 99, 100

[30] M. Bouchiat, J. Brossel, and L. Pottier. Evidence for Rb-rare-gas molecules from the relaxation of polarized Rb atoms in a rare gas. experimental results. *The Journal of Chemical Physics*, 56(7):3703–3714, 1972. → pages 25

[31] M. A. Bouchiat, T. Carver, and C. Varnum. Nuclear polarization in He^3 gas induced by optical pumping and dipolar exchange. *Physical Review Letters*, 5(8):373, 1960. → pages 24

[32] U. Brackmann. Laser dyes. *Göttingen (Germany): Lambda Physik AG. D*, 37079, 2000. → pages 76

[33] F. Brandi, I. Velchev, W. Hogervorst, and W. Ubachs. Vacuum-ultraviolet spectroscopy of Xe: Hyperfine splittings, isotope shifts, and isotope-dependent ionization energies. *Physical Review A*, 64(3):032505, 2001. → pages 42, 94, 112

[34] S. R. Breeze, S. Lang, I. Moudrakovski, C. I. Ratcliffe, J. A. Ripmeester, G. Santyr, B. Simard, and I. Zuger. Coatings for optical pumping cells and short-term storage of hyperpolarized xenon. *Journal of Applied Physics*, 87(11):8013–8017, 2000. → pages 26, 44

[35] M. Bruce, W. Layne, C. Whitehead, and J. Keto. Radiative lifetimes and collisional deactivation of two-photon excited xenon in argon and xenon. *The Journal of chemical physics*, 92(5):2917–2926, 1990. → pages 42

[36] E. Brunner. Optimization of pump cells: Simulation and experiments. In *Hyperpolarized Xenon-129 Magnetic Resonance*, pages 72–85. 2015. → pages 52, 54, 66

[37] D. Budker and D. F. J. Kimball. *Optical magnetometry*. Cambridge University Press, 2013. → pages 129, 130

[38] D. Budker and M. Romalis. Optical magnetometry. *Nature Physics*, 3(4):227, 2007. → pages 129

[39] D. Budker, W. Gawlik, D. Kimball, S. Rochester, V. Yashchuk, and A. Weis. Resonant nonlinear magneto-optical effects in atoms. *Reviews of modern physics*, 74(4):1153, 2002. → pages 130

[40] N. Cabibbo. Unitary symmetry and leptonic decays. *Physical Review Letters*, 10(12):531, 1963. → pages 3

[41] F. Calaprice, W. Happer, D. Schreiber, M. Lowry, E. Miron, and X. Zeng. Nuclear alignment and magnetic moments of ^{133}Xe, ^{133}Xe^m, and ^{131}Xe^m by spin exchange with optically pumped ^{87}Rb. *Physical review letters*, 54(3):174, 1985. → pages 25

[42] G. Cates, D. Benton, M. Gatzke, W. Happer, K. Hasson, and N. Newbury. Laser production of large nuclear-spin polarization in frozen xenon. *Physical review letters*, 65(20):2591, 1990. → pages 25, 73

[43] G. Cates, R. Fitzgerald, A. Barton, P. Bogorad, M. Gatzke, N. Newbury, and B. Saam. Rb-^{129}Xe spin-exchange rates due to binary and three-body collisions at high xe pressures. *Physical Review A*, 45(7):4631, 1992. → pages 24, 25

[44] C. H. Chen, G. S. Hurst, and M. G. Payne. Direct counting of Xe atoms. *Chemical Physics Letters*, 75(3):473–477, Nov. 1980. ISSN 0009-2614. doi:10.1016/0009-2614(80)80558-6. URL http://www.sciencedirect.com/science/article/pii/0009261480805586. → pages 42

[45] D. Cho, K. Sangster, and E. Hinds. Search for time-reversal-symmetry violation in thallium fluoride using a jet source. *Physical Review A*, 44(5):2783, 1991. → pages 6

[46] J. H. Christenson, J. W. Cronin, V. L. Fitch, and R. Turlay. Evidence for the 2π decay of the K_2^0 meson. *Physical Review Letters*, 13(4):138, 1964. → pages 3

[47] T. Chupp and M. Ramsey-Musolf. Electric dipole moments: a global analysis. *Physical Review C*, 91(3):035502, 2015. → pages x, 5, 6, 112

[48] T. Chupp, R. Hoare, R. Walsworth, and B. Wu. Spin-exchange-pumped ^{3}He and ^{129}Xe zeeman masers. *Physical review letters*, 72(15):2363, 1994. → pages 113

[49] A. Corney. *Atomic and laser spectroscopy*. Clarendon Press Oxford, 1978. → pages 20

[50] M. Coulombe and J. Bauche. Interpretation of the isotope shifts in the arc spectrum of xenon. *Proc. R. Soc. Lond. A*, 343(1635):443–451, 1975. → pages 42

[51] K. Coulter, T. Chupp, A. McDonald, C. Bowman, J. Bowman, J. Szymanski, V. Yuan, G. Cates, D. Benton, and E. Earle. Neutron polarization with a polarized 3he spin filter. *Nuclear Instruments and Methods in Physics Research Section A: Accelerators, Spectrometers, Detectors and Associated Equipment*, 288(2-3):463–466, 1990. → pages 25

[52] S. C. Cullen and E. G. Gross. The anesthetic properties of xenon in animals and human beings, with additional observations on krypton. *Science*, 113(2942):580–582, 1951. → pages 38

[53] G. D'amico, G. Pesce, and A. Sasso. High resolution spectroscopy of stable xenon isotopes. *Hyperfine Interactions*, 127(1-4):121–128, 2000. → pages 81, 92, 97

[54] S. Davidson, E. Nardi, and Y. Nir. Leptogenesis. *Physics Reports*, 466(4-5):105–177, 2008. → pages 2

[55] T. Dawson. Development of a xenon polarizer for magnetometry in neutron electric dipole moment experiments, 2013. → pages 62

[56] H. Dehmelt. Modulation of a light beam by precessing absorbing atoms. *Physical Review*, 105(6):1924, 1957. → pages 129

[57] W. Demtröder. *Laser Spectroscopy 2: Experimental Techniques*. Springer, 2015. → pages 34

[58] R. H. Dicke. Coherence in spontaneous radiation processes. *Physical Review*, 93(1):99, 1954. → pages 38

[59] B. Driehuys, a. Cates, E. Miron, K. Sauer, D. Walter, and W. Happer. High-volume production of laser-polarized ^{129}Xe. *Applied Physics Letters*, 69(12):1668–1670, 1996. → pages 25, 55

[60] H. E. Edgerton and P. Y. Cathou. Xenon flash tube of small size. *Review of Scientific instruments*, 27(10):821–825, 1956. → pages 38

[61] C. Eichhorn, S. Fritzsche, S. Löhle, A. Knapp, and M. Auweter-Kurtz. Time-resolved fluorescence spectroscopy of two-photon laser-excited $8p$, $9p$, $5f$, and $6f$ levels in neutral xenon. *Physical Review E*, 80(2):026401, 2009. → pages 42

[62] M. Fertl. *A laser based mercury co-magnetometer for the neutron electric dipole moment search*. PhD thesis, ETH Zurich, 2013. → pages 130

[63] A. Fink, D. Baumer, and E. Brunner. Production of hyperpolarized xenon in a static pump cell: Numerical simulations and experiments. *Physical Review A*, 72(5):053411, 2005. → pages x, 25, 53, 54, 55

[64] R. Fitzgerald, M. Gatzke, D. C. Fox, G. Cates, and W. Happer. ^{129}Xe spin relaxation in frozen xenon. *Physical Review B*, 59(13):8795, 1999. → pages 73

[65] V. Flambaum, A. Geddes, and A. Viatkina. Isotope shift, nonlinearity of king plots, and the search for new particles. *Physical Review A*, 97(3):032510, 2018. → pages 97

[66] C. J. Foot. *Atomic physics*, volume 7. Oxford University Press, 2005. → pages 30, 32, 94, 133

[67] G. Fricke, C. Bernhardt, K. Heilig, L. Schaller, L. Schellenberg, E. Shera, and C. Dejager. Nuclear ground state charge radii from electromagnetic interactions. *Atomic Data and Nuclear Data Tables*, 60(2):177–285, 1995. → pages xi, 98, 99

[68] M. Gatzke, G. Cates, B. Driehuys, D. Fox, W. Happer, and B. Saam. Extraordinarily slow nuclear spin relaxation in frozen laser-polarized ^{129}Xe. *Physical review letters*, 70(5):690, 1993. → pages 73

[69] M. B. Gavela, A. Le Yaouanc, L. Oliver, O. Pène, J. C. Raynal, and T. N. Pham. Contribution of the triangle graphs to the neutron electric dipole moment. *Zeitschrift für Physik C Particles and Fields*, 23(3):251–261, Sep 1984. ISSN 1431-5858. doi:10.1007/BF01546193. URL https://doi.org/10.1007/BF01546193. → pages 5

[70] A. Goehlich, T. Kawetzki, and H. Döbele. On absolute calibration with xenon of laser diagnostic methods based on two-photon absorption. *The Journal of chemical physics*, 108 (22):9362–9370, 1998. → pages 42

[71] R. Golub, D. Richardson, and S. K. Lamoreaux. *Ultra-cold neutrons*. CRC Press, 1991. → pages 3

[72] M. Göppert-Mayer. Elementary processes with two quantum transitions (reprint). *Annalen der Physik*, 18(7-8):466–479, 2009. → pages 30, 32

[73] W. Gornik, S. Kindt, E. Matthias, H. Rinneberg, and D. Schmidt. Off-Resonant *E*2 Transition Observed in Two-Photon Absorption in Xe I. *Physical Review Letters*, 45(24): 1941–1944, Dec. 1980. doi:10.1103/PhysRevLett.45.1941. URL http://link.aps.org/doi/10.1103/PhysRevLett.45.1941. → pages 42

[74] B. Graner, Y. Chen, E. Lindahl, B. Heckel, et al. Reduced limit on the permanent electric dipole moment of ^{129}Hg. *Physical review letters*, 116(16):161601, 2016. → pages 6, 14, 130, 131

[75] K. Green, P. G. Harris, P. Iaydjiev, D. J. R. May, J. M. Pendlebury, K. F. Smith, M. van der Grinten, P. Geltenbort, and S. Ivanov. Performance of an atomic mercury magnetometer in the neutron EDM experiment. *Nuclear Instruments and Methods in Physics Research Section A: Accelerators, Spectrometers, Detectors and Associated Equipment*, 404(23): 381–393, Feb. 1998. ISSN 0168-9002. doi:10.1016/S0168-9002(97)01121-2. URL http://www.sciencedirect.com/science/article/pii/S0168900297011212. → pages 7, 14, 106

[76] D. Griffiths. Introduction to elementary particles. *Introduction to Elementary Particles, by David Griffiths, pp. 400. ISBN 0-471-60386-4. Wiley-VCH, March 1987.*, page 400, 1987. → pages 2

[77] A. Grosz, M. J. Haji-Sheikh, and S. C. Mukhopadhyay. *High sensitivity magnetometers*. Springer, 2017. → pages 7, 127, 129, 130

[78] B. Grover. Noble-gas nmr detection through noble-gas-rubidium hyperfine contact interaction. *Physical Review Letters*, 40(6):391, 1978. → pages 25, 42

[79] G. Grynberg and B. Cagnac. Doppler-free multiphotonic spectroscopy. *Reports on Progress in Physics*, 40(7):791, 1977. → pages 34

[80] T. Hänsch, S. Lee, R. Wallenstein, and C. Wieman. Doppler-free two-photon spectroscopy of hydrogen $1s - 2s$. *Physical Review Letters*, 34(6):307, 1975. → pages 35

[81] W. Happer. Optical pumping. *Reviews of Modern Physics*, 44(2):169, 1972. → pages 42, 129

[82] W. Happer, E. Miron, S. Schaefer, D. Schreiber, W. Van Wijngaarden, and X. Zeng. Polarization of the nuclear spins of noble-gas atoms by spin exchange with optically pumped alkali-metal atoms. *Physical Review A*, 29(6):3092, 1984. → pages 24, 42

[83] H. Horiguchi, R. Chang, and D. Setser. Radiative lifetimes and two-body collisional deactivation rate constants in Ar for Xe ($5p^56p$), Xe ($5p^56p$), and Xe ($5p^57p$) states. *The Journal of Chemical Physics*, 75(3):1207–1218, 1981. → pages 101, 105

[84] J. J. Hudson, D. M. Kara, I. Smallman, B. E. Sauer, M. R. Tarbutt, and E. A. Hinds. Improved measurement of the shape of the electron. *Nature*, 473(7348):493, 2011. → pages 6

[85] C. J. Humphreys and E. Paul. Interferometric wavelength determinations in the first spectrum of ^{136}Xe. *JOSA*, 60(10):1302–1310, 1970. → pages 112

[86] E. Hunt and H. Carr. Nuclear magnetic resonance of ^{129}Xe in natural xenon. *Physical Review*, 130(6):2302, 1963. → pages 26

[87] Y. Ichikawa, M. Chikamori, Y. Ohtomo, E. Hikota, Y. Sakamoto, T. Suzuki, C. Bidinosti, T. Inoue, T. Furukawa, A. Yoshimi, et al. Search for electric dipole moment in ^{129}Xe atom using active nuclear spin maser. In *EPJ Web of Conferences*, volume 66, page 05007. EDP Sciences, 2014. → pages 113

[88] T. Inoue, S. Ando, T. Aoki, H. Arikawa, S. Ezure, K. Harada, T. Hayamizu, T. Ishikawa, M. Itoh, K. Kato, et al. Experimental search for the electron electric dipole moment with laser cooled francium atoms. *Hyperfine Interactions*, 231(1-3):157–162, 2015. → pages 5

[89] D. A. Jackson and M. Coulombe. Hyperfine structure in the arc spectrum of xenon. *Proc. R. Soc. Lond. A*, 327(1569):137–145, 1972. → pages 42

[90] D. A. Jackson and M. Coulombe. Hyperfine structure in the arc spectrum of xenon. ii. *Proc. R. Soc. Lond. A*, 335(1601):127–140, 1973. → pages

[91] D. A. Jackson and M. Coulombe. Isotope shifts in the arc spectrum of xenon. *Proc. R. Soc. Lond. A*, 338(1614):277–298, 1974. → pages

[92] D. A. Jackson and M. Coulombe. Isotope shifts in the arc spectrum of xenon. ii. *Proc. R. Soc. Lond. A*, 343(1635):453–459, 1975. → pages 42

[93] Y.-Y. Jau, N. N. Kuzma, and W. Happer. High-field measurement of the ^{129}Xe- Rb spin-exchange rate due to binary collisions. *Physical review A*, 66(5):052710, 2002. → pages 25

[94] J. Jin. *Electromagnetic analysis and design in magnetic resonance imaging*, volume 1. CRC press, 1998. → pages 131

[95] E. G. Jones. Hyperfine structure in the arc spectrum of xenon. *Proc. R. Soc. Lond. A*, 144 (853):587–595, 1934. → pages 41

[96] W. King. Isotope shifts in atomic spectra. *Physics of Atoms and Molecules, New York: Plenum Press, 1984*, 1984. → pages 94, 95, 96

[97] M. Kobayashi et al. M. kobayashi and t. maskawa, prog. theor. phys. 49, 652 (1973). *Prog. Theor. Phys.*, 49:652, 1973. → pages 3

[98] I. Kominis, T. Kornack, J. Allred, and M. Romalis. A subfemtotesla multichannel atomic magnetometer. *Nature*, 422(6932):596, 2003. → pages 130

[99] J. Kopecky, J. C. Sublet, J. Simpson, R. Forrest, and D. Nierop. Atlas of neutron capture cross sections. Technical report, International Atomic Energy Agency, 1997. → pages 7

[100] S. E. Korchak, W. Kilian, and L. Mitschang. Configuration and performance of a mobile ^{129}Xe polarizer. *Applied magnetic resonance*, 44(1-2):65–80, 2013. → pages 25

[101] F. Kuchler, E. Babcock, M. Burghoff, T. Chupp, S. Degenkolb, I. Fan, P. Fierlinger, F. Gong, E. Kraegeloh, W. Kilian, et al. A new search for the atomic EDM of ^{129}Xe at FRM-II. *Hyperfine Interactions*, 237(1):95, 2016. → pages 11, 113

[102] S. K. Lamoreaux. The electric dipole moments of atoms: Limits on P, T violating interactions within the atom. *Nuclear Instruments and Methods in Physics Research Section A: Accelerators, Spectrometers, Detectors and Associated Equipment*, 284(1):43–49, 1989. → pages 11

[103] J. Lenz and S. Edelstein. Magnetic sensors and their applications. *IEEE Sensors journal*, 6 (3):631–649, 2006. → pages 7, 127, 128

[104] J. E. Lenz. A review of magnetic sensors. *Proceedings of the IEEE*, 78(6):973–989, 1990. → pages 7

[105] M. Levenson and N. Bloembergen. Observation of two-photon absorption without doppler broadening on the $3s - 5s$ transition in sodium vapor. *Physical Review Letters*, 32(12):645, 1974. → pages 35

[106] Y. Masuda, K. Hatanaka, S.-C. Jeong, S. Kawasaki, R. Matsumiya, K. Matsuta, M. Mihara, and Y. Watanabe. Spallation ultracold neutron source of superfluid helium below 1 K. *Physical review letters*, 108(13):134801, 2012. → pages 4

[107] T. Meersmann and G. Pavlovskaya. Spin exchange optical pumping (SEOP)–concepts and practical considerations. In *Hyperpolarized Xenon-129 Magnetic Resonance*, pages 49–71. 2015. → pages 22, 23

[108] W. F. Meggers. *Interference Measurements in the Spectra of Argon, Krypton and Xenon*. US Government Printing Office, 1921. → pages 41

[109] W. F. Meggers and C. Humphreys. Interference measurements in the spectra of noble gases. *J. Research Nat. Bur. of Stand.*, 13:293–309, 1934. → pages 41

[110] K. Mikami, M. Tanaka, and Y. Yamamoto. Probing new intra-atomic force with isotope shifts. *The European Physical Journal C*, 77(12):896, 2017. → pages 97

[111] A. Miller and T. Momose. Unpublished work. → pages 18

[112] A. K. Mills, Y.-F. Chen, K. W. Madison, and D. J. Jones. Widely tunable, single-mode optical frequency synthesizer with a 100 kHz uncertainty. *JOSA B*, 26(7):1276–1280, 2009. → pages 133

[113] P. J. Mohr, D. B. Newell, and B. N. Taylor. Codata recommended values of the fundamental physical constants: 2014. *Journal of Physical and Chemical Reference Data*, 45(4):043102, 2016. → pages 3

[114] C. E. Moore. Atomic energy levels, vol. iii (molybdenum through lanthanum and hafnium through actinium). *Circular of the National Bureau of Standards*, 467, 1958. → pages 41

[115] S. Murthy, D. Krause Jr, Z. Li, and L. Hunter. New limits on the electron electric dipole moment from cesium. *Physical review letters*, 63(9):965, 1989. → pages 6

[116] I. Nelson and T. Walker. Rb-Xe spin relaxation in dilute Xe mixtures. *Physical Review A*, 65(1):012712, 2001. → pages 25

[117] P. Nikolaou, A. M. Coffey, L. L. Walkup, B. M. Gust, N. Whiting, H. Newton, S. Barcus, I. Muradyan, M. Dabaghyan, G. D. Moroz, et al. Near-unity nuclear polarization with an open-source ^{129}Xe hyperpolarizer for NMR and MRI. *Proceedings of the National Academy of Sciences*, 110(35):14150–14155, 2013. → pages 25, 42

[118] P. Nikolaou, A. M. Coffey, M. J. Barlow, M. S. Rosen, B. M. Goodson, and E. Y. Chekmenev. Temperature-ramped ^{129}Xe spin-exchange optical pumping. *Analytical chemistry*, 86(16):8206–8212, 2014. → pages 25

[119] P. Nikolaou, A. M. Coffey, L. L. Walkup, B. M. Gust, C. D. LaPierre, E. Koehnemann, M. J. Barlow, M. S. Rosen, B. M. Goodson, and E. Y. Chekmenev. A 3d-printed high power nuclear spin polarizer. *Journal of the American Chemical Society*, 136(4):1636–1642, 2014. → pages 25

[120] J. J. Olivero and R. Longbothum. Empirical fits to the voigt line width: A brief review. *Journal of Quantitative Spectroscopy and Radiative Transfer*, 17(2):233–236, 1977. → pages 64

[121] R. Pattie, N. Callahan, C. Cude-Woods, E. Adamek, L. J. Broussard, S. Clayton, S. Currie, E. Dees, X. Ding, E. Engel, et al. Measurement of the neutron lifetime using a magneto-gravitational trap and in situ detection. *Science*, 360(6389):627–632, 2018. → pages 3

[122] T. A. Paul and F. Merkt. High-resolution spectroscopy of xenon using a tunable fourier-transform-limited all-solid-state vacuum-ultraviolet laser system. *Journal of Physics B: Atomic, Molecular and Optical Physics*, 38(22):4145, 2005. → pages 42

[123] J. Pendlebury, W. Heil, Y. Sobolev, P. Harris, J. Richardson, R. Baskin, D. Doyle, P. Geltenbort, K. Green, M. Van Der Grinten, et al. Geometric-phase-induced false electric dipole moment signals for particles in traps. *Physical Review A*, 70(3):032102, 2004. → pages 16, 17

[124] J. Pendlebury, S. Afach, N. Ayres, C. Baker, G. Ban, G. Bison, K. Bodek, M. Burghoff, P. Geltenbort, K. Green, et al. Revised experimental upper limit on the electric dipole moment of the neutron. *Physical Review D*, 92(9):092003, 2015. → pages 1, 6

[125] M. Pfeffer and O. Lutz. ^{129}Xe gas NMR spectroscopy and imaging with a whole-body imager. *Journal of Magnetic Resonance, Series A*, 108(1):106–109, 1994. → pages 20

[126] R. Picker. How the minuscule can contribute to the big picture: the neutron electric dipole moment project at triumf. In *Proceedings of the 14th International Conference on Meson-Nucleon Physics and the Structure of the Nucleon (MENU2016)*, page 010005, 2017. → pages v, xii, 4, 5, 6

[127] M. S. Pindzola, M. G. Payne, and W. R. Garrett. Two-photon excitation of xenon. *Physical Review A*, 24(6):3115–3119, Dec. 1981. doi:10.1103/PhysRevA.24.3115. URL http://link.aps.org/doi/10.1103/PhysRevA.24.3115. → pages 37

[128] M. Plimmer, P. Baird, C. Foot, D. Stacey, J. Swan, and G. Woodgate. Isotope shift in xenon by doppler-free two-photon laser spectroscopy. *Journal of Physics B: Atomic, Molecular and Optical Physics*, 22(10):L241, 1989. → pages xvii, 35, 42, 90, 95, 96, 97, 100

[129] R. Pohl, A. Antognini, F. Nez, F. D. Amaro, F. Biraben, J. M. Cardoso, D. S. Covita, A. Dax, S. Dhawan, L. M. Fernandes, et al. The size of the proton. *Nature*, 466(7303):213, 2010. → pages 99

[130] D. Pritchard, J. Apt, and T.-W. Ducas. Fine structure of Na 4*d* D2 using high-resolution two-photon spectroscopy. *Physical Review Letters*, 32(12):641, 1974. → pages 35

[131] I. Pykett, B. Rosen, F. Buonanno, and T. Brady. Measurement of spin-lattice relaxation times in nuclear magnetic resonance imaging. *Physics in Medicine & Biology*, 28(6):723, 1983. → pages 51

[132] I. I. Rabi, N. F. Ramsey, and J. Schwinger. Use of rotating coordinates in magnetic resonance problems. *Reviews of Modern Physics*, 26(2):167, 1954. → pages 27

[133] G. Racah. On a new type of vector coupling in complex spectra. *Physical Review*, 61(7-8): 537, 1942. → pages 41

[134] D. Raftery, H. Long, T. Meersmann, P. Grandinetti, L. Reven, and A. Pines. High-field nmr of adsorbed xenon polarized by laser pumping. *Physical Review Letters*, 66(5):584, 1991. → pages 25

[135] W. Ramsay and M. W. Travers. Argon and its companions. *Proceedings of the Royal Society of London*, 67(435-441):329–333, 1901. → pages 38

[136] N. F. Ramsey. A molecular beam resonance method with separated oscillating fields. *Physical Review*, 78(6):695, 1950. → pages 11

[137] M. B. Rankin, J. P. Davis, C. Giranda, and L. C. Bobb. Two-photon-excited bidirectional emission in xenon. *Optics communications*, 70(4):345–349, 1989. → pages 38, 76, 80

[138] T. D. Raymond, N. Bwering, C.-Y. Kuo, and J. W. Keto. Two-photon laser spectroscopy of xenon collision pairs. *Physical Review A*, 29(2):721–734, Feb. 1984. doi:10.1103/PhysRevA.29.721. URL http://link.aps.org/doi/10.1103/PhysRevA.29.721. → pages 35, 37, 106

[139] B. Regan, E. D. Commins, C. J. Schmidt, and D. DeMille. New limit on the electron electric dipole moment. *Physical Review Letters*, 88(7):071805, 2002. → pages 6

[140] D. Robbes. Highly sensitive magnetometersa review. *Sensors and Actuators A: Physical*, 129(1-2):86–93, 2006. → pages 128

[141] M. Romalis, E. Miron, and G. Cates. Pressure broadening of Rb D1 and D2 lines by ^{3}He, ^{4}He, N_2, and Xe: Line cores and near wings. *Physical Review A*, 56(6):4569, 1997. → pages 64

[142] M. Rosenberry and T. Chupp. Atomic electric dipole moment measurement using spin exchange pumped masers of ^{129}Xe and ^{3}He. *Physical review letters*, 86(1):22, 2001. → pages 6, 11, 25, 113

[143] M. Rumi and J. W. Perry. Two-photon absorption: an overview of measurements and principles. *Advances in Optics and Photonics*, 2(4):451–518, 2010. → pages 35

[144] I. C. Ruset. *Hyperpolarized 129Xe production and applications*. PhD thesis, University of New Hampshire (Department of Physics), 2005. → pages 25, 26, 42, 47

[145] B. Saam. T_1 relaxation of ^{129}Xe and how to keep it long. In *Hyperpolarized Xenon-129 Magnetic Resonance*, pages 122–141. 2015. → pages 26, 55

[146] A. Sakharov. Violation of CP invariance, C asymmetry, and baryon asymmetry of the universe. *JETP Lett.*, 5:24, 1967. → pages 2

[147] E. B. Saloman. Energy levels and observed spectral lines of xenon, Xe I through Xe LIV. *Journal of physical and chemical reference data*, 33(3):765–921, 2004. → pages xiii, 19, 38, 39, 41, 112

[148] R. P. Saxon and J. Eichler. Theoretical calculation of two-photon absorption cross sections in atomic oxygen. *Physical Review A*, 34(1):199, 1986. → pages 36

[149] L. Schearer. Optical pumping of $^3P_2$ argon and xenon atoms. *Physics Letters A*, 28(9): 660–661, 1969. → pages 42

[150] R. Seiler, T. Paul, M. Andrist, and F. Merkt. Generation of programmable near-fourier-transform-limited pulses of narrow-band laser radiation from the near infrared to the vacuum ultraviolet. *Review of scientific instruments*, 76(10):103103, 2005. → pages 35, 42

[151] J. Smith, E. Purcell, and N. Ramsey. Experimental limit to the electric dipole moment of the neutron. *Physical Review*, 108(1):120, 1957. → pages 6

[152] K. Smith, N. Crampin, J. Pendlebury, D. Richardson, D. Shiers, K. Green, A. Kilvington, J. Moir, H. Prosper, D. Thompson, et al. A search for the electric dipole moment of the neutron. *Physics Letters B*, 234(1-2):191–196, 1990. → pages 13

[153] I. I. Sobelman. *Atomic spectra and radiative transitions*, volume 12. Springer Science & Business Media, 2012. → pages 41

[154] D. A. Steck. Quantum and atom optics. *Oregon Center for Optics and Department of Physics, University of Oregon*, 47, 2007. → pages 92, 93

[155] N. J. Stone. Table of nuclear magnetic dipole and electric quadrupole moments. *Atomic Data and Nuclear Data Tables*, 90(1):75–176, 2005. → pages x, 20, 21, 93

[156] R. L. Sutherland. *Handbook of nonlinear optics*. CRC press, 2003. → pages 35

[157] M. Suzuki, K. Katoh, and N. Nishimiya. Saturated absorption spectroscopy of Xe using a GaAs semiconductor laser. *Spectrochimica Acta Part A: Molecular and Biomolecular Spectroscopy*, 58(11):2519–2531, 2002. → pages 92, 95

[158] A. L. Van Geet and D. Hume. Measurement of proton relaxation times with a high resolution nuclear magnetic resonance spectrometer. direct method. *Analytical Chemistry*, 37(8):983–988, 1965. → pages 51

[159] L. Vasilenko, V. Chebotaev, and A. Shishaev. Line shape of two-photon absorption in a standing-wave field in a gas. *ZhETF Pisma Redaktsiiu*, 12:161, 1970. → pages 33, 34

[160] T. Vold, F. J. Raab, B. Heckel, and E. Fortson. Search for a permanent electric dipole moment on the ^{129}Xe atom. *Physical review letters*, 52(25):2229, 1984. → pages 112

[161] M. Wagshul and T. Chupp. Optical pumping of high-density Rb with a broadband dye laser and GaAlAs diode laser arrays: Application to ^{3}He polarization. *Physical review A*, 40(8):4447, 1989. → pages 25

[162] T. G. Walker and W. Happer. Spin-exchange optical pumping of noble-gas nuclei. *Reviews of Modern Physics*, 69(2):629, 1997. → pages 8, 24

[163] N. Whiting, P. Nikolaou, N. A. Eschmann, B. M. Goodson, and M. J. Barlow. Interdependence of in-cell xenon density and temperature during Rb/^{129}Xe spin-exchange optical pumping using VHG-narrowed laser diode arrays. *Journal of Magnetic Resonance*, 208(2):298–304, 2011. → pages 25

[164] J. Wiebe. Design and construction of custom inductive receive coils for low-feld AFP NMR using hyperpolarized xenon. *Unpublished undergraduate thesis*, 2011. → pages 62

[165] J. N. Wienands. *Coils, fields and xenon: towards measuring xenon spin precession in a magnetic field for the UCN collaboration*. PhD thesis, University of British Columbia, 2016. → pages 49

[166] G. K. Woodgate. Elementary atomic structure, second edition. 2002. → pages 19

[167] C.-S. Wu, E. Ambler, R. Hayward, D. Hoppes, and R. P. Hudson. Experimental test of parity conservation in beta decay. *Physical review*, 105(4):1413, 1957. → pages 2

[168] T. Xia, S. Morgan, Y.-Y. Jau, and W. Happer. Polarization and hyperfine transitions of metastable ^{129}Xe in discharge cells. *Physical Review A*, 81(3):033419, 2010. → pages 41

[169] A. Yoshimi, K. Asahi, K. Sakai, M. Tsuda, K. Yogo, H. Ogawa, T. Suzuki, and M. Nagakura. Nuclear spin maser with an artificial feedback mechanism. *Physics Letters A*, 304(1-2):13–20, 2002. → pages 113

Appendix A

Supporting Materials

A.1 Magnetometry Techniques

There are various techniques of magnetometry suitable for measuring magnetic field with different magnitudes and time dependence. Some common techniques are listed below; a thorough presentation of magnetic sensors is given by Refs. [77] and [103]. A distinction is made between vector magnetometers, which are sensitive only to one component of the magnetic field (B_x, B_y, B_z), and scalar magnetometers, which measure the magnitude $|B_0|$. Vector magnetometers include induction coils, Hall effect, fluxgates and SQUIDs. Scalar magnetometers include proton precession and optically pumped atomic magnetometers.

Induction Coil

The most conceptually simple magnetic sensors are induction coils. At their simplest these are completely passive wire loops in which a voltage will be induced by Faraday induction; that is, by a changing magnetic flux $V = -d\phi/dt$. Sensitivity to the signal can be increased with an op-amp (active electronics) or by inserting a ferromagnetic core to increase the flux density (passive). Their sensitivity can be as good at 20 fT [103], and is primarily to AC fields in the range 1 Hz to 1 MHz. Induction coils are a vector magnetometer because they sense only the magnetic field component normal to the coil plane.

Fluxgate

A fluxgate works by applying a driving magnetic field H_E to saturate a ferromagnetic core such that B reaches a maximum, and sensing the voltage $V = Hd\mu/dt$ corresponding to the changing permeability $\mu = B/H$. Measurement of the desired (background) field is possible because it shifts the saturation point of the magnetic core, causing a hysteresis effect. A typical fluxgate consists of a pair of solenoidal coils wrapped around one or two saturable magnetic cores. One coil drives

an AC field to saturate the magnetic core twice per cycle with reversing direction while the other measures the flux from *B*. This technique requires one sensor per component of the magnetic field vector. The sensitivity is from $10^{-2} - 10^7$nT and can measure DC or AC up to 10 kHz, limited by the need to sweep the saturating field.

SQUID

Superconducting Quantum Interference Device (SQUID) is a vector magnetometer device consisting of a superconducting coil cooled below its critical temperature T_c. Below T_c any field passing through the coil area would induce current which flows with zero resistance; furthermore, the flux through the coil will be quantized. The coil is split at one or two points by a non-superconducting "Josephson Junction," through which the measured current becomes an oscillating function of magnetic field, due to an interference effect of the quantized flux. The small area of the SQUID loop is often coupled to a larger coil via a flux transformer [140]. A null-field technique with feedback allows measurement of larger DC fields. SQUIDs are sensitive from 10 fT up to 1 nT but require cryogenic cooling. Specific orientations of two SQUIDs can detect magnetic field vector gradients.

Hall Effect

The Hall probe measures the effect of the Lorentz force $F = q\vec{v} \times \vec{B}$ on a current travelling through a thin conductor. A current travelling along $\vec{x}$ will generate a detectable voltage across the $\vec{y}$ direction in response to a field applied along $\vec{z}$. Typically a semiconductor is used to see a larger Hall effect. The Hall probe is a vector magnetometer and is sensitive from approximately $10^{-5} - 10^{-1}$T over DC-1MHz.

Magneto-resistance

Certain materials such as permalloy increase their resistance in response to an applied magnetic field. A current passed through a thin film of magnetized metal will measure less resistance if the film magnetization is aligned with an applied field. These sense $10^{-6} - 10^{-3}$T over DC - 1GHz. Layered structures of ferromagnet and conductor can exhibit so-called Giant Magneto-resistance with sensitivity $10^{-7} - 10^{-1}$T.

Faraday rotation

The Faraday effect is rotation of the plane of polarized light as it travels through a magneto-optic crystal with polarization parallel to both the crystal axis and to an applied magnetic field [103]. There is a different index of refraction for each circular component of the light, creating a phase difference resulting in rotation. The strength of the effect depends on the crystal's Verdet constant. Sensitivity of 10^{-11}T has been obtained with response DC-GHz.

Proton precession magnetometers

Proton magnetometers align the spins in a hydrogen-rich fluid such as benzene by briefly applying a strong B field, generating a Boltzmann polarization. When this field is turned off, the protons precess around the ambient field at the Larmor frequency $\omega = \gamma B$ and induce a voltage in a sensing coil. It can be sensitive from $10^{-10} - 10^{-4}$T A variation on the technique uses RF to polarize the electronic spins of nearby free radicals, which then polarize the proton nuclear spins by the Overhauser Effect. The detection is analogous but an order of magnitude more sensitive. Any nuclear spin can be used in a similar manner to the proton magnetometer, although typically this requires the optical pumping described below.

A.1.1   Optically Pumped Atomic Magnetometers

Optically pumped atomic magnetometers measure the Zeeman splitting of atomic levels in a magnetic field, by detecting the precession frequency of an optically pumped sample. A thorough review of optical magnetometry is Ref. [37]. Optical magnetometry has been performed on paramagnetic alkali metal vapours of Rb, Cs, K and on metastable ^{4}He, in addition to diamagnetic ^{3}He (through spin exchange optical pumping) and ^{199}Hg. Typical configurations measure either the longitudinal (M_z) or transverse (M_x) component of the precessing magnetization. Many optically pumped magnetometers are classified as being *double resonant* [77]: they use resonant light to couple electronic states for optical pumping and detection, along with resonant RF radiation to couple Zeeman sublevels and initiate precession. Other variations use modulated transverse (or *synchronous*) optical pumping instead of RF. Detection of the magnetization (M_z or M_x) is typically through the absorption of resonant probe light, but detection may also be performed by NMOR or even SQUID. In general, atomic magnetometers are scalar magnetometers, measuring only the magnitude $|B_0|$. However, measurement of the vector components of $|B_0|$ may be achieved by applying a strong offset field $\vec{B}_{offset}$ along each component, one at a time [77]; then to first order, the magnitude $|\vec{B}_0 + \vec{B}_{offset}|$ depends only on the component of $|B_0|$ parallel to $\vec{B}_{offset}$.

Optical pumping of atomic vapours has been demonstrated starting with sodium by Alfred Kastler in 1949 [81]. The idea for using lamp-based optical pumping to measure magnetic fields was proposed in the 1950s and 60s, by Dehmelt [56] and Bloom [26], and enabled sensing of fields as low as 10^{-12} T. Recent laser advances have expanded the usability of the technique to different gases and lower fields [38].

M_z and M_x types

The M_z magnetometer type [37, 77] uses circular polarized light with $\vec{k}||\vec{B}_0$ (i.e, $\vec{k}||\hat{z}$) as a pump and probe. The atomic ensemble is continuously pumped by the light, while a resonant orthogonal RF field couples the Zeeman-split sublevels, driving the atoms away from $\hat{z}$. One sweeps the RF

frequency through resonance while looking for changes in absorption. The signal has slow response but high accuracy. In contrast, the M_x magnetometer type [37, 77] uses a beam of circular polarized light where $\vec{k}$ has a component perpendicular to B_0 in order to measure the precession frequency. Pump and probe may be achieved using two orthogonal beams or a single combined beam. There is again a persistent RF field driving the precession. Measurements of the precession frequency are sampled from the detected oscillating signal and used as feedback to the RF coils. The response is fast but somewhat less accurate. Both types suffer from dead zones; that is, relative orientations of $\vec{k}$ and $\vec{B}_0$ where the desired magnetization component cannot be sampled. The sensitivity at low fields is typically limited by broadening of the resonance due to spin exchange relaxation; however, spin exchange relaxation free (SERF) magnetometers have been shown to remove this broadening by making collisions more frequent than the rate of precession [98].

Bell-Bloom type

The Bell-Bloom magnetometer operates with a circular polarized light beam $\vec{k} \perp \vec{B}_0$ which is modulated at the nominal Larmor precession frequency. Modulation of either the amplitude, frequency, or polarization is possible. This removes the need for resonant RF radiation, meaning it is not a double-resonance type. Bell and Bloom were the first to demonstrate such a technique and called it optically driven spin precession [19]; it is also known as transverse or synchronous optical pumping. Precise determination of the precession frequency may come from feedback of a detected photodiode signal to the oscillator providing the modulation; another method is to monitor the free spin precession via NMOR. An example of a Bell-Bloom type is the Univ. Washington ^{199}Hg EDM measurement [74].

Free Spin Precession

Free spin precession refers to a magnetometer in which there is no persistent RF field driving the atoms. After being polarized either by longitudinal optical pumping followed by an RF $\pi/2$ pulse, or by transverse optical pumping, the population is allowed to precess freely about B_0. Detection of the precession frequency is by measuring the modulated transmission of a weak circular polarized probe beam $\vec{k} \perp \vec{B}_0$ or by the rotation of a linearly polarized probe beam by NMOR. An example of this type is the ^{199}Hg comagnetometer used in previous nEDM experiments [16, 62]. The technique has also been demonstrated for non-cohabiting magnetometers [2].

Nonlinear magneto-optical rotation

Nonlinear magneto-optical rotation (NMOR) magnetometers measure a rotation of the polarization vector of linear polarized light transmitted through a gas which has been polarized through optical pumping [39]. The rotation is caused by the difference in refractive index for right- and left-circular

polarized beams in the polarized medium. It is nonlinear since the signal depends on the population difference of Zeeman sublevels in the ground state, which in turn depends on the degree of polarization by optical pumping. The ^{199}Hg EDM measurement at Univ. Washington uses NMOR to detect the free spin precession of the polarized nuclei [74].

A.2 NMR Q-Factor Measurement

To increase the gain of our NMR pickup coil, we use a "tuning box" which forms together with the pickup a tuned RLC circuit. The current in the circuit is given by Kirchhoff's law [94]:

$$I = V\left(R + \frac{i}{\omega C} - i\omega L\right) \tag{A.1}$$

The resonance frequency is:

$$\omega_r = 1/\sqrt{LC} \tag{A.2}$$

In particular, at resonance the voltage across the capacitor will be

$$V_c = \frac{V}{R}\sqrt{\frac{L}{C}} = VQ, \tag{A.3}$$

where $Q = \frac{1}{R}\sqrt{\frac{L}{C}}$ is the quality factor or Q-factor of the circuit. The Q-factor is given empirically by

$$Q = \frac{\omega_r}{\Delta\omega}, \tag{A.4}$$

where $\Delta\omega$ is the half-power (-3dB) full width of the resonance. Therefore Q represents a signal gain. In our pickup circuit the measured voltage will by Q times the induced emf.

Due to their different respective gyromagnetic ratios, Xe and H_2O have different Larmor precession frequencies in the same field B_0. We often operate near the maximum acheivable field. The corresponding resonance frequencies for Xe and H_2O differ by approximately a factor of four. We built tuning boxes resonant at 15.555 kHz and 58.82 kHz for Xe and H_2O respectively. The exact frequency was determined by a suitable capacitor to tune the circuit. Each circuit has its own Q-factor.

We determine the Q-factor of each circuit theoretically and experimentally. The results are given in Table A.1. We calculate the theoretical Q-factor by first principles using Equation A.3 and by simulation in software package LTspice using an AC voltage source. In the simulation Q is calculated by two methods: first by $Q = \frac{\omega_0}{\Delta\omega}$ at -3dB points, and second by the ratio of peak power to input.

We measure the Q-factor of the circuit experimentally by sweeping an input voltage in frequency, recording the resonance ω_r and full-width $\Delta\omega$ at -3dB points of the frequency spectrum.
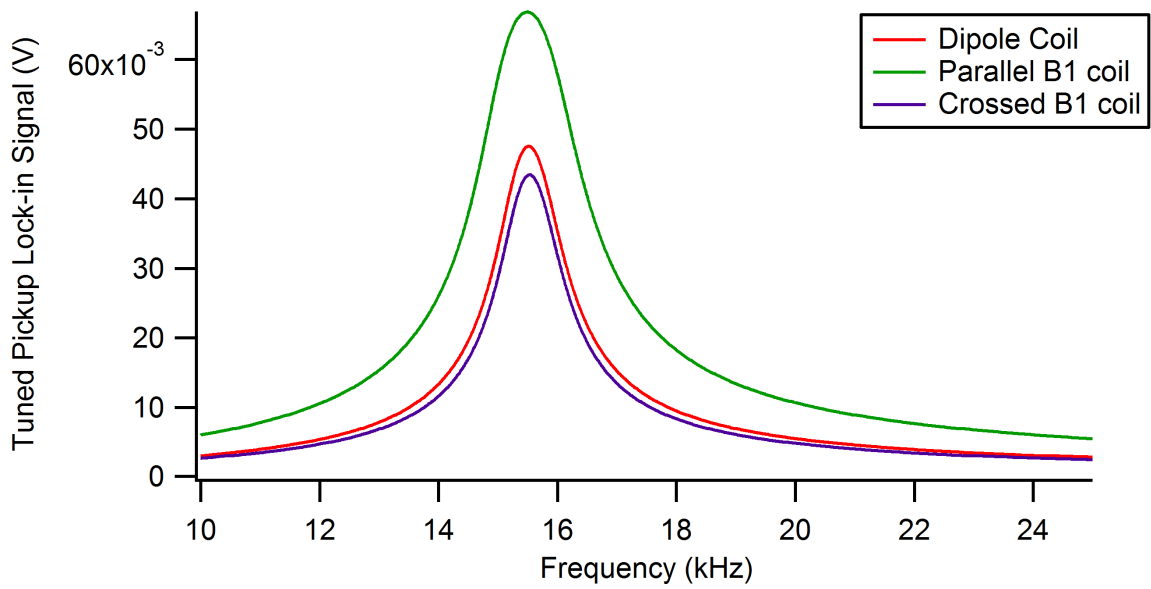
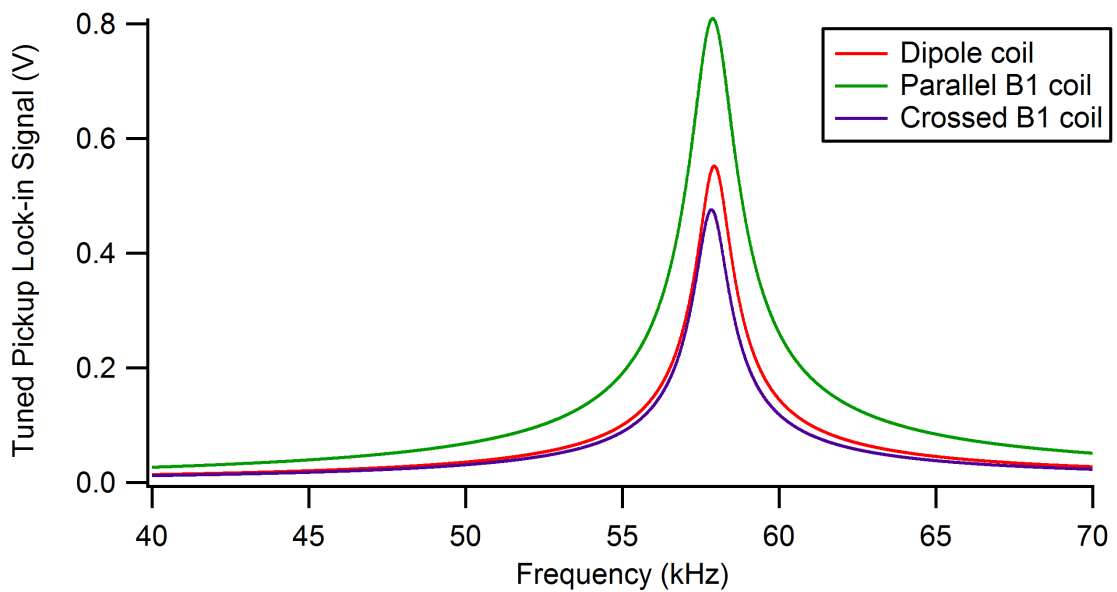**Figure A.1:** Tuning box resonance at 15kHz

Figure A.2: Tuning box resonance at 58kHz

132

Table A.1: Q-factor measurements for tuning boxes "Xe" (resonance 15.555kHz) and "Water" (resonance 58.82 kHz)

	"Xe"	"Water"
R (Ω)	9.3	9.3
L (mH)	4.13	4.13
C (nF)	25.9	1.67
$\omega_r/2\pi$ (kHz)	15.555	58.82
	Q_{Xe}	Q_{H_2O}
First principles LRC series	42.6	167.7
LTspice (0 Ω input)	42.7	172.9
LTspice (2.2 Ω input)	33.4	137.6
Network Signal Analyzer ($< 5\Omega$ input), $\frac{\omega_0}{\Delta\omega}$	23.0	46.6
Lock-in amplifier, $\frac{\omega_0}{\Delta\omega}$	26.0	38.9

The first test was performed driving LRC with the output of a network signal analyzer and recording the voltage across C; comparison of the measured Q-factors agreed within 10% with the observed peak voltage on resonance ($Q = V_c/V_{in}$). The second test was performed with the lock-in amplifier by inducing a real EMF, by driving a magnetic dipole (either a small 3-turn dipole coil, or the B_1 saddle coil pair) with the reference output and recording the mutual induction power spectrum while sweeping the reference frequency. The power spectrum is shown in Fig. A.2 and Fig. A.1. The measured Q-factor is much smaller than predicted from first principles; this discrepancy may be due to capacitive coupling of the RF coils, as well as lossy electronic components. In the case of the network signal analyzer, part of the discrepancy is due to the small output impedance of the measurement device. Similar loss in Q-factor was observed in simulations using LTspice software when an additional series resistor representing input impedance was added to the model. Experimental results using both methods yielded agreement within 20% for each Q-factor. We take the values $Q = 26.0$ for the 15.555 kHz resonant RLC circuit ("Xe") when calculating polarization estimates, and $Q = 38.9$ for the 58.82 kHz RLC circuit ("Water").

A.3   Frequency comb method

For greater laser frequency resolution, we beat our OPSL light against a fiber-based self-referenced frequency comb described in [112]. The method of obtaining the beatnote follows the description in [66], and a brief description follows here. The comb is a pulsed femtosecond fiber laser with a repetition rate of $f_{rep} = 125$ MHz. It generates light at evenly spaced "teeth", 125 MHz apart, over the entire wavelength range of $1 - 2\,\mu$m, each with near 10 kHz linewidth. The formula for the center frequency of the nth comb tooth is given by:
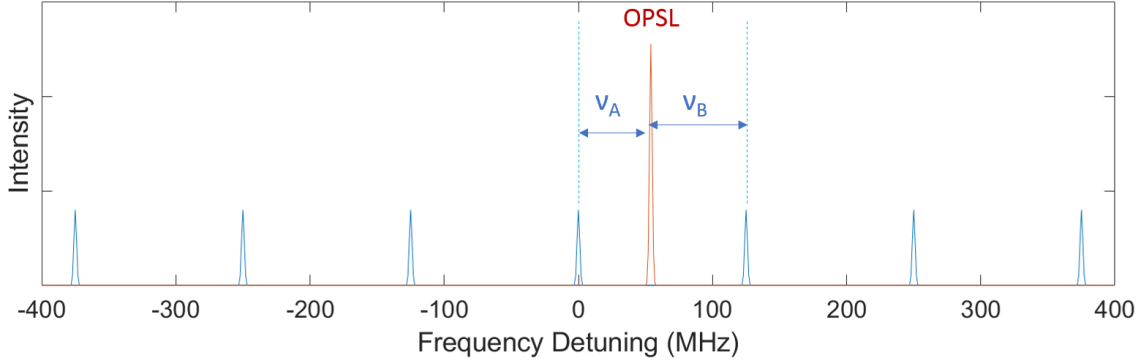
$$\nu_{comb}(n) = f_{ceo} + n f_{rep} \tag{A.5}$$

Figure A.3: Lowest-frequency beatnotes ν_A and ν_B generated by mixing OPSL light with the self referenced frequency comb. The detuning on the x-axis is relative to $\nu_{comb}(n)$.

where f_{ceo} is the offset frequency where the first tooth would be located if the comb was extended down to zero frequency. The offset can be determined by beating the comb against its own SHG to obtain a difference frequency. The doubled comb also has equally spaced teeth $2f_{rep}$ apart:

$$\nu_{doubled}(i) = 2f_{ceo} + 2if_{rep}, \tag{A.6}$$

The difference frequency generated by beating the nth comb tooth of the fundamental against its nearest-frequency SHG neighbour allows determination of the offset f_{ceo}:

$$\nu_{doubled}(i = n/2) - \nu_{comb}(n) = 2f_{ceo} + 2(n/2)f_{rep} - f_{ceo} - nf_{rep} = f_{ceo} \tag{A.7}$$

In practice f_{ceo} can be determined by the difference frequency between any two teeth of the respective combs. In the lab we measure a beatnote aroud 340 MHz to determine the offset. Both f_{rep} and f_{ceo} can be frequency stabilized to RF synthesizers locked to a 10 MHz GPS reference. This yields absolute frequency determination of the comb teeth.

Our OPSL light at 1009 nm is always within 125 MHz of a comb tooth. We pick off some of the OPSL light and couple it into a fiber where it is mixed with comb light and detected by a photodiode. This generates a difference frequency at $\nu_{beat} = \nu_{OPSL} - \nu_{comb}$ against each nearest comb tooth, which tells us how far detuned light is away from that respective comb tooth. Since the comb teeth are evenly spaced f_{rep} apart, we see the lowest frequency beatnotes at $\nu_A = \nu_{OPSL} - \nu_{comb}(n)$ and at $\nu_B = \nu_{comb}(n+1) - \nu_{OPSL}$, as shown in Fig. A.3. If we already know the OPSL frequency to within 62.5 MHz by another source such as a wavemeter, then we can determine the position of the nearest comb tooth by Equation A.5, and use our beatnote to determine our absolute frequency based on the detuning from that nearest tooth. In practice, we know the OPSL frequency only with 100 MHz uncertainty, and cannot assign the nearest comb tooth with absolute certainty based on wavemeter readings alone. We overcome this limitation by recording the frequency of a beatnote
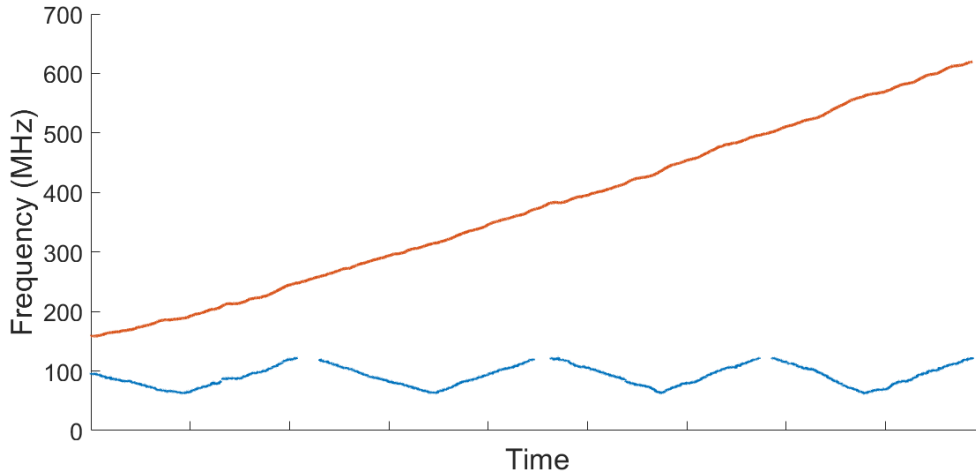
Figure A.4: Beatnote (blue) and wavemeter (red) readings during a monotonic increasing sweep of the OPSL frequency, while recording the second-nearest neighbour beatnote frequency ν_B.

in the range 62.5-125 MHz (the second-nearest neighbour frequency) using an RFSA (Advantest U3700 series) as a function of time, while applying a monotonic voltage ramp to the OPSL PZT to increase the OPSL frequency, as shown in Fig. A.4. We observe the trend in the beatnote - whether it is increasing or decreasing - and use this knowledge to determine whether the particular beatnote under observation is beating against a higher or lower frequency comb tooth, so we can unwrap the data accordingly.

The comb described above is capable of absolute frequency measurements with sub-MHz accuracy. However, the comb had no free port at the time of Xe experiments, so it was necessary to redirect light from the f_{ceo} stabilization loop to obtain the comb light used to generate our beatnote. This introduced an uncertainty that precludes absolute frequency measurements. We measured the unlocked f_{ceo} before and after experiments and observed a 2 MHz drift over two hours. Additionally, we experienced frequent loss of the 10 MHz clock signal used to lock f_{rep}, which was obtained from a GPS reference frequency generator with satellite receiver. Without the clock signal, the uncertainty in f_{rep} is on the order of tens or hundreds of Hz, which multiplies by $n \approx 2000000$ comb teeth to generate absolute frequency uncertainty of hundreds of MHz. With continued technical efforts it should be possible to obtain absolute frequency measurements in Xe spectroscopy.